

# Digital Fourier Microscopy and its Application to Soft Matter Systems

Inaugural dissertation

for the attainment of the title of doctor  
in the Faculty of Mathematics and Natural Sciences  
at the Heinrich Heine University Düsseldorf

presented by

**Manuel Alejandro Escobedo Sánchez**  
from Mexico City, Mexico.

Düsseldorf, May, 2022.



from the institute for Experimental softmatter group  
at the Heinrich Heine University Düsseldorf

Published by permission of the  
Faculty of Mathematics and Natural Sciences at  
Heinrich Heine University Düsseldorf

Examiners:

1. Prof. Dr. Stefan U. Egelhaaf
2. Prof. Dr. Jürgen Horbach

Date of oral examination:



## Declaration of Originality

I declare under oath that I have produced my thesis independently and without any undue assistance by third parties under consideration of the 'Principles for the Safeguarding of Good Scientific Practice at Heinrich Heine University Düsseldorf. To the best of my knowledge it is not substantially the same as any that I have submitted, or, is being concurrently submitted for a degree or diploma or other qualification at the Heinrich Heine University Düsseldorf or any other University or similar institution except as specified in the text.

I further state that this thesis contains no material previously published or written by another person except where due reference is made by correct citation. This includes any thoughts taken over directly or indirectly from printed books and articles as well as all kinds of online material. It also includes my own translations from sources in a different language.

I also agree that the thesis may be tested for plagiarized content with the help of plagiarism software. I am aware that failure to comply with the rules of good scientific practice has grave consequences and may result in expulsion from the programme.

Düsseldorf, 13.05.2022

Manuel Alejandro Escobedo Sánchez



Soft matter systems consist of microscopic substances dispersed in a dispersion medium. Usually, the microscopic substance is composed of colloidal particles, with a typical size from a few nanometers to a few micrometers. The particles' motion is mainly governed by thermal agitation. Conversely, when thermal agitation does not play a role in the system's dynamics, the particles (referred to as grains) can only move due to the drag of external forces. Having for both types of systems a wide range of applicability in everyday use. Hence, the importance of experimentally studying microscopic or macroscopic properties. Recently, Digital Fourier Microscopy (DFM) has been introduced. It is a conceptual framework applied to a time series of images to obtain static and dynamic properties of colloidal systems. In this thesis, we present an optimization of the DFM analysis scheme and show a variety of its applications. The different optimization algorithms decrease the computational time of analysis.

Also, we present an extension of the theoretical framework by including the effects of moderate multiple scattering, allowing us to define a limit of applicability of the techniques for moderately turbid suspensions. We employ, as well, DFM to extract microrheological properties such as the complex viscosity for various systems, including viscous, visco-elastic, biological, and other complex fluids. In addition, we use DFM to study the contribution of polydispersity to the velocity deviations of sedimenting colloidal systems. Moreover, we extend the physical understanding of the transition between colloidal and granular dynamics by using real and reciprocal space observables. Complementary, we present the polydisperse Langevin model, computer simulations, and experimental results.

Furthermore, we study the extension of the DFM framework to X-Ray radiographs, where we extract the dynamics of sedimenting and fluidized granular suspensions. Finally, we introduce the Rheo-DFM framework and use it to characterize the shear profile imposed by a plate-plate shear cell to a colloidal system.



*Pus... ¿Qué hiciste Hipólito?*



---

## Contents

<b>1</b>	<b>Introduction</b>	<b>1</b>
<b>2</b>	<b>Analysis of soft matter in Real and Fourier space</b>	<b>3</b>
2.1	Static Correlations . . . . .	3
2.2	Dynamic Correlations . . . . .	7
2.3	Langevin picture of Brownian motion . . . . .	10
2.4	Generalized Brownian Particle in a viscoelastic medium, viscometry	13
2.5	Brownian Particle in the presence of an external Force, the linear regime . . . . .	15
2.6	Intermediate scattering function from a distribution of velocities . . .	17
2.7	Polydisperse Langevin Description . . . . .	19
2.7.1	Reduced Units . . . . .	21
2.7.2	Analytical Gaussian Model under the presence of gravity . . .	22
2.7.3	Polydisperse Ermack-McCammon Algorithm . . . . .	24
2.7.4	Simulation Example and validation . . . . .	27
<b>3</b>	<b>Experimental Methods</b>	<b>29</b>
3.1	Optical Regimes . . . . .	29
3.2	Digital Fourier Microscopy and Heterodyne Near Field Scattering . .	31
<b>4</b>	<b>Summary of Experimental Results</b>	<b>35</b>
4.1	Optimized algorithms for DFM . . . . .	35
4.1.1	Temporal sampling optimization . . . . .	36
4.1.2	Spatial sampling optimization . . . . .	41
4.2	Effect of moderate multiple scattering in heterodyne near field scattering . . . . .	45
4.2.1	HNFS Signal in Real Space . . . . .	46
4.2.2	HNFS Signal in Reciprocal Space . . . . .	49
4.3	Microliter viscometry . . . . .	52
4.3.1	Ideal, biological and visco-elastic fluids . . . . .	53
4.3.2	Tracer size in microliter viscometry . . . . .	59
4.4	Velocity deviations from the sedimentation of dilute systems . . . . .	62
4.4.1	Polydisperse Langevin Model . . . . .	63
4.4.2	Experimental Results . . . . .	68
4.5	From colloid to grain. A dynamic description of sedimentation in dilute systems . . . . .	72
4.5.1	Effect of an external force in real and reciprocal space observables: mean squared displacement and intermediate scattering function . . . . .	73

4.5.2	Experimental Results . . . . .	81
4.6	Digital Fourier Analysis of X-Ray radiographs of granular suspensions	86
4.6.1	Samples, X-ray Radiographs and Data Analysis . . . . .	87
4.6.2	X-DFA on Syntetic Radiographs . . . . .	92
4.7	Dynamics of sheared particles: Rheo-DFM . . . . .	105
<b>5</b>	<b>Conclusions</b>	<b>112</b>
	<b>References</b>	<b>118</b>

# 1 Introduction

Soft matter systems consist of a microscopic substance dispersed in a dispersion medium [1]. Usually, the microscopic substance is composed of colloidal particles, with a typical size from a few nanometers to a few micrometers. The dispersion medium is often a liquid. These particles are considered small enough to minimize the effects of gravity. These systems are present in everyday life [2]. Examples are seen in the food industry [3], like chocolate or milk, to name a few, in most common everyday technological appliances, like the liquid crystal inside of screens [4]. Moreover, the variety of these systems is also present in Biology, such as cells, bacteria, and proteins [5].

The microscopic properties of colloidal dispersions (for simplicity, samples) are experimentally studied with electromagnetic radiation by analyzing the signal resulting from the interaction of this probing radiation with the sample [6–8]. Thus, different experimental techniques are named according to the electromagnetic radiation properties (wavelength, coherence, etc.), such as the case of Optical Microscopy, Dynamic and Static Light scattering (DLS and SLS). On the other hand, macroscopic properties can be determined by the system’s flow properties. These experiment types are known as Rheology tests [9, 10]. For example, the shear viscosity is the property that describes the opposition of a suspension to flow. The viscosity is susceptible to particle shape, size, and concentration. It can also reflect the interaction between particles, as well as internal structural changes or aggregation [9]. Furthermore, in order to gain more insights into how the microscopic and macroscopic properties are linked, a combination of the previously described techniques has been developed [11–14].

Recently, Digital Fourier Microscopy (DFM) has been introduced [7]. It is a conceptual framework applied to a time series of images to obtain microscopic properties of colloidal systems. It allows the extraction of static and dynamic properties of the studied sample by performing image analysis on a series of acquired images using an optical microscope. Where no restriction of the illumination properties is imposed, thus various imaging conditions, i.e., an incandescent poly-chromatic lamp, fluorescence imaging, laser, etc, can be employed. With this framework, spatial-temporal information in the reciprocal space is obtained, similar to a Dynamic Light Scattering experiment (DLS), without the need for specialized equipment.

The purpose of this work is to illustrate some of the contributions and applications of the theoretical framework of DFM, including its basic description and extensions. The content of this thesis is presented as follows. Chapter two summarizes the basic concepts of soft matter systems, including static and dynamic

correlations, the Langevin picture of Brownian motion, and the main definitions of observables. In chapter three, we introduce the different optical regimes and the theoretical framework of Digital Fourier Microscopy.

In chapter four, we summarize all our experimental results, where each subsection presents a different application of the DFM framework. These include Optimized algorithms for DFM (Sec.4.1), Effect of moderate multiple scattering in heterodyne near field scattering (Sec.4.2), Microliter viscometry (Sec.4.3), Velocity deviations from sedimentation of dilute systems (Sec. 4.4), From colloid to grain, a dynamic description of sedimentation in dilute systems (Sec. 4.5), Digital Fourier Analysis of X-Ray radiographs of granular suspensions (Sec.4.6), and Dynamics of sheared particles: Rheo-DFM (4.7). Finally, in chapter five, we present our conclusions.

## 2 Analysis of soft matter in Real and Fourier space

### 2.1 Static Correlations

Soft matter systems consist of a microscopic substance dispersed in a dispersion medium [1]. Usually, the microscopic substance is composed of colloidal particles, with typical size from a few nanometers to a few micrometers, and the dispersion medium is often to be a liquid. These particles are considered small enough to minimize the effects of gravity, but larger than the dispersion medium molecules. Hence, the liquid can be approximated as a continuum.

For simplicity, we will consider a system of  $N$  spherical particles of diameter  $\sigma$  immersed in a liquid. These type of systems are very sensitive to external forces and thermal agitation, which is also known as Brownian motion (random movement of the particles due to constant collisions with the molecules of the solvent). Furthermore, these particles interact between themselves via a pair-wise interaction potential, denoted by  $U(\mathbf{r})$ . Where  $\mathbf{r}$  is the distance vector that connects the center of mass between two particles.

In the following we will consider simple pair-wise interaction potential, having  $U(\mathbf{r})$  to be spherically symmetric, i.e. it only depends on the magnitude of  $\mathbf{r}$ , hence  $U(\mathbf{r})=U(r)$ .

One of the simplest form of pair-wise interaction potential is the so-called Hard Sphere potential. It represents how particles are not allowed to interpenetrate or overlap, this is achieved by having a very strong repulsion when  $r < \sigma$ . The mathematical representation of a Hard Sphere potential is given by,

$$U_{HS}(r) = \begin{cases} \infty & r < \sigma \\ 0 & r \geq \sigma. \end{cases} \quad (1)$$

Although in nature there are many different interaction potentials, it is out of the scope of this work to describe in detail all of them. For more information regarding classical statistical mechanics theoretical framework, please refer to [1, 15–18].

Once the interaction between particles is sketched, we can define useful quantities to describe the studied system. One of them is the bulk number density ( $\rho$ ),

$$\rho = \frac{N}{V}. \quad (2)$$

It indicates the number of particles ( $N$ ) in the total volume ( $V$ ). Even though it is usually used, a more convenient quantity to represent the amount of particles in the solution is the particle volume fraction ( $\phi$ ). It is defined as the ratio between the occupied volume of the particles ( $NV_p$ ) over  $V$ . Having  $V_p$  as the volume of

one particle, thus the expression of volume fraction is given by

$$\phi = \frac{NV_p}{V} = \frac{\pi}{6}\sigma^3\rho. \quad (3)$$

Fig.1 displays rendered Hard Sphere systems with different volume fractions. The left panel shows a dilute one with  $\phi=0.05$ , and the right panel depicts a concentrated one with  $\phi=0.35$ .

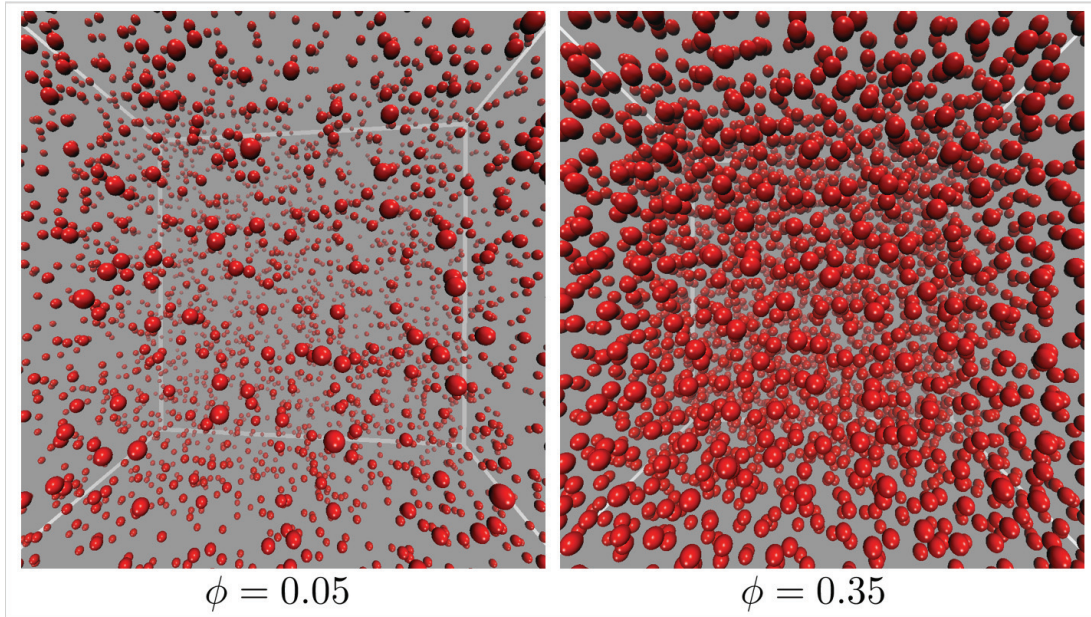


Fig. 1: Snapshots of Hard Sphere systems with different volume fraction ( $\phi$ ),  $\phi=0.05$  (left), and  $\phi=0.35$  (right). The illustrations were made by rendering the particle coordinates from our Monte Carlo computer simulations based on the Metropolis algorithm [18].

As bulk property,  $\rho$  does not contain any information of the configuration of the system, i.e. internal arrangement or micro-structure. Thus, it is necessary to define a function capable of describing the position of each particle. This is achieved by introducing the spatial-density  $\rho(\mathbf{x})$ , as it encloses the position of each particle in the system. Each particle is considered point-like, and in any given configuration of the system, the spatial-density is given by,

$$\rho(\mathbf{x}) = \sum_{\mathbf{N}} \delta(\mathbf{x} - \mathbf{x}_j). \quad (4)$$

The ensemble average over all possible configurations of  $\rho(\mathbf{x})$  for an homogeneous system is known as the average one-particle density,  $\rho_0(\mathbf{x})$ ,

$$\rho_0(\mathbf{x}) = \langle \rho(\mathbf{x}) \rangle = \frac{N}{V} = \rho. \quad (5)$$

Eq.(5) doesn't contain any new information when compared to Eq.(2). Thus, in order to be able to study structural arrangements or density fluctuations, another tool has to be introduced. This is the case of density correlations.

Correlation is a statistical operation for estimating fluctuations or changes of a variable with respect to another. When the variable is compared with itself, the operation is known as auto-correlation, and cross-correlation when the comparison is made among different variables [19]. For our purposes, the correlation is one of the main operations for studying density fluctuations over a sample. These fluctuations could be spatial density fluctuations or temporal density fluctuations.

A correlation function that captures spatial density fluctuations is the two particle density correlation, also known as the density-density correlation function. It is given by,

$$\rho^2(\mathbf{x}, \mathbf{x}') = \langle \rho(\mathbf{x})\rho(\mathbf{x}') \rangle. \quad (6)$$

When Eq.(6) is normalized, it is known as the pair distribution function or radial distribution function [15, 16, 18],

$$g(|\mathbf{x} - \mathbf{x}'|) = \frac{\rho^2(\mathbf{x}, \mathbf{x}')}{\rho_0(\mathbf{x})\rho_0(\mathbf{x}')} = \frac{1}{\rho^2} \left\langle \sum_{j=1}^N \sum_{i=1, i \neq j}^N \delta(\mathbf{x} - \mathbf{x}_i) \delta(\mathbf{x} - \mathbf{x}'_j) \right\rangle. \quad (7)$$

The radial distribution function  $g(r)$  indicates the probability of finding a particle at a certain distance  $r = |\mathbf{x} - \mathbf{x}'|$  from another particle, where  $\mathbf{x}$  and  $\mathbf{x}'$  are each corresponding particle coordinates.

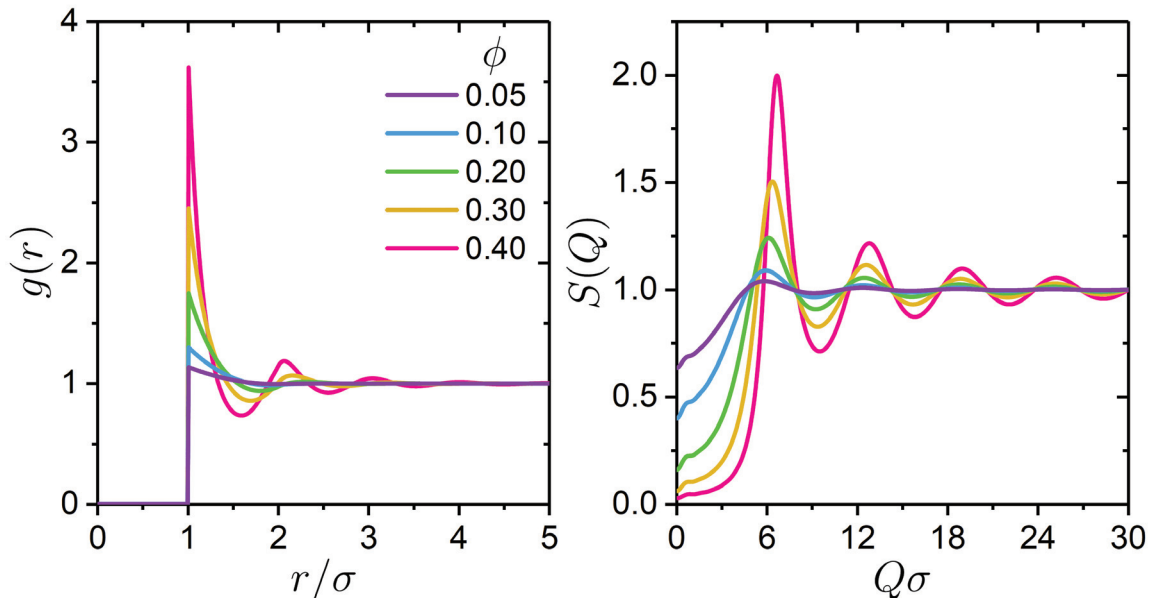


Fig. 2: Radial distribution function from a hard sphere dispersion at different volume fractions (left) and its corresponding structure factors (right). Data has been obtained from Monte Carlo simulations using the Metropolis algorithm for a system composed of 1024 particles, and an ensemble average over  $10^6$  configurations.

For hard sphere systems, the radial distribution has three main features: It is zero for  $r < \sigma$ , it presents a distinct peak at  $r = \sigma$ , and it displays oscillations around the unity for intermediate distances. Moreover, due to its normalization

$g(r) = 1$  when  $r \rightarrow \infty$ . This because for large distances, the homogeneity of the system makes equally probable to find a particle, as all spatial correlations are averaged out. An illustration of the radial distribution for a hard sphere dispersion is illustrated on the left panel of Fig.2.

Another common tool for studying structural arrangement is the Fourier space version of the density-density correlation function (Eq.(6)), is the Structure factor  $S(Q)$  [1]. In order to obtain it, let us start by performing a spatial Fourier transform of Eq.(4),

$$\hat{\rho}(\mathbf{Q}) = \sum_{\mathbf{N}} \exp(-i\mathbf{Q} \cdot \mathbf{x}_j). \quad (8)$$

In the Fourier space, a collection of  $N$  localized particles, is described by a superposition of planar waves, having the position of each particle ( $\mathbf{x}_j$ ) projected onto the wave vector  $\mathbf{Q}$ . The magnitude of  $\mathbf{Q}$  is  $Q = 2\pi/L$ . Hence,  $\mathbf{Q}$  can be thought as a "measuring ruler" of inverse length  $L$ . Then, the calculation of the structure factor is similarly defined as Eq.(6), i.e.

$$S(\mathbf{Q}) \equiv \frac{1}{N} \langle \hat{\rho}(\mathbf{Q}) \hat{\rho}^*(\mathbf{Q}) \rangle = 1 + \frac{1}{N} \left\langle \sum_{l=1}^N \sum_{n \neq l}^N \exp(-i\mathbf{Q} \cdot (\mathbf{x}_l - \mathbf{x}_n)) \right\rangle. \quad (9)$$

Here, (\*) refers to the complex conjugate. Moreover, it is worth noting that the only difference between Eq.(6) and Eq.(9) is their normalization. Furthermore, the structure factor is related to the radial distribution function by [1],

$$S(\mathbf{Q}) = 1 + \rho \int e^{-i\mathbf{Q} \cdot \mathbf{r}} [g(\mathbf{r}) - 1] d\mathbf{r} + (2\pi)^3 \rho \delta(\mathbf{Q}). \quad (10)$$

Thus,  $S(\mathbf{Q})$  shows similar behaviour as  $g(\mathbf{r})$  (Fig.2 right panel). The main difference relies in the probing length scale, having  $\mathbf{Q}$  instead of  $\mathbf{r}$ . Moreover, it also contains peaks that represent the mean inter-particle distance at  $Q\sigma \approx 2m\pi$ , for  $m=1$ . These, become more evident for volume fractions larger than  $\phi \sim 0.20$ , as for these volume fractions the system becomes more structurized. Hence, more peaks appear for  $m = 2, 3, \dots$

As a final remark we mention the limiting behaviour of  $S(Q)$ . It is obtained at the large wave vector limit, i.e.  $S(Q \rightarrow \infty) = 1$ , reminding that higher wave vectors imply smaller probed length scales.

## 2.2 Dynamic Correlations

In the previous section we have introduced the use of correlations as a statistical function to quantify similarity. This is carried out by a variable multiplication and an average over all possible configurations that represent the same system's state. The latter is referred as an ensemble average. When computing static quantities, the temporal path or how the configurations are changing in time is irrelevant. Thus, if dynamical behaviour is of interest, the time dependence has to be introduced. In the following, we will assume the Ergodic hypothesis, which states that the overall ensemble average is equivalent to a sufficiently sampled time average [1].

The dynamical behavior of a system that undergoes Brownian motion can be represented as a stochastic or random process. Mathematically, multiple types of stochastic processes exist [19, 20] and usually, for systems in equilibrium, there are two types: The first one is known as stationary stochastic process. It is defined as a stochastic process where its joint probability distribution function does not depend on time shifts. This is a direct consequence of time-invariance of a physical system [19]. The other type of stochastic process is the one known as wide sense stationary process. It is defined by three conditions: The first moment of the distribution doesn't vary with time, it has a finite second moment for any given time, and at least possess stationary increments. That means, stationary only in time increments or equivalently to time differences [20, 21].

Stationary or wide sense stationary processes of a dynamical arbitrary function  $f(t)$  can be characterized by the dynamical auto-correlation function  $C(\tau)$ . It is defined as

$$C(\tau) = \langle f(t_0)f(t_0 + \tau) \rangle_{t_0}, \quad (11)$$

where  $t_0$  is starting time.  $C(\tau)$  captures the similarity of  $f(t)$  for a given  $t_0$ , when compared to itself at different later time ( $t_0+\tau$ ). The time  $\tau$  is known as delay time and it is defined as  $\tau = k\Delta t$ ,  $k$  an integer, and  $\Delta t$  the sampling time. The brackets  $\langle \rangle_{t_0}$  indicate that an average over all starting times  $t_0$  is performed. If the interest is in the shape of  $C(\tau)$  rather than the absolute magnitude, it is convenient to normalize Eq.(11) and obtain the normalized dynamical auto-correlation function. There are two possibilities of normalization [21],

$$\mathcal{C}(\tau) = [C(\tau) - \langle f(t_0) \rangle_{t_0}^2] / \langle f(t_0) \rangle_{t_0}^2. \quad (12)$$

and

$$c(\tau) = [C(\tau) - \langle f(t_0) \rangle_{t_0}^2] / \langle f^2(t_0) \rangle_{t_0}. \quad (13)$$

In both cases the baseline has been subtracted, and divided by either the square of the first moment (Eq.(12)) or by the second moment (Eq.(13)). Usually, Eq.(13)

is the one being used due to its similarity to the correlation coefficient [21]. It starts at the unity for  $\tau = 0$ , and for sufficiently large delay times it decays to zero.

When the stationary status is not known apriori, it is convenient to use the structure function or the mean square change [21],

$$D(\tau) = \langle [f(t_0 + \tau) - f(t_0)]^2 \rangle_{t_0}. \quad (14)$$

This because of the possibility of having another type of stationary process that is not wide sense or stationary process, where Eq.(11) is not well-defined [21]. Moreover, for stationary processes the structure and the auto-correlation functions are related through [21]

$$D(\tau) = 2C(0) - 2C(\tau). \quad (15)$$

Some properties of the structure functions are: They start at zero for  $\tau = 0$ , are always positive, and reach to a maximum value of  $2C(0)$ . It is important to point out that although it has a similar name, the structure function has nothing to do with the structure factor from Eq.(9).

The expressed concepts in Eq.(11) can be applied to the dynamical density

$$\rho(\mathbf{x}, t) = \sum_{\mathbf{N}} \delta(\mathbf{x} - \mathbf{x}_j(t)), \quad (16)$$

and obtain the normalized density-density correlation function in the real space. It is the temporal counterpart of the radial distribution function  $g(\mathbf{r})$  known as the van Hove function [22]. Using the same definition for the distance between particles as in Eq.(7), the van Hove function is defined as

$$G(\mathbf{r}, \tau) = \frac{1}{N\rho} \left\langle \sum_{j=1}^N \sum_{i=1}^N \delta[\mathbf{r} - (\Delta\mathbf{x}_{ji}(t_0, \tau))] \right\rangle_{t_0} \quad (17)$$

where  $\Delta\mathbf{x}_{ji}(t_0, \tau) = \mathbf{x}_j(t_0 + \tau) - \mathbf{x}_i(t_0)$  is the displacement between particles  $i, j$  in the time interval  $\tau$ . The double summation of Eq.(17) can be split into the self and distinct terms. The self van Hove function is defined when  $i = j$ , i.e.

$$G_s(\mathbf{r}, \tau) = \frac{1}{N\rho} \left\langle \sum_{j=1}^N \delta[\mathbf{r} - (\Delta\mathbf{x}_i(t_0, \tau))] \right\rangle_{t_0} \quad (18)$$

where  $\Delta\mathbf{x}_i(t_0, \tau)$  is the traveled distance per particle. The self part represents the probability of a particle being at  $\mathbf{x}(t_0)$  at  $t_0$  and then displaced by  $\Delta\mathbf{x}_i$  during  $\tau$ .

The complementary part of Eq.(18)  $i \neq j$ , is known as the distinct van Hove function

$$G_d(\mathbf{r}, \tau) = \frac{1}{N\rho} \left\langle \sum_{j=1}^N \sum_{i \neq j}^N \delta[\mathbf{r} - (\Delta\mathbf{x}_{ji}(t_0, \tau))] \right\rangle_{t_0}. \quad (19)$$

Noting that for  $\tau=0$ ,  $G_d(\mathbf{r}, \tau=0) = g(\mathbf{r})$ . Hence, the distinct part of the van Hove function represents the dynamical analogue of the radial distribution function.

In a similar manner, the dynamical Fourier density is defined by

$$\hat{\rho}(\mathbf{Q}, t) = \sum_{\mathbf{N}} \exp(-i\mathbf{Q} \cdot \mathbf{x}_j(t)). \quad (20)$$

It is used to obtain the collective dynamical structure factor [1],

$$S_c(\mathbf{Q}, \tau) = \frac{1}{N} \left\langle \sum_{j=1}^N \sum_{j=1}^N \exp[-i\mathbf{Q} \cdot \Delta\mathbf{x}_{ji}(t_0, \tau)] \right\rangle_{t_0}, \quad (21)$$

and subsequently it can be decomposed in a self and distinct part.

To conclude this section, we show the result of computing the structure function (Eq.(14)) of the dynamical Fourier density (Eq.(20)), obtaining

$$D(\mathbf{Q}, \tau) = 2S(\mathbf{Q}) - 2S_c(\mathbf{Q}, \tau). \quad (22)$$

By defining the collective intermediate scattering function [1, 23]

$$f_c(Q, \tau) \equiv \frac{S_c(\mathbf{Q}, \tau)}{S(\mathbf{Q})} \quad (23)$$

Eq.(22) can be expressed as

$$D(\mathbf{Q}, \tau) = 2S(\mathbf{Q}) [1 - f_c(\mathbf{Q}, \tau)], \quad (24)$$

The previous two equations are the main observables obtained in experiments such as Digital Fourier Microscopy (DFM) and Dynamic Light Scattering (DLS) [1, 7, 8, 24], while Eq.(18) and Eq.(19) can be calculated through particle coordinates extracted by means of particle tracking algorithms from optical microscopy expedients [25].

### 2.3 Langevin picture of Brownian motion

The first person to introduce a mathematical description for particle dispersions undergoing Brownian motion was A. Einstein in 1905 [26]. His work was based on the diffusion equations of A. Fick [27], where an ensemble of particles is considered and their concentration tends to be uniform over all available space. The latter leads to the diffusion equation for the particle concentration  $\rho(\mathbf{x}, t)$ . The work was later extended by M. Smoluchowski (1916) [28] introducing the equation named after him. This equation is able to describe the density fluctuations of a colloidal sample in the presence of an external field. A more general equation, similar to Schrödinger's equation, was obtained by Fokker-Planck (1916-1917), which describes the temporal evolution of the probability distribution function  $w(\mathbf{x}, t)$  from a stochastic process that results from Brownian motion [19, 29, 30].

In the following we will summarize an alternative approach obtained by P. Langevin in 1908 [31]. It has been widely used for performing computer simulations to study the dynamics of colloidal suspensions with many different interactions [32], and it is equivalent to the solution of the Smoluchowski equation [1]. The Langevin framework is based on a stochastic equation of motion that describes the position  $\mathbf{x}(t)$  of a Brownian particle under the influence of a fluctuating random force. This in order to account for the thermal collisions of the solvent molecules with the Brownian particle. For simplicity we will derive it in one dimension but it can be easily extended to three.

Following Newton's second law, the Langevin equation for a particle in an ideal viscous fluid is

$$m\ddot{x}(t) = -\xi\dot{x}(t) - \frac{d}{dx}U_{\text{ext}}(x) + f(t), \quad (25)$$

where  $m$  is the mass of the particle. The first term on the right hand side of the equation corresponds to the frictional force that the particle experiences due to the continuous collisions with the solvent molecules. It is proportional to the particle velocity and the proportionality constant  $\xi$  is known as the friction coefficient. For a spherical particle  $\xi = 3\pi\eta\sigma$ , with  $\eta$  the shear viscosity of the solvent and  $\sigma$  the particle diameter. The second term in Eq.(25) corresponds to the force generated by an external potential  $U_{\text{ext}}(x)$ , this can be the gravitational, electric or the resulting one from the superposition of inter-particle interactions. Finally, the third term corresponds to the Gaussian stochastic force  $f(t)$ . It satisfies three properties:  $f(t)$  is Gaussian distributed, its first moment is zero,  $\langle f(t) \rangle = 0$ , and it is delta convoluted  $\langle f(t)f(t') \rangle = 2\xi k_B T \delta(t - t')$ . Here  $k_B$  is the Boltzmann constant and  $T$ , the temperature. The latter represents the fluctuation-dissipation theorem [33, 34].

It is worth mentioning that a sum of random Gaussian variables is also a Gaussian variable, and a random Gaussian variable is uniquely defined through its first two moments, the mean and variance [19]. Thus, the probability distribution function  $P(x)$  of a Gaussian random variable  $x$  is given by:

$$P(x) = \frac{1}{\sqrt{2\pi\sigma^2}} \exp \left[ -\frac{(x - \langle x \rangle)^2}{2\sigma^2} \right] \quad (26)$$

where  $\langle x \rangle$  is the mean of  $x$  and  $\sigma^2 = \langle [x - \langle x \rangle]^2 \rangle$  the variance.

In the following only small inertial effects are considered thus, the second derivative in Eq.(25) is safely neglected. This leads the over damped Langevin equation,

$$\dot{x}(t) = -\frac{1}{\xi} \frac{d}{dx} U_{\text{ext}}(x) + \frac{1}{\xi} f(t). \quad (27)$$

Here, we present the solution of Eq.(27) for a free particle, i.e. no external interactions ( $U_{\text{ext}}(x) = 0$ ). However, in Sec.2.5 we discuss the coupling of a particle to an external force. The solution, considering the initial condition for a starting time  $t_0$  to be  $x(t=t_0) = x_0$ , is given by,

$$x(t_0 + \tau) = x_0 + \frac{1}{\xi} \int_{t_0}^{t_0+\tau} f(t') dt'. \quad (28)$$

Where  $\tau$  is a delay time. Due to the nature of a stochastic differential equation, the solution shown in Eq.(28) lacks of meaning. Rather it is more convenient to estimate average quantities, such is the case of the mean value  $\langle x(t) \rangle$ . Recalling the properties of the stochastic force  $f(t)$ , we obtain,

$$\langle x(t_0 + \tau) \rangle - \langle x(t_0) \rangle = \frac{1}{\xi} \int_{t_0}^{t_0+\tau} \langle f(t') \rangle dt' = 0. \quad (29)$$

The previous result illustrates a condition of stationarity, and it can also be seen as the first moment of the one dimension probability distribution function  $w(x, \tau | t_0)$ .

We continue by computing the second moment or variance,

$$\sigma_x^2(\tau) = \langle [x(t_0 + \tau) - \langle x(t_0 + \tau) \rangle]^2 \rangle = \frac{1}{\xi^2} \int_{t_0}^{t_0+\tau} \int_{t_0}^{t_0+\tau} \langle f(s)f(t') \rangle ds dt'. \quad (30)$$

By using the second property of  $f(t)$  we obtain

$$\sigma_x^2(\tau) = \frac{2k_B T}{\xi} \tau = 2D\tau, \quad (31)$$

where  $D$  is the diffusion coefficient. Eq.(31) relates to the Mean Squared Displacement (MSD) by,

$$\langle \Delta x^2(t_0, \tau) \rangle = \langle [x(t_0 + \tau) - x_0]^2 \rangle = \sigma_x^2(\tau). \quad (32)$$

Thus, for a system with stationary first moment the variance and MSD are equal. The rearrangement of Eq.(31) leads to the Einstein's relation

$$D = \frac{\langle \Delta x^2(t_0, \tau) \rangle}{2\tau} = \frac{k_B T}{\xi}, \quad (33)$$

and by using the Stokes's friction coefficient of a sphere ( $\xi = 3\pi\eta\sigma$ ) the right hand side of the equation is also known as the Stokes-Einstein relation.

By substitution of Eq.(29) and Eq.(31) in Eq.(26) the distribution  $w(x, \tau|t_0)$  can be found and expressed as follows:

$$w(x, \tau|t_0) = \frac{1}{\sqrt{4\pi D\tau}} \exp \left[ -\frac{(\Delta x(t_0, \tau))^2}{4D\tau} \right]. \quad (34)$$

Eq.(34) is the exact solution of the Fokker-Plank equation, and for this case  $w(x, \tau|t_0)$  corresponds to the self part of the van Hove function (Eq.18) [1].

Once the probability distribution function is known, we can proceed to calculate the self intermediate scattering function along the  $x$  axis  $f(Q_x, \tau)$  by computing

$$\begin{aligned} f(Q_x, \tau) &= \langle \exp [iQ_x \Delta x(t_0, \tau)] \rangle \\ &= \int \exp [iQ_x \Delta x(t_0, \tau)] w(\Delta x, \tau|t_0) d\Delta x \\ &= \exp \left[ -\frac{1}{2} Q_x^2 \langle \Delta x^2(t_0, \tau) \rangle \right], \end{aligned} \quad (35)$$

or equivalently

$$f(Q_x, \tau) = \exp [-Q_x^2 D\tau]. \quad (36)$$

Eq.(35) and Eq.(36) are two important results. The first one, has been used for measuring the MSD in light-scattering experiments for dilute tracer particles in different complex media [23, 35, 36]. The second one, when combined with the Stokes-Einstein relation (Eq.(33)) is very useful for characterizing the particle size in a dilute colloidal suspension. However, special attention has to be taken as it has to be considered that in an experimentally accessible colloidal suspension, the particles are very unlikely to have the same particle size, rather they follow a particle size distribution. This leads to a distribution of diffusion coefficients, thus an averaged measured diffusion coefficient is obtained [5, 37]. For narrow distributions, and without losing generality, we will use a Gaussian distribution to represent the distribution of diffusion coefficients and illustrate a possible exten-

sion of Eq.(36). This approach is also known as the cumulant method [37,38],

$$\begin{aligned}
f(Q_x, \tau) &= \int_0^\infty \exp[-Q_x^2 D \tau] P(D) dD \\
&= \exp[-Q_x^2 \langle D \rangle \tau] \int_{-\infty}^\infty \exp[-Q_x^2 (D - \langle D \rangle)] P(D - \langle D \rangle) d(D - \langle D \rangle) \\
&= \exp\left[-Q_x^2 \langle D \rangle \tau \left\{1 - \frac{1}{2} Q_x^2 \langle D \rangle \tau \frac{\delta_D^2}{\langle D \rangle^2}\right\}\right], \tag{37}
\end{aligned}$$

where  $\delta_D^2$  is the variance of the diffusion coefficient distribution and the ratio  $\delta_D/\langle D \rangle$  is known as the coefficient of variation or polydispersity index of the diffusion coefficient.

## 2.4 Generalized Brownian Particle in a viscoelastic medium, viscometry

The purpose of this section is to sketch an abbreviated derivation of the Generalized Stokes-Einstein relation (GSE), and to introduce the line of arguments for understanding the foundations of passive one-point micro-rheology. This by following ref [39]. Mason and Weitz were the first to experimentally test the GSE relation (1995). They were able to probe bulk visco-elastic properties such as the complex viscosity ( $\eta^*(\omega)$ ) or the visco-elastic modulus ( $G^*(\omega)$ ) of complex fluids. This by relating them to the Laplace transformation of the mean squared displacement of tracer particles. These relations were obtained via a Laplace analysis of the Generalized Langevin Equation [40,41]. The later approach was the beginning of a new experimental method known as passive micro-rheology, and it has been applied to a broad type of biological and complex systems [36,42–45].

To improve the experimental errors associated with the Laplace technique, a Fourier analysis of the generalized Langevin equation was introduced [35,39,46]. In the following we will present the Fourier analysis of the generalized Langevin equation for a particle with velocity ( $v(t) = \dot{x}(t)$ ) and without external forces [16],

$$m\dot{v}(\tau) = f(\tau) - \int_0^\tau \zeta(\tau - t')v(t')dt'. \tag{38}$$

Here, for simplicity, we have set  $t_0 = 0$ . The previous equation differs from Eq.(25) in the frictional term, here  $\zeta(\tau)$  is the memory function that describes the local viscoelastic response of an isotropic, complex fluid. The viscoelasticity of a fluid relapses in its ability to store and dissipate energy upon mechanical perturbations [9]. In order to proceed, the properties described in Sec.2.3 for the stochastic random force  $f(\tau)$  will be assumed unaltered except for the fluctuation-dissipation relation, taking the form  $\langle f(0)f(\tau) \rangle = 2k_B T \zeta(\tau)$  [16,33,47]. Noticing that with  $\zeta(\tau) = \xi\delta(\tau)$  Eq.(25) is recovered.

In addition, let us consider that the distribution of random forces is entirely decoupled from a past distribution  $v(0)$ . This imposes

$$\langle v(0)f(\tau) \rangle = 0. \quad (39)$$

Eq.(38) can be solved for  $v(\omega)$  in the Fourier temporal space. We will show the results using the same mathematical assumptions as in [39]. Using the convolution theorem, it is possible to obtain

$$v^*(\omega) = \frac{f^*(\omega) + mv(0)}{i\omega m + \zeta^*(\omega)}. \quad (40)$$

Moreover, it is possible to relate the memory function ( $\zeta^*(\omega)$ ) with the velocity autocorrelation function by multiplying Eq.(40) by  $v(0)$  and perform an ensemble average. The previous leads to

$$\langle v(0)v^*(\omega) \rangle = \frac{k_B T}{i\omega m + \zeta^*(\omega)}, \quad (41)$$

where we have made use of the equipartition theorem, i.e.  $m\langle v(0)v(0) \rangle = k_B T$ . The first term in the denominator of Eq.(41) is the contribution of inertial effects and, again, will be assumed negligible for the following [41].

Finally, in order to relate the memory function to the complex viscosity it is needed to know the exact solution of the flow field for an arbitrary complex fluid surrounding a moving sphere. For this, the authors in references [39–41, 48] have assumed and successfully proven that a natural extension of the case of purely viscous systems can be assumed, taking the form

$$\eta^*(\omega) = \frac{\zeta^*(\omega)}{3\pi\sigma}. \quad (42)$$

Hence, the relation between the complex viscosity and the velocity auto-correlation function is obtained,

$$\eta^*(\omega) = \frac{k_B T}{3\pi\sigma \langle v(0)v^*(\omega) \rangle}. \quad (43)$$

Eq.(43) can be expressed in terms of the mean squared displacement  $\langle \Delta x^2(t_0, \tau) \rangle$  by means of the following one dimensional identity [39]

$$\mathcal{F} \{ \langle \Delta x^2(t_0, \tau) \rangle \} = \frac{2}{(i\omega)^2} \mathcal{F} \{ \langle v(0)v(\tau) \rangle \} \quad (44)$$

giving,

$$\eta^*(\omega) = \frac{2k_B T}{3\pi\sigma (i\omega)^2 \mathcal{F} \{ \langle \Delta x^2(t_0, \tau) \rangle \}}. \quad (45)$$

The previous relation is the Generalized Stokes-Einstein (GSE) relation, and it is frequently presented in terms of the complex viscoelastic modulus  $G^*(\omega) =$

$i\omega\eta^*(\omega)$  [9, 49]. This gives rise to

$$G^*(\omega) = \frac{2k_B T}{3\pi\sigma i\omega \mathcal{F}\{\langle \Delta x^2(t_0, \tau) \rangle\}}. \quad (46)$$

The previous equations are the main ingredients for performing microliter viscometry (Eq.(45)) and passive microrheology (Eq.(46)). The latter is achieved by computing the mean squared displacement from computer based particle tracking analysis of microscopy images of tracer particles [43] or by measuring the self intermediate scattering function in dynamic light scattering type experiments performed under non-interacting, dilute tracer concentration [23, 35, 36, 50]. In which, from Eq.(35), the following relation is applied

$$\langle \Delta x^2(t_0, \tau) \rangle = -\frac{2}{Q_x} \ln [f(Q_x, \tau)]. \quad (47)$$

## 2.5 Brownian Particle in the presence of an external Force, the linear regime

In the previous sections we presented the solution of the Langevin equation for a free Brownian particle in an ideal viscous fluid (Sec. 2.3) and in a generalized viscoelastic medium (Sec.2.4). In the following, we present an extension to the particle in an ideal viscous fluid by adding the effect of an external potential,  $U_{\text{ext}}(\mathbf{x})$ . This, leads to an external force

$$\mathbf{F}_D = -\nabla U_{\text{ext}}(\mathbf{x}). \quad (48)$$

In particular, we present it for potentials that lead to a constant external force, such is the case of the gravitational potential or an electric field. For this, we will consider an homogeneous and isotropic viscous medium, where the mobility tensor is constant ( $\boldsymbol{\mu} = \mu$ ), thus its inverse can be expressed as the friction coefficient ( $\zeta = \xi = 1/\mu$ ). Hence, a linear relation of the dragged velocity ( $\mathbf{v}_D$ ) and the external force is found. This, is also known as a linear regime or a Stokes flow [1, 51, 52], having

$$\mathbf{v}_D = \frac{1}{\xi} \mathbf{F}_D. \quad (49)$$

Since  $\mathbf{F}_D$  acts in one specific direction, a description of the Langevin equation in three dimensions is necessary. Thus, by considering  $\mathbf{F}_D$  in  $\hat{z}$ , the three Cartesian coordinates are given by

$$\dot{x}(t) = \frac{1}{\xi} f_x(t), \quad \dot{y}(t) = \frac{1}{\xi} f_y(t), \quad \dot{z}(t) = \frac{1}{\xi} f_z(t) + v_D \quad (50)$$

where  $f_x, f_y, f_z$  are the stochastic forces per coordinate, and  $x_0, y_0, z_0$  the initial conditions of the system at  $t=t_0$ . The solution per coordinate is

$$\begin{aligned} x(t_0 + \tau) &= x_0 + \int_{t_0}^{t_0+\tau} \frac{1}{\xi} f_x(t') dt' \\ y(t_0 + \tau) &= y_0 + \int_{t_0}^{t_0+\tau} \frac{1}{\xi} f_y(t') dt' \\ z(t_0 + \tau) &= z_0 + \int_{t_0}^{t_0+\tau} \frac{1}{\xi} f_z(t') dt' + v_D \tau \end{aligned} \quad (51)$$

Then, the first moment is given by

$$\langle x(t_0 + \tau) \rangle = x_0, \quad \langle y(t_0 + \tau) \rangle = y_0, \quad \langle z(t_0 + \tau) \rangle = z_0 + v_D \tau, \quad (52)$$

where the perpendicular coordinates to the external force ( $x, y$ ) exhibit the same first moment as Eq.(29). Noting that for systems that present drift, ie., systems without a stationary first moment, the mean squared displacement per coordinate

$$\begin{aligned} \langle \Delta x^2(t_0, \tau) \rangle &= \langle [x(t_0 + \tau) - x_0]^2 \rangle = \langle [y(t_0 + \tau) - y_0]^2 \rangle = 2D\tau, \\ \langle \Delta z^2(t_0, \tau) \rangle &= \langle [z(t_0 + \tau) - z_0]^2 \rangle = 2D\tau + v_D^2 \tau^2 \end{aligned}$$

is not the same as the variance, such is the case of the  $z$  component, i.e.

$$\begin{aligned} \sigma_x^2(\tau) &= \langle [x(t_0 + \tau) - \langle x(t_0 + \tau) \rangle]^2 \rangle \\ &= \langle [y(t_0 + \tau) - \langle y(t_0 + \tau) \rangle]^2 \rangle \\ &= \langle [z(t_0 + \tau) - \langle z(t_0 + \tau) \rangle]^2 \rangle \\ &= 2D\tau. \end{aligned} \quad (53)$$

Thus, the perpendicular coordinates to the direction of the force has the same expression of the probability distribution function  $w(x, \tau|t_0)$  in Eq.(34). In contrast, the one parallel to the direction of  $\mathbf{F}_D$ , has the main difference in the first moment, i.e.

$$\begin{aligned} w(x, \tau|t_0) = w(y, \tau|t_0) &= \frac{1}{\sqrt{4\pi D\tau}} \exp \left[ -\frac{(\Delta y(t_0, \tau))^2}{4D\tau} \right], \\ w(z, \tau|t_0) &= \frac{1}{\sqrt{4\pi D\tau}} \exp \left[ -\frac{(\Delta z(t_0, \tau) - v_D \tau)^2}{4D\tau} \right]. \end{aligned} \quad (54)$$

Once the probability distribution function per coordinate is obtained, we can proceed to calculate  $f(\mathbf{Q}, \tau)$  of the 3 dimensional displacement

$$\Delta \mathbf{r}(t_0, \tau) = \Delta x(t_0, \tau) \hat{i} + \Delta y(t_0, \tau) \hat{j} + \Delta z(t_0, \tau) \hat{k}.$$

This, by computing

$$\begin{aligned} f(\mathbf{Q}, \tau) &= \langle \exp [i\mathbf{Q} \cdot \Delta \mathbf{r}(t_0, \tau)] \rangle \\ &= \iiint \exp [i\mathbf{Q} \cdot \Delta \mathbf{r}] w(\Delta x, \tau|t_0) w(\Delta y, \tau|t_0) w(\Delta z, \tau|t_0) d\Delta x d\Delta y d\Delta z \\ &= \exp [-Q^2 D\tau] \exp [iQ_z v_D \tau] \end{aligned} \quad (55)$$

where  $Q = |\mathbf{Q}|$  is the magnitude of the wave vector  $\mathbf{Q}$ . The previous result can be interpreted as a convolution of intermediate scattering functions that encloses statistical independent motion information as,

$$f(Q, \tau) = f_B(Q, \tau) f_D(Q, \tau) \quad (56)$$

where  $f_B(Q, \tau)$  is the intermediate scattering function containing the exponential decay from the Brownian motion, with a characteristic time scale  $\tau_B = 1/DQ^2$  that can be thought analogously as in Eq.(31), i.e.  $1/Q^2 \sim L^2 \sim D\tau$ . The second term,  $f_D(Q, \tau)$  is the one corresponding to the drag from  $\mathbf{F}_D$ , it involves a unitary phasor with frequency  $\omega_D = Qv_D$  or characteristic time  $\tau_D = 1/Qv_D$ . This has the characteristics of ballistic motion, i.e.  $1/Q \sim L \sim v_D\tau$ . Hence, the Fourier space description of the particle motion contains analogue information as in the real space.

## 2.6 Intermediate scattering function from a distribution of velocities

The results in the previous section was performed by solving the Langevin equation of one particle in the presence of a constant external force. In order to generalize it to a distribution of particles, we include a velocity distribution  $P(v)$  in the description. The velocity distribution arises from the fact that each particle of the system can couple differently to the external force, thus imposing different velocities per particle. Some examples are when  $\mathbf{F}_D$  is related to the particle size as in gravity and electrophoresis experiments, or when a spatial velocity profile is distributed over the sample volume. In these cases,  $f_D(Q, \tau)$  for wave vectors parallel to  $\mathbf{F}_D$  becomes the weighted superposition of all possible velocities, i.e.

$$f_D(Q, \tau) = \int_{-\infty}^{\infty} \exp[iQv\tau] P(v) dv. \quad (57)$$

Hence, depending on the velocity distribution, the analytical expression of  $f_D(Q, t)$  can be obtained.

In the following, we show two different examples of  $P(v)$ . The first example is a narrow distribution of velocities approximated by a normal distribution. In this case, a similar cummulant analysis as in Sec.2.3 for  $f_D(Q, t)$  can be performed, thus

$$\begin{aligned} f_D(Q, \tau) &= \int_{-\infty}^{\infty} \exp[iQv\tau] P(v) dv \\ &= \exp[iQ\langle v \rangle \tau] \int_{-\infty}^{\infty} \exp[iQ(v - \langle v \rangle)\tau] P(v - \langle v \rangle) d(v - \langle v \rangle) \\ &= \exp[iQ\langle v \rangle \tau] \exp\left[-\frac{1}{2}Q^2\delta_v^2\tau^2\right]. \end{aligned} \quad (58)$$

Here,  $\langle v \rangle$  is the mean velocity of the distribution and  $\delta_v$  is the standard deviation. We would like to stress out the factorization steps, as this can be performed for any velocity distribution. Furthermore, the final expression of Eq.(58) can be thought of as if  $f_D(Q, \tau)$  has two main contributions. One being the mean directed motion, indicated by the unitary phasor term containing  $\langle v \rangle$ . The second one, the exponential decay containing  $\delta_v$ , is the relative directed motion to the mean directed one. Hence, as a general remark, the intermediate scattering function of a distribution of velocities can be decomposed into the mean directed motion ( $\langle v \rangle$ ), and the relative directed contribution to it ( $v' = v - \langle v \rangle$ ), as

$$f_D(Q, \tau) = \exp [iQ\langle v \rangle\tau] \int_{-\infty}^{\infty} \exp [iQv'\tau] P(v') d(v') \quad (59)$$

here,  $P(v')$  is the relative to the mean velocity distribution.

The second example of velocity distribution is the one present in rheology experiments [9]. Where mechanical deformations of two parallel plates impose a linear velocity profile along one axis ( $\hat{z}$ ), i.e.  $v'(z) = \gamma z$ .  $\gamma$  is known as shear rate. For this case, the integral of Eq.(59) is performed along a certain length ( $L$ ) that encloses the velocity distribution [12, 13], leading to

$$\begin{aligned} f_D(Q, \tau) &= \exp [iQ\langle v \rangle\tau] \frac{1}{L} \int_{-L/2}^{L/2} \exp [iQ\gamma\tau z] dz \\ &= \exp [iQ\langle v \rangle\tau] \frac{\sin (Q\gamma\tau L/2)}{Q\gamma\tau L/2}. \end{aligned} \quad (60)$$

Again, Eq.(60) shows two terms, the unitary phasor from the mean directed motion enclosed in  $L$ , and the second term regarding the relative motion to it.

As a concluding remark, we would like to point out that even though the previous results were shown for one dimensional velocity distributions. The expression shown in Eq.(57) can be generalized to any coordinate system, where the choice of such system will depend on the type of dynamics. The spherical coordinate system is the most common for bacteria, or active systems [53–57]. Furthermore, due to the isotropy of the motion, the relevant information is obtained over the radial projection on  $\mathbf{Q}$ , resulting in a much simpler description ultimately being a 1-D problem [8].

## 2.7 Polydisperse Langevin Description

The overall idea of this section is to introduce an extension of the Langevin model for polydisperse systems by taking into account an ensemble of particles, which is described by a particle size distribution  $\mathcal{P}(\sigma)$ . Although we consider dilute non interacting systems, in Section (2.7.3) we introduce the effect of interactions for the Ermack-McCammon algorithm of Brownian Dynamics simulations. In our description, each particle is considered to be under the influence of an external force in the linear regime, hence a Stokes flow is considered. This leads to a drag velocity  $v_D$ , and adds an extra contribution in the over-damped Langevin equation in the direction of the force. Thus, for a particle of diameter  $\sigma$  (represented as a subscript) the correspondent Langevin equation in the direction of the external force is

$$\dot{z}_\sigma(t) = \frac{1}{\xi} f_z(t) + v_{D\sigma}, \quad (61)$$

where  $f_z$  is the stochastic force. It satisfies three properties:  $f_z$  is gaussian distributed, its first moment is zero,  $\langle f_z \rangle = 0$ , and it is delta convoluted  $\langle f_z(t) f_z(t') \rangle = 2\xi k_B T \delta(t - t')$ . Here,  $k_B$  is the Boltzmann constant,  $T$  the temperature, and  $\xi$  is known as the friction coefficient. For a spherical particle  $\xi = 3\pi\eta\sigma$ , with  $\eta$  the zero shear viscosity of the solvent.

The solution of Eq.(61) is given by,

$$z_\sigma(t_0 + \tau) = z_0 + \int_{t_0}^{t_0+\tau} \frac{1}{\xi} f_z(t') dt' + v_{D\sigma} \tau. \quad (62)$$

Here,  $z_0 = z(t = t_0)$  is the initial conditions of the system. We proceed by using Eq.(62) and compute the Mean Squared Displacement (MSD) per particle ( $\langle \Delta z_\sigma^2(t_0, \tau) \rangle_{t_0}$ ), obtaining

$$\langle \Delta z_\sigma^2(t_0, \tau) \rangle_{t_0} = 2D_\sigma \tau + v_{D\sigma}^2 \tau^2 \quad (63)$$

where  $D_\sigma = k_B T / \xi$  is the free diffusion coefficient of a particle with diameter  $\sigma$ , and  $\langle \dots \rangle_{t_0}$  indicates a time average. For sake of clarity, we recall that  $t_0$  is the starting time and  $\tau$  is the delay time.

Now, we introduce the overall MSD by considering an ensemble average ( $\langle \dots \rangle_E$ ) over a distribution of particle size  $\mathcal{P}(\sigma)$ , i.e.

$$\langle \Delta z^2(t_0, \tau) \rangle_{t_0, E} = \int \langle \Delta z_\sigma^2(t_0, \tau) \rangle_{t_0} \mathcal{P}(\sigma) d\sigma. \quad (64)$$

The previous leads to the following expression,

$$\langle \Delta z^2(t_0, \tau) \rangle_{t_0, E} = 2\langle D \rangle_E \tau + \langle v_D^2 \rangle_E \tau^2. \quad (65)$$

The last expression is a general description, as we have not introduced any functional form of  $\mathcal{P}(\sigma)$ . Hence, it is implied that all of the previous averages exist within the desired distribution description.

In order to differentiate relative to directed motion, we make use of the variance of the velocity

$$\delta_v^2 = \langle v_D^2 \rangle_E - \langle v_D \rangle_E^2, \quad (66)$$

and combine it with Eq.(65). Thus,

$$\begin{aligned} \langle \Delta z^2(t_0, \tau) \rangle_{t_0, E} &= 2\langle D \rangle_E \tau + (\langle v_D \rangle_E^2 + \delta_v^2) \tau^2 \\ &= 2\langle D \rangle_E \tau + \langle v_D \rangle_E^2 (1 + CV_v^2) \tau^2, \end{aligned} \quad (67)$$

where  $CV_v = \delta_v / \langle v_D \rangle_E$  is the coefficient of variation or polydispersity index of the velocity. By following the delay time dependence, Eq.(67) describes two types of motion: diffusive, as the ensemble MSD is proportional to  $\tau$ , and ballistic, where the MSD is proportional to  $\tau^2$ . Additionally, the motion can be seen as relative motion and collective directed motion. Being the diffusive and the  $\delta_v$  terms relative motions to the collective contribution term  $\langle v_D \rangle_E$ .

In the reciprocal space, a similar analysis can be performed over the Intermediate Scattering Function (ISF). Choosing  $Q_z$  as the wave vector in the direction of the external force, and by combining Eq.(37) and Eq.(58) the ISF takes the following form,

$$\begin{aligned} f(Q_z, \tau) &= \exp \left[ -Q_z^2 \langle D \rangle_E \tau \left\{ 1 - \frac{1}{2} Q_z^2 \langle D \rangle_E \tau \frac{\delta_D^2}{\langle D \rangle_E^2} \right\} \right] \\ &\quad \times \exp \left[ i Q_z \langle v_D \rangle_E \tau - \frac{1}{2} Q_z^2 \delta_v^2 \tau^2 \right] \end{aligned} \quad (68)$$

where  $\delta_D^2$  is the variance of the diffusion coefficient distribution, and the ratio  $CV_D = \delta_D / \langle D \rangle$  is known as the coefficient of variation or polydispersity index of the diffusion coefficient. Given the fact that  $D$  is related to  $\sigma$ , changes in the size coefficient of variation  $CV_\sigma = \delta_\sigma / \langle \sigma \rangle$  imply changes in  $CV_D = \delta_D$ . It was found that for  $CV_\sigma < 0.1$ , the term containing  $\delta_D^2$  becomes negligible [37]. This is also corroborated and analyzed in Section (4.4). Experimentally, it is possible to measure the real part of Eq.(68). Thus, the measured intermediate scattering function is

$$f_m(Q_z, \tau) = \exp \left[ -Q_z^2 \langle D_\sigma \rangle_E \tau - \frac{1}{2} Q_z^2 \delta_v^2 \tau^2 \right] \cos(Q_z \langle v_{D\sigma} \rangle_E \tau). \quad (69)$$

### 2.7.1 Reduced Units

The use of reduced units helps to find characteristic scales that describe a system, and it is useful to generalize the description to different equivalent systems [18]. To start, we consider the mean diameter  $\langle\sigma\rangle_E$  as the unit length. Hence, a particle coordinate in reduced units is

$$z^*(t) = z(t)/\langle\sigma\rangle_E \quad (70)$$

where (\*) denotes reduced units. For pure Brownian motion the ensemble MSD in reduced units takes the following form.

$$\begin{aligned} \langle\Delta z^{*2}(t_0, \tau)\rangle_{t_0, E} &= \left\langle \left| \frac{z(t_0 + \tau)}{\langle\sigma\rangle_E} - \frac{z(t_0)}{\langle\sigma\rangle_E} \right|^2 \right\rangle_{t_0, E} = \frac{1}{\langle\sigma\rangle_E^2} \langle\Delta z^2(t_0, \tau)\rangle_{t_0, E} \\ &= 2 \frac{\langle D \rangle_E}{\langle\sigma\rangle_E^2} \tau. \end{aligned} \quad (71)$$

With the previous, it is possible to define a temporal scale of the ensemble, addressed as the ensemble Brownian time ( $t_B^*$ ), where

$$t_B^* \equiv \frac{\langle\sigma\rangle_E^2}{\langle D \rangle_E}. \quad (72)$$

Thus, the reduced time

$$\tau^* = \frac{\tau}{t_B^*}, \quad (73)$$

and by substitution of Eq.(72) in Eq.(71) considering Eq.(73) the complete reduced ensemble MSD takes the form

$$\langle\Delta z^{*2}(t_0, \tau^*)\rangle_{t_0, E} = 2\tau^*. \quad (74)$$

It follows by reducing Eq.(65) by making use of the previous results,

$$\langle\Delta z^{*2}(t_0, \tau^*)\rangle_{t_0^*, E} = 2\tau^* + \frac{\langle v_D \rangle_E^2 \langle\sigma\rangle_E^2}{\langle D \rangle_E^2} (1 + CV_v^2) \tau^{*2}. \quad (75)$$

Eq.(75) reveals the ensemble Péclet number,

$$\text{Pe}^* \equiv \frac{\langle v_D \rangle_E \langle\sigma\rangle_E}{\langle D \rangle_E}. \quad (76)$$

Finally, Eq.(75) takes the following form.

$$\langle\Delta z^{*2}(t_0, \tau^*)\rangle_{t_0^*, E} = 2\tau^* + \text{Pe}^{*2} (1 + CV_v^2) \tau^{*2}. \quad (77)$$

In addition, with the reduced wave vector,  $Q_z^* = Q_z \langle\sigma\rangle_E$ , it is possible to write Eq.(69) in reduced units,

$$f_m(Q_z^*, \tau^*) = \exp \left[ -Q_z^{*2} \tau^* - \frac{1}{2} Q_z^{*2} CV_v^2 \text{Pe}^{*2} \tau^{*2} \right] \cos(Q_z^* \text{Pe}^* \tau^*). \quad (78)$$

### 2.7.2 Analytical Gaussian Model under the presence of gravity

The settling of particles in a suspension is the most common example of particles in the presence of an external force. In a dilute suspension, the particles motion is governed by the force balance between the effect of the gravitational field, buoyancy and the frictional force. This leads to a steady state motion with constant settling velocity also known as the Stokes velocity  $v_s = \Delta\rho g\sigma^2/18\eta$ , where  $\Delta\rho = \rho_s - \rho_p$  is the difference between the solvent and particle densities,  $g$  is the gravitational acceleration,  $\sigma$  the particle diameter, and  $\eta$  the viscosity of the solvent. For fixed particle composition, bigger particles will sediment more rapidly than smaller ones. In nature, most of the suspensions present a particle size distribution  $\mathcal{P}(\sigma)$ . Usually, the distributions that describe the polydispersity of various systems are known to be: Normal (Gaussian), Log-Normal or Weibull [58].

The quantity that represents the relative broadness of the distribution is given by the size coefficient of variation ( $CV_\sigma$ ), defined as the ratio of the standard deviation of the distribution ( $\delta_\sigma$ ) by the mean value  $\langle\sigma\rangle$ , i.e.  $CV_\sigma = \delta_\sigma/\langle\sigma\rangle$ . For simplicity in the notation, we have used ( $\langle\dots\rangle$ ) to represent the ensemble average ( $\langle\dots\rangle_E$ ). A suspension is referred as monodisperse if its size distribution is narrow, i.e.  $CV_\sigma \sim 0$ , thus the size variation is negligible, contrary to the one referred as polydisperse. As a consequence of the particle size distribution, the overall sedimentation motion can be represented by a velocity distribution. Having its corresponding velocity coefficient of variation quantified by  $CV_v = \delta_v/\langle v_s\rangle$ , and depending on the functional form of  $\mathcal{P}(\sigma)$  a relationship between the velocity ( $CV_v$ ) and the size coefficient of variation ( $CV_\sigma$ ) can be found.

In the following we make use of a Gaussian distribution as size distribution, i.e.

$$\mathcal{P}(\sigma) = \begin{cases} 0 & \sigma \leq 0 \\ \frac{1}{\sqrt{2\pi}\delta_\sigma^2} \exp\left[-\frac{(\sigma-\langle\sigma\rangle)^2}{2\delta_\sigma^2}\right] & \sigma > 0 \end{cases} \quad (79)$$

where  $\langle\sigma\rangle$  is the mean particle diameter, and  $\delta_\sigma$  is the standard deviation of the distribution. The previous is motivated on the fact that narrow distributions can be characterized by the first two moments [59]. Once the distribution is defined, it is possible to compute all of the characteristic physical quantities ( $\langle v\rangle, \langle D\rangle, t_B^*$ , and  $Pe^*$ ). This, in order to describe them by the distribution variables,  $\langle\sigma\rangle$  and  $\delta_\sigma$ .

For the velocity, the second moment of the distribution is computed. Therefore,

$$\langle v_s\rangle = \frac{\Delta\rho g}{18\eta} \langle\sigma^2\rangle = \frac{\Delta\rho g}{18\eta} \langle\sigma\rangle^2 (1 + CV_\sigma^2). \quad (80)$$

Where we have used the definition of variance,  $\delta_\sigma^2 = \langle\sigma^2\rangle - \langle\sigma\rangle^2$ . For the Diffusion

coefficient, the first negative moment of the distribution needs to be obtained, as

$$\langle D \rangle = \frac{k_B T}{3\pi\eta} \left\langle \frac{1}{\sigma} \right\rangle, \quad (81)$$

which, analytically, is not a simple task. However, we have solved it by numerical integration. Our result is shown in Fig.3.

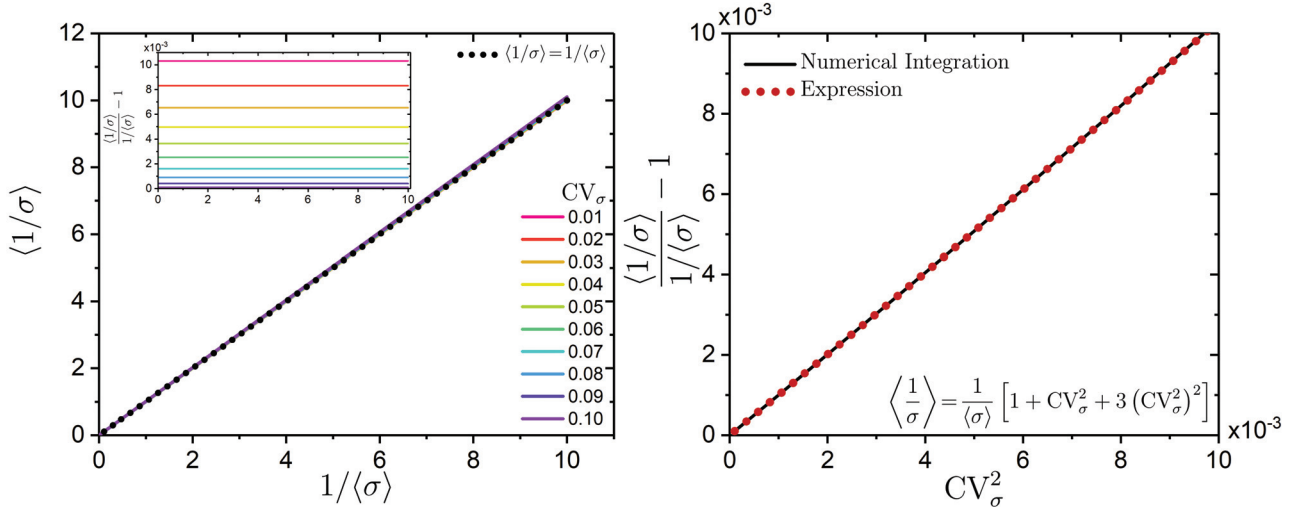


Fig. 3: The left panel shows a comparison of the numerical integration of the first negative moment for a Gaussian distribution  $\langle 1/\sigma \rangle$  with the inverse of the first moment  $1/\langle \sigma \rangle$ , and as an inset we show the obtained constant value for the relative deviation between the two moments. The right panel shows the relative deviations of the two moments as a function of the square of the coefficient of variation  $CV_\sigma$  (black line). The found quadratic relation is shown as red dots, the analytical expression is shown as legend.

The numerical results are plotted against the inverse of the first moment  $1/\langle \sigma \rangle$  (left panel Fig.3). A linear dependence with zero intercept was found. Moreover, we proceeded to extract the relative difference from them, having found a constant value for different polydispersities (shown as inset). Then, we plotted  $[\langle 1/\sigma \rangle / (1/\langle \sigma \rangle)] - 1$  versus  $CV_\sigma^2$  (right panel Fig.3). This, in order to be able to extract a polynomial relation with  $CV_\sigma^2$ . We proceeded to fit a second degree polynomial (for  $CV_\sigma^2$ ) to the numerical integration data, obtaining coefficients that were rounded to the algebraic expression that is shown as legend. Strikingly, we found a very good agreement with the extracted expression and the numerical integration results, as their relative difference was found to be less than 0.01%. For simplicity, we neglected the  $\sim \mathcal{O}((CV_\sigma^2)^2)$ , as with the first order in  $CV_\sigma^2$  the accuracy of the expression was found to be 99.97% among the tested interval. Hence, we consider the first negative moment of  $\sigma$  to be,

$$\langle D \rangle = \frac{k_B T}{3\pi\eta} \left\langle \frac{1}{\sigma} \right\rangle = \frac{k_B T}{3\pi\eta} \frac{1}{\langle \sigma \rangle} (1 + CV_\sigma^2 + 3CV_\sigma^4) \simeq \frac{k_B T}{3\pi\eta} \frac{1}{\langle \sigma \rangle} (1 + CV_\sigma^2). \quad (82)$$

It is worth mentioning that this is a numerical analysis, and if higher precision is needed, the order of description can be increased.

Once  $\langle v_s \rangle$  and  $\langle D \rangle$  are obtained, the ensemble Brownian time takes the form,

$$t_B^* \equiv \frac{\langle \sigma \rangle^2}{\langle D \rangle} \simeq \frac{3\pi\eta}{k_B T} \langle \sigma \rangle^3 \frac{1}{1 + \text{CV}_\sigma^2}. \quad (83)$$

Finally, for the ensemble Péclet

$$\text{Pe}^* \equiv \frac{\langle v_s \rangle \langle \sigma \rangle}{\langle D \rangle} \simeq \frac{\pi \Delta \rho g}{6 k_B T} \langle \sigma \rangle^4 \quad (84)$$

### 2.7.3 Polydisperse Ermack-McCammon Algorithm

#### Stochastic Force

Here, we briefly describe an extension, by including polydispersity, of the Ermack-McCammon algorithm without Hydrodynamic interactions. This algorithm is one of the most used algorithms for performing Brownian dynamics simulations [32]. For simplicity, we derive it for one dimension. We start by the discretization of the solution of the Langevin equation in 1-D for a particle of diameter  $\sigma$  represented as a subscript. Thus,

$$x_\sigma(t_0 + \Delta t) = x_\sigma(t_0) + \beta D_\sigma F_\sigma \Delta t + \delta x_\sigma(\Delta t), \quad (85)$$

where  $\beta = 1/k_B T$ ,  $D_\sigma$  is the particle free diffusion coefficient, and  $\Delta t$  is a discretized representation of a delay time  $\tau$ .  $F_\sigma$  is the external net force acting over the particle, and in general it is the linear superposition of the force arising from the interaction potential and other types of forces like gravity, electric, etc.  $\delta x_\sigma(t_0)$  is a random displacement due to collisions between the particle and the solvent molecules. It satisfies the fluctuation-dissipation theorem [33, 34], i.e.

$$\begin{aligned} \langle \delta x_\sigma(t) \rangle_t &= 0, \\ \langle \delta x_\sigma(t) \delta x_\sigma(t') \rangle_t &= 2D_\sigma \Delta t \delta(t - t'), \end{aligned} \quad (86)$$

where  $t$  and  $t'$  are two arbitrary times that are only correlated when  $t = t'$ . Moreover, numerically it is computed by

$$\delta x_\sigma(\Delta t) = \sqrt{2D_\sigma \Delta t} \mathcal{P}_{\text{Gauss}}, \quad (87)$$

where  $\mathcal{P}_{\text{Gauss}}$  is a number that follows a random Gaussian distribution function with first moment zero and a unitary second moment.

In reduced units Eq.(85) takes the following form

$$x_\sigma^*(t_0 + \Delta t^*) = \frac{1}{\langle \sigma \rangle} x_\sigma(t_0 + \Delta t^*) = x_\sigma^*(t_0) + \frac{D_\sigma}{\langle D \rangle} \beta \langle \sigma \rangle F_\sigma \Delta t^* + \delta x_\sigma^*(\Delta t^*). \quad (88)$$

Here we have obtained the reduced time units by  $\Delta t^* = \Delta t / t_B^* = \Delta t \langle D \rangle / \langle \sigma \rangle^2$ . Naturally, the reduced units of force over the ensemble ( $F^*$ ) are obtained, where

$$\beta \langle \sigma \rangle F_\sigma \equiv F_\sigma^* = \frac{F_\sigma}{F^*}. \quad (89)$$

Thus,

$$F^* = \frac{1}{\beta \langle \sigma \rangle}. \quad (90)$$

Finally, Eq.(88) takes the form

$$x_\sigma^*(t_0 + \Delta t^*) = x_\sigma^*(t_0) + \frac{D_\sigma}{\langle D \rangle} F_\sigma^* \Delta t^* + \delta x_\sigma^*(\Delta t^*). \quad (91)$$

As consequence of the reduced units, Eq.(86) is

$$\begin{aligned} \langle \delta x_\sigma^*(t) \delta x_\sigma^*(t') \rangle_t &= \frac{1}{\langle \sigma \rangle^2} \langle \delta x_\sigma(t) \delta x_\sigma(t') \rangle_t \\ &= \frac{1}{\langle \sigma \rangle^2} 2D_\sigma \Delta t \delta(t - t') \\ &= 2 \frac{D_\sigma}{\langle D \rangle} \Delta t^* \delta(t - t'). \end{aligned} \quad (92)$$

From Eq.(82) and  $D_\sigma = k_B T / 3\pi\eta\sigma$ , the diffusion coefficients ratio can be obtained,

$$\frac{D_\sigma}{\langle D \rangle} = \frac{\langle \sigma \rangle}{\sigma} \left( \frac{1}{1 + \text{CV}_\sigma^2} \right). \quad (93)$$

Finally, the stochastic displacement correlation is

$$\langle \delta x_\sigma^*(t) \delta x_\sigma^*(t') \rangle_t = 2 \frac{\langle \sigma \rangle}{\sigma} \left( \frac{1}{1 + \text{CV}_\sigma^2} \right) \Delta t^* \delta(t - t'). \quad (94)$$

In the following, we obtain the corresponding expressions regarding the external force term of Eq.(91). As it depends on the type of considered external force. For our purposes, we will obtain it for the gravitational force and the one related to the interaction potential.

#### External Force: Gravity

As an example of external force interacting with the particle, we consider the effect of the gravitational force. Taking into account the balance between the buoyant and the weight of a particle when immersed in a liquid, i.e.

$$F_g = \Delta \rho g \frac{\pi \sigma^3}{6}, \quad (95)$$

Here, the definition of  $\Delta \rho$  sets the force sign. Recalling  $F^*$  (Eq.(90)) Eq.(95) in reduced units takes the following form,

$$F_g^* = \frac{\pi \Delta \rho g}{6 k_B T} \sigma^3 \langle \sigma \rangle. \quad (96)$$

The physical constants that are in the right hand term of Eq.(96) can be replaced by the ones of  $\text{Pe}^*$  (Eq.(84)). Then,

$$F_g^* = \text{Pe}^* \frac{\sigma^3}{\langle \sigma \rangle^3}. \quad (97)$$

Finally, by multiplying Eq.(93) with Eq.(97), the corresponding term for the discretized displacement (Eq.(91)) takes the form,

$$\frac{D_\sigma}{\langle D \rangle} F_g^* = \text{Pe}^* \frac{\sigma^2}{\langle \sigma \rangle^2} \left( \frac{1}{1 + \text{CV}_\sigma^2} \right). \quad (98)$$

### Continuous Hard Sphere-Like interaction potential

For the interaction potential, we make use of an extended version of the continuous potential that reproduces hard sphere-like interactions. The use of this type of potentials is crucial, as the discontinuous nature of the hard sphere potential creates an ill imposed problem for the calculation of the force in the discretized Brownian dynamics algorithm (Eq.(88)). The pair-wise interaction force is defined

$$F \equiv -\frac{dU(r)}{dr}, \quad (99)$$

where  $r$  is the magnitude of the distance vector between the center of two particles, and  $U(r)$  is the interaction potential. For one component systems, the continuous potential  $U_{\text{cp}}(r)$  has the form [60],

$$U_{\text{cp}}(r) = \begin{cases} A\epsilon \left[ \left(\frac{\sigma}{r}\right)^\lambda - \left(\frac{\sigma}{r}\right)^{\lambda-1} \right] + \epsilon & r < B\sigma \\ 0 & r \geq B\sigma, \end{cases} \quad (100)$$

where,

$$A = \lambda \left( \frac{\lambda}{\lambda - 1} \right)^{\lambda-1}, \quad B = \frac{\lambda}{\lambda - 1}. \quad (101)$$

Here,  $\sigma$  is the particle diameter,  $\lambda$  reflects the repulsive (term with power  $\lambda$ ) and attractive behaviour (term with power  $\lambda-1$ ), and  $\epsilon$  is the energy parameter used as amplitude. It is also used to define a reduce temperature  $T^* = k_B T / \epsilon$ . The values of  $\lambda = 50$ , and  $T^* = 1.4737$  were found to ensure thermodynamic consistency to reproduce physical properties of hard core potentials [61].

The natural extension of Eq.(100) for two particles of different size is given by.

$$U_{\text{cp}}(r) = \begin{cases} A\epsilon \left[ \left(\frac{\sigma_{ij}}{r}\right)^\lambda - \left(\frac{\sigma_{ij}}{r}\right)^{\lambda-1} \right] + \epsilon & r < B\sigma_{ij} \\ 0 & r \geq B\sigma_{ij}, \end{cases} \quad (102)$$

again,  $r$  is the magnitude of the distance vector between the center of two particles,  $\sigma_{ij} = 1/2(\sigma_i + \sigma_j)$  is the minimum distance between the two particles of diameter  $\sigma_i$  and  $\sigma_j$  respectively. Moreover, we have assumed the Lorentz-Berthelot mixing rules, i.e. for all crossed terms  $\epsilon$  and  $\lambda$  are equal [62–64]. This is

Hence, the interaction force between particles for distances  $r < B\sigma_{ij}$  is given by

$$F_{\text{cp}}(r) = -\frac{dU_{\text{cp}}(r)}{dr} = \frac{A\epsilon}{\sigma_{ij}} \left[ \lambda \left(\frac{\sigma_{ij}}{r}\right)^{\lambda+1} - (\lambda-1) \left(\frac{\sigma_{ij}}{r}\right)^\lambda \right]. \quad (103)$$

In reduced units Eq.(103) takes the following form,

$$F_{\text{cp}}^*(r^*) = \beta \langle \sigma \rangle F_{\text{cp}}(r^*) = \frac{A}{T^* \sigma_{ij}^*} \left[ \lambda \left( \frac{\sigma_{ij}^*}{r^*} \right)^{\lambda+1} - (\lambda-1) \left( \frac{\sigma_{ij}^*}{r^*} \right)^{\lambda} \right]. \quad (104)$$

Finally, the total force acting over a particle  $i$  expressed for the discretized displacement (Eq.(88)) is obtained. Having,

$$\frac{D_{\sigma}}{\langle D \rangle} F_p^*(r^*) = \sum_j \frac{A}{T^* \sigma_{ij}^* \sigma_{ii}^* (1 + \text{CV}_{\sigma}^2)} \left[ \lambda \left( \frac{\sigma_{ij}^*}{r^*} \right)^{\lambda+1} - (\lambda-1) \left( \frac{\sigma_{ij}^*}{r^*} \right)^{\lambda} \right]. \quad (105)$$

#### 2.7.4 Simulation Example and validation

In this section, we show a comparison between the results of the polydisperse Ermack-McCammon Brownian Dynamics simulations (BD) (Sec.2.7.3) and the analytical results from the Polydisperse Langevin description (Sec.2.7). Moreover, the observables in the real space (MSD) and reciprocal space (ISF) were obtained for such numerical experiments. This simulation run was selected for a system with polydispersity index  $\text{CV}_{\sigma} = 0.07$  and  $\text{Pe}^* = 150$  using an ensemble of 1024 particles. In reciprocal space, we chose the scattering wave vector that covers a length scale of one particle diameter i.e.  $Q_z^* = 2\pi$ . Our results are shown as closed symbols in Fig.4.

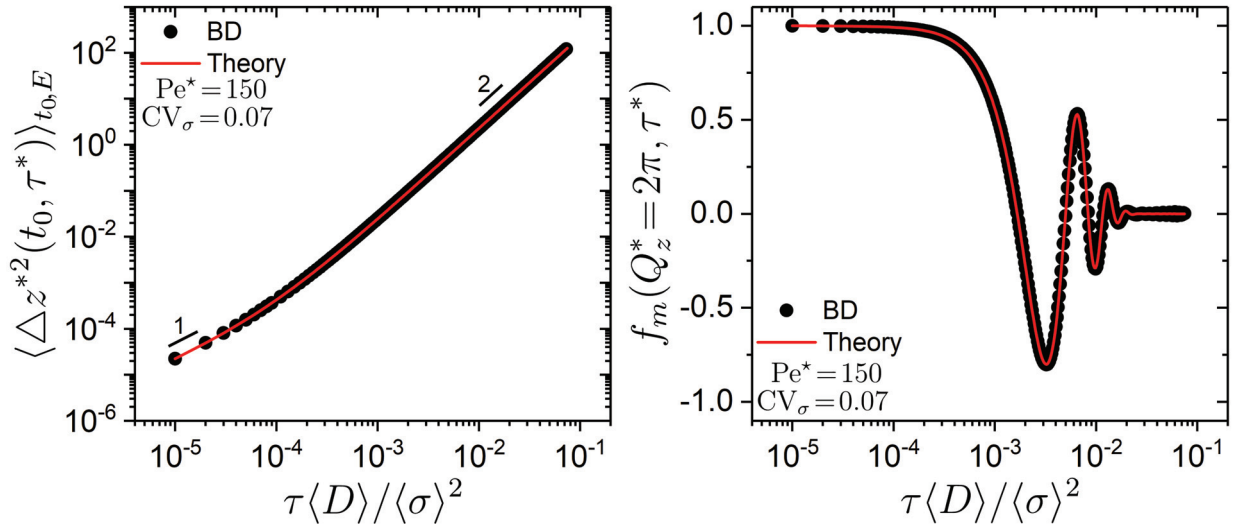


Fig. 4: Comparison of the obtained analytical expressions of Eq.(77) and Eq.(78) (continuous lines) with the MSD (left panel) and ISF (right panel) computed from the polydisperse Ermack-McCammon Brownian Dynamics simulations (BD) using the polydisperse Langevin description (closed symbols). The physical parameters of the simulation run are written as legend in the figures

Finally, we show a comparison between the analytical expressions from Eq.(77) and Eq.(78) (shown as continuous line in Fig.4) with the observables computed from the computer simulations. The comparison shows a very good agreement

between the theoretical expressions and the simulations results. Thus, proving the validity of the theoretical expressions and the implementation in the Ermack-McCammon algorithm. Furthermore, these analytical expressions provide the theoretical framework to be used for comparison with experiments in the following of this work.

### 3 Experimental Methods

#### 3.1 Optical Regimes

Colloidal dispersions (for simplicity, samples) are experimentally studied with electromagnetic radiation by analyzing the signal resulting from the interaction of this probing radiation with the sample [6–8]. Different experimental techniques are named according to the electromagnetic radiation properties (wavelength, coherence, etc.) and the region where the signal is collected. In the following, we will consider visible, coherent, and incoherent light as probing radiation and two-dimensional sensors or digital cameras as detectors. Although here we only show the basics of the conceptual framework for those radiation types, the presented concepts can also be extended to X-Rays or any other type of radiation [65, 66]. The distance  $z$  from the sample plane ( $z=0$ ) where the signal is collected define different detection zones and, based on them, different measuring techniques are established. A basic illustration is shown in Fig.5.

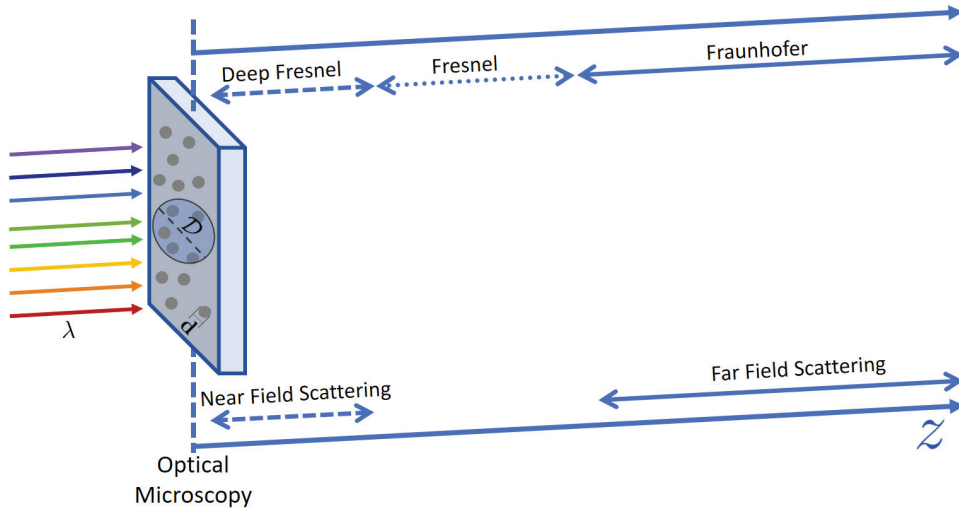


Fig. 5: Different detection zones defined as a function of the detection position  $z$ .

The transition between the different optical regimes depends on the following physical properties: illumination width ( $\mathcal{D}$ ), wavelength of the radiation source ( $\lambda$ ), and the size of the radiated objects ( $\mathbf{d}$ ) [65–67]. In the following,  $\mathcal{D} \gg \mathbf{d}$  is considered. The optical microscopy plane is defined at  $z=0$ . Then, for small distances  $z < \mathbf{d}\mathcal{D}/\lambda$ , the region of Deep Fresnel, Shadowgraphy, or Near Field scattering is defined [66–68]. In this region, the collected signal is characterized by having static spatial properties independent of  $z$ , i.e. the spatial auto-correlation function of the scattered field is invariant upon propagation within this region [65, 67]. In contrast, for large distances  $z > \mathcal{D}^2/\lambda$ , the spatial properties change. This can be observed on how an image gets bigger while moving to larger  $z$  values. This regime is known as the Fraunhofer or the Far Field region [66, 67, 69]. The

intermediate regime, for  $\mathbf{dD}/\lambda < z < \mathcal{D}^2/\lambda$ , is known as the Fresnel regime. [66,67].

The present work was performed using detection schemes based in the dashed regions of, i.e. Optical Microscopy and Near-Field scattering. In Fig.5, we present images of colloidal particles of size  $7.32\mu\text{m}$  recorded at different values of  $z$  in Fig.(6). The imaging setup consists of two illumination light sources, a laser, and a narrowly distributed monochromatic light emitting diode (LED). The images were captured by a 20X microscope objective and a Complementary metal–oxide–semiconductor (CMOS) digital camera. In the sample plane, similar image content can be appreciated for both imaging conditions, i.e. bright blob for particles in focus. When  $z$  increases, the scattered light from the laser illumination superimpose, leading to a speckle pattern that does not change its spatial characteristics within this detection zone ( $z = (1-3)\text{mm}$  Fig.5). Conversely, all of the spatial information of the sample is lost for the LED illumination at distances outside of the sample plane (homogeneous gray images Fig.5  $z = (1, 2, 3)\text{mm}$ .). This because of the different properties of the illumination sources, such as temporal and spatial coherence [66]. However, for the regions where spatial information is preserved, the image content represents a density map of the sample [7].

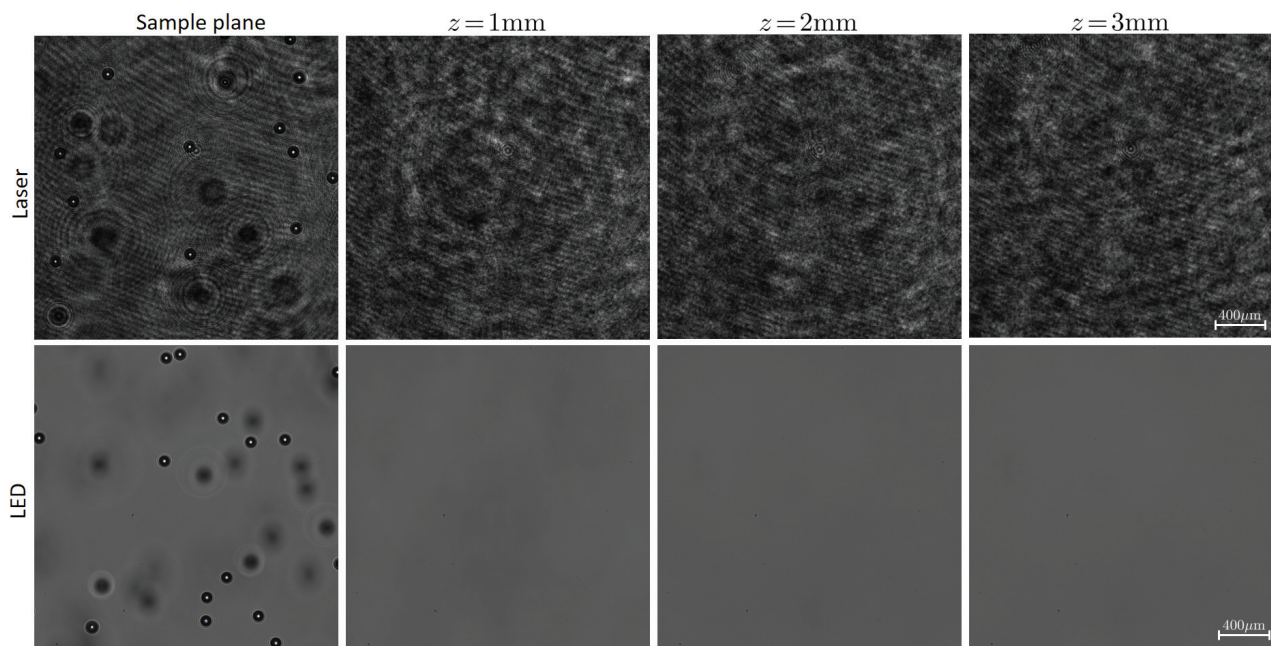


Fig. 6: Illustration of the type of images resulting from illuminating a sample with a laser (HNFS) and a monochromatic LED (Optical Microscopy) as a function of the detection position ( $z$ ).

The corresponding framework capable of describe the image content for both presented cases will be introduced in the following section.

### 3.2 Digital Fourier Microscopy and Heterodyne Near Field Scattering

Digital Fourier Microscopy (DFM) is a conceptual framework applied to a time series of images. Each of these images, denoted by  $i(\mathbf{x}, t)$ , represent a density map of the studied sample, and by performing an image analysis, the spatio-temporal information in the reciprocal space can be obtained. Thus, similar information as in a Dynamic Light Scattering experiment (DLS) is extracted [7]. The images can be acquired by means of an optical microscope using various imaging conditions, i.e. an incandescent poly-chromatic lamp, fluorescence imaging, etc.

If the light source consists of a laser and the imaged plane is in the near field scattering region (Fig.5), the imaging technique is known as Heterodyne Near Field Scattering (HNFS) [24, 70]. Examples of images acquired by different optical microscopy configurations and HNFS are shown in Fig.7.

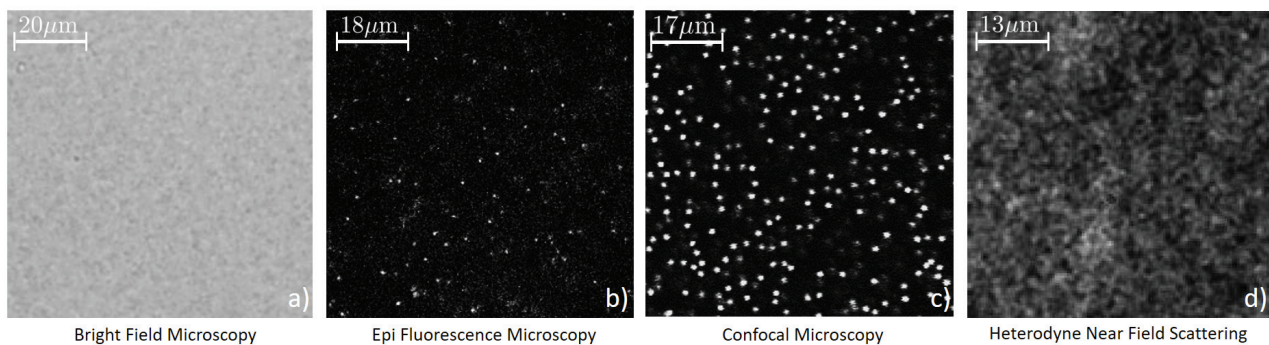


Fig. 7: Images of different colloidal dispersions obtained using different Optical Microscopy techniques and Heterodyne Near Field Scattering.

In HNFS,  $i(\mathbf{x}, t)$  consists of a speckle pattern in the deep Fresnel regime [24]. It is formed by the superposition of the reference electric field  $e_0(\mathbf{x})$ , with the scattered electric field generated by all the illuminated particles  $e_s(\mathbf{x}, t)$ . Thus,

$$i(\mathbf{x}, t) \sim |e_0(\mathbf{x}) + e_s(\mathbf{x}, t)|^2 \sim i_0(\mathbf{x}) + e_0 e_s^*(\mathbf{x}, t) + e_0^* e_s(\mathbf{x}, t). \quad (106)$$

The far field light scattering information, such as the intermediate scattering function ( $f(Q, \tau)$ ) and the average scattered intensity [8, 71], are extracted by a Digital Fourier Analysis (DFA) or also known as Differential Dynamic Algorithm (DDA) [24, 70, 72].

The previous scheme can be extended to different kinds of light sources and imaging configurations. Due to their experimental differences, each application has its own name. bright-field Differential Dynamic Microscopy (bDDM) is defined when the images are obtained in the sample plane using a bright field microscope. When a monochromatic light source, such as a light emitting diode (LED) is used, it will be referred as monochromatic Differential Dynamic Microscopy (mDDM).

If a narrow bandpass filter is used for acquiring images such that a specific wavelength is captured then,  $\lambda$  Differential Dynamic Microscopy ( $\lambda$ DDM) and when the images are acquired by a confocal microscope, confocal Differential Dynamic Microscopy (conDDM).

For microscopy based images,  $i(\mathbf{x}, t)$  is formed by a convolution of the three dimensional point-spread function  $K(\mathbf{x} - \mathbf{x}', z)$  with the sample density  $\rho(\mathbf{x}', z, t)$  via

$$i(\mathbf{x}, t) = i_0(\mathbf{x}) + \int K(\mathbf{x} - \mathbf{x}', z) \rho(\mathbf{x}', z, t) d\mathbf{x}' dz, \quad (107)$$

where  $i_0$  is a stationary uniform background contribution. In the following we present the key ideas behind DFA. For more detailed information please refer to [7, 70, 72].

A schematic representation of the DFA algorithm is shown in Fig.8. It is performed as follows: First, record a series of images  $i(\mathbf{x}, t)$  (represented in the first column in the main loop ( $\tau$ -loop) in Fig.8). Then, the fluctuating signal is calculated as,

$$\Delta i(\mathbf{x}, t, \tau) = i(\mathbf{x}, t + \tau) - i(\mathbf{x}, t), \quad (108)$$

which accounts for the difference between two images separated by a delay time  $\tau = m\Delta t$ ,  $m \in \mathbb{N}$ ,  $\Delta t = 1/\text{FPS}$ , and FPS (Frames Per Second) is the sampling rate. Here, we will refer to  $t$  as starting time.

Then, the power spectrum of the fluctuating signal  $\mathcal{T}_{\text{rs}}(\mathbf{q}, t, \tau)$  is calculated by a discrete Fourier transform (third column  $\tau$ -loop, Fig.8),

$$\mathcal{T}_{\text{rs}}(\mathbf{q}, t, \tau) = |\mathcal{F} [\Delta i(\mathbf{x}, t, \tau)]|^2, \quad (109)$$

where  $\mathbf{q}$  is the image wave vector. Its magnitude is discretized by  $q = n\Delta q$ , having  $\Delta q = 2\pi/L$ ,  $L$  is the image size and  $n$  the pixel number. Furthermore, the magnitude of  $q$  is related to the magnitude of the scattering wave vector  $Q = (4\pi n_s/\lambda) \sin(\theta/2)$  by

$$Q = \sqrt{2}k \left[ 1 - \sqrt{1 - \left(\frac{q}{k}\right)^2} \right]^{\frac{1}{2}}, \quad (110)$$

being  $n_s$  the refractive index in the medium of propagation,  $\theta$  the scattering angle, and  $\lambda$  the wavelength of light,  $k = 2\pi n_s/\lambda$  is the wave vector from the illumination source in the medium of propagation [70, 73]. The previous relation arise from the fact that the calculated Fourier transform is a 2D projection of the 3D scattering process [24, 73]. Special care has to be taken while performing the numerical Fourier transform, this in order to avoid spectral leakage. It occurs

when inhomogeneities in the intensity are present at the borders of the  $\Delta i(\mathbf{x}, t, \tau)$  images. To overcome this, a careful window scheme should be applied [74].

Finally, the structure function  $D(\mathbf{Q}, \tau)$  is determined. For signals that can be considered stationary, the signal statistics do not depend on the starting time  $t_k$ . An average over  $t_k$  is performed, obtaining the time averaged structure function (the result is represented as a colored arrow coming out of the  $\tau$ -loop) [75]:

$$D(\mathbf{Q}, \tau) = \langle \mathcal{T}_{\text{RS}}(\mathbf{Q}(\mathbf{q}), t_k, \tau) \rangle_{t_k}. \quad (111)$$

This relates to the real part of the intermediate scattering function (ISF),  $f(\mathbf{Q}, \tau)$  via,

$$D(\mathbf{Q}, \tau) = A(\mathbf{Q}) [1 - f(\mathbf{Q}, \tau)] + B(\mathbf{Q}). \quad (112)$$

The term  $A(\mathbf{Q}) [1 - f(\mathbf{Q}, \tau)]$  describes the contribution associated to the dynamics of the studied system ( $f(\mathbf{Q}, \tau)$ ) and the location and optical appearance given by the imaging technique of the sample ( $A(\mathbf{Q})$ ) [7].  $B(\mathbf{Q})$  is the power spectrum of the detection noise, unavoidably present even when there are no dispersed particles.

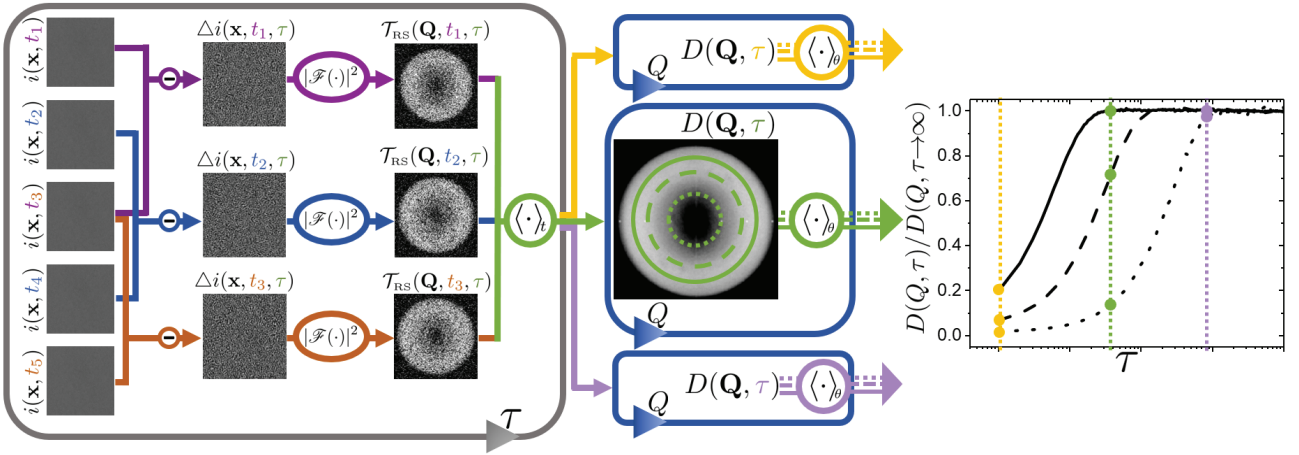


Fig. 8: Schematic representation of the DFA algorithm.

Since  $A(\mathbf{Q})$  depends on the imaging technique, for DDM it has the form [7]

$$A(\mathbf{Q}) = 2N|\hat{K}(\mathbf{Q})|^2 S(\mathbf{Q}) \quad (113)$$

and for HNFS [65]

$$A(\mathbf{Q}) = 4I_s(\mathbf{Q}) = 4\phi T(\mathbf{Q})P(\mathbf{Q})S(\mathbf{Q}) \quad (114)$$

where  $N$  is the number of particles,  $|\hat{K}(\mathbf{Q})|^2$  is the power spectrum of the imaging point-spread function,  $S(\mathbf{Q})$  is the structure factor. Moreover,  $\phi$  is the volume fraction of the system,  $T(\mathbf{Q})$  is the optical transfer function of the collection optics, and  $P(\mathbf{Q})$  is the particles form factor. In some cases, when the point spread

function can be calculated, Eq.(113) is exactly the same as Eq.(114) [7].

Numerically,  $A(\mathbf{Q})$  and  $B(\mathbf{Q})$  are estimated according to the following procedure. The power spectrum of the detection noise or background term,  $B(\mathbf{Q})$ , is taken as an average of all  $D(\mathbf{Q}, \tau)$  determined at short delay times ( $\tau \rightarrow 0$ ) and  $\mathbf{Q}$  values so large ( $\mathbf{Q} \rightarrow \mathbf{Q}_{max}$ ) that, due to the limited optical resolution of the imaging set-up, barely contain information of the system but rather the background [36, 50].  $B(\mathbf{Q})$  is taken to be constant for all  $\mathbf{Q}$  values thus,

$$B(\mathbf{Q}) \simeq B'(\mathbf{Q}) = D(\mathbf{Q} \rightarrow \mathbf{Q}_{max}, \tau \rightarrow 0), \quad (115)$$

where  $B'(\mathbf{Q})$  is the estimated value of  $B(\mathbf{Q})$ .  $A(\mathbf{Q})$  can be determined from the long-time decorrelation plateau as,  $D(\mathbf{Q}, \tau \rightarrow \infty) = A(\mathbf{Q}) + B(\mathbf{Q})$ . Finally, the intermediate scattering function can be obtained via the following equation,

$$\beta(\mathbf{Q})f(\mathbf{Q}, \tau) = \frac{D(\mathbf{Q}, \tau \rightarrow \infty) - D(\mathbf{Q}, \tau)}{D(\mathbf{Q}, \tau \rightarrow \infty) - B'(\mathbf{Q})}, \quad (116)$$

where  $\beta(\mathbf{Q}) \simeq 1 - [B(\mathbf{Q}) - B'(\mathbf{Q})] / A(\mathbf{Q})$  takes into account the signal to noise ratio and the accuracy of the estimation of  $B(\mathbf{Q})$ .

The analytical expression of  $f(\mathbf{Q}, \tau)$  depends on the particular system dynamics and can be used to extract useful information. For isotropic motion, the dynamics depend only on the magnitude of the scattering wave vector  $\mathbf{Q}$ . Hence, to improve statistics, an azimuthal average over the polar angle  $\theta$  in the  $Q$  plane is performed. It is represented as the middle loops ( $Q$ -loops) in Fig.8. Moreover, for dilute Brownian systems  $f(Q, \tau) = \exp(-\tau/\tau_c)$ . It contains a characteristic time  $\tau_c = 1/D_0Q^2$ , with  $D_0$  the free diffusion coefficient. With the previous, the hydrodynamic radius ( $R_H$ ) of the beads in suspension can be obtained. This dynamical measurement is known to be particle sizing, and in order to obtain it, the Stokes-Einstein relation is used, i.e.  $D_0 = k_B T / 6\pi\eta R_H$ , with  $k_B$  being the Boltzmann's constant,  $T$  the temperature,  $\eta$  the system's viscosity.

## 4 Summary of Experimental Results

### 4.1 Optimized algorithms for DFM

The DFM image analysis requires heavy post processing computation in order to extract the spatio-temporal information from an experiment. The bottle neck in the calculations of the structure function ( $D(Q, \tau)$ ) has two sources: The temporal, which involves the total number of images acquired for the calculation of  $D(Q, \tau)$ . The spatial, where the consideration of the size (amount of pixels) of an image is needed to optimize the computation of the 2-D Fast Fourier transform. In order to reduce computational time, more powerful computational architectures are used, such as Graphical Processing Units or GPUs [53, 76]. Nevertheless, it is still needed an efficient statistical scheme that reduces the number of calculations, thus minimizing the computational time. This, without compromising the final results.

To illustrate the efficiency and performance of different sampling algorithms, let us consider the calculation of  $D(Q, \tau)$  for an acquired set of 50,000 images captured with a sampling rate of 100 FPS. We obtained the images using HNFS. The studied sample is a particle suspension of polystyrene particles ( $\sigma=330$  nm) in ultra-pure water (18 M $\Omega$ cm), with particle volume fraction of  $\phi=5 \times 10^{-5}$ .

The HNFS experimental setup is described by three components: Illumination, sample container and collecting optics. The illumination consisted of a He-Ne laser with wavelength  $\lambda_0 = 632.8$  nm and power 30 mW (JDSU Uniphase). Its beam was spatially filtered and collimated, yielding a parallel beam with diameter 10 mm. The sample was contained in a flat rectangular glass cuvette of 4cm height, 10mm width, and 1mm optical path (21-G-1 Starna GmbH).

The scattered intensity pattern was imaged with an optical arrangement consisting of a microscope objective (CFI Plan Fluor 20X 0.5NA) and a tube lens (Thorlabs ITL200). The later projected an image onto an 8 bit CMOS black and white camera. The camera is equipped with a sensor of  $1280 \times 1024$  pixels, each of area  $4.8 \times 4.8 \mu\text{m}^2$  (AVT Mako-U130). A more detailed description can be found in [77]. In the following, some types of different optimization algorithms are presented. The first subsection deals with the temporal averaging schemes, and the second shows an optimization of the spatial information per image. It is worth mentioning that although the application of the algorithms is presented for one type of imaging technique, such algorithms can also be applied to any type of DFM imaging configuration as shown in [7, 78].

#### 4.1.1 Temporal sampling optimization

Digital Fourier Microscopy (DFM) is a conceptual framework applied to a time series of images, denoted by  $i(\mathbf{x}, t_k)$  and represented in the first column of Fig.8. Where  $t_k = k\Delta t$ ,  $\Delta t = 1/\text{FPS}$ , and FPS is the sampling rate.  $k \in \mathbb{N}$ ,  $k \leq N$ , and  $N$  corresponds to the total number of acquired images, i.e the maximum acquired time is  $t_N = N\Delta t$ . A density map of the studied sample is represented in the information content within  $i(\mathbf{x}, t_k)$ , and by an image analysis the spatio-temporal fluctuations in the reciprocal space can be obtained. Thus, similar information as in light scattering experiments is obtained [7].

The previous analysis is done by obtaining the fluctuating signal  $\Delta i(\mathbf{x}, t_k, \tau)$  (represented in the second column of Fig.8) between two images separated by delay time  $\tau = p\Delta t$ ;  $p \in \mathbb{N}$ , and  $p \leq N - 1$ . The later is achieved by performing the subtraction between a starting image  $i(\mathbf{x}, t_k)$ , and the subsequently delayed  $i(\mathbf{x}, t_k + \tau)$ . Thus,

$$\Delta i(\mathbf{x}, t_k, \tau) = i(\mathbf{x}, t_k + \tau) - i(\mathbf{x}, t_k). \quad (117)$$

Then, the power spectrum of the fluctuating signal is calculated by a discrete Fourier transform, obtaining an image denoted by  $\mathcal{T}_{\text{rs}}(\mathbf{Q}, t_k, \tau)$  (represented in the third column of Fig.8),

$$\mathcal{T}_{\text{rs}}(\mathbf{Q}, t_k, \tau) = |\mathcal{F} [\Delta i(\mathbf{x}, t_k, \tau)]|^2, \quad (118)$$

where  $\mathbf{Q}$  is the scattering wave vector (Eq.(110)). For signals that can be considered stationary and isotropic, the signal statistics, and hence, the power spectrum do not depend on the starting time  $t_k$  nor on the direction of the scattering wave vector  $\mathbf{Q}$ . An average over  $t_k$  and an azimuthal average over the polar angle  $\theta$  in the  $Q$  plane is performed to improve statistics, obtaining the time averaged structure function (represented in the fourth and fifth column of Fig.8) [75]:

$$D(Q, \tau) = \langle \mathcal{T}_{\text{rs}}(\mathbf{Q}, t_k, \tau) \rangle_{t_k, \theta}. \quad (119)$$

In order to optimize the temporal sampling in the DFM analysis, it is convenient to write the temporal average of Eq.(119) in its discretized form

$$D(Q, \tau) = \left\langle \frac{1}{\mathcal{O}} \sum_{k=1}^{\mathcal{O}} \mathcal{T}_{\text{rs}}(\mathbf{Q}, t_k, \tau) \right\rangle_{\theta}. \quad (120)$$

here,  $t_k$  takes the values from  $k \in \{1, 2, 3, \dots, \mathcal{O} = N - p\}$  and  $\mathcal{O}$  corresponds to the maximum number of elements in the set of  $\mathcal{T}_{\text{rs}}$  images available for the time average per delay time. For covering a long range of delay times, a large number of images are recorded, and for optimizing the corresponding computational time, it is convenient to choose  $\tau = p\Delta t$  such as  $p$  follows a logarithmic progression.

An example of the computational time needed to evaluate  $D(Q, \tau)$  for different number  $M$  of  $\mathcal{T}_{rs}$  images, such as  $M \leq \mathcal{O}$ , is represented in Fig.9. It was taken from a total set of  $N = 50,000$  images for 250 logarithmically separated  $\tau$ .

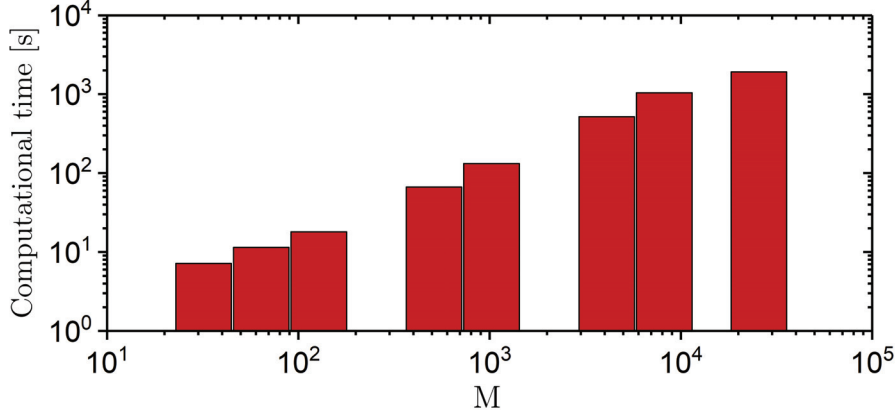


Fig. 9: Computational time needed to compute the image structure function  $D(Q, \tau)$  as a function of the number of elements  $M$  (Eq.(120)). The computation was performed for 250 logarithmically separated delay times ( $\tau$ ) from a total set of 50,000 images.

It is clear that, by increasing  $M$ , the computational time increases. Thus, a careful selection of the  $M$  elements that better represent the average is advised for reducing the computational time to the minimum. Moreover, the total  $\mathcal{T}_{rs}$  image set could carry some issues. For example, a  $\mathcal{T}_{rs}(\mathbf{Q}, t_k, \tau)$  image and its consecutive one  $\mathcal{T}_{rs}(\mathbf{Q}, t_{k+1}, \tau)$  may contain some temporal overlapping region from the experimental time line, leading to some redundancy or "similarity" in the information between them. This because the captured dynamics may have not evolved sufficiently among these pair of  $\mathcal{T}_{rs}$  images. Thus, they barely contain relevant different temporal information for the computation of  $D(Q, \tau)$ . To address this issue, here we introduce three sampling algorithms, i.e. selection rules of the  $k$ -elements to perform the time average of Eq.(120):

1. Redundant Algorithm (R), consists in taking all  $\mathcal{T}_{rs}$  available for a specific  $\tau = p\Delta t$ , this translates into taking  $t_k$  such as  $k \in \{1, 2, 3, \dots, \mathcal{O} = N - p\}$ . The later is a brute force method for computing  $D(Q, \tau)$ . It is considered to be a reliable algorithm when all elements are considered besides its inefficient numerical implications. In the following this algorithm is used as a control scheme.
2. Reduced Redundant (RR), is a sampling rule that leads to a reduction of the intrinsic redundancy between  $\mathcal{T}_{rs}$  elements. It consists in introducing a skipping rule among all  $\mathcal{T}_{rs}$  available for a specific  $\tau = p\Delta t$ , this translates onto taking  $t_k$  such as  $k \in \{1, 1 + \epsilon, 1 + 2\epsilon, 1 + 3\epsilon, \dots, \}$ . Here,  $\epsilon$  is the skipping factor that leads to a maximum number of elements of  $(\mathcal{O} - 1)/\epsilon$  and it is given by  $\epsilon = p^\alpha$ , where  $\alpha$  is the average redundant exponent. Here we took  $\alpha$  to have the value of 0.75

3. Sampling Uniformly at Random (SUR), is a Monte Carlo-like method used as sampling scheme. It is based on assigning equal probability to all of the available  $\mathcal{T}_{\text{RS}}$ , where  $D(Q, \tau)$  is computed using a certain number of random but not repeated  $\mathcal{T}_{\text{RS}}$  elements. Thus, shuffling all of the different  $t_k$  available per delay time ( $\tau$ ). The later is an adaptation of the random clipping scheme proposed by Schätzel [21, 79, 80].

To illustrate the efficiency and performance of the previously described sampling algorithms, let us consider the calculation of  $D(Q, \tau)$  from a set of  $N = 50,000$  images. This, at  $\tau = 1000\Delta t$ , the previous leads to a total of  $\mathcal{O} = 49,000$  available  $\mathcal{T}_{\text{RS}}$  elements from which, for keeping the number of  $\mathcal{T}_{\text{RS}}$  small, we consider a subset of  $M = 128$  elements. The computation of  $D(Q, \tau)$  by the R sampling scheme is performed over the first consecutive 128  $\mathcal{T}_{\text{RS}}$  elements. This means selecting  $t_k = t_1, t_2, \dots, t_{128}$ . Moreover, by using the RR sampling scheme, the  $t_k$  elements are taken with  $\epsilon = 1000^{0.75} \sim 178$ , these correspond to  $t_k = t_1, t_{179}, t_{357}, t_{1069}, \dots, t_{22,785}$ . Finally, for the SUR scheme, 128  $t_k$ 's were taken randomly from the 49,000 available, this by considering equal probability without replacement.

As consequence, each sampling scheme covers different measurement time. A graphical representation is devised by plotting all the  $k$  values per scheme, as  $k = t_k/\Delta t$  (Shown in the left panel of Fig.10). The elements taken with the R algorithm have sampled a very small amount of the measurement time, oppositely to the RR and SUR schemes. Being SUR the algorithm that covers the whole measurement time.

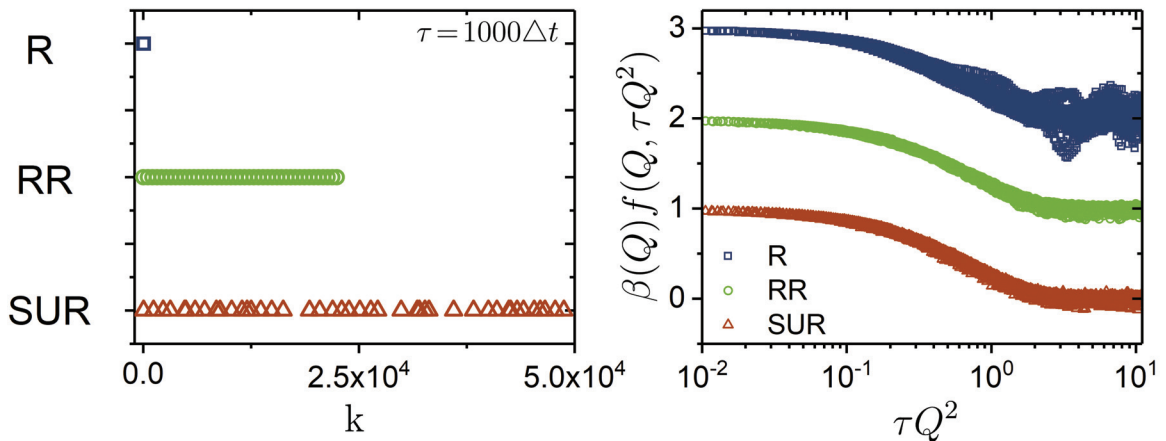


Fig. 10: Representation of the reached sampled time of R, RR and SUR sampling schemes (Left panel). The right panel shows  $\beta(Q)f(Q, \tau)$  obtained from the result of  $D(Q, \tau)$  by the three sampling schemes (as described in Eq.(116)). The results are plotted as a function of  $\tau Q^2$  for a  $Q$  range that covers the majority of sampled length scales of an image ( $0.7 \leq Q \leq 4.5$ ) [ $\mu\text{m}^{-1}$ ]. Curves are shifted by one for clarity.

The right panel of Fig.10 shows the extracted  $\beta(Q)f(Q, \tau)$  (Eq.(116)) obtained from the three different sampling schemes, R, RR, and SUR to compute  $D(Q, \tau)$ .

They are plotted as a function of  $\tau Q^2$  for a  $Q$  range that covers the majority of sampled length scales of an image ( $0.7 \leq Q \leq 4.5$ ) [ $\mu\text{m}^{-1}$ ]. For particles undergoing free diffusion, all of the  $\beta(Q)f(Q, \tau)$  should collapse onto a master curve, as seen for the three cases. The main difference between the three, comes from the spreading and the presence of oscillations at the decorrelated plateau for the R scheme ( $\tau Q^2 \geq 1$ ), but they don't appear for the RR and SUR schemes. These indicate the reduced data significance from the R sampling scheme, as the overall sampled time is the smallest of the three schemes.

In order to quantify the statistical convergence of the structure function  $D(Q, \tau)$  for the different sampling schemes, we proceeded to compute the coefficient of variation per sampling scheme, i.e.

$$\text{CV}(Q, \tau) = \frac{\sqrt{\frac{1}{M-1} \sum_{k=1}^M [\langle \mathcal{T}_{\text{rs}}(\mathbf{Q}, t_k, \tau) \rangle_{\theta} - D(Q, \tau)]^2}}{D(Q, \tau)}, \quad (121)$$

and performed a frequency count including all  $Q$  and  $\tau$  values. The value of this coefficient reflects the relative deviation of the three sampling schemes to  $D(Q, \tau)$  computed with all possible  $\mathcal{T}_{\text{rs}}$ . To illustrate it, the evolution of the frequency counts as a function of different  $M$  values is shown in Fig.11.

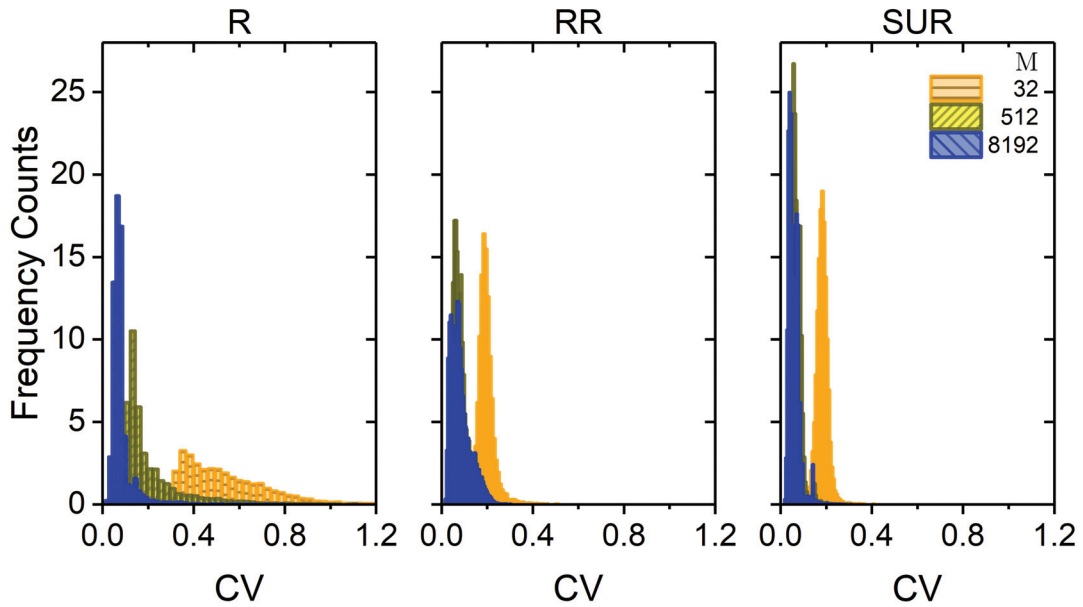


Fig. 11: Frequency count of the different  $\text{CV}(Q, \tau)$  obtained for different  $M$  values. Results from the redundant scheme (R) are shown in the left panel. The center and left panel show the ones obtained from RR and SUR schemes, respectively.

Results for the redundant scheme (R) are shown in the left panel, while the results from the RR and SUR are presented in the center and right panel. Focusing on the small number of  $\mathcal{T}_{\text{rs}}$  elements ( $M=32$ ) (red frequency counts in Fig.11), the

data from the redundant algorithm (R) shows a wider histogram when compared to the ones from RR and SUR. This indicates the difference in effectiveness of the sampling time between them. Moreover, this difference can be depicted by following the shift to smaller values of the mode of the distribution, where the RR and SUR sampling schemes have a faster tendency to approach close to zero for smaller values of  $M$ . It is worth noting that, despite the obtained values, SUR and RR algorithms have the narrower histograms. However, the data obtained from the SUR scheme presents the narrowest histograms, indicating that this sampling scheme is the most effective of the three.

To test the effectiveness of the sampling schemes, we systematically increased  $M$  and obtained the evolution of the mode from the frequency counts, obtaining an asymptotic value of  $CV(Q, \tau) = 0.05$  (left panel of Fig.12). The R scheme achieves the asymptotic value for  $M \sim 4,000$ . The RR and SUR reach it with a smaller number of  $M$ , being  $M = 512$  enough to get as close to  $CV = 0.06$ . Thus, the total number of  $\mathcal{T}_{rs}$  elements gets reduced. As a consequence, the computational time of the calculation of  $D(Q, \tau)$  gets majorly improved, being reduced by an order of magnitude, as shown in Fig.9.

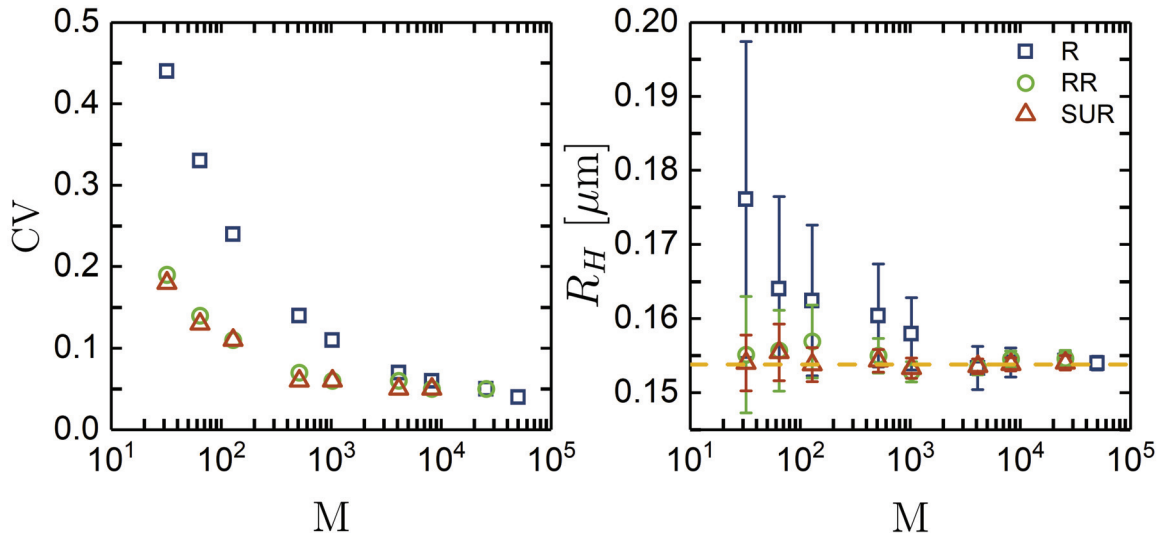


Fig. 12: Statistical convergence of CV (left) and  $R_H$  (right) for all three algorithms plotted for different number of image pairs ( $M$ ). The dashed line represents the convergence value of  $R_H = 0.153 \mu\text{m}$

The effect of the statistical convergence of  $D(Q, \tau)$  can also be studied by extracting a physical quantity encoded in  $f(Q, \tau)$ . Such is the case of the hydrodynamic radius  $R_H$  present in the characteristic time of  $f(Q, \tau)$  for purely diffusive systems (Eq.(36)). For this purpose, we obtained  $f(Q, \tau)$  for different  $M$  values and extracted  $R_H$  by performing a cumulant fit [38]. Our results are shown in the right panel of Fig.12, where the error bars represent the propagation of the 95% confidence interval from the  $R_H$ . The extracted values of  $R_H$  show similar trend like the modal value of  $CV(Q, \tau)$ , where the SUR scheme converges within the

smallest image pairs that we have used ( $M=32$ ), while the RR needs 4 times more number of  $\mathcal{T}_{\text{RS}}$  elements to converge ( $M=128$ ) hence, the SUR scheme shows the highest optimization for performing time averages.

#### 4.1.2 Spatial sampling optimization

The power spectrum is of fundamental importance in the DFM scheme (Eq.(118)). Due to the large number of images involved, its determination is a highly-demanding computational task. For images made of  $N_p \times N_p$  pixels, the computational time of the two dimensional fast fourier transform (2DFFT) is  $N_p^2 \log_2(N_p)$  [7, 81]. An illustration of the dependence of the computational time as a function of the image size is shown in Fig.13. The calculations were performed over a total number of 50,000 images, using 250 logarithmically spaced delay times, and  $M=3072$ .

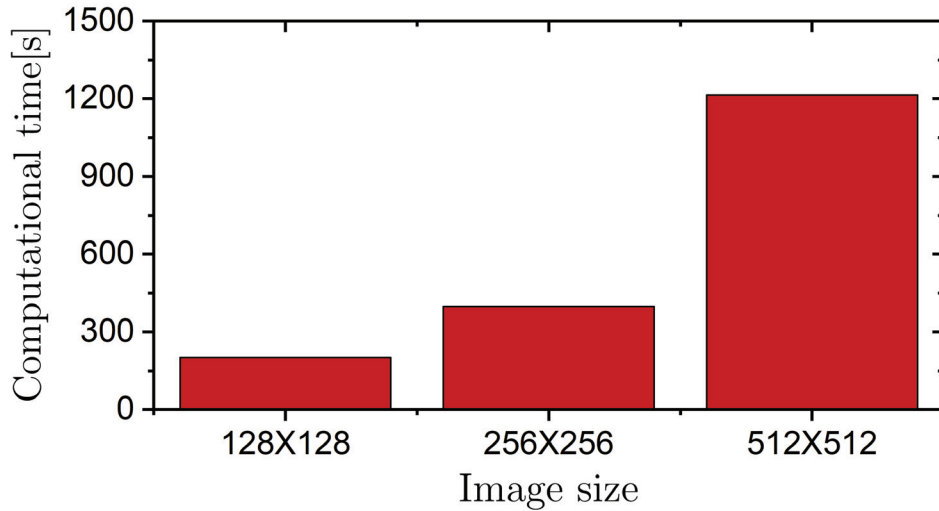


Fig. 13: Computational time as a function of the image size. The calculations were performed over a total number of 50,000 images, using 250 logarithmically spaced delay times, and  $M=3072$ .

The previous indicates that a reduction in image size would contribute to lowering the computational time. Thus, an algorithm that is able to reduce the acquired image size without compromising spatial information would benefit in speeding up the calculations. In the following we make use of an algorithm called Digital Data Reduction (DDR), based on a digital image interpolation algorithm. The main purpose is to reduce the image size by enhancing the significant data per pixel, thus reducing spatial instead of temporal redundancy. This is accomplished by matching the digital resolution (due to the fixed pixel size), and the optical resolution without losing relevant spatial data [82]. The latter is a frequency space criterion, given that for an image acquired with an optical microscope the limiting optical frequency will be given by its correspondent resolution limit. Thus, if the mismatch is considerable, an important amount of pixels of the performed calculations will have no contribution to the analysis. In order to quantify the

matching of the resolutions, a matching factor  $\delta$  is defined as

$$\delta \equiv \frac{K_R}{K_{Ny}} \quad (122)$$

where,

$$K_R = \frac{\pi}{0.61\lambda} \text{NA}, \quad K_{Ny} = \frac{N_p}{2} \Delta k = \pi \frac{M'}{p_s}, \quad (123)$$

where  $K_R$  is the corresponding frequency for the Rayleigh resolution criteria of the optical element that generates the image [83] and  $K_{Ny}$  is the corresponding Nyquist frequency due to a fixed pixel size ( $p_s$ ) of the sensor [82].  $K_{Ny}$  can be obtained from maximum frequency from the discretization  $\Delta k$  of the reciprocal space,  $\Delta k = 2\pi/L$  [73, 82], where  $L = N_p p_s / M'$  corresponds to the image size, which depends on the magnification  $M'$  of the imaging system, the number of pixels  $N_p$  and the pixel size  $p_s$ . The ratio  $p_s/M'$  is also known as pixel pitch.

Digital Data Reduction (DDR) reduces the effective image size using a bicubic interpolation that performs antialiasing. This can be found as a standard routine in MATLAB known as *imresize*. An example of this procedure is presented in Fig.14. DDR1 stands for an image reduction 1, i.e. keeping the same image size, as in comparison for DDR2 and DDR4, leading to a reduction of 0.5 and 0.25 per dimension, respectively. Then, the final image is 1, 1/4, 1/16 of the original image size, accordingly. As can be appreciated from Fig.14, an increase on DDR scheme leads to higher values of  $\delta$ , thus modifying the amount of data per pixel in the reciprocal space. The latter can be summarized in three regimes: The first one, over sampling regime ( $\delta < 0.5$ ), where a greater area (or number of pixels) contains no spectral information compared to the circle of the power spectrum (dark area). The second regime, good sampling condition ( $0.5 \leq \delta \leq 1.0$ ), where the dark area is reduced. Notice that the circle of the power spectrum is still fully visible. It should be pointed that  $\delta = 1$  is the optimal sampling condition but hardly achieved due to the fixed pixel size from the sensor and optical conditions in the imaging setup. In the third regime ( $\delta > 1.0$ ), the power spectrum limits are outside from the area of the image, leading to a loss of larger frequencies. Because of this, the third regime is known as the under sampling. The effects of DDR in the power spectra are quantified and summarized in Fig.15.

For an overall static analysis  $D(Q, \tau \rightarrow \infty)$  was obtained, and it is shown in Fig.15. DDR4 ( $\delta = 1.24$ ) exhibits a reduction to 85% of the  $Q$  range when compared to an unaltered range of DDR1 ( $\delta = 0.31$ ) and DDR2 ( $\delta = 0.62$ ). This is because for DDR1 and DDR2 the circle of the power spectrum is inside the image boundaries as mentioned before. Then, special care has to be taken in order to not violate the conditions for extracting an estimated value of  $B(Q)$ , as described by (Eq.115).

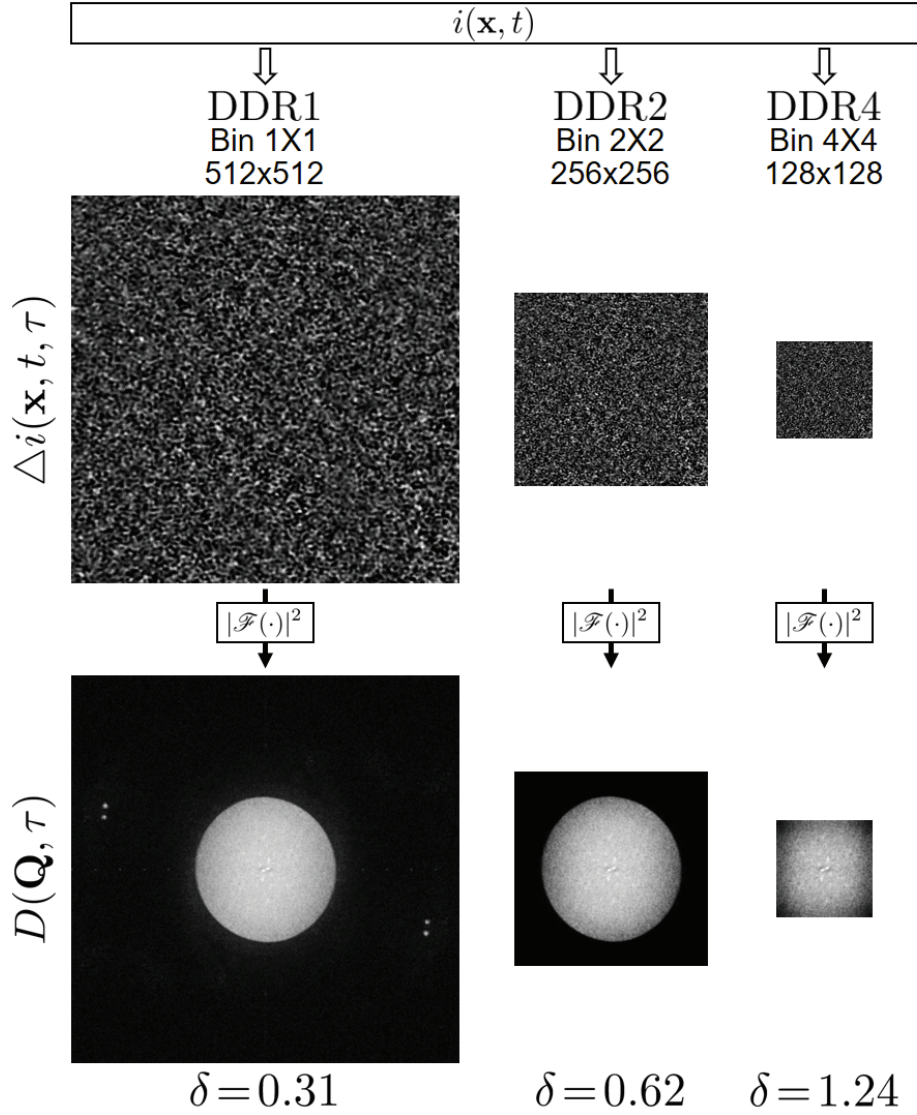


Fig. 14: Graphical representation of the DDR algorithm for the fluctuating signal from HNFS speckle images (upper), and their corresponding power spectra (lower). All of the upper images represent the same spatial area.

The main effect of DDR2 is that it introduces an effective optical transfer function (OTF) when compared to DDR1; having a stronger effect DDR4. A possible explanation is that DDR interpolates between pixels, leading to an effective pixel size that alters its captured spatial resolution (maximum accessible frequency). This translates into a stronger curvature of  $D(Q, \tau \rightarrow \infty)$  for higher  $Q$  values.

To further study a possible effect of DDR to the extracted dynamical information, we proceeded to obtain the intermediate scattering functions per scattering wave vector  $Q$ . Our results are plotted as a function of  $\tau Q^2$  (lower left of Fig.15). As expected for particles undergoing free diffusion, all results collapse onto a master curve. Thus, DDR does not affect the extracted  $f(Q, \tau)$ . Additionally, we extracted the characteristic times ( $\tau_c = 1/DQ^2$ ) from each  $Q$  per DDR scheme. Results are shown in Fig.15 (lower right). It can be observed that for DDR2 and DDR4,  $\tau_c(Q)$  overlaps with the ones extracted from the unaltered DDR1, reas-

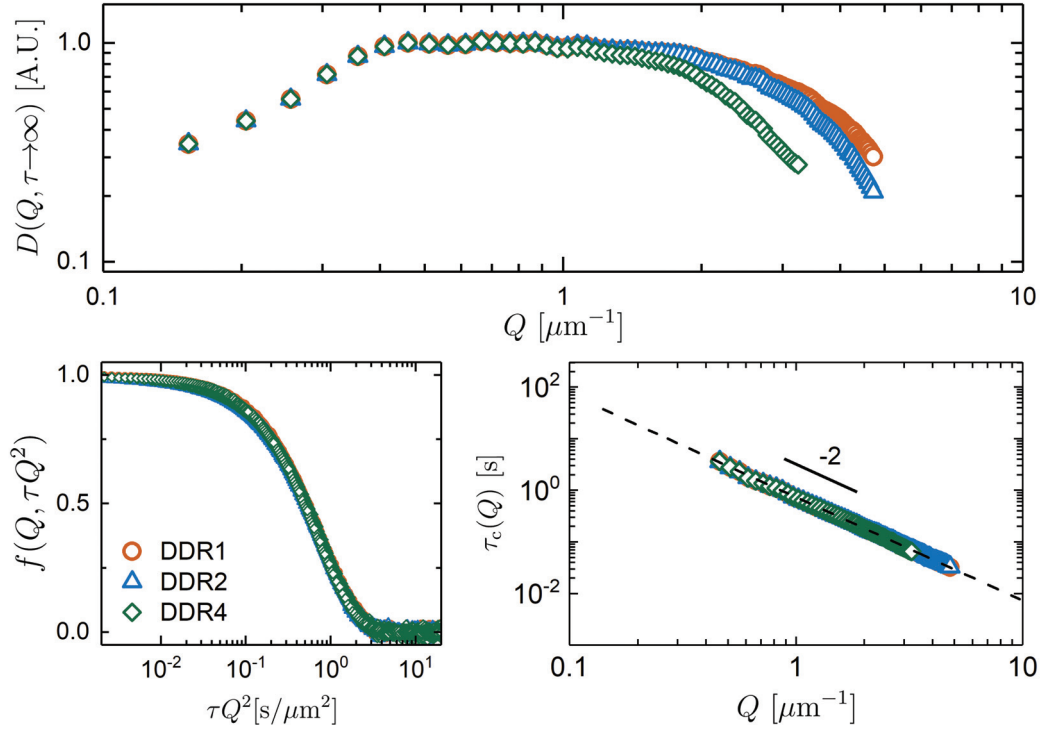


Fig. 15: Azimuthal averaging of the long time limit of the structure function  $D(Q, \tau \rightarrow \infty)$  (upper),  $f(Q, \tau Q^2)$  (lower left) and the extracted characteristic times ( $\tau_c(Q) = 1/DQ^2$ ) for the different digital data reduction schemes: DDR1 (circles), DDR2 (triangles) and DDR4(diamonds).

ensuring that the DDR scheme has no effect in the extracted dynamics. Hence, an optimized spatial post processing scheme can be performed to reduce computational time.

## 4.2 Effect of moderate multiple scattering in heterodyne near field scattering

DFM is very successful for studying soft matter and biological systems, so far it has been restricted to samples showing single scattering only, that is dilute, index-matched transparent suspensions or images from very thin optical depth (for a detailed review see Ref. [7] and included references). This limits the range of applications since many soft matter systems are intrinsically turbid showing multiple scattering. For example, if there is a refractive index mismatch, the maximum concentration that can be sampled gets reduced. This because most of the light suffers multiple scattering, thus the transmitted light is significantly reduced and all the relations in Eq.(106,107) do not hold. The reduction of transmitted light can be quantified by the transmittance,  $\mathcal{T} = I_T/I_0$ , i.e. the ratio of the transmitted light through a sample ( $I_T$ ) by the transmitted light through sample made of pure solvent under the same optical configuration. Another very useful quantity is called the reflectance, defined by  $\mathcal{R} = 1 - \mathcal{T}$ .

In the following a summary of the relevant findings of Ref. [77] is presented. The statistical properties of the HNFS signal including moderate multiple scattering are computed for the real and reciprocal space. Then, validated with experiments where the turbidity is controlled through the particle volume fraction. Here the samples consists of polystyrene particles ( $\sigma = 330\text{nm}$ ) in ultra pure water. An illustration of the level of turbidity and its corresponding  $\mathcal{R}$  for some of the samples used in this work is shown in Fig.16.

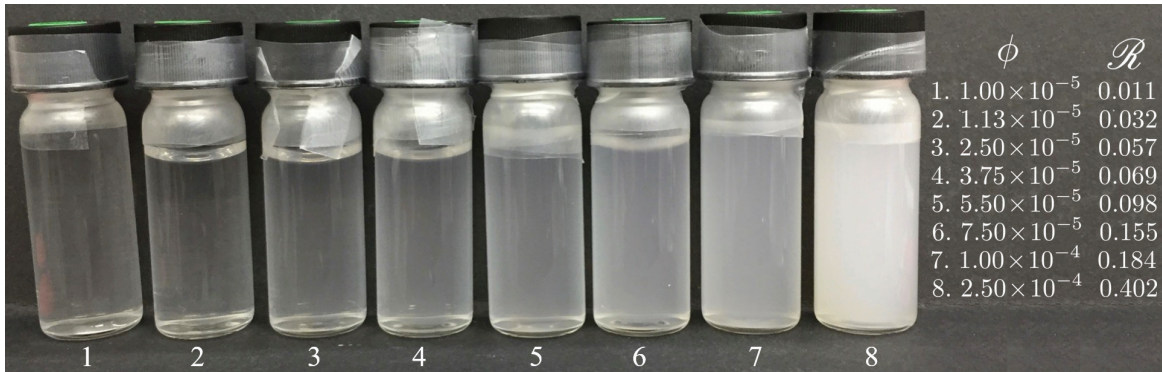


Fig. 16: Effect of the concentration, or volume fraction, on the degree of turbidity and its corresponding reflectance ( $\mathcal{R}$ ). The volume fraction increases from left to right. The samples consisted of polystyrene particles ( $\sigma = 330\text{nm}$ ) in ultra pure water.

The reflectance values were obtained by measuring the transmittance of the samples in a rectangular quartz cuvette of optical path 1mm. The light source used is a He-Ne laser beam with 10mm beam width, which has 18.9mW as output power and wavelength  $\lambda_0 = 632.8\text{nm}$ . The intensity  $I_T$  of the transmitted laser beam was measured by a Laser power meter (Coherent Fieldmate with a Silicon photodiode). Experiments were carried out by the setup described in Ref. [77]. A series of 50,000 images of  $480 \times 480$  pixels were recorded at a rate of 100 FPS

for all of the studied samples. The camera used is an 8 bit CMOS black and white camera with  $1280 \times 1024$  pixels each of area  $6.7 \times 6.7 \mu\text{m}^2$  (Allied Vision Technologies, Marlin-131).

#### 4.2.1 HNFS Signal in Real Space

In HNFS the transmitted light acts as a reference beam or local oscillator. Its static electric field  $e_T(\mathbf{x})$  interferes with light scattered by the sample, which has an electric field  $e_{sc}(\mathbf{x}, t)$ . The electric field of the scattered light,  $e_{sc}(\mathbf{x}, t)$ , can be thought as a superposition of different electric fields  $e_p(\mathbf{x}, t)$  which all arrive at the detection plane, but have undergone different numbers of scattering events,  $p$ , while traversing the sample:

$$\mathbf{e}_{sc}(\mathbf{x}, t) = \sum_{p=1}^N e_p(\mathbf{x}, t). \quad (124)$$

It contains contributions from single scattering,  $e_S(\mathbf{x}, t) = e_1(\mathbf{x}, t)$ , and, if present, from multiple scattering,  $e_M(\mathbf{x}, t) = \sum_{p>1} e_p(\mathbf{x}, t)$ , which includes all multiple-scattering contributions, i.e. double, triple, etc. scattering. Similar to the case of far field scattering [84–86], formally these contributions can be separated to yield the total scattered electric field

$$e_{sc}(\mathbf{x}, t) = e_1(\mathbf{x}, t) + \sum_{p=2}^N e_p(\mathbf{x}, t) = e_S(\mathbf{x}, t) + e_M(\mathbf{x}, t). \quad (125)$$

In the following we will continue as in [77]:

1.  $e_S(\mathbf{x}, t)$  and  $e_M(\mathbf{x}, t)$  are Gaussian-distributed random variables with mean zero and phases uniformly distributed between  $-\pi$  and  $+\pi$ ,
2.  $e_S(\mathbf{x}, t)$  and  $e_M(\mathbf{x}, t)$  are statistically independent,
3.  $|e_M| \lesssim |e_S| < |e_{tr}|$ , i.e. only moderate multiple scattering.

Then, the intensity pattern captured by the camera is

$$\begin{aligned} i(\mathbf{x}, t) &= |e_{tr}(\mathbf{x}) + e_S(\mathbf{x}, t) + e_M(\mathbf{x}, t)|^2 \\ &\approx i_{tr}(\mathbf{x}) + e_{tr}(\mathbf{x})e_S^*(\mathbf{x}, t) + e_{tr}^*(\mathbf{x})e_S(\mathbf{x}, t) \\ &\quad + e_{tr}(\mathbf{x})e_M^*(\mathbf{x}, t) + e_{tr}^*(\mathbf{x})e_M(\mathbf{x}, t), \end{aligned} \quad (126)$$

where  $i_{tr}(\mathbf{r}) = |e_{tr}(\mathbf{r})|^2$ , note that Eq.(126) is an extension of Eq.(106). Due to assumption 3., terms that are second order in the contributions from single and multiple scattering can be neglected, ensuring heterodyne detection is still met [8, 24, 70, 87].

We then proceed to extract the fluctuating signal, it can be split into single-scattering and multiple-scattering contributions according to

$$\Delta i(\mathbf{x}, t, \tau) = \Delta i_S(\mathbf{x}, t, \tau) + \Delta i_M(\mathbf{x}, t, \tau), \quad (127)$$

with the single-scattering signal

$$\begin{aligned} \Delta i_S(\mathbf{x}, t, \tau) &= e_{\text{tr}}(\mathbf{x})e_S^*(\mathbf{x}, t+\tau) + e_{\text{tr}}^*(\mathbf{x})e_S(\mathbf{x}, t+\tau) \\ &\quad - e_{\text{tr}}(\mathbf{x})e_S^*(\mathbf{x}, t) - e_{\text{tr}}^*(\mathbf{x})e_S(\mathbf{x}, t) \end{aligned} \quad (128)$$

and analogous the multiple-scattering signal  $i_M(\mathbf{r}, t, \tau)$ .

The electric fields of the single and multiple-scattered light,  $\mathbf{e}_S(\mathbf{r}, t)$  and  $\mathbf{e}_M(\mathbf{r}, t)$ , are assumed to be Gaussian distributed and statistically independent (assumptions (1, 2)) and, moreover,  $e_{\text{tr}}(\mathbf{x})$  is essentially constant. Therefore,  $\Delta i(\mathbf{r}, t, \tau)$  is also Gaussian distributed with mean zero. Hence, the position- and time-averaged probability distribution is

$$\begin{aligned} \langle P(\Delta i(\mathbf{x}, t, \tau)) \rangle_{\mathbf{x}, t} &= P(e_{\text{tr}}(\mathbf{x})e_S(\mathbf{x}, \tau)) P(e_{\text{tr}}(\mathbf{x})e_M(\mathbf{x}, \tau)) \\ &= \frac{1}{\sqrt{2\pi\sigma_{\text{sc}}^2(\tau)}} \exp\left(-\frac{\Delta i^2(\tau)}{2\sigma_{\text{sc}}^2(\tau)}\right), \end{aligned} \quad (129)$$

where  $\sigma_{\text{sc}}^2(\tau) = \sigma_S^2(\tau) + \sigma_M^2(\tau)$  is the second moment of the distribution. It depends on the second moments of the distributions of the single-scattering and multiple-scattering signals,  $\sigma_S$  and  $\sigma_M$ , respectively.

In the extreme multiple-scattering limit, the intensity pattern  $i(\mathbf{r}, t)$  is a homodyne-like speckle pattern and  $i(\mathbf{r}, t)$  an exponentially distributed random variable. Since  $\Delta i(\mathbf{r}, t, \tau)$  represents the difference between two of such patterns, its values obey a Laplace probability distribution with variance  $2b_M^2(\tau)$  [87–89]:

$$\langle P(\Delta i(\mathbf{r}, t, \tau)) \rangle_{\mathbf{r}, t} = \frac{1}{2b_M(\tau)} \exp\left(-\frac{|\Delta i(\tau)|}{b_M(\tau)}\right). \quad (130)$$

Images  $i(\mathbf{x}, t)$  for different levels of  $\mathcal{R}$  are shown in Fig.17 (top). For  $\mathcal{R} = 0.011$  the superposition of the reference beam and the HNFS speckles can be appreciated. The previous gets screened by a different speckle pattern for higher values of  $\mathcal{R}$ , being this a visible indication of the appearance of moderate multiple scattering. To quantify this effect, we computed the corresponding  $\langle P(\Delta i(\mathbf{x}, t, \tau)) \rangle$  for  $\tau = 0.01\text{s}$  (symbols in bottom). The extracted data shows an increase in the width and a change in shape of the probability distributions for  $\mathcal{R}$  values where their corresponding images displayed the effect of moderate multiple scattering.

To quantify the quality of the fit, the coefficient of determination ( $R^2$ ) is extracted and presented in Fig.18. The main findings can be summarized into four regions:

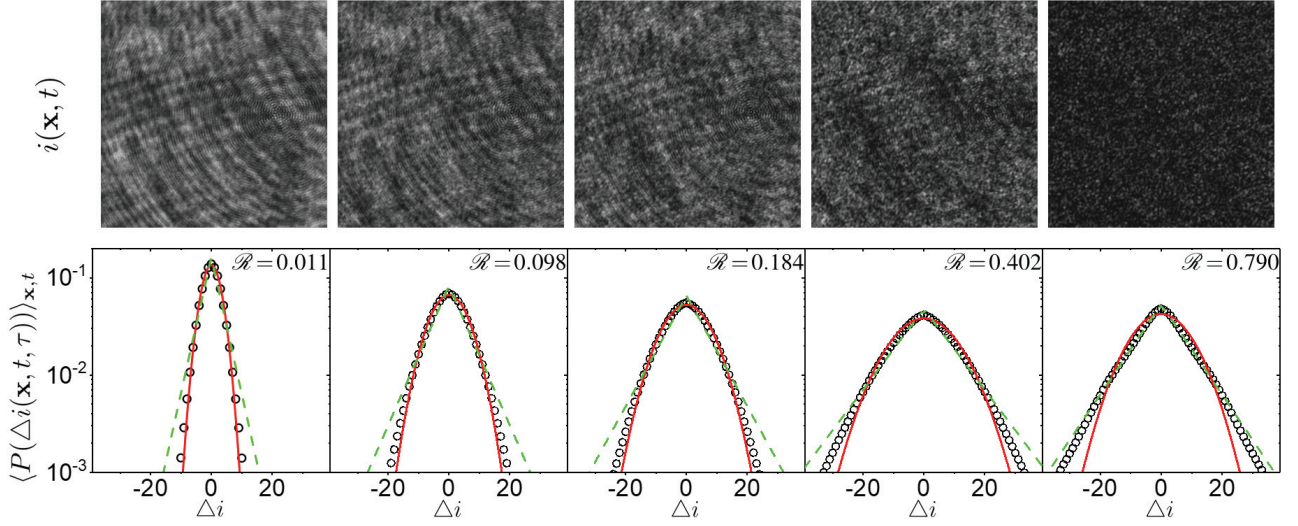


Fig. 17: Images of different samples composed of polystyrene particles ( $\sigma = 330\text{nm}$ ) in ultra pure water for different levels of reflectance (top) and probability distributions from the HNFs signal,  $\langle P(\Delta i(\mathbf{x}, t, \tau)) \rangle_{\mathbf{x}, t}$  (bottom), computed for  $\tau = 0.01\text{s}$  (symbols). The continuous lines represent the fit for a Gaussian distribution functions while the dotted for the the Laplace distribution functions.

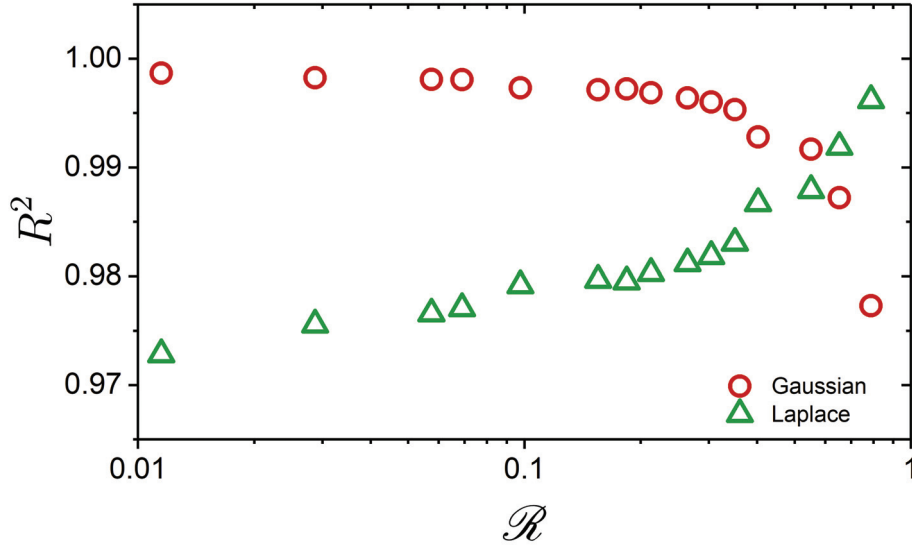


Fig. 18: Coefficient of determination  $R^2$  as a function of  $\mathcal{R}$  for fits based on a Gaussian and a Laplace probability distribution

- Single scattering, for small reflectance values ( $0 < \mathcal{R} < 0.15$ ) where a Gaussian distribution is a very good approximation for  $\langle P(\Delta i(\mathbf{x}, t, \tau)) \rangle$  having  $R^2 > 0.998$ , whereas the Laplace distribution shows smaller values.
- Moderate multiple scattering, corresponding to intermediate reflectances ( $0.15 < \mathcal{R} < 0.30$ ). Having a noticeable decrease of the quality of the Gaussian fits and, correspondingly, an increase of the quality of the Laplace fits.
- The cross-over, for ( $0.30 < \mathcal{R} < 0.45$ ). Where the  $R^2$  from the two fits is observed indicating that the heterodyne signal becomes comparable to the homodyne signal from the multiple scattering. In this region a combination of the Gaussian and Laplace distributions can be used to describe the data.

- Multiple scattering, for  $(0.45 < \mathcal{R})$  where the signal becomes mainly homodyne and it is very well described by a Laplace distribution.

#### 4.2.2 HNFS Signal in Reciprocal Space

In order to obtain far-field-like information, the power spectrum of the HNFS signal is computed. The HNFS signal  $\Delta i(\mathbf{r}, t, \tau)$  (Eq. 127) is Fourier transformed to yield  $\Delta I(\mathbf{q}, t, \tau)$ . In the following Fourier transformed variables are indicated by capital letters.

$$\Delta I(\mathbf{q}, t, \tau) = \Delta I_S(\mathbf{q}, t, \tau) + \Delta I_M(\mathbf{q}, t, \tau), \quad (131)$$

where  $\mathbf{q}$  is the spatial-frequency vector in the plane being imaged. The single-scattering contribution is given by

$$\begin{aligned} \Delta I_S(\mathbf{q}, t, \tau) \sim & E_S^*(\mathbf{q}, t+\tau) + E_S(-\mathbf{q}, t+\tau) \\ & - E_S^*(\mathbf{q}, t) - E_S(-\mathbf{q}, t) \end{aligned} \quad (132)$$

taking  $E_{\text{tr}}(\mathbf{q}) \sim \delta(\mathbf{q})$  into account. The multiple-scattering contribution  $\Delta I_M(\mathbf{q}, t, \tau)$  is similarly defined. The squared modulus or power spectrum is

$$\begin{aligned} \mathcal{T}_{\text{rs}}(\mathbf{Q}, t, \tau) = & |\Delta I_S(\mathbf{q}, t, \tau)|^2 + |\Delta I_M(\mathbf{q}, t, \tau)|^2 \\ & + 2 \operatorname{Re}\{\Delta I_S(\mathbf{q}, t, \tau)\Delta I_M^*(\mathbf{q}, t, \tau)\}. \end{aligned} \quad (133)$$

This equation is a compact notation for the full expression that has 64 terms. Finally, the structure function  $D(\mathbf{Q}, \tau)$  is determined. Due to the time average, the cross-terms of the single-scattering and multiple-scattering contributions vanish since they are statistically independent. Thus the structure function is given by

$$\begin{aligned} D(Q, \tau) &= \langle \mathcal{T}_{\text{rs}}(\mathbf{Q}(\mathbf{q}), t, \tau) \rangle_{t, \theta} \\ &= 4I_S(Q) - 4 \operatorname{Re}\{\langle E_S(\mathbf{Q}, t)E_S^*(\mathbf{Q}, t+\tau) \rangle_{t, \theta}\} + \\ &\quad 4I_M(Q) - 4 \operatorname{Re}\{\langle E_M(\mathbf{Q}, t)E_M^*(\mathbf{Q}, t+\tau) \rangle_{t, \theta}\}, \end{aligned} \quad (134)$$

where  $I_S(Q) = \langle E_S(\mathbf{Q}, t)E_S^*(\mathbf{Q}, t) \rangle_{t, \theta}$  is the single-scattering intensity and  $I_M(Q) = \langle E_M(\mathbf{Q}, t)E_M^*(\mathbf{Q}, t) \rangle_{t, \theta}$  the multiple-scattering intensity. The decorrelation of multiple-scattered light typically occurs much faster than the frame rate of the camera and hence  $\langle E_M(\mathbf{Q}, t)E_M^*(\mathbf{Q}, t+\tau) \rangle_{t, \theta} \approx 0$  for the delay times  $\tau$  considered in our experiments. Therefore, the observed structure function becomes

$$D(Q, \tau) = 4I_S(Q) [1 - f(Q, \tau)] + 4B_{\text{eff}}(Q), \quad (135)$$

where  $f(Q, \tau) = \operatorname{Re}\{\langle E_S(\mathbf{Q}, t)E_S^*(\mathbf{Q}, t+\tau) \rangle_{t, \theta}\} / I_S(Q)$  is the intermediate scattering function and the effective ‘baseline’  $B_{\text{eff}}(Q) = I_M(Q) + B(Q)$  contains delay-time-independent contributions due to the (moderate) multiple scattering and background noise  $B(Q)$  caused by, e.g. the camera shot noise. Recalling the

numerical estimation of  $f(Q, \tau)$  given by Eq.(116),

$$\beta(\mathbf{Q})f(\mathbf{Q}, \tau) = \frac{D(\mathbf{Q}, \tau \rightarrow \infty) - D(\mathbf{Q}, \tau)}{D(\mathbf{Q}, \tau \rightarrow \infty) - B'(\mathbf{Q})}, \quad (136)$$

where  $B'(\mathbf{Q})$  is the estimated background noise from a single scattering measurement Eq.(115), thus

$$\beta(\mathbf{Q}) \sim 1 - \frac{I_M(\mathbf{Q}) + \delta_\beta(\mathbf{Q})}{I_S(\mathbf{Q})} \quad (137)$$

taking  $\delta_\beta(\mathbf{Q}) \equiv B(\mathbf{Q}) - B'(\mathbf{Q})$ . The expression obtained in Eq.(137) is only valid for moderate multiple scattering. If multiple scattering dominates, the signal is homodyne and other relations hold. [87, 88].

The analytical expression of  $f(\mathbf{Q}, \tau)$  depends on the particular system dynamics and can be used to extract useful information. For isotropic motion, the dynamics depend only on the magnitude of the scattering wave vector  $\mathbf{Q}$ . Hence, to improve statistics, an azimuthal over the polar angle  $\theta$  in the  $Q$  plane is performed. Moreover, for dilute Brownian systems  $f(Q, \tau) = \exp(-\tau/\tau_c)$ . It contains a characteristic time  $\tau_c = 1/D_0Q^2$ , with  $D_0$  the free diffusion coefficient. With the previous, the hydrodynamic radius of the beads in suspension ( $R_H$ ) can be obtained. This dynamical measurement is known to be particle sizing, and in order to obtain it, the Stokes-Einstein relation is used, i.e.  $D_0 = k_B T / 6\pi\eta R_H$ , with  $k_B$  being the Boltzmann's constant,  $T$  the temperature,  $\eta$  the system's viscosity.

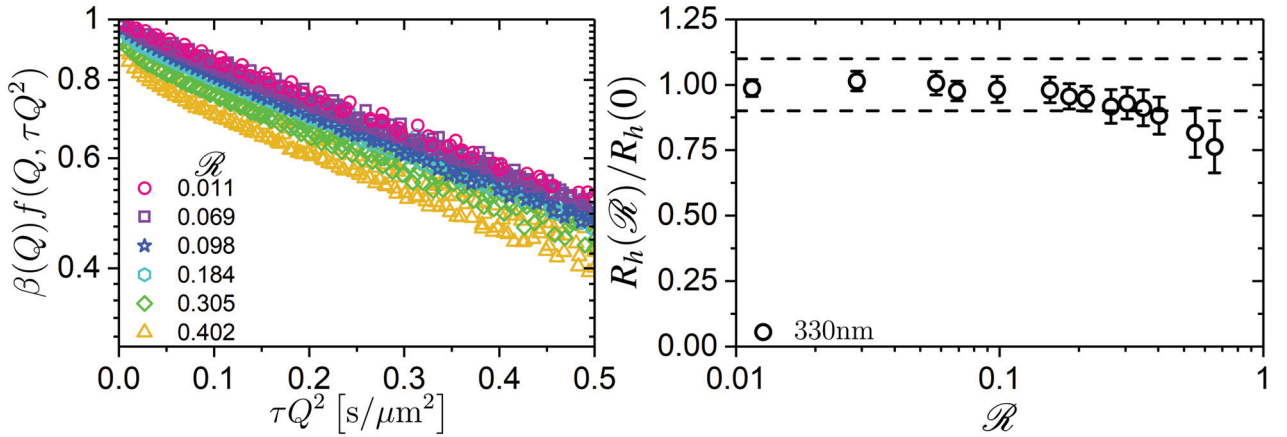


Fig. 19:  $\beta(Q)f(Q, \tau Q^2)$  for different values of  $\mathcal{R}$  from different samples composed of polystyrene particles ( $\sigma = 330\text{nm}$ ) in ultra pure water(left). The effect of moderate multiple scattering is summarized in two main contributions to  $\beta(Q)f(Q, \tau)$ . The first one is a reduction in  $\beta(Q)$  as  $\mathcal{R}$  increases. The second one, for  $\mathcal{R} > 0.3$ , a faster decay at short  $\tau Q^2$  starts to appear. However, each  $\beta(Q)f(Q, \tau)$  maintains parallel among different  $\mathcal{R}$  obtaining similar slopes, thus similar slopes, i.e. Diffusion coefficients ( $D_0$ ), describe each system dynamics. The  $Q$  range represents the majority of the sampled wavelengths of the acquired images ( $0.75 \leq Q \leq 6.5[1/\mu\text{m}]$ ). Normalized hydrodynamic radius ( $R_h(\mathcal{R})/R_h(0)$ ) as a function of  $\mathcal{R}$  (right). The dashed lines indicate a deviation of  $\pm 10\%$  from  $R_h(0)$ .

Examples of  $\beta(Q)f(Q, \tau)$  for some of the measured samples is shown in Fig.19 for different  $\mathcal{R}$  values. The effect of moderate multiple scattering is summarized

in two main contributions to  $\beta(Q)f(Q, \tau)$ . The first one, as sketched in Eq.(137), a reduction in  $\beta(Q)$  as  $\mathcal{R}$  increases. The second one, for  $\mathcal{R} > 0.3$ , a faster decay at short  $\tau Q^2$  starts to appear. However, at  $\tau Q^2 > 0.5$  each  $\beta(Q)f(Q, \tau)$  maintains parallel among different  $\mathcal{R}$ , thus similar slopes, i.e. Diffusion coefficients ( $D_0$ ), describe each system dynamics. It is important to mention that the data is represented in  $\tau Q^2$  scale where for freely, non-interactive Brownian particles,  $f(Q, \tau Q^2)$  collapse onto master curve.

We proceeded to obtain each slope of  $\beta(Q)f(Q, \tau)$  by extracting the characteristic time ( $\tau_c = 1/D_0 Q^2$ ) via a standard cumulant analysis [38]. With the extracted diffusion coefficient, the normalized hydrodynamic radius  $R_h(\mathcal{R})/R_h(0)$  is calculated and presented in the right hand side of Fig.19. As suggested by  $\beta(Q)f(Q, \tau)$ , the extracted  $R_h(\mathcal{R})/R_h(0)$  starts to deviate significantly for  $\mathcal{R} > 0.3$ , observing a deviation grater than 10 %. Additionally, the uncertainty in the determined values starts to increase. Hence, the limit of applicability of the HNFS technique is obtained, this is in agreement with the previously described in Sec.4.2.1.

### 4.3 Microliter viscometry

A macroscopic approach to characterize colloidal suspensions is by determining its flow properties. The shear viscosity is the property that describes the opposition of a suspension to flow. The viscosity is susceptible to the particle shape, size, and particle concentration. It can also reflect the interaction between particles, as well as internal structural changes or aggregation [9]. Depending on how an instrument can impose a flow onto the sample, the shear viscosity can be measured by viscometers or mechanical rheometers. The first ones are only allowed to measure the liquid under one type of flow condition, fixed by the geometry of the instrument. Mechanical rheometers can impose several types of flow by deforming the sample, thus being able to characterize systems with more complex behaviour. If the flow is produced by a constant deformation at a given shear rate ( $\dot{\gamma}$ ), the extracted viscosity is known as the steady shear viscosity  $\eta(\dot{\gamma})$ , and if the flow is made by applying small amplitude oscillatory shear (SAOS) a frequency-dependent complex viscosity is measured  $\eta^*(\omega)$ .

The frequency dependent viscosity is related to the visco-elastic complex modulus by  $\eta^*(\omega) = G^*(\omega)/i\omega$ , where  $G^*(\omega) = G'(\omega) + iG''(\omega)$ , and  $G^*(\omega)$  displays the ability of a system to store ( $G'$ ) or dissipate ( $G''$ ) energy. The connection between the steady shear and the oscillatory shear viscosities is given by the empirical rule known as the Cox-Merz rule. It states that, for very small frequencies and shear rates, both viscosities are equal [90]. The main limitation for the frequencies or rates probed by a Rheometer is given by its limited torque resolution of the instrument.

An extension of SAOS experiments can be extracted from passive micro-rheology or micro-viscometry [36, 42–44, 91–93]. This is achieved by combining the Cox-Merz rule, the Generalized Stokes Einstein relations, and the Mean Squared Displacement (MSD) of tracer particles in the suspension of interest. The MSD can be extracted by means of particle tracking algorithms, applied to optical microscopy images from suspensions where the visibility of tracer particles is possible, i.e. fairly transparent samples. The tracer particle size is limited to the optical resolution of the microscope, and the ability of tracking algorithms to identify it. Additionally, the MSD can be obtained from the intermediate scattering function measured in dynamic light scattering experiments, thus breaking the limitation of size from the tracer particles, and depending on the optical conditions of the suspensions, i.e. transparent or turbid, Quasi-elastic DLS or Diffusing Wave Spectroscopy can be employed [35, 40, 41, 46, 94].

In the following, the main findings of Ref. [36] are presented and organized as

follows: The first subsection introduces the application of the DFM framework for micro-viscometry, and its application on different suspensions: an ideal viscous fluid, a biological colloidal suspension made of lysozyme proteins, and a visco-elastic polymer suspension. In the second subsection, the particle size for tracer conditions is discussed, as well as possible outlooks for the applicability of the technique.

#### 4.3.1 Ideal, biological and visco-elastic fluids

The combination of microliter viscometry and the Digital Fourier Microscopy framework will be denoted as  $\eta$ -DFM. The approach consists in taking images acquired by an optical microscope of tracer particles added to the system under study. The tracers should be non interacting, thus not altering significantly the system to study. As a consequence, the concentration of tracer particles in suspension should be dilute. Then, the MSD is obtained via the structure function  $D(Q, \tau)$  from a DFM analysis (Eq.174). Finally, by combining the Generalized Stokes Einstein relations and the Cox-Merz rule the steady shear viscosity can be estimated.

The data analysis goes as follows, it starts by obtaining the azimuthally averaged structure function from a DFM analysis

$$D(Q, \tau) = A(Q) [1 - f(Q, \tau)] + B(Q). \quad (138)$$

Under tracer conditions, the intermediate scattering function  $f(Q, \tau)$  can be related to the mean squared displacement  $\langle \Delta \mathbf{x}^2(\tau) \rangle$  [23, 94, 95],

$$f(Q, \tau) = \exp \left[ -\frac{Q^2}{2d} \langle \Delta \mathbf{x}^2(\tau) \rangle \right]. \quad (139)$$

This is a generalization for  $d$  spatial dimensions of Eq.(35). Since the motion of the particles is projected onto a two dimension sensor, namely a camera  $d=2$ . Finally by combining Eq.(138) and Eq.(139) the MSD of the tracers can be obtained

$$\langle \Delta \mathbf{x}^2(\tau) \rangle = -\frac{2d}{Q^2} \ln \left[ 1 - \frac{D(Q, \tau) - B(Q)}{A(Q)} \right] \quad (140)$$

where  $A(Q)$  and  $B(Q)$  can be estimated following the procedure described by Eq.(115) and Eq.(116). Other numerical approaches can be found in [91, 92].

The obtained MSD then can be related to the rheological and viscometric properties of the medium via the Generalized Stokes-Einstein relation (GSE), recalling Eq.(46)

$$G^*(\omega) = \frac{2dk_B T}{3\pi\sigma i\omega \mathcal{F} \{ \langle \Delta \mathbf{x}^2(\tau) \rangle \}} \quad (141)$$

where  $k_B$  is the Boltzmann constant,  $T$  is the temperature,  $\sigma$  is the tracer diameter, and  $\mathcal{F}\{\langle\Delta\mathbf{x}^2(\tau)\rangle\}$  is the Fourier transform of the MSD. Assuming a local power law for the MSD, it is possible to approximate it with [39]

$$i\omega\mathcal{F}\{\langle\Delta\mathbf{x}^2(\tau)\rangle\}\approx\langle\Delta\mathbf{x}^2(1/\omega)\rangle\Gamma[1+\alpha(\omega)]i^{-\alpha(\omega)}\quad(142)$$

where  $\Gamma$  represents the gamma function,  $\alpha(\omega)=|\partial\ln\langle\Delta\mathbf{x}^2(\tau)\rangle/\partial\ln\tau|_{\tau=1/\omega}$  accounts for the characteristics of the sample and takes values between 0 and 1. If viscous behaviour dominates,  $\alpha\approx 1$ , and for elastic behaviour  $\alpha\approx 0$  (A full description can be found in [35, 36, 39]). Plugging this approximation in Eq.(141) the magnitude of the complex modulus  $G^*(\omega)$  becomes

$$G(\omega)=|G^*(\omega)|=\frac{2dk_B T}{3\pi\sigma\langle\Delta\mathbf{x}^2(1/\omega)\rangle\Gamma[1+\alpha(\omega)]}\quad(143)$$

and the real (elastic)  $G'(\omega)$  and complex (loss)  $G''(\omega)$  parts (moduli) of  $G^*(\omega)$  are given by,

$$G'(\omega)=G(\omega)\cos[\pi\alpha(\omega)/2],\quad G''(\omega)=G(\omega)\sin[\pi\alpha(\omega)/2].\quad(144)$$

The complex viscosity can be calculated using its definition as

$$\eta^*(\omega)=G^*(\omega)/i\omega.\quad(145)$$

Finally, the corresponding steady shear viscosity is estimated via the Cox-Merz rule,

$$|\eta^*(\omega)|_{\omega\rightarrow 0}\equiv\eta(\dot{\gamma})_{\dot{\gamma}\rightarrow 0}.\quad(146)$$

In order to validate  $\eta$ -DFM, we have applied it to different type of suspensions. The first application is a series of **ideal liquids**, Glycerol-water mixtures. The viscosity of these mixtures have frequently been examined, and have become a reference system to test viscometry and microrheology techniques. In our study, we tested glycerol-water mixtures with glycerol mass fraction ranging from 0% to 57%, each containing polystyrene spheres of size  $\sigma=330\text{nm}$  as tracers. The tracer particles volume fraction was set to  $5\times 10^{-5}$ .

We have obtained transmission images using an upright bright field microscope (Nikon Eclipse 80i), equipped with a 20X microscope objective, and an 8 bit CMOS black and white camera (Mako-U130, Allied Vision Technologies). The application of DFM to the previously described optical configuration is known as bright field Differential Dynamic Microscopy (DDM) [75]. Under this optical configuration, a series of 20,000 images were recorded at 100 FPS and, subsequently, we analysed them using the SUR algorithm (described Sec.4.1). Full details on the experimental conditions as well as other experimental techniques employed in this work can be found in [36].

The output of the analysis leads to the intermediate scattering function  $f(Q, \tau)$ . It is expected to scale with  $Q^2$  as indicated in Eq.(139), this can be used to test tracer conditions. Indeed, if represented as a function of  $\tau Q^2$ , all  $f(Q, \tau)$  obtained for a specific glycerol content but different  $Q$  values fall on top of each other onto a master curve for the employed  $Q$  range, as shown in the inset of the left panel of Fig.20. The selected  $Q$  range,  $(0.70 - 4.75) [\mu\text{m}^{-1}]$ , covers the majority of the length scales sampled by the images.

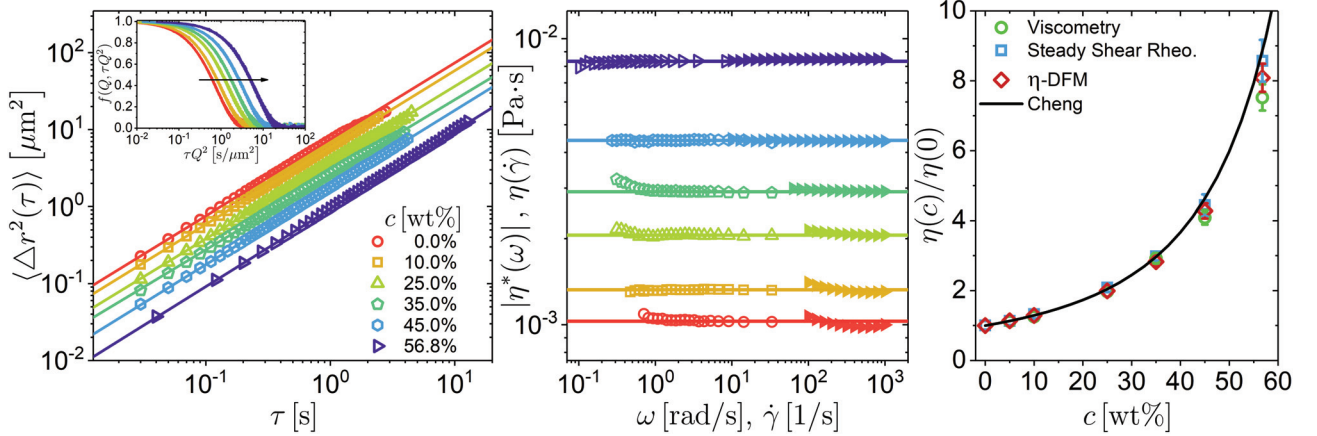


Fig. 20: Results obtained for ideal fluids (glycerol-water mixtures) applying  $\eta$ -DFM. Mean squared displacement (MSD) for tracers with a diameter  $\sigma = 330\text{nm}$  in glycerol-water mixtures (left panel), and its corresponding Intermediate scattering functions  $f(Q, t)$  as a function of  $\tau Q^2$ , the arrow represents an increase in glycerol concentration (inset left panel). Magnitude of the extracted frequency dependent viscosity  $\eta^*(\omega)$  compared with steady shear viscosity from rheology experiments for different glycerol concentrations (middle panel). Comparison of the normalized viscosity,  $\eta(c)/\eta(0)$ , as a function of glycerol mass fraction ( $c$ ) determined by  $\eta$ -DFM, steady shear rheology, viscometry measurements, and literature data (right panel) [96].

As the viscosity of the liquid mixture increases, the decay of  $f(Q, \tau)$  is shifted to larger delay times. We proceed to extract the MSD as expressed by Eq.(140), taking under consideration data points that satisfy  $f(Q, \tau) > 0.1$ , this to ensure enough signal to noise ratio. The correspondent MSD is shown as open symbols in the left panel of Fig.20. Similarly to  $f(Q, \tau)$  a shift in the MSD can be seen, reflecting a slow down in dynamics due to the increase of glycerol concentration. The linear dependence in the MSD indicates purely diffusive motion, being consistent with the motion of particles in an ideal (Newtonian) liquid.

Proceeding with the  $\eta$ -DFM analysis, the modulus of the complex viscosity  $|\eta^*(\omega)|$  was computed following Eq.(144) and Eq.(145). The results are plotted (open symbols) and compared with steady shear measurements (closed symbols) in the middle panel of Fig.20. This shows an agreement of the steady shear viscosity and the magnitude of the complex viscosity, displaying no significant dependence on  $\omega$  and  $\dot{\gamma}$  for all glycerol concentrations. Thus, confirming the Cox-Merz rule and the validity of  $\eta$ -DFM. Additionally, for systems with a very low viscosity,

$\eta$ -DFM complements the limited sensitivity of the mechanical rheometry at low frequencies. The viscosity  $\eta$  for the same glycerol-water mixtures was also measured by viscometry.

Finally, we proceeded to extract by extrapolation the zero shear viscosity, and normalize it with the one obtained for pure water (right panel Fig.20). The extracted values from  $\eta$ -DFM agrees with the ones from steady shear rheology and viscometry. Small differences can be appreciated at glycerol concentrations higher than 45%. A reason of this comes from the uncertainty of the low viscosity of water, having a larger impact in the normalized viscosity. Nevertheless, the overall agreement proves the validity of  $\eta$ -DFM in ideal fluids.

We performed the second application of  $\eta$ -DFM to series of **biological fluids**, a series of protein suspensions made of different volume fractions of Lysozyme proteins dissolved in a buffer solution of pH 4.5. To each of the protein suspensions,  $1\mu\text{m}$  polystyrene spheres coated with hydrophilic PEG 300 were added to perform as particle tracers. Their coating was chosen in order to minimize protein-particle interactions, and the particles volume fraction was fixed as above. Using the same optical configurations as for the glycerol-water mixtures, we recorded a series of 50,000 at 50 FPS and analyzed them (for more information please refer to [36]). The intermediate scattering function ( $f(Q, \tau)$ ) and MSD were determined for a Q range of  $(0.70 - 3.5)[\mu\text{m}^{-1}]$  (inset left panel of Fig.21).

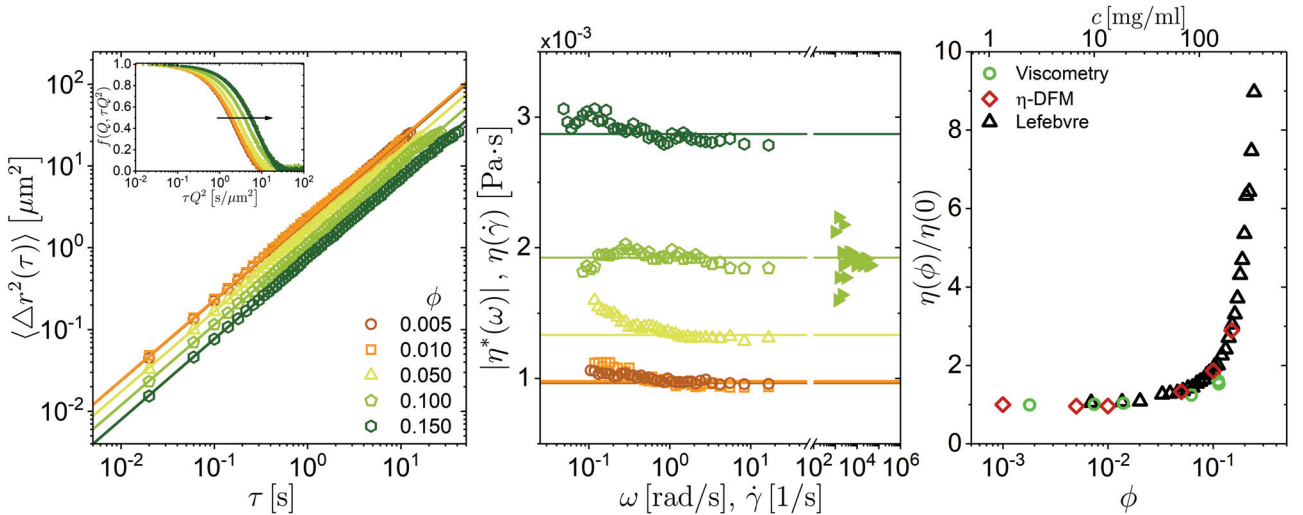


Fig. 21: Results obtained by applying  $\eta$ -DFM to a biological fluids, lysozyme aqueous suspensions with different volume fractions ( $\phi$ ). Mean squared displacement (MSD) for PEG coated tracers with a diameter of  $1\mu\text{m}$  (left panel), and its corresponding Intermediate scattering functions  $f(Q, t)$  as a function of  $\tau Q^2$ , the arrow represents an increase in lysozyme volume fraction (inset left panel). Modulus of the complex viscosity,  $|\eta^*(\omega)|$ , and steady-shear viscosity  $\eta^*(\dot{\gamma})$  as a function of angular frequency  $\omega$  and shear rate  $\dot{\gamma}$  (middle panel) determined by  $\eta$ -DFM (open symbols) and steady-shear measurements (obtained at  $T=25^\circ\text{C}$  and  $\phi=0.12$ ; [97] filled right triangle). Comparison of the normalized viscosity,  $\eta(\phi)/\eta(0)$ , as a function of lysozyme volume fraction (bottom axis) and concentration (top axis) of lysozyme solutions as determined by  $\eta$ -DFM, viscometry measurements and literature data (as indicated).

Having analogous behaviour as the glycerol-water mixtures, the  $f(Q, \tau)$  collapses onto a master curve when plotted as a function of  $\tau Q^2$  (inset). The MSD shows a shift to larger delay times  $\tau$  as the protein concentration increases. Indicating an increase in protein-protein interactions. Additionally, the MSD increases linearly with delay time  $\tau$ , implying that the protein solutions behave as an ideal fluid in the explored time window. As a consequence,  $|\eta^*(\omega)|$  do not depend on  $\omega$  (middle panel Fig.21) apart from small fluctuations at small  $\omega$ . This is due to the poorer statistics of  $f(Q, \tau)$  at large  $\tau$ , translating into fluctuations in the MSD, and consequently as numerical noise for  $|\eta^*(\omega)|$ . The magnitude of  $\eta^*(\omega)$  is consistent with previous measurements [97] (middle panel of Fig.21, filled symbols), where unlike to the glycerol-water mixtures, we did not perform steady-shear measurements with the lysozyme solutions since they are inhibited by a shear thinning effect caused by the formation of a dense film of adsorbed protein at the air-solution interface [98]. However, a comparison of the results obtained with  $\eta$ -DFM with conventional viscosity measurements, and literature data is presented in the left panel of Fig.21. In which, the agreement reinforce the validity of  $\eta$ -DFM.

Our third application was done to a **visco-elastic fluid**, an aqueous poly-ethylene oxide (PEO) solution. The solution contained 900 kDA PEO at a mass fraction of 2.1%. Due to their non ideal viscous behaviour, these type of solutions are frequently used to test rheological and microrheology techniques [35, 36, 41, 91, 92], in our case we used it to illustrate the performance of  $\eta$ -DFM in the presence of non ideal viscous behaviour. We added polystyrene particles of  $\sigma = 330\text{nm}$  as tracers at fixed tracer volume fraction of  $7.5 \times 10^{-4}$ , and proceeded to acquire a series of 125,000 images at a rate of 100 FPS. The images were recorded under similar conditions as described above. In depth experimental details are described in Ref. [36].

We proceeded to extract  $f(Q, \tau)$  over a  $Q$  range of  $(1.6 - 4.75)[\mu\text{m}^{-1}]$ , and plot it as a function of  $\tau Q^2$  (inset right panel Fig.22). Again, for different  $Q$  values, we observe that they overlap onto a master curve. By continuing the analysis, the MSD is extracted and plotted in the right panel of Fig.22). Where, by a careful inspection, a linear increase at larger delay times  $\tau$  is seen, and a deviation from this relation is appreciable in the lowest measured decade of delay times. We can infer a sub-diffusive tracer dynamics due to the smaller slope of the MSD at the mentioned region. To test this finding, we obtained  $|\eta^*(\omega)|$  and compared it with steady shear and SAOS measurements (middle panel Fig.22). Where we can see a very good agreement for all of the mentioned techniques, and even following the shear thinning behaviour at higher shear rates, hence further reinforcing the reliability of  $\eta$ -DFM and confirming the applicability of the Cox-Merz rule Eq.(146).

Shear thinning is a non-trivial rheological behaviour, it can be investigated by analyzing the behaviour of the viscous ( $G'(\omega)$ ), and elastic ( $G''(\omega)$ ) moduli. Both accessible to the  $\eta$ -DFM framework by following Eq.(144).

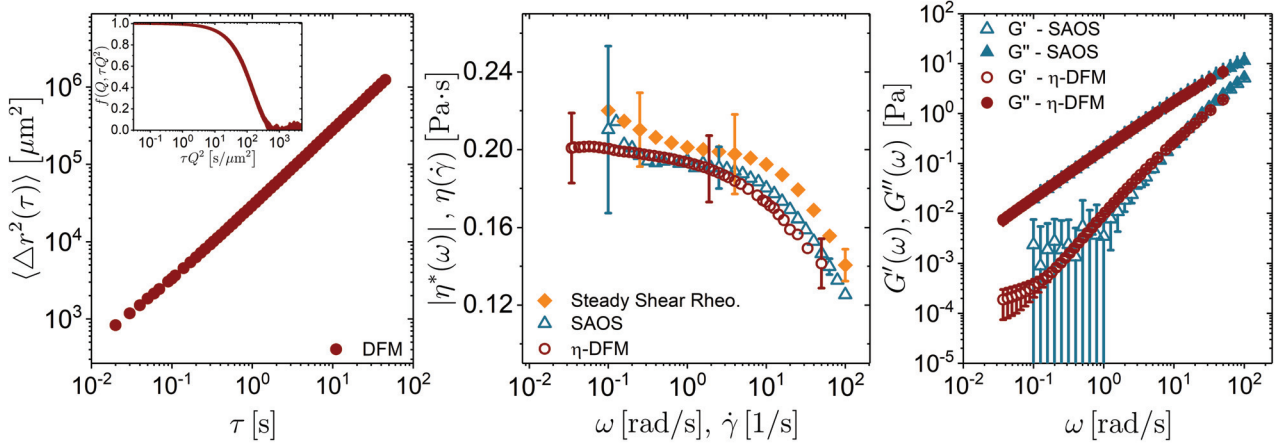


Fig. 22: Results obtained by applying  $\eta$ -DFM to a visco-elastic fluid, PEO solution containing tracer particles with a diameter of 330nm. Mean-squared displacement (MSD), as a function of delay time  $\tau$  (left panel) and the corresponding intermediate scattering function  $f(Q, \tau)$  for a range of  $Q$  values as a function of  $\tau Q^2$  (inset left panel). Note that, in this representation,  $f(Q, \tau)$  for different  $Q$  fall on top of each other. Modulus of the complex viscosity,  $|\eta^*(\omega)|$ , and steady-shear viscosity  $\eta^*(\dot{\gamma})$  as a function of angular frequency  $\omega$  and shear rate  $\dot{\gamma}$ , determined by  $\eta$ -DFM, SAOS, and steady-shear measurements (as indicated). Elastic,  $G'(\omega)$ , and loss,  $G''(\omega)$ , modulus extracted from  $\eta$ -DFM and SAOS as a function of angular frequency  $\omega$ .

Finally, we obtained the viscous and elastic moduli, and compared them with the ones from mechanical SAOS experiments (right panel Fig.22). Depending on the values of  $G'(\omega)$  and  $G''(\omega)$  two regions can be observed: The first one, at low frequencies, the viscous behaviour dominates, appreciable when  $G''(\omega)$  has greater values than  $G'(\omega)$ , additionally this is the region where  $|\eta^*(\omega)|$  shows almost no change as a function of  $\omega$ , corresponding to the linear increase of the MSD. The second region is at large frequencies, where both moduli start to converge for our accessed frequency window, and hence, the elastic contribution becomes relevant. This leads to a decrease in  $|\eta^*(\omega)|$ , and translates onto the sub-diffusive behaviour in the MSD. Furthermore, at higher frequencies accessible by our  $\eta$ -DFM measurements, we could infer a cross of the two moduli, indicating a transition from liquid to solid-like behaviour.

To conclude this section, we would like to point out that for all of the  $\eta$ -DFM applications, a decade of frequencies was accessible, smaller than accessible by mechanical rheometer. Thus,  $\eta$ -DFM is a complementary technique, and a reliable method to determine not only the zero shear viscosity but also the visco-elastic behaviour of fluids.

### 4.3.2 Tracer size in microliter viscometry

The founding concept of micro-viscometry or micro-rheology relies on the definition of tracer particle, as stated above, it is defined as a non-interacting probing particle inserted into a sample of interest. The motion of the tracer particles is influenced by the sample visco-elastic properties. For the tracer particles, the sample is considered as a continuum, and based on the previous description, the following assumptions are made: the frequency dependent viscosity  $\eta^*(\omega)$  is proportional to the memory function, and in addition, the proportionality term is given by the expression of the stokes friction coefficient ( $\xi = 3\pi\eta\sigma$ ) [39, 99].

In all of the presented applications, the particle size was always bigger than the characteristic length scale of the studied system. For example, in glycerol-water mixtures, the solution molecules size is of the order of Ångstroms, compared to the nanometer sized tracer particles. Similar case has the protein suspensions, where the lysozyme's size ranges in the order of a few nanometers [100], and the used tracer particle diameter was  $1\mu\text{m}$ . Additionally, for the visco-elastic polymeric solution, the average mesh size of 8nm [35] is significantly smaller than the 330nm of the tracer particles. Thus, the required conditions are proven to be fulfilled by the successful application of  $\eta$ -DFM and other micro-viscometry techniques [35, 36, 41, 46, 91, 92]. However, we wanted to test the possibility of having a colloidal suspension where a small portion of the system could be used as tracers. Keeping in mind that, the characteristic length scale of the system would be similar to the probing tracers, leading to possible violation of the requirements to perform micro-viscometry. Nevertheless, the previous would have the benefit that no extra care has to be taken for the selection of the tracer system in order to suppress tracer-suspension interactions.

The data analysis for such type of experiments are not easily performed in the DFM framework using bright field microscopy as imaging technique. The reason of this is due to the image content, where for the non dilute concentrations, collective properties are captured, thus the expression for the intermediate scattering function (Eq.(139)) is not valid for all probed length scales. Thus, different strategies are followed, such is the case of selecting scattering wave vectors where only self properties can be extracted [50]. Another approach is to introduce optical tracers, obtained by surface treating some of the particles to enhance their scattering signal, resulting in an averaged captured signal that encompasses only self information [23]. For this reason, we propose to exploit the versatility of the DFM framework by using fluorescence microscopy as imaging technique, using in our case confocal microcopy. In these type of techniques, the image content is made of fluorescence signal obtained from optically excited objects that are labeled with a fluorescent dye, thus introducing an analogue to optical tracers which

has been successfully used for extracting the MSD in Quasi-elastic Dynamic Light Scattering experiments [94, 95].

In the following, we present the results obtained for applying  $\eta$ -DFM in a **structured fluid**, consisting of a mixture of fluorescently labeled (Rhodamine-B) and non labeled, sterically stabilized poly methyl methacrylate (PMMA) particles of size  $\sigma = 300\text{nm}$ . The particles are immersed in an organic solvent mixture composed of cis-Decahydronaphthalene and Tetrahydronaphthalene (80/20 volume ratio). This solvent mixture ensures index matching between solvent and particles, reducing Van der Waals interactions, and additionally, it has been proven that the inter-particle interactions are considered to be hard sphere-like [101–104].

We synthesized the particles following a similar procedure as Antl. et al. [105], and for all of the studied samples, the optical tracers volume fraction was fixed to be in the order of  $\phi \sim 0.01$ . Particle suspensions were prepared with different total volume fractions, ranging from  $\phi = 0.01$  to  $\phi = 0.30$  (similar sample preparation protocol can be found in [106, 107]). Our studied samples were imaged using a Nikon A1R-MP confocal scanning unit mounted on a Nikon Ti-U inverted microscope with a Nikon Plan Apo 40X oil immersion objective ( $\text{NA} = 1.3$ ), employing a solid state laser with a wavelength of 561nm as excitation light source. The total number of images was adjusted in order to properly probe the long time dynamics of each measured volume fraction, contrary to the acquisition rate which was fixed at 30 FPS. Additionally, we performed SAOS experiments in order to compare the magnitude of the complex viscosity  $\eta^*(\omega)$ .

The intermediate scattering function ( $f(Q, \tau)$ ) was determined for a  $Q$  range of  $(1.5 - 4.5)[\mu\text{m}^{-1}]$ , and plotted as a function of  $\tau Q^2$  for different suspension volume fractions (inset left panel Fig.23). As shown, the data collapses onto a master curve for this scaling representation, indicating the validity of the applicability Eq.(139). We proceed to extract the MSD, and plot it with open symbols in the left panel of Fig.23, which have a similar behaviour than the glycerol-water mixtures and the protein suspensions. A shift in the MSD is seen as increasing the suspension volume fraction, along with a linear dependence for the lowest volume fractions. For the highest volume fraction shown,  $\phi = 0.3$ , a linear dependence is seen for short times  $\tau < 0.4\text{s}$ , an inflection regime for intermediate times  $0.4\text{s} < \tau < 2.0\text{s}$ , and linear regime for large times  $\tau > 2.0\text{s}$ . This corresponds for previously described dynamical transition of the short-, long-time diffusion of hard sphere fluids [95].

We proceeded with the  $\eta$ -DFM analysis and extracted the modulus of the complex viscosity  $\eta^*(\omega)$ . The results are plotted (open symbols) and compared with SAOS measurements (closed symbols) in the middle panel of Fig.23. Where we

can see a very good agreement between them, and the data obtained by  $\eta$ -DFM is able to follow the shear thinning behaviour at higher frequencies. As seen before,  $\eta$ -DFM complements the limited sensitivity of the mechanical measurements at low frequencies, thus covering frequencies where no significant dependence of  $|\eta^*(\omega)|$  on  $\omega$  is seen, allowing us to extrapolate for extracting the zero shear viscosity. To test this finding, we proceeded to obtain the normalized viscosity,  $\eta(\phi)/\eta(0)$  for SAOS and  $\eta$ -DFM and compare it with the Quemada analytical expression [108] (right panel Fig.23).

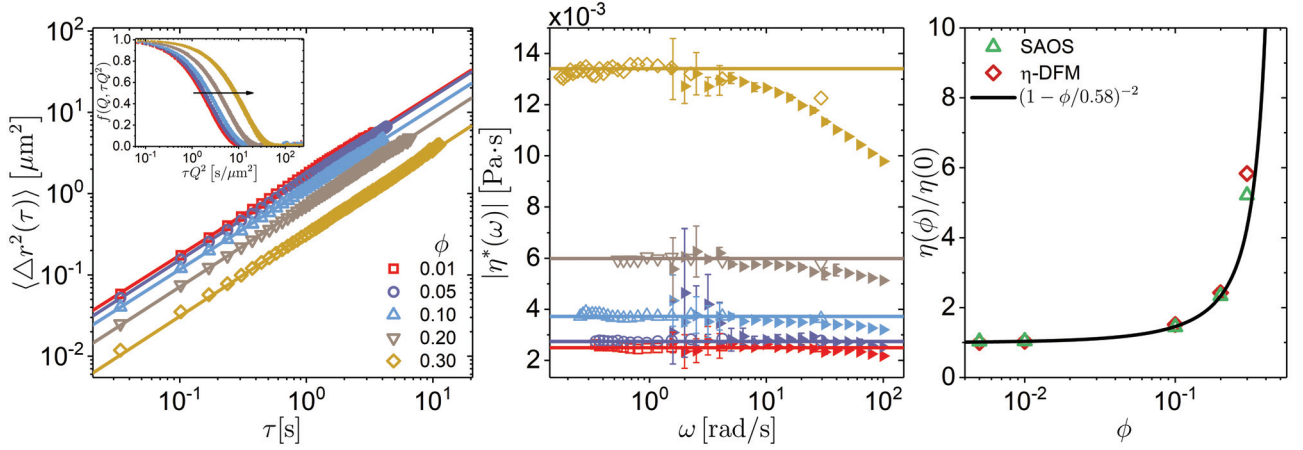


Fig. 23: Results obtained for structural fluids (hard-sphere colloidal suspensions) applying  $\eta$ -DFM. Mean squared displacement (MSD) for optical tracers with a diameter of 300nm for different volume fractions of hard-sphere colloidal suspensions (left panel), and its corresponding  $f(Q, \tau)$  as a function of  $\tau Q^2$  for  $(1.5 \leq Q \leq 4.5)[\mu\text{m}^{-1}]$ . Note that, in this representation,  $f(Q, \tau)$  for different  $Q$  fall on top of each other. The arrow represents an increase in the suspension volume fraction (inset left panel). Magnitude of the extracted frequency dependant viscosity  $\eta^*(\omega)$  (open symbols) compared with small amplitude oscillatory shear SAOS (closed symbols) from rheology experiments for different volume fraction concentrations (middle panel). Comparison of the normalized viscosity,  $\eta(\phi)/\eta(0)$ , as a function of volume fraction  $\phi$  determined by  $\eta$ -DFM, SAOS measurements, and the analytical Quemada expression (solid line) [108] (right panel)

The Quemada expression has been shown to capture the trend of the normalized viscosity of hard-spheres [9]. The experimentally extracted  $\eta(\phi)/\eta(0)$  follows the Quemada theoretical expression, having a small deviation between the extracted from SAOS and  $\eta(\phi)/\eta(0)$ . The reason of this is due to the difficulties for the error associated by extracting the zero shear viscosity for the frequencies where the resolution of the mechanical rheometer is met. Nevertheless, the overall good agreement in the complex viscosity, and the normalized viscosity, proves the viability of applying  $\eta$ -DFM in suspensions where a few components of the same system are used as tracers. Furthermore, our results supports the validity of using the Microrheology approach to study rheological properties of structure fluids for volume fractions up to 0.3, where an in depth analysis for higher volume fractions is still needed to fully validate the approach towards the different phase transitions of a hard sphere fluid. However,  $\eta$ -DFM leads to be a very powerful tool to test the universality of the General Stokes Einstein relations [99, 109].

#### 4.4 Velocity deviations from the sedimentation of dilute systems

The settling of particles in a suspension is the most common example of particles in the presence of an external force. In a dilute suspension, the settling motion is governed by the force balance among the gravitational field, buoyancy and the frictional force. This leads to a steady state motion with constant settling velocity, also known as the stokes velocity  $v_s = \Delta\rho g\sigma^2/18\eta$ , where  $\Delta\rho = \rho_p - \rho_s$  is the density difference between the particle and solvent densities,  $g$  is the gravitational acceleration,  $\sigma$  the particle diameter, and  $\eta$  the viscosity of the solvent. For fixed particle composition, bigger particles settle faster than smaller ones.

In nature, most of the suspensions present a particle size distribution  $\mathcal{P}(\sigma)$ . The quantity that represents the relative broadness of the distribution is given by the size coefficient of variation  $CV_\sigma = \delta_\sigma / \langle\sigma\rangle$ , defined as the ratio of the standard deviation of the distribution ( $\delta_\sigma$ ) by the mean value  $\langle\sigma\rangle$ . A suspension is referred as monodisperse if its size distribution is narrow, i.e.  $CV_\sigma \sim 0$ , thus the size variation is negligible, contrary to the one referred as polydisperse. As a consequence of the particle size distribution, the overall settling motion can be represented by a velocity distribution. Which has its corresponding velocity coefficient of variation quantified by  $CV_v = \delta_v / \langle v_s \rangle$ , and depending on the functional form of  $\mathcal{P}(\sigma)$  a relationship between  $CV_v$  and  $CV_\sigma$  can be found. Hence, the settling of the suspended particles is composed by two types of movement, a mean collective one, given by the mean collective velocity  $\langle v_s \rangle$  and a relative, given by the relative velocity of the individual particles,  $v'_s = v_s - \langle v_s \rangle$ , with respect to the mean collective velocity  $\langle v_s \rangle$ .

Experimentally, Dynamic Light Scattering (DLS) is able to characterize the dynamics of suspended particles. However, conventional far field dynamic light scattering techniques are only sensitive to the relative motion, this is due to its homodyne detection scheme that is able to extract the square modulus of the intermediate scattering function  $f(Q, \tau)$  [8]. Conversely, in heterodyne detection schemes, the real part of  $f(Q, \tau)$  is obtained. Thus, making it sensitive to the mean collective motion and the relative one. Examples of this detection scheme are the one called Heterodyne Near Field Scattering (HNFS), which is based in Digital Fourier Microscopy (DFM) conceptual framework (Sec. 3). Additionally, the mean static scattered light can be obtained, allowing the possibility to compare the size polydispersity of a system with the corresponding from the velocity distribution.

In the following, we characterize the settling dynamics of three dilute aqueous suspensions by means of HNFS measurements. Two of the suspensions were composed of polystyrene particles of mean diameter  $\langle\sigma\rangle = 7.32\mu\text{m}$  and  $\langle\sigma\rangle = 7.84\mu\text{m}$

(PS06005 Bangs Laboratories, PS/Q-R-B660 microParticles GmbH). The third sample consisted of silica particles with  $\langle\sigma\rangle = 3.92\mu\text{m}$  (SiO2-F-L1490 microParticles GmbH). The previous systems led to a Péclet range of  $\text{Pe} \geq 150$ , having  $\text{Pe} = v_s\sigma/D$  as the number that expresses the ratio between gravitational and thermal diffusive ( $D$ ) motion. Our experimental results were compared with theoretical expressions and Brownian dynamics computer simulations, where a Gaussian particle size distribution was taken into account. This led us to introduce an analytical relationship between  $\text{CV}_v$  and  $\text{CV}_\sigma$ , that was corroborated by the comparison of the dynamical analysis of  $f(Q, \tau)$  and the Mie Scattering analysis of the static light scattering information.

#### 4.4.1 Polydisperse Langevin Model

In nature, many suspensions are constituted by a distribution of particle sizes, in the following we will consider a Gaussian distribution, this is

$$\mathcal{P}(\sigma) = \frac{1}{\sqrt{2\pi}\delta_\sigma} \exp\left[-\frac{(\sigma - \langle\sigma\rangle)^2}{2\delta_\sigma^2}\right], \quad (147)$$

where  $\langle\sigma\rangle$  is the mean particle diameter, and  $\delta_\sigma$  is the standard deviation of the distribution. For simplicity in the notation, we have used ( $\langle\dots\rangle$ ) to represent the ensemble average ( $\langle\dots\rangle_E$ ). Often is useful to describe the broadness of the distribution by the size coefficient of variation or polydispersity index, defined by the ratio of the standard deviation over the mean value, i.e.  $\text{CV}_\sigma = \delta_\sigma/\langle\sigma\rangle$ .

The complete description of the dynamics of the dilute suspension can be obtained by adding the contribution from each individual particle size of the distribution, i.e. for each  $\sigma$  a Langevin equation can be employed. The motion imposed by gravity corresponds to the one of low Reynolds number, this holds true for latex particles smaller than  $\sigma \leq 10\mu\text{m}$  ( $\text{Re} = \rho_s\sigma v_s/\eta \leq 10^{-4}$ ), thus a Stokes flow is considered (also known as the linear regime as expressed in Eq.(49)) and the inertial effects in the Langevin equation are safely neglected [1, 51, 52]. We proceeded to numerically simulate the dynamics of particles described by the over-damped Langevin equation using the polydisperse Ermak-McCammon algorithm (Sec.2.7.3). It was done in reduced units denoted by (\*), using the mean particle diameter  $\langle\sigma\rangle$  as unit of distance, the ensemble Brownian time  $t_B^* \equiv \langle\sigma\rangle^2/\langle D\rangle$  as unit of time, and  $F^* = k_B T/\langle\sigma\rangle$  as unit of force (Sec.2.7.1). In the direction parallel to gravity ( $\hat{z}$ ), the corresponding reduced over-damped Langevin equation (Eq.(27)) for a particle of diameter  $\sigma$  takes the following form

$$\dot{z}_\sigma^*(t^*) = \frac{D_\sigma}{\langle D\rangle} f_z^*(t^*) - F_u^*(z^*) - \frac{D_\sigma}{\langle D\rangle} \text{Pe}^* \sigma^{*3}, \quad (148)$$

where  $D_\sigma$  is the particle diffusion coefficient, and  $\langle D\rangle$  is the mean diffusion co-

efficient over the size distribution. The stochastic force is represented by  $f_z^*$ , and  $F_u^*$  is the net force arising from the interaction potential between particles. In our case we made use of a continuous approximation for a hard sphere potential, with the corresponding parameters to ensure thermodynamic consistency [61]. Finally, the last term of Eq.(148) represents the sedimentation, as it comes forth the force balance between the buoyant and the resulting force from the gravitational potential in reduce units, being proportional to the ensemble Péclet number  $Pe^* = \langle v_s \rangle \langle \sigma \rangle / \langle D \rangle$ . For more details please refer to Sec.2.7.3.

In order to compare with HNFS experiments, we analytically calculated the corresponding real part of the intermediate scattering function  $f(Q^*, \tau^*, \sigma^*)$  per particle size. This, by taking  $Q^* = Q \langle \sigma \rangle$  oriented parallel to  $\hat{z}$ , and obtained the mean over the size distribution [5, 37], i.e.

$$f(Q^*, \tau^*) = \int f(Q^*, \tau^*, \sigma^*) \mathcal{P}(\sigma^*) d\sigma^*. \quad (149)$$

The previous can be analytically calculated, leading to

$$f(Q^*, \tau^*) = \exp \left[ -Q^{*2} \tau^* \left\{ 1 - \frac{1}{2} Q^{*2} \tau^* CV_D^2 \right\} - \frac{1}{2} Q^{*2} CV_v^2 Pe^{*2} \tau^{*2} \right] \cos(Q^* Pe^* \tau^*), \quad (150)$$

where  $CV_D = \delta_D / \langle D \rangle$  is the diffusion coefficient of variation or polydispersity index of the diffusion coefficient caused by the distribution of particles. For a detailed description please refer to Sec.2.3 and 2.7. In real units Eq.(150) is,

$$f(Q, \tau) = \exp \left[ -Q^2 \langle D \rangle \tau \left\{ 1 - \frac{1}{2} Q^2 \langle D \rangle \tau CV_D^2 \right\} - \frac{1}{2} Q^2 CV_v^2 \langle v_s \rangle^2 \tau^2 \right] \cos(Q \langle v_s \rangle \tau). \quad (151)$$

The computer simulations were performed using different size polydispersity indexes,  $0.0 \leq CV_\sigma \leq 0.1$ , illustrated in the left panel of Fig.24. We have used a total number of 1024 particles and the simulation box size was set in order to have a volume fraction of  $\phi = 5 \times 10^{-5}$ , providing the dilute regime for the simulated system. Finally, the chosen probing wavelength was set to satisfy  $Q \langle \sigma \rangle = 2\pi$ , as for this value distances of the order of the mean particle size are probed. With the previously described simulation parameters, we studied the effect of the particle size distribution for purely diffusive motion dynamics, i.e.  $Pe^* = 0$ . Results are shown in the middle panel of Fig.24. Under these conditions, the intermediate scattering functions superimpose for all the  $CV_\sigma$  values, having no significant dependency over the polydispersity. Moreover, we hardly see any change of the characteristic delay time from the ln-linear representation (inset) of  $f(Q^*, \tau^*)$ . Hence, we conclude that for analytically describing the intermediate scattering function in the explored polydispersity range at  $Pe^* = 0$ , the term that includes  $CV_D$  in Eq.(150) can be neglected. The latter is in agreement with the previously

found by Pusey and van Megen [110,111].

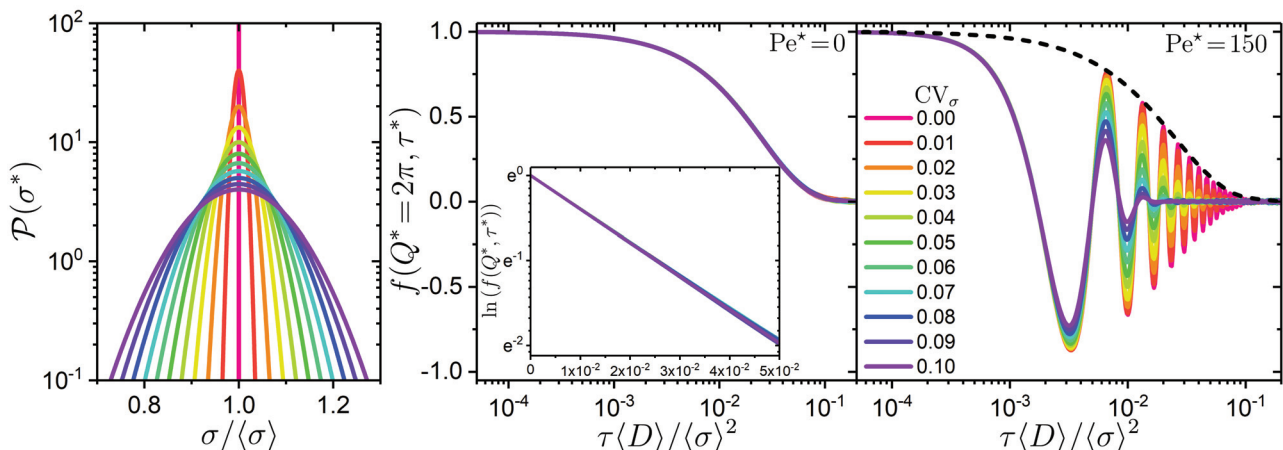


Fig. 24: Results obtained from the computer simulations using the polydisperse Langevin model for different  $CV_\sigma$  values of normally distributed particle sizes (left panel). Intermediate scattering functions ( $f(Q^*, \tau^*)$ ) computed at  $Q^* = Q(\sigma) = 2\pi$  and  $Pe^* = 0$  for all  $CV_\sigma$ , along with its corresponding ln-linear representation as inset (center panel). For all  $CV_\sigma$ ,  $f(Q^*, \tau^*)$  follows closely a single exponential decay. In addition, no significant dependence on polydispersity can be seen. Right panel represents  $f(Q^*, \tau^*)$  for  $Q^* = 2\pi$  and  $Pe^* = 150$ . The dashed envelope corresponds to  $Pe^* = 0$  (purely diffusive), and the oscillatory behaviour is related to the collective ballistic motion. Furthermore, the additional damping effect comes from the relative ballistic motion, it is due to the effect of polydispersity in the settling velocity as expressed in Eq.(150)

We continued to analyze the effect of the polydispersity in the dynamics of settling particles using the polydisperse Langevin model by setting  $Pe^* = 150$ , as this represents the Péclet value from our experimental systems. Results are shown in the right panel of Fig.24. The effect of mean collective motion is expressed as strong oscillations in  $f(Q^*, \tau^*)$ , and for the monodisperse case (pink curve), has an envelope described by the purely diffusive motion of  $Pe^* = 0$  (represented by the dashed line). Conversely, for polydisperse systems where an additional damping term is seen, the single exponential from diffusion, does not represent the envelope of the oscillations, where an additional damping term is seen. This extra term arises from the relative motion in addition to the mean collective motion, due to the different velocities imposed by the particle size distribution in the system. It has a stronger effect for higher polydispersities, as it is able to almost completely damp the oscillations of the mean collective motion ( $CV_\sigma = 0.1$ , light purple line).

The extra damping term is analytically described by the quadratic term in the exponential function of Eq.(150) and Eq.(151). Thus, by combining the main findings of the studied Péclet, it is possible to obtain a general expression that captures diffusive, relative directed, and mean collective motion. In real units it

is given by,

$$f(Q, \tau) = \exp\left[-Q^2\langle D\rangle\tau - \frac{1}{2}Q^2\delta_v^2\tau^2\right] \cos\left[Q\langle v_s\rangle\tau\right] \quad (152)$$

recalling that  $\langle D\rangle$  is the mean diffusion coefficient,  $\langle v_s\rangle$  is the mean collective velocity, i.e. mean settling velocity, and  $\delta_v$  is the standard deviation of the velocity distribution. The corresponding characteristic times are given by  $\tau_B(Q) = 1/\langle D\rangle Q^2$  for the diffusive time scale,  $\tau_{\delta_v} = \sqrt{2}/Q\delta_v$ , and  $\tau_{\langle v_s\rangle} = 1/Q\langle v_s\rangle$  for the velocity deviations and mean velocity characteristic times respectively. Noting the  $Q$  scale dependence for the type of dynamics described, having a  $Q^2$  dependence for random motion, and  $Q$  for directed motion.

Given that the settling velocity is a function of the particle size, the relationship between the size ( $CV_\sigma$ ) and the velocity ( $CV_v$ ) coefficients of variation can be obtained, having for normally distributed particle size

$$CV_v = 2CV_\sigma. \quad (153)$$

This relationship is only valid when the velocity distribution is related to the size distribution, and will not hold for other types of velocity distributions caused for example: by convection or other non steady state phenomena. Hence, the relative motion to the mean collective from a settling system can be applied as a direct dynamical measurement for estimating the polydispersity of a system.

Complementary to a dynamical measurement, Static Light Scattering (SLS) is sensitive to the particle size distribution, having an effect in the total scattered light intensity  $I_s(Q)$ . This is because  $I_s(Q)$  is the superposition of all the individual scattering intensities per particle  $I_p(Q)$ , i.e.

$$I_s(Q) = \int I_p(Q, \sigma)\mathcal{P}(\sigma)d\sigma. \quad (154)$$

$I_p(Q)$  can be calculated via the Raleigh-Gans-Debye scattering theory (RGD) if the particles are smaller than the wavelength of the illumination light source. As we worked with particles bigger than the wavelength of light, Mie theory was used instead [112, 113]. The analytical solution of Mie theory is not trivial, making it difficult to operate with. To overcome this, we employed numerical calculations that are based on the Bohren-Huffman Mie-MATLAB routines [113, 114], and were adapted for computing the average intensity of a distribution of particles. Our numerical scheme was validated by comparison with the ones obtained from MiePlot-software utilizing the same particle distribution [115].

Once our numerical calculations were validated, we proceeded to explore the effects of polydispersity in  $I_s(Q)$ , fixing the mean particle size and its corresponding

refractive index for two cases resembling our experimental systems:  $\langle\sigma\rangle = 3.92\mu\text{m}$  silica ( $\text{SiO}_2$ ), and  $\langle\sigma\rangle = 7.88\mu\text{m}$  polystyrene particles. The refractive index of the particles was assumed homogeneous over the whole sphere, with an average particle refractive index. Furthermore, we had used literature values related to the experimentally studied systems, taking  $n_p = 1.434$  for  $\text{SiO}_2$  and  $n_p = 1.587$  for polystyrene [116]. As we worked with aqueous suspensions, the refractive index of water was chosen to be  $n_s = 1.332$ , for monochromatic red light  $\lambda = 0.632\mu\text{m}$ . The shape of  $\mathcal{P}(\sigma)$  and  $\text{CV}_\sigma$  were selected to be the same as previously described.

Our results are shown in Fig.25, where for increasing polydispersity an evident smearing of the different minimum values of  $I_s(Q)$  is seen. This is similar for both of the studied conditions (silica left panel, polystyrene right panel), thus  $\text{CV}_\sigma$  and  $\langle\sigma\rangle$  can be estimated by comparing the numerical Mie theory calculations from a distribution of particles to the measured  $I_s(Q)$ . It is worth mentioning that in Mie theory the first minimum value has no fixed position, oppositely to the Rayleigh-Gans-Debye theory (RGD) where  $Q\langle\sigma\rangle = 8.98$  [8,110,112,113] and a mean particle size can not be obtained by reading this  $Q$  value. This deviation between theories is due to the complete consideration of all of the optical properties of the scattering process involved in Mie theory, such as refractive index of the medium and particles, absorbance, and reflectivity of the particles [113]. Nevertheless, for these systems we found that a good estimation can be found at  $Q\langle\sigma\rangle \sim 2\pi$ .

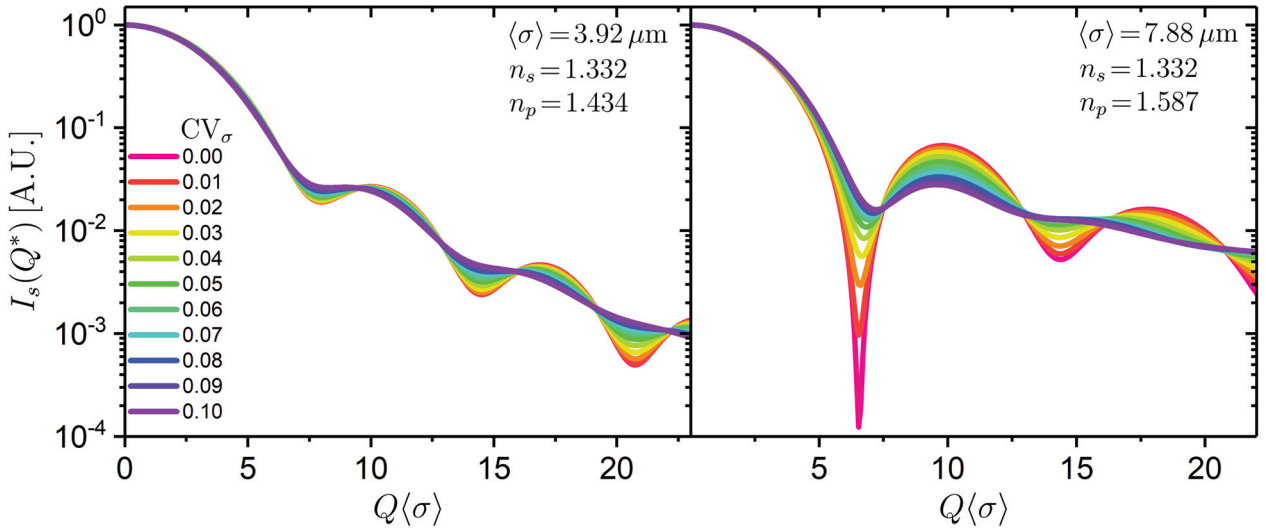


Fig. 25: Numerical calculations of Mie theory for the total scattered intensity  $I_s(Q)$  as a function of the degree of polydispersity  $\text{CV}_\sigma$ , obtained for two different particle sizes and compositions. The particle sizes were chosen to match the ones from the experimentally studied systems of this work, i.e.  $\langle\sigma\rangle = 3.92\mu\text{m}$  ( $\text{SiO}_2$ ), and  $\langle\sigma\rangle = 7.88\mu\text{m}$  (polystyrene). Similarly with the refractive indexes, we employed  $n_p = 1.434$  for  $\text{SiO}_2$  particles, and  $n_p = 1.587$  for polystyrene particles [116].

#### 4.4.2 Experimental Results

Experiments were carried out using the HNFS setup described in Sec.4.1. In addition, a sample chamber was added to the setup in order to reduce thermal instabilities. This led to fluctuations inside of the chamber of  $\pm 0.2\text{C}$ . Our measurement protocol is as follows: samples were diluted from a stock suspension and poured in a glass cuvette of 4cm height and 1mm optical path (21-G-1 Starna GmbH). The cuvette was sealed with a stopper leaving a small air bubble in order to help re-disperse the particles for resetting their initial conditions. In addition, a 3D printed plastic sample holder was used to avoid heat conduction that could cause convection inside of the sample cell. The filled cuvette along with the sample holder was placed in the instrument and left to thermalize for 1 hour. After thermalization, the sample (placed in the plastic holder to avoid direct hand contact with it) was rigorously agitated by hand, using the air bubble as stirrer for 30 seconds. Afterwards, the glass cuvette was placed back into the instrument. A waiting time period was set before starting the image acquisition, having 0.75h for silica  $3.92\mu\text{m}$  particles, 1.5h for polystyrene  $7.32\mu\text{m}$  and 2h for polystyrene  $7.84\mu\text{m}$ . After this time, a constant settling velocity was found and the image acquisition was started. At the start of the acquisition time, the sedimentation front was located at least at  $\sim 1.5\text{cm}$  from the observation window, allowing a sufficient measurement time without any stratification effects, as this phenomenon is known to alter the bulk particle distribution. Furthermore, in order to avoid back flow, the observation area is located at 1.2cm from the bottom of the cell. Hence, bulk information was assumed to be captured.

The resetting process was carried out in order to have a complete set of three independent experiments, a summary of the experimental details of each experiment are shown in Table 1.

Sample	Volume fraction	FPS	Acq. Time[min]	Image size [pixel]	Image size [ $\text{mm}^2$ ]
silica $3.92\mu\text{m}$	$2.5 \times 10^{-6}$	75	30	$512 \times 512$	6.04
polystyrene $7.32\mu\text{m}$	$5.0 \times 10^{-5}$	50	60	$1024 \times 1024$	24.16
polystyrene $7.84\mu\text{m}$	$5.0 \times 10^{-5}$	50	60	$1024 \times 1024$	24.16

Table 1: Summary of the experimental details from the different measured samples.

Dynamical measurements were performed using a 2X 0.1NA microscope objective as collecting optics, resulting in a sufficiently large field of view. This led to a  $Q$  range of  $(0.1 - 0.9) [\mu\text{m}^{-1}]$ , corresponding to distances ( $L = 2 * \pi/Q$ ) larger than the particle size. For this  $Q$  range and Péclet values, the diffusion term in Eq.(152) can be safely neglected. This because the ratio between  $\tau_B/\tau_{\delta_v} \sim 10$ . Furthermore, it was confirmed by a non-linear fit of Eq.(152) to the experimental data, where no meaningful data was extracted for  $\tau_B(Q)$ . Intermediate scattering functions obtained from one of the three independent measurements per particle

size are shown as symbols in Fig.26. The continuous line represents the computer simulations of the polydisperse Langevin model, using as input parameters the extracted values from the numerical fitting of Eq.(152) to these experimental data.

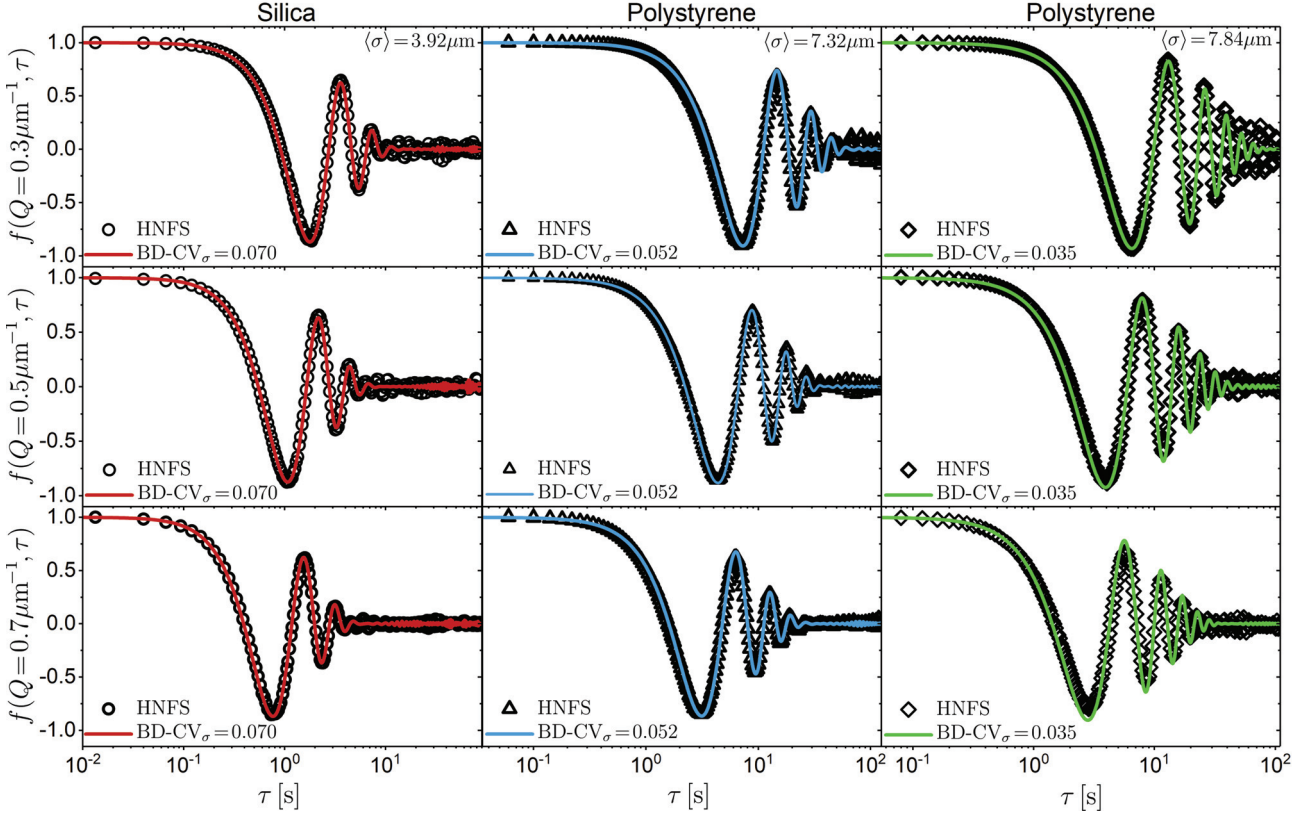


Fig. 26: Measured Intermediate scattering functions  $f(Q, \tau)$  (open symbols) compared with computer simulations using the polydisperse Langevin model (lines). The left corresponds to the silica  $3.92\mu\text{m}$  sample, the center to the polystyrene  $7.32\mu\text{m}$  sample, and the right to the polystyrene  $7.84\mu\text{m}$  sample. The input parameters for the simulations were obtained from the extracted values of fitting Eq.(152) to the experimental data without free parameters.

We have found a very good agreement between computer simulations and the HNFS measurements for all of the studied  $Q$  range, corroborating our theoretical description of settling particles. At this point, we would like to stress out the difference in number and amplitude of the oscillations in  $f(Q, \tau)$  for the different measured samples, as this indicates the difference in polydispersity among them as the diffusive term in Eq.(152) has been neglected (see above). The number of oscillations and the height of the amplitudes get higher for smaller  $CV_\sigma$ . Qualitatively, the most polydisperse sample was the silica particles, as the amplitude of the oscillations are the smallest of the three. To quantify it, the mean and standard deviation of the extracted characteristic times was computed. These results are presented in Fig.27. The straight line in each case represents a linear fit with a fixed slope of  $-1$ , and the intercept was left as free parameter.

The value of  $-1$  is the expected slope for both of the characteristic times in a log-log representation. This is because they are inversely proportional to  $Q$ . In all of the three particle systems, a very good agreement with the predicted  $Q$

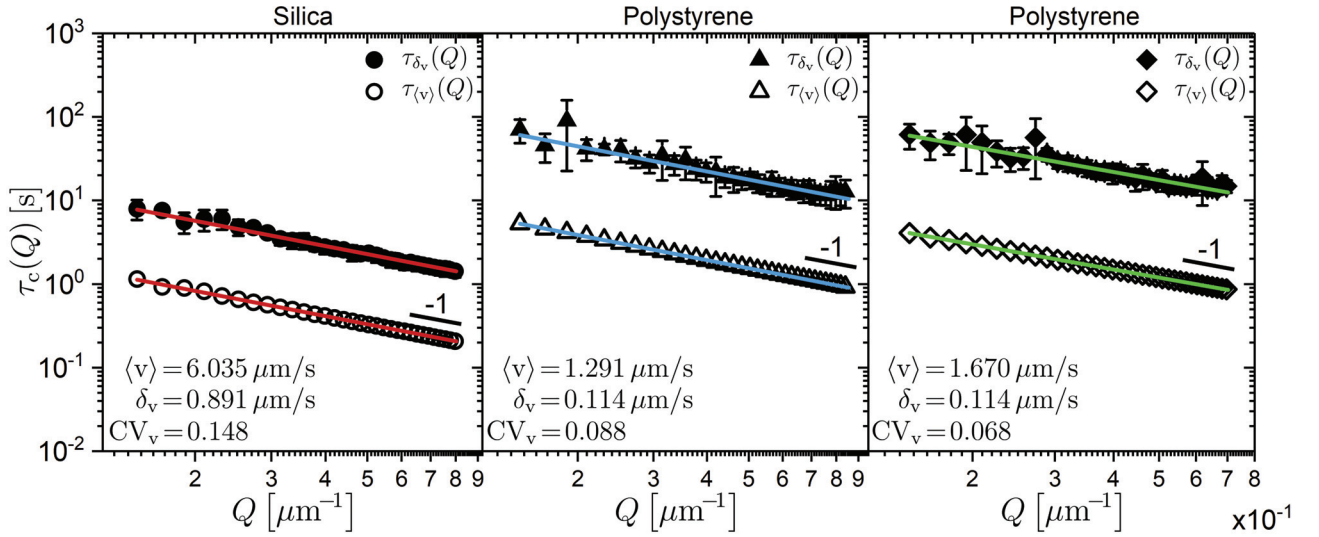


Fig. 27: Mean and standard deviation of the extracted characteristic times  $\tau_{\delta_v}(Q) = \sqrt{2}/Q\delta_v$ , and  $\tau_{\langle v \rangle}(Q) = 1/Q\langle v \rangle$  from the three independent measurements explored per particle size. The straight lines represent a linear regression with fixed slope of  $-1$ . The extracted mean velocity ( $\langle v \rangle$ ) and velocity deviations ( $\delta_v$ ) are shown as legends in each panel. The left panel corresponds to the silica  $3.92\mu\text{m}$  sample (red), the center panel to the polystyrene  $7.32\mu\text{m}$  sample (blue), and the right panel to the polystyrene  $7.84\mu\text{m}$  sample (green). Note the separation between  $\tau_{\delta_v}$  and  $\tau_{\langle v \rangle}(Q)$  increases as the value of  $CV_v$  decreases.

scaling was found, thus  $\langle v \rangle$ ,  $\delta_v$  were subsequently extracted from the intercept values. Then,  $CV_v$  was computed. Note the separation between  $\tau_{\delta_v}$  and  $\tau_{\langle v \rangle}(Q)$  increases as the value of  $CV_v$  decreases. These results are shown as legends in its corresponding panel of Fig.27, and in Table 2.

Sample	$Pe^*$	$\langle \sigma \rangle [\mu\text{m}]$ (SLS)	$CV_\sigma$ (SLS)	$\langle v_s \rangle [\mu\text{m/s}]$ (DLS)	$CV_v$ (DLS)	$CV_v/CV_\sigma$
silica $3.92\mu\text{m}$	179.3	3.76	0.080	6.035	0.148	1.850
polystyrene $7.32\mu\text{m}$	178.0	7.00	0.045	1.291	0.088	1.956
polystyrene $7.84\mu\text{m}$	225.1	7.88	0.035	1.670	0.068	1.943

Table 2: Summary of the extracted experimental information from the different measured samples. These results represent the average value from the three performed dynamical measurements (DLS) and Static Light Scattering (SLS) sample characterization.

Finally, we characterized the measured samples by means of SLS obtaining  $I_s(Q)$  from the long delay time limit of HNFS [24], and by comparing them to Mie theory calculations. For this purpose, we employed a 20X 0.5NA microscope objective as collecting optics. This led to a  $Q$  range of  $(0.1 - 4.7) [\mu\text{m}^{-1}]$ , allowing us to cover the first minimum of  $I_s(Q)$  for all of the samples ( $(0.1 - 3.1) [\mu\text{m}^{-1}]$  for  $\text{SiO}_2$  particles, and  $(0.1 - 1.7) [\mu\text{m}^{-1}]$  for polystyrene) without the need of correcting for smearing effects due to the optical transfer function, as it increases towards large  $Q$  values [65, 68]. Furthermore, in order to reduce the amount of acquired data, we lowered the Frame Rate to 0.33Hz. Results of the comparison of Mie theory calculations (solid line) with the experimental ones (open symbols) are shown in Fig.28 and summarized in Table 2.

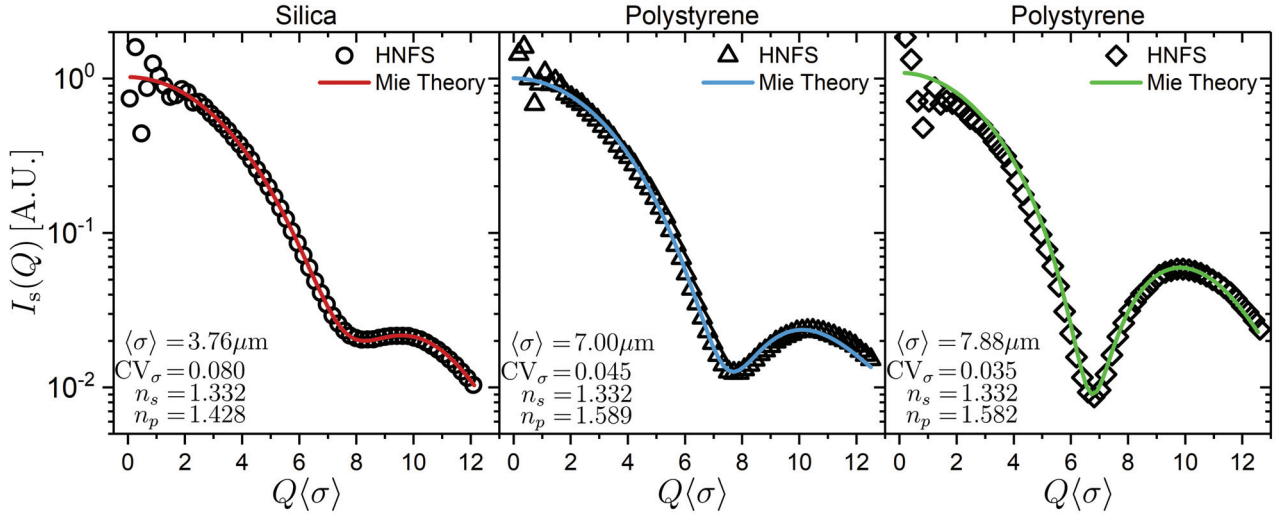


Fig. 28: Comparison of the total scattered intensity  $I_s(Q)$  obtained from HNFS experiments (symbols) with Mie theory numerical calculations (solid lines). The left panel corresponds to the silica  $3.92\mu\text{m}$  sample, the center panel to the polystyrene  $7.32\mu\text{m}$  sample, and the right panel to the polystyrene  $3.84\mu\text{m}$  sample. Input values for computing the numerical calculations of the Mie theory are written as legends for each case.

Our characterization using SLS is in good agreement with the dynamical one. We inferred this, as the silica  $3.92\mu\text{m}$  (left panel) and polystyrene  $7.32\mu\text{m}$  (center panel) samples have  $\sim 4\%$  difference in mean particle size, and less than  $1\%$  for the polystyrene  $7.84\mu\text{m}$  sample. In addition, we obtained from all of the measured samples  $CV_v/CV_\sigma \approx 2$  (Eq.(153)). It is worth mentioning that for both polystyrene samples we obtained the smallest relative difference from the theoretical value of 2, having obtained an average of  $\sim 3\%$  difference. However, we obtained  $\sim 7.5\%$  for the silica  $3.92\mu\text{m}$  sample. These difference could come from the SLS characterization, as we have assumed an homogeneous refractive index distribution over the whole sphere. This is supported by the fact that some particle batches could contain optical core-shell type particles [117], making the Mie theory more involved. A step further in this direction was discarded, as we consider these deviations relatively small being within experimental errors. In addition, the minimum of the form factor is less pronounced as the polystyrene cases (because of a smaller refractive index difference), thus larger uncertainty in determination of the polydispersity is expected. Despite these differences, we conclude that we were able to differentiate the degree of polydispersity among different samples. Thus, with these results, we experimentally demonstrate the validity of Eq.(152), (Eq.(153), and the overall theoretical description of the Polydisperse Langevin model.

#### 4.5 From colloid to grain. A dynamic description of sedimentation in dilute systems

Systems under sedimentation of immersed colloidal and granular particles are the two ends of a collection of dynamical regimes. The motion of colloidal systems is characterized by the random or Brownian motion of the particles (referred as colloids) in them. By this, the overall sample concentration is going to be homogeneous over the whole sample volume, i.e., the particles will not sediment. This process is also known as free diffusion, and it is quantified by the diffusion coefficient  $D$ . Free diffusion is the result of thermal agitation, arising from the random collisions of the solvent molecules with the colloids in the system. As a result, no preferred orientation in the motion is present.

On the other hand, when thermal agitation does not play a role in the dynamics of the system, the particles (referred as grains) can only move due to the drag of external forces. This kind of systems are known to be athermal or granular. Granular systems are affected by gravity causing grains to settle or sediment. Between the previously described dynamical limits (colloidal-granular) it is possible to find systems that present combination of both dynamical behaviours, i.e. colloidal systems that present strong thermal agitation that ultimately sediment or granular systems in which a remaining of thermal agitation is still detectable [118].

In consequence, the response of a system to gravity and thermal agitation can be used to characterize its dynamical behaviour. For this matter, it is convenient to define physical quantities to evaluate the interplay of these. Such is the case of the Péclet number, i.e.,  $Pe = v_D \sigma / D$ , where  $v_D$  is the drag velocity due to the presence of gravity,  $\sigma$  is the particles diameter, and  $D$  its their corresponding diffusion coefficient. Although  $Pe$  assist for this matter, the value on its own fails to describe the possible dynamical behaviour. Thus, it is convenient to study the dynamical behaviour under different Péclet values and its impact on physical observables.

The purpose of this section is to quantify the effect of an external force on physical observables in the real and reciprocal space, and to illustrate a possible dynamical phase diagram. This result is general for any dragging force, such as gravity in sedimentation or in electrophoresis experiments. Specifically, we focus on the mean squared displacement and the intermediate scattering function of a dilute-polydisperse system in the presence of the gravitational force. The layout of the work is presented in the following way. We begin by presenting the polydisperse Langevin model and the corresponding observables in the real and reciprocal space. Then, we show a systematic study by applying the model to Brownian dynamics simulations. Finally, we corroborate our theoretical results with sedimentation experiments of different particle sizes using Heterodyne Near

Field scattering.

#### 4.5.1 Effect of an external force in real and reciprocal space observables: mean squared displacement and intermediate scattering function

The dynamics of a system composed of particles undergoing Brownian motion in the presence of an external force can be described by the individual Langevin equation of each particle. For our purposes, we will consider a non-interacting dilute system. The system is composed of different particle sizes followed by a size distribution  $\mathcal{P}(\sigma)$ . In addition, a linear relation of the dragged velocity ( $v_D$ ) with the external force is assumed. Thus, a Stokes flow is considered and the inertial effects of the Langevin equation are safely neglected.

The corresponding over-damped Langevin equation for a particle of size  $\sigma$  in the direction of the external force takes the following form,

$$\dot{z}_\sigma(t) = \frac{1}{\xi} f_z(t) + v_{D\sigma}. \quad (155)$$

Where,  $\xi = 3\pi\eta\sigma$  is the friction coefficient,  $\eta$  is the zero shear viscosity of the solvent, and  $f_z(t)$  is the stochastic force.

The real space observable, the Mean Squared Displacement (MSD), is then computed by the solution of Eq.(155). Thus, the MSD per particle is

$$\langle \Delta z_\sigma^2(t, \tau) \rangle_t = 2D_\sigma \tau + v_{D\sigma}^2 \tau^2. \quad (156)$$

Here,  $\langle \dots \rangle_t$  states a starting time average,  $D_\sigma = k_B T / 3\pi\eta\sigma$  is the free diffusion coefficient of a particle of diameter  $\sigma$ ,  $k_B$  is Boltzmann's constant, and  $T$  the temperature. The overall ensemble of particles is described by a particle size distribution function ( $\mathcal{P}(\sigma)$ ), which has  $\langle \sigma \rangle_E$  and  $\delta_\sigma^2$  as its first and second moments. Usually, it is convenient to define the size coefficient of variation or polydispersity index as  $CV_\sigma = \delta_\sigma / \langle \sigma \rangle_E$ .

To obtain an observable that represents the whole ensemble of particles, an average over  $\mathcal{P}(\sigma)$  is performed (represented by  $\langle \dots \rangle_E$ ), i.e.

$$\begin{aligned} \langle \Delta z^2(t, \tau) \rangle_{t,E} &= \int \langle \Delta z_\sigma^2(t, \tau) \rangle_t \mathcal{P}(\sigma) d\sigma \\ &= 2\langle D \rangle_E \tau + \delta_v^2 \tau^2 + \langle v_D \rangle_E^2 \tau^2 \\ &= 2\langle D \rangle_E \tau + (1 + CV_v^2) \langle v_D \rangle_E^2 \tau^2, \end{aligned} \quad (157)$$

where we have employed the definition of the variance of the velocity,  $\delta_v^2 = \langle v_D^2 \rangle_E - \langle v_D \rangle_E^2$ . The previous result shows two delay time ( $\tau$ ) dependencies. The first one, corresponds to the Brownian or diffusive behaviour, where the MSD is

proportional to  $\tau$ , and the second one where the MSD is proportional to  $\tau^2$  is the ballistic behaviour imposed by the external force. Moreover, the overall motion can also be considered as directed collective motion, for the case of the mean drag velocity  $\langle v_D \rangle_E$ , and the relative motion to it, as is the case of  $\langle D \rangle_E$ , and  $\delta_v$  terms. Furthermore,  $CV_v = \delta_v / \langle v_D \rangle_E$  represents the velocity coefficient of variation of the velocity distribution. Depending on the functional relation between the drag velocity and the particle size, and the functional form of  $\mathcal{P}(\sigma)$ , a relation between  $CV_v$  and  $CV_\sigma$  can be found. It is worthwhile to mention that in Eq.(157) we have left  $CV_v$  and we have not introduced a relationship with  $CV_\sigma$ , as this result is a general one. It comes without assuming any functional form of the velocity distribution, and in principle, an analogous result can be obtained without the assumption that the velocity distribution is related to the particle distribution, where the  $\langle \dots \rangle_E$  is replaced by the integral over the diffusion coefficient distribution and a velocity distribution.

In order to generalize the description, and easily find characteristic scales, it is convenient to use reduced units [18]. For the polydisperse Langevin model (Sec.2.7), they are:  $\langle \sigma \rangle_E$  for unit length,  $t_B^* = \langle \sigma \rangle_E^2 / \langle D \rangle_E$  as unit of time. Thus, the MSD (Eq.(157)) in reduced units takes the following form

$$\langle \Delta z^{*2}(t^*, \tau^*) \rangle_{t^*, E} = 2\tau^* + Pe^{*2} (1 + CV_v^2) \tau^{*2}, \quad (158)$$

where  $\tau^* = \tau / t_B^*$  is the reduced delay time,  $Pe^* = \langle v_D \rangle_E \langle \sigma \rangle_E / \langle D \rangle_E$  is the ensemble Péclet number, which quantifies the relevance of the thermal agitation versus the external force for the overall ensemble.

The main contribution of each kind of dynamics (diffusive or ballistic) to the MSD can be quantified by calculating the delay time needed for the system to translate a unit of distance  $\langle \sigma \rangle_E$ , thus  $\langle \Delta z^{*2}(t, \tau) \rangle_{t, E} = 1$ . We will refer to this delay time as  $\tau_{\langle \sigma \rangle}^*$ , and it is obtained by solving the quadratic function of Eq.(158). This results in

$$\tau_{\langle \sigma \rangle}^* = \frac{-1 + \sqrt{1 + (1 + CV_v^2) Pe^{*2}}}{(1 + CV_v^2) Pe^{*2}}. \quad (159)$$

Eq.(159) has the limit  $\tau_{\langle \sigma \rangle}^* \rightarrow 1/2$  for  $Pe^* \rightarrow 0$ . This corresponds to the delay time needed to translate the unit distance  $\langle \sigma \rangle_E$  for particles undergoing pure Brownian motion. Moreover, for  $Pe^* \rightarrow \infty$ ,  $\tau_{\langle \sigma \rangle}^* \rightarrow 0$ . The latter implies that as higher the Péclet number gets, the contribution of the external force dominates, thus there is no significant Brownian motion in the translation of the particles. A graphic representation of Eq.(159) is shown in Fig.29 for different  $Pe^*$  and  $CV_v$  values. It has been scaled with the result of the limit  $Pe^* \rightarrow 0$ , as this introduces normalized axis, i.e.,  $2\tau_{\langle \sigma \rangle}^* \rightarrow 1$ , and  $2\tau_{\langle \sigma \rangle}^* \rightarrow 0$  for  $Pe^* \rightarrow \infty$ . By visual inspection of Fig.29, we can observe that the dynamical behaviour is similar for all of the  $CV_v$

tested, as all curves fall on top of each other. Moreover, we estimated the relative deviation of  $\sim 1.94\%$  between the monodisperse case,  $CV_v = 0$ , and the highest velocity coefficient of variation ( $CV_v = 0.20$ ) at the largest  $Pe^*$ . Furthermore, this dynamical behaviour can be summarized onto the following dynamical regimes: The first one is the colloidal regime, it is found for  $Pe^* < 0.1$ , as  $2\tau_{\langle\sigma\rangle}^* \simeq 1$ . Then, the colloidal with external force regime is found. It is the one where the external force starts to act, as it adds a ballistic contribution to the MSD. We infer the upper limit at  $Pe^* \simeq 100$ , where  $2\tau_{\langle\sigma\rangle}^* \simeq 0.01$ . Finally, the third regime is found for  $Pe^* > 700$ . Here, the contribution of the external force completely overtakes the diffusive one. Thus, the thermal agitation becomes negligible. This regime is addressed as the ballistic-athermal or granular regime.

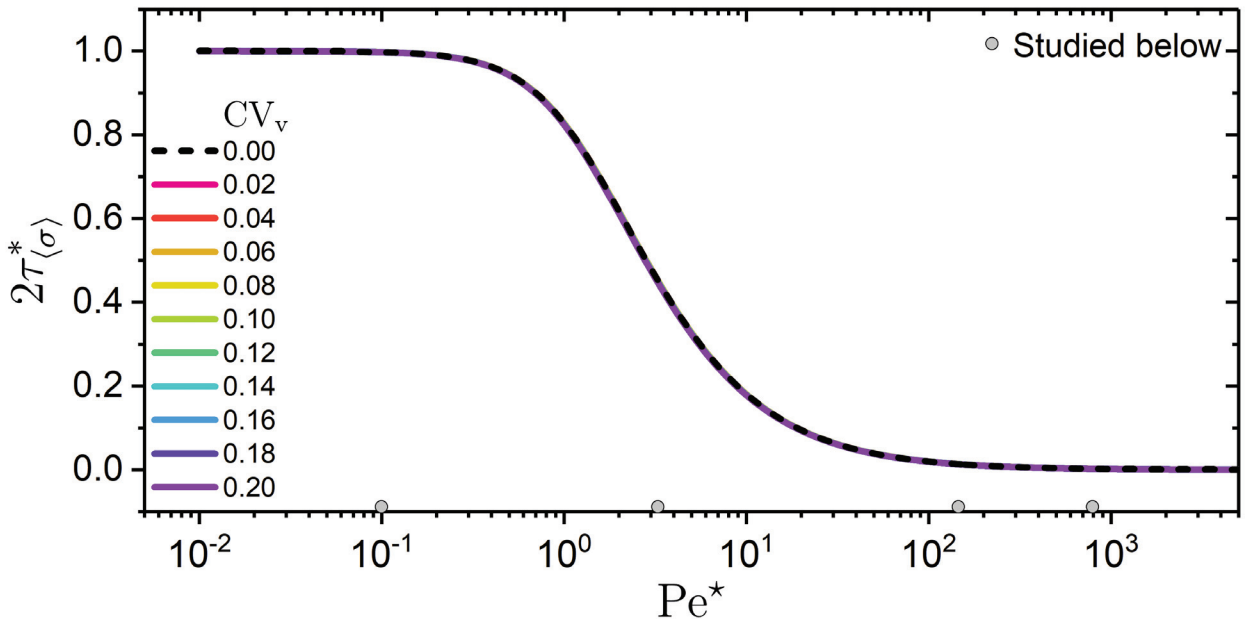


Fig. 29: Normalized  $\tau_{\langle\sigma\rangle}^*$  as a function of the ensemble Péclet number ( $Pe^*$ ) for different velocity coefficients of variation ( $CV_v$ ) values. By this normalization,  $2\tau_{\langle\sigma\rangle}^* \rightarrow 1$  for  $Pe^* \rightarrow 0$  as seen.  $\tau_{\langle\sigma\rangle}^*$  is the delay time needed for a system to translate a unit distance  $\langle\sigma\rangle_E$ . The lower small grey circles correspond to the  $Pe^*$  values of the experimentally studied samples (Sec.4.5.2).

To further develop our findings, and study the influence of the external force in the real space observable, namely the mean squared displacement, we performed Brownian dynamics simulations. An extension of the Ermack-McCammon algorithm including the system polydispersity was employed (for further description of the model please refer to Sec.2.7). For this, we have considered  $\mathcal{P}(\sigma)$  to be a Gaussian distribution, leading to  $CV_v \simeq 2CV_\sigma$ . Furthermore, we have considered the force balance among the effect of the gravitational force, the buoyancy of the particles and the friction as the external force, leading to  $v_D = v_s = \Delta\rho g \sigma^2 / 18\eta$  as the terminal settling velocity, where  $\Delta\rho = \rho_s - \rho_p$  is the density difference between the solvent and particle densities. The computer simulations were performed for an overall volume fraction of  $\phi = 5 \times 10^{-4}$ , including an ensemble of 512 particles.

In different runs, we studied different polydispersities i.e.  $0 \leq \text{CV}_\sigma \leq 0.1$ . In addition, we selected four different Péclet regions,  $\text{Pe}^\star = \{1, 33, 150, 800\}$ , they correspond to  $2\tau_{\langle\sigma\rangle}^\star = \{0.8, 0.05, 0.01, 0.002\}$ .

Our results are summarized in Fig.(30). As an overview, we corroborated that the MSD has the same shape for all of the studied polydispersities in the selected Péclet numbers. This can be inferred from the superposition of all of the MSD's in Fig.(30). Moreover,  $\text{Pe}^\star = 0$  (free diffusion represented by dashed line) has been included as reference to compare the effects of the external force. For  $\text{Pe}^\star = 1$ , the external force starts to play a role, as a deviation from the linear regime is seen for  $\tau/t_B^\star > 1$ . Conversely, for most of the delay times where  $\tau/t_B^\star < 1$  the behaviour of the MSD is proportional to  $\tau^\star$ . In addition, the results superimpose to the MSD obtained for  $\text{Pe}^\star = 0$ . For higher  $\text{Pe}^\star$  values, this behaviour gradually shifts towards smaller delay times. The transition time between colloidal motion and ballistic motion ( $\tau_{c-g}^\star$ ) in the MSD, is approximated when the magnitude of both terms in Eq.(158) are equal. Thus,  $\tau_{c-g}^\star \sim 2/([1 + \text{CV}_v^2]\text{Pe}^{\star 2})$  and its value is reduced by two orders of magnitude for  $\text{Pe}^\star = 33$  when compared to  $\text{Pe}^\star = 1$ , and four orders for  $\text{Pe}^\star = 150$ . Finally, for  $\text{Pe}^\star = 800$  the linear diffusive behaviour is overtaken by the quadratic behaviour of the MSD. Hence, the motion in this  $\text{Pe}^\star$  is dominated by the external force.

The previous sheds information over the different dynamical regimes found, where three main regimes can be used to describe the motion, i.e., Colloidal ( $\text{Pe}^\star < 1$ ), colloid in the presence of an external force ( $1 < \text{Pe}^\star < 150$ ), and finally for  $\text{Pe}^\star > 800$  the granular regime is found. These results, when compared to the ones obtained by using  $\tau_{\langle\sigma\rangle}^\star$ , show different Péclet values for defining the boundaries of each dynamical regime. The reason of this comes from the lack of a proper boundary definition, as depending on which of both observables is used, the upper boundary is set.

A clearer boundry can be set by introducing experimental limitations of the instrumental capability to detect small displacements. Thus, depending on the experimental capabilities the boundary could be defined. For example, the localization uncertainty obtained from tracking algorithms from bright field microscopy images is  $\sim 10\text{nm}$  [25]. This is half of the minimum distance needed in order to capture the linear regime at  $\text{Pe}^\star = 150$ . This Péclet value corresponds to  $\langle\sigma\rangle_E = 7.32\mu\text{m}$  polystyrene particles in water ( $\langle D \rangle_E = 0.0084\mu\text{m}^2/\text{s}$ ), thus  $\langle \Delta z^{*2}(t, \tau) \rangle_{t,E} = 10^{-5}$ . This corresponds to an average displacement  $\sqrt{\langle \Delta z^2(t, \tau) \rangle_{t,E}} = 23\text{nm}$ , hence at this  $\text{Pe}^\star$ , the displacement is barely detected. Furthermore,  $\text{Pe}^\star = 800$  corresponds to  $11\mu\text{m}$  polystyrene particles in water ( $\langle D \rangle_E = 0.0056\mu\text{m}^2/\text{s}$ ), and in order to detect displacements related to Brownian motion  $\sqrt{\langle \Delta z^{*2}(t, \tau) \rangle_{t,E}} \leq$

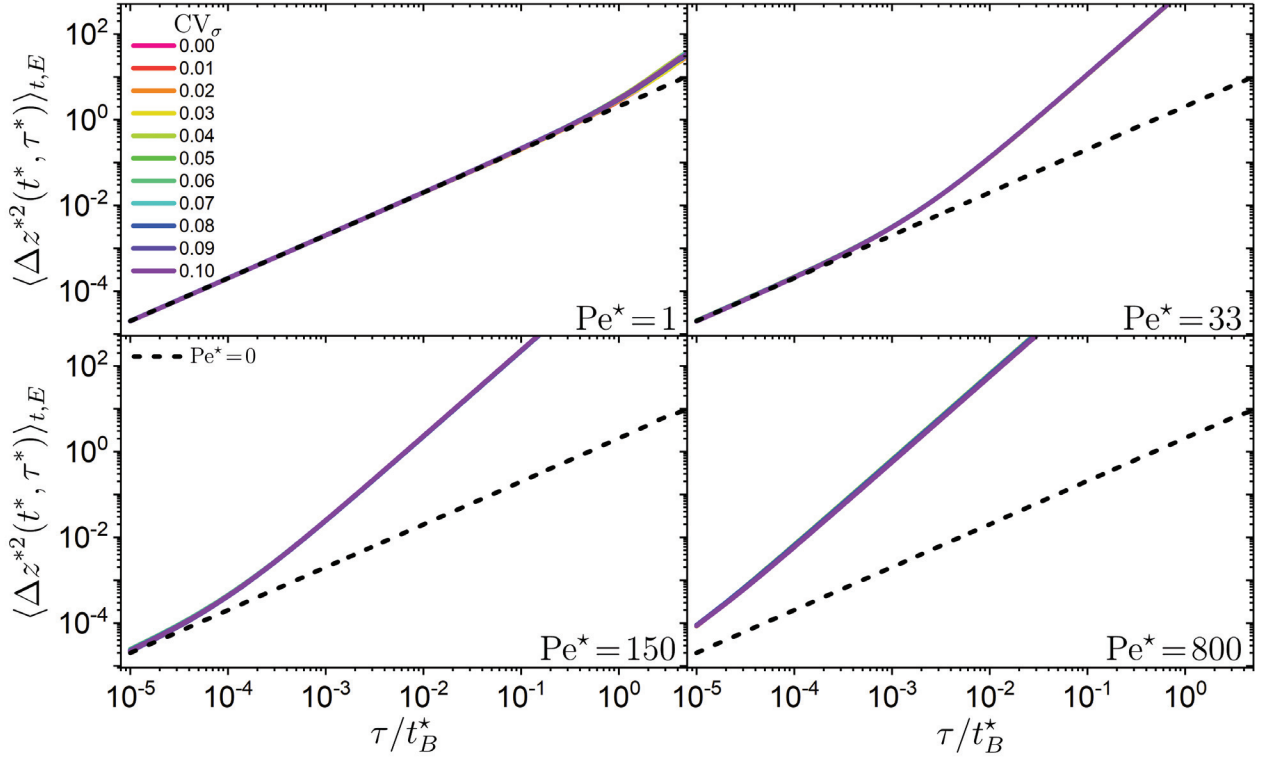


Fig. 30: Computer simulation results of the time and ensemble mean squared displacements ( $\langle \Delta z^{*2}(t^*, \tau^*) \rangle_{t,E}$ ) of systems with dynamics that include Brownian motion in the presence of an external force. This force imposes a settling velocity ( $v_s$ ), and is the result of the force balance among the effect of the gravitational potential, the buoyancy of the particles and the friction of the solvent. The contribution of the external force is quantified by the ensemble Péclet number ( $Pe^* = \langle v_D \rangle_E \langle \sigma \rangle_E / \langle D \rangle_E$ ). The ensemble of particles is described by a Gaussian distribution with size coefficient of variation  $CV_\sigma$ . The (\*) represents reduced units, where  $\langle \sigma \rangle_E$  is taken for unit length,  $t_B^* = \langle \sigma \rangle_E^2 / \langle D \rangle_E$  as unit of time.

$10^{-3}$  needs to be properly sampled. This implies a detection of position smaller  $\sqrt{\langle \Delta z^2(t, \tau) \rangle_{t,E}} \leq 11\text{nm}$ . Hence, the granular boundary is perfectly defined by the experimental limitations.

A similar analysis can be performed to the intermediate scattering function (ISF) in the reciprocal space. The real part of the ISF is experimentally accessible by heterodyne-like scattering techniques [7, 24, 77]. Thus, for comparison purposes, we will represent it as  $f(Q, \tau)$ . In real units, the real part of the ISF of an ensemble of particles under the influence of an external force and thermal agitation has the following form:

$$f(Q, \tau) = \exp \left[ -Q^2 \langle D \rangle_E \tau - \frac{1}{2} Q^2 \delta_v^2 \tau^2 \right] \cos(Q \langle v_D \rangle_E \tau). \quad (160)$$

Here, we have considered the wave vector  $Q$  to be parallel of the direction of the external force. Moreover, Eq.(160) encodes in different functional forms the two types of motion of the system, having a cosine term for the mean directed collective motion (for  $\langle v_D \rangle_E$ ) and the exponential term for the relative motion to it (including  $\langle D \rangle_E$  and  $\delta_v^2$ ). In addition, each contribution contains the corresponding characteristic times:  $\tau_{\langle v \rangle}(Q) = 1/Q \langle v_D \rangle_E$  for the mean directed collective

motion,  $\tau_B(Q) = 1/Q^2 \langle D \rangle_E$  and  $\tau_{\delta_v}(Q) = \sqrt{2}/Q\delta_v$ , for the diffusive and velocity deviations characteristic times, respectively. Noting the  $Q$  scale dependence for the type of dynamics described, having a  $Q^2$  dependence for Brownian motion, and  $Q$  for directed motion.

It is possible to write Eq.(160) in reduced units, obtaining

$$f(Q^*, \tau^*) = \exp \left[ -Q^{*2}\tau^* - \frac{1}{2}Q^{*2}CV_v^2Pe^{*2}\tau^{*2} \right] \cos(Q^*Pe^*\tau^*). \quad (161)$$

The previous translates into the three characteristic times in reduced units, i.e.,  $\tau_{\langle v \rangle}^*(Q^*) = 1/Q^*Pe^*$ ,  $\tau_B^*(Q^*) = 1/Q^{*2}$  and  $\tau_{\delta_v}^*(Q^*) = \sqrt{2}/Q^*Pe^*CV_v$ .

In order to explore the effect of the external force in the real part of the ISF, we also used computer simulations including the polydisperse Langevin model. We have selected the same simulation parameters as before and in addition, we opted for a proving wavelength of the order of an average particle size, i.e.,  $Q^* = Q\langle \sigma \rangle_E = 2\pi$ . A summary of our results is shown in Fig.31, where the case of  $Pe^* = 0$  and  $CV_\sigma = 0$  has been included for comparison purposes (dashed line). This case is analytically described by the  $Q^{*2}$  term in the exponential decay function from Eq.(161).

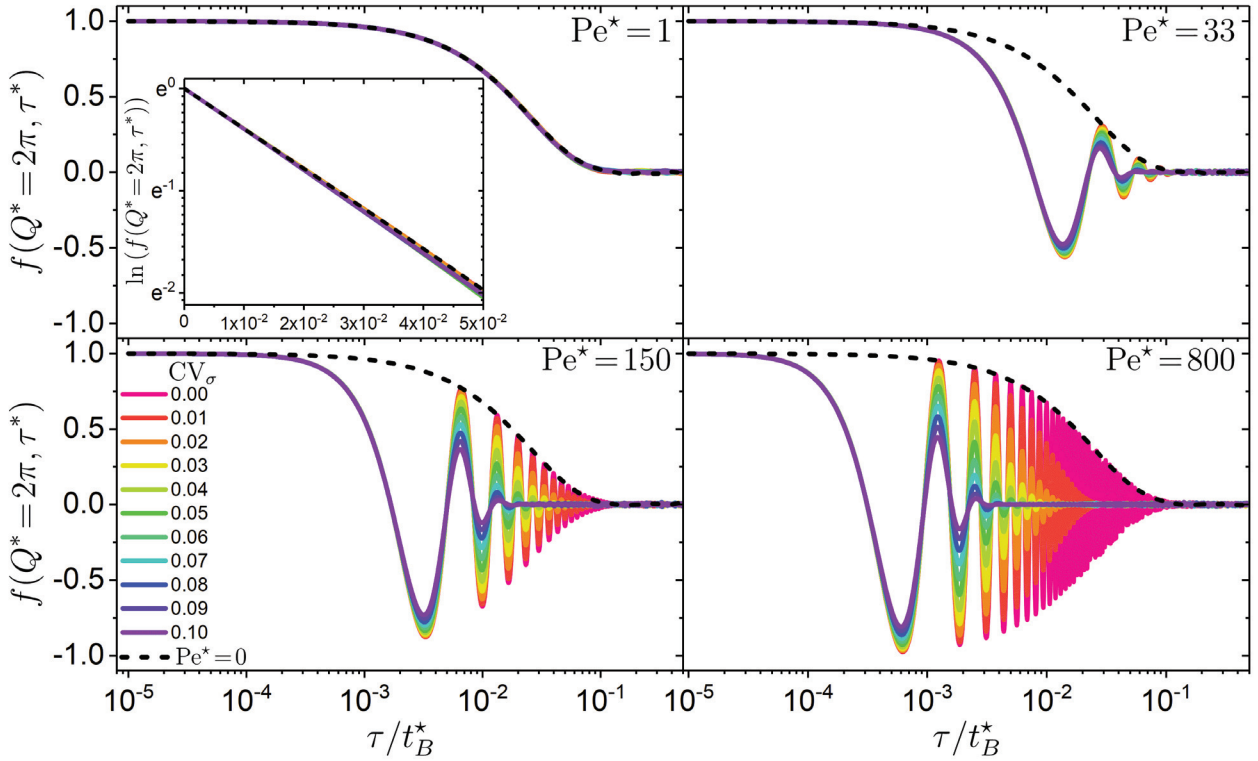


Fig. 31: Summary of the results obtained from computer simulations using the polydisperse Langevin model for the real part of the intermediate scattering function ( $f(Q^*, \tau^*)$ ). The computer simulations were performed for different ensemble Péclet ( $Pe^*$ ) and polydispersity values ( $CV_\sigma$ ). For comparison purposes, the case of  $Pe^* = 0$  and  $CV_\sigma = 0$  is shown for all  $Pe^*$  as dashed lines, it is analytically described by the  $Q^{*2}$  term in the exponential decay function from Eq.(161).

Contrary to the MSD, the ISF present changes for different  $CV_\sigma$  for  $Pe^* \geq 1$ . Starting from the case of  $Pe^* = 1$ , a small effect due to the polydispersity and the external force can be appreciable close to the decay value of the function, i.e.,  $f(Q^*, \tau^*) = 1/e$  (showed in the top-left panel of Fig.31 along with a lin-log representation of  $f(Q^*, \tau^*)$  as inset). This effect is seen as deviations from  $Pe^* = 0$  and it becomes more noticeable for  $CV_\sigma > 0.05$  (inset). Moreover, the oscillatory behaviour from the mean directed collective motion is hardly seen. Thus, for this length scale and  $Pe^*$ , the majorly dynamical behaviour can mainly be considered to be Brownian.

The mean directed collective motion starts to become appreciable for an increased  $Pe^*$ . As  $Pe^* = 33$  (top-right panel of Fig.31) shows few oscillations at larger  $\tau^*$ . Moreover, for small polydispersity values,  $CV_\sigma < 0.05$ , the envelope of the function is the case of  $Pe^* = 0$ . Thus, for those  $CV_\sigma$  the  $CV_v$  information can not be retrieved. Similarly to the case of  $Pe^* = 1$ , a gradual shift from the envelope of  $Pe^* = 0$  is seen for  $CV_\sigma > 0.06$ . This separation becomes more noticeably for  $CV_\sigma = 0.10$ , showing that  $CV_v$  contributes to the decorrelation of  $f(Q^*, \tau^*)$ . This effect is described by the second term in the exponential function from Eq.(161) and becomes more significant at even greater  $Pe^*$  values. In this Péclet regime the Brownian motion and the contribution of the external force are both important for describing the dynamical behaviour of the system for all of the studied  $CV_\sigma$ . Hence, this region is addressed as the colloid in the presence of an external force.

Large values of the  $Pe^*$  imply a higher contribution of the external force on the overall dynamics of the system. This is seen for the case of  $Pe^* = 150$  (bottom-left panel of Fig.31), where stronger oscillations in  $f(Q^*, \tau^*)$  are present due to the imposed mean directed collective motion. This implies a more relevant contribution from  $CV_v$ , as the envelope of the overall  $f(Q^*, \tau^*)$  deviates from the  $Pe^* = 0$  at  $CV_\sigma > 0.02$ , translating in a reduction of half order of magnitude at the  $1/e$  value of  $f(Q^*, \tau^*)$  for  $CV_\sigma > 0.05$ . Thus, the effect of  $CV_v$  dominates the dynamics of the system becoming the main source in the decorrelation of  $f(Q^*, \tau^*)$ , leaving the contribution of the Brownian motion to the short time regime of the function. This sets an indication of the dynamical transition where the effect of the thermal agitation can be considered negligible.

Finally, for  $Pe^* = 800$  (lower-right panel of Fig.31), the Brownian contribution to the dynamics of the system becomes negligible. This is seen by the deviation of  $f(Q^*, \tau^*)$  from the case of  $Pe^* = 0$  at shorter delay times ( $\tau^* \sim 10^{-3}$ ) for  $CV_\sigma > 0.02$ . As it becomes overtaken by the effect of  $CV_v$ . The previous sets up the granular regime, it is seen by an increased number of oscillations present within the  $Pe^* = 0$  envelope. In addition, also overtakes the Brownian contribu-

tion, as the envelope of  $f(Q^*, \tau^*)$  deviates from the  $Pe^* = 0$  for polydispersities as small as  $CV_\sigma = 0.01$ . The previous is in agreement with the obtained information from the analysis of the MSD. However, one of the advantages of the reciprocal space is the ability to unfold the length scale information, or  $Q$  dependence. This is achieved by close inspection of the characteristic times that corresponds to each dynamical information (Eq.(161)), i.e. ,  $\tau_{\langle v \rangle}^*(Q^*)$ ,  $\tau_B^*(Q^*)$ , and  $\tau_{\delta_v}^*(Q^*)$ . The latter can be generalized by the diagram sketched in Fig.32.

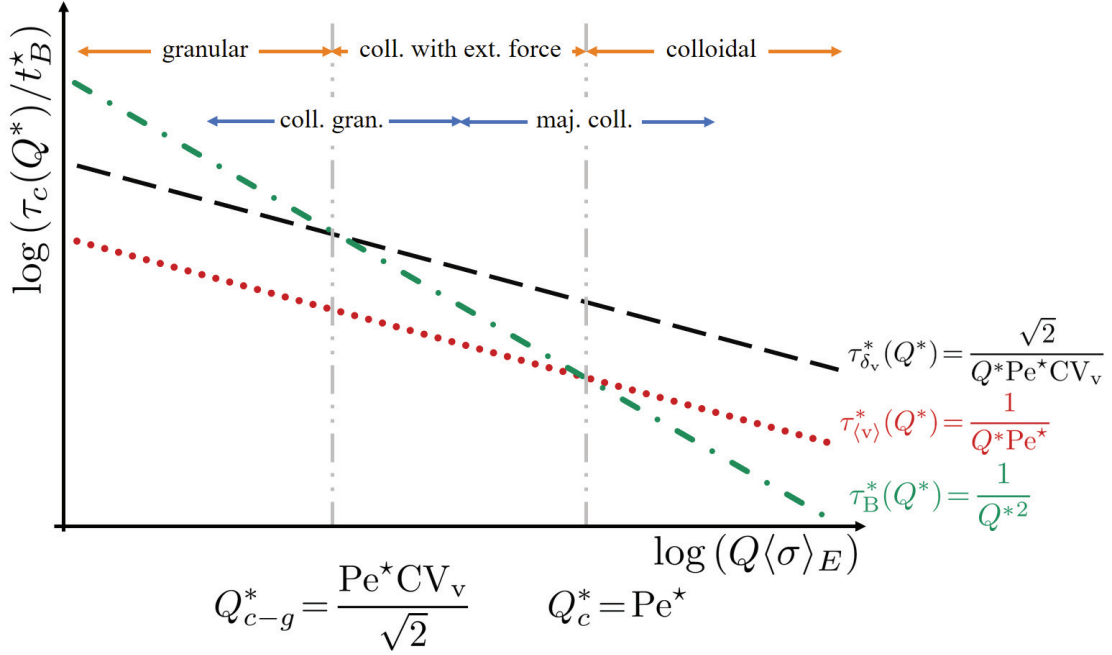


Fig. 32: Dynamical diagram described by the different characteristic times from each type of motion in reduced units. The red dotted line corresponds to the ballistic mean directed collective motion  $\tau_{\langle v \rangle}^*(Q^*) = 1/Q^*Pe^*$ , the black big dashed line to the ballistic relative motion  $\tau_{\delta_v}^*(Q^*) = \sqrt{2}/Q^*Pe^*CV_v$ , and the green dashed-dotted to the random Brownian motion  $\tau_B^*(Q^*) = 1/Q^{*2}$ . The overall dynamics can be described by three regions: the colloidal, the colloidal with external force and the granular. These regions are separated by two characteristic length scales,  $Q_c^* = Pe^*$  addressed as the colloidal length scale, as marks the transition point between the colloidal and colloid with external force, and the colloid to granular for  $Q_{c-g}^* = Pe^*CV_v/\sqrt{2}$ . As it marks the transition between a colloid with external force to granular.

The information in the diagram can be summarized by three dynamical regimes: colloidal, colloidal with external force, and granular. The boundary between them is defined by two characteristic length scales. The first,  $Q_c^* = Pe^*$ , will be addressed as the colloidal length scale. It is obtained when  $\tau_B^*(Q^*) = \tau_{\langle v \rangle}^*(Q^*)$ , and sets the boundary between the colloidal and colloidal with external force dynamical regimes. The second, addressed as colloid to granular,  $Q_{c-g}^* = Pe^*CV_v/\sqrt{2}$ , is obtained when  $\tau_B^*(Q^*) = \tau_{\delta_v}^*(Q^*)$ . It sets the boundary between the colloid with external force and the granular dynamical regimes.

With the previous as reference, the colloidal regime is met for  $Q^* > Q_c^*$ , i.e. smaller length scales, where the Brownian characteristic time ( $\tau_B^*(Q^*)$ ) is responsible to decorrelate  $f(Q^*, \tau^*)$  (represented as dash-dotted line in Fig.32). This, as it is the fastest characteristic time (appearing first from bottom to top in the diagram of Fig.32). Then, the colloid with external force is defined for  $Q_{c-g}^* < Q^* < Q_c^*$ . Here, the characteristic time from the mean directed collective motion ( $\tau_{\langle v \rangle}^*(Q^*)$ ) starts to appear (represented as dotted line in Fig.32). Moreover, the decorrelation of  $f(Q^*, \tau^*)$  is only caused by  $\tau_B^*(Q^*)$ , as it is located below the characteristic time from the relative to the mean motion  $\tau_{\delta_{\langle v \rangle}}^*(Q^*)$  (represented as big-dashed line in Fig.32). Finally, for  $Q^* < Q_{c-g}^*$ , i.e. larger length scales, the granular dynamical behaviour is defined. The definition becomes natural, as all of the contributions due to the external force dominate the description of the dynamics, having  $\tau_B^*$  greatly above  $\tau_{\langle v \rangle}$  and  $\tau_{\delta_{\langle v \rangle}}^*$ . Furthermore, the main contribution for the decorrelation of  $f(Q^*, \tau^*)$  is due to  $\tau_{\delta_{\langle v \rangle}}^*$ . Interestingly, for length scales around  $Q_{c-g}^*$ , a mixed description of the dynamics is found. As for  $Q^* = Q_{c-g}^*$ , the contribution of  $\tau_{\delta_{\langle v \rangle}}^*$  becomes equally significant as  $\tau_B^*$ . As a consequence, both terms contribute to the decorrelation of  $f(Q^*, \tau^*)$ , leading to a mixed dynamical behaviour. We will refer to this as the colloidal-granulate regime. Finally, for length scales around to  $Q^* = Q_c^*$ , the dynamics become mainly colloidal as the decorrelation of  $f(Q^*, \tau^*)$  is caused by  $\tau_B^*(Q^*)$  with a barely visible contribution of  $\tau_{\delta_{\langle v \rangle}}^*$ .

#### 4.5.2 Experimental Results

To corroborate our findings, we performed Heterodyne Near Field Scattering experiments of dilute suspensions in steady state sedimentation. The main observable from this scattering technique is the real part of the intermediate scattering function ( $f(Q, \tau)$ ). Moreover, the multi- $Q$  resolution of the technique allowed us to measure different length scales simultaneously. The experiments were carried out using the HNFS setup described in Sec.4.1. It was equipped with CFI Plan Fluor 20X 0.5NA Microscope objective, allowing us to capture a  $Q$  range of  $(0.3 - 4.7)[\mu\text{m}^{-1}]$ . This translates onto about an order of magnitude in reduced units of the scattering wave vector  $Q^*$ . In addition, steady state was ensured by adding a sample chamber to reduce thermal instabilities. The experiments were carried out at 19C with fluctuations inside of the chamber of  $\pm 0.2$ C. The polydispersity of each particle batch was defined by the manufacturer synthesis protocol, and for comparison purposes, it was characterized by the static light scattering information (SLS) from the instrument. Thus, within the same experiments, static and dynamic information were measured. Furthermore, to fix the dependence of the Péclet number to the mean particle size, we opted for fixing the particle composition. Thus, different sizes of polystyrene particles were selected

( $\rho_p = 1.048 \text{ g/cm}^3$ ). A summary of the measured samples is shown in Table 3.

Sample	Volume fraction	FPS	Acq.Time[min]	Image size	Pe*	$\langle\sigma\rangle_E[\mu\text{m}](\text{SLS})$	CV $_{\sigma}(\text{SLS})$
PS-2.00 $\mu\text{m}$	$1.0 \times 10^{-5}$	25	120	1024 $\times$ 1024	1.2	1.82	0.120
PS-5.00 $\mu\text{m}$	$3.0 \times 10^{-5}$	50	60	1024 $\times$ 1024	35.0	4.76	0.062
PS-7.32 $\mu\text{m}$	$5.0 \times 10^{-5}$	50	60	1024 $\times$ 1024	150.0	7.00	0.045
PS-11.00 $\mu\text{m}$	$1.0 \times 10^{-4}$	50	40	1024 $\times$ 1024	880.0	10.56	0.056

Table 3: Summary of the experimental details from the different measured samples.

Our measurement protocol is as follows: samples were diluted from stock suspension and poured in glass cuvette of 1mm optical path and 40mm of height (21-G-1 Starna GmbH). The cuvette was sealed with a stopper leaving a small air bubble in order to help re-disperse the particles for resetting their initial conditions. In addition, the cuvette was attached to a 3D printed plastic sample holder to avoid heat conduction that could cause convection inside of the sample cell. The filled cuvette along with the sample holder was placed in the instrument and left to thermalize for 1 hour. After thermalization, the sample (in the plastic holder to avoid direct contact with it) was rigorously agitated by hand using the air bubble for 30 seconds, afterwards it was placed back into the instrument. Before starting the image acquisition a waiting time period was set. Having 50h for PS-2.00 $\mu\text{m}$  particles, 8.5h for PS-5.00 $\mu\text{m}$ , 1.5h for for PS-7.32 $\mu\text{m}$  and 0.75h for PS-11 $\mu\text{m}$ . After this time, a constant settling velocity was found and the image acquisition was started. At this stage, the sedimentation front was located at  $\sim 1.5\text{cm}$  above the observation window. This allowed us to have a sufficient measurement time without any stratification effects, as this phenomenon alters the bulk particle distribution. Moreover, in order to avoid back flow perturbation, the observation area is located at 1.2cm from the bottom of the cell. Hence, bulk information was assumed to be captured. The resetting process was carried out in order to have a complete set of three independent experiments. A summary of one measurement type per sample is illustrated in Fig.33. For comparison purposes, we show length scales that satisfy  $Q^* < 2\pi$ . The reduction on the number of  $Q^*$  is due to the fixed  $Q$  range of the instrument. In order to differentiate Brownian to ballistic motion, we have scaled the delay time axis to  $\tau Q$ , as this is the natural scale for ballistic motion ,i.e.,  $1/Q \sim v\tau$ .

The  $\tau Q$  scaling causes a gradual spreading among the different  $f(Q^*, \tau Q)$  for the case of  $\text{Pe}^* = 1.2$  (upper-left Fig.33). This is expected for this  $\text{Pe}^*$ , as the dynamical behaviour is majorly described by colloidal dynamics. The colloidal behaviour scales with  $Q^2$  as  $1/Q^2 \sim D\tau$ . Additionally, an oscillation from the mean directed collective motion contribution starts to appear at  $\tau Q \sim 10$  for  $Q^* < 1$ . This effect becomes more visible for higher Péclet values, as the contribution of the external force increases. For example, at  $\text{Pe}^* = 35$  (upper-right Fig.33), higher amplitude oscillations with up to three periods are seen. Furthermore, all of  $f(Q^*, \tau Q)$  align

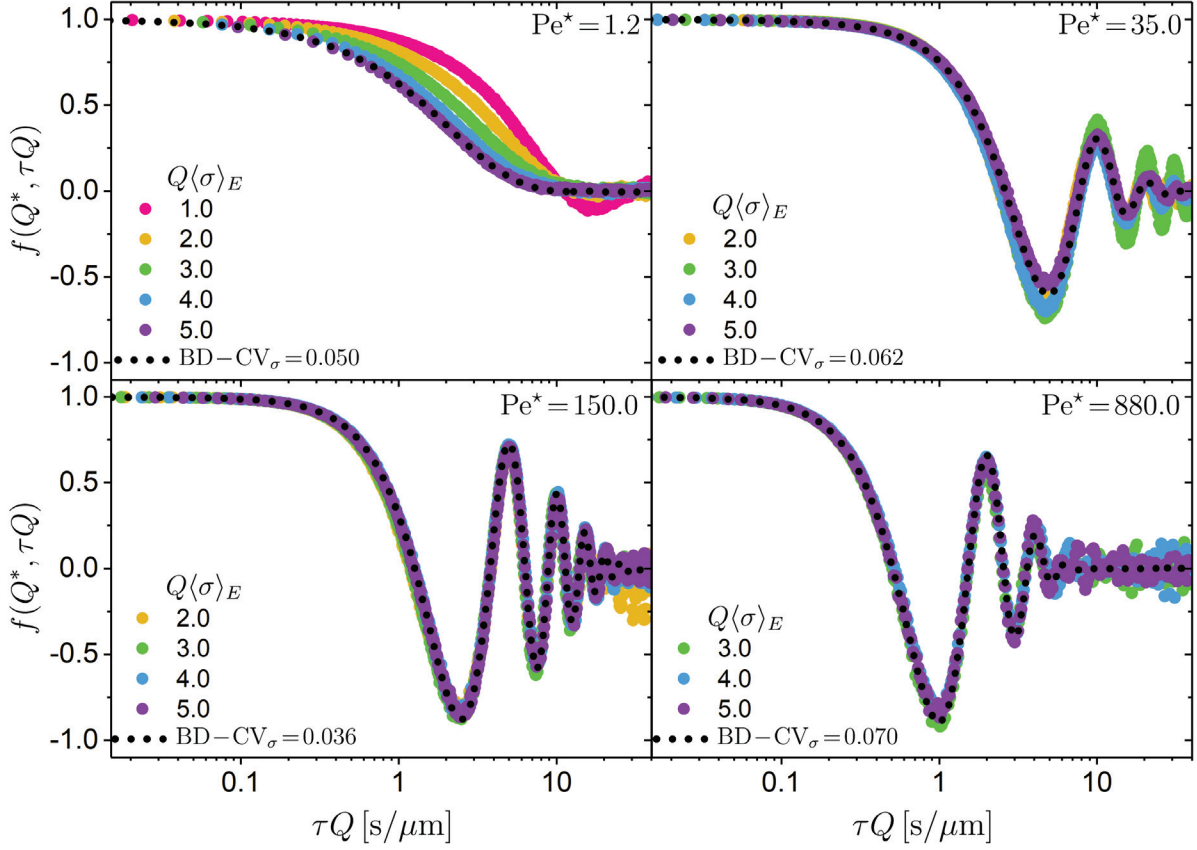


Fig. 33: Summary of the measured  $f(Q, \tau)$  from settling suspensions for different ensemble Péclet values (different colors). The different  $Pe^*$  were obtained by changing the particle size as indicated in Table 3. The dotted line represent Brownian dynamics simulation using the polydisperse Langevin model taking as input the corresponding  $Pe^*$  and a tuned  $CV_\sigma$ .

by this scaling. This shows that the overall dynamics are governed by ballistic-like motion. However, a small spreading becomes visible at the first minimum of the function,  $\tau Q \sim 5.0$ . This is due to the small but still present contribution of the Brownian motion, as this is the only contribution of Eq.(161) that depends on  $Q$  in this representation. In contrast, for  $Pe^* = 150$  (lower-left Fig.33), this spreading is hardly seen. Here, all of the  $f(Q^*, \tau Q)$  tend to collapse onto a master curve in the ballistic  $\tau Q$  scaling. Additionally, the importance of the external force becomes more dominant, as the first minimum in the oscillations shifts towards smaller  $\tau Q$  ( $\tau Q \sim 2.5$ ). This trend is seen also for  $Pe^* = 880$  (lower-right Fig.33), where the first minimum is at  $\tau Q \sim 1.0$ . However, the measured  $f(Q^*, \tau Q)$  at this  $Pe^*$  value contains less number of periods ( $\sim 2$ ) when compared to  $Pe^* = 150$  ( $\sim 4$ ). The reason of this is due to the difference in polydispersity, as it can be seen from the value of  $CV_\sigma$  extracted from the comparison with Brownian Dynamics simulations using the polydisperse Langevin model (dotted lines). We used as input parameters the extracted mean  $Pe^*$  from the characteristic times (Fig.34), leaving the value of the polydispersity as a free parameter.

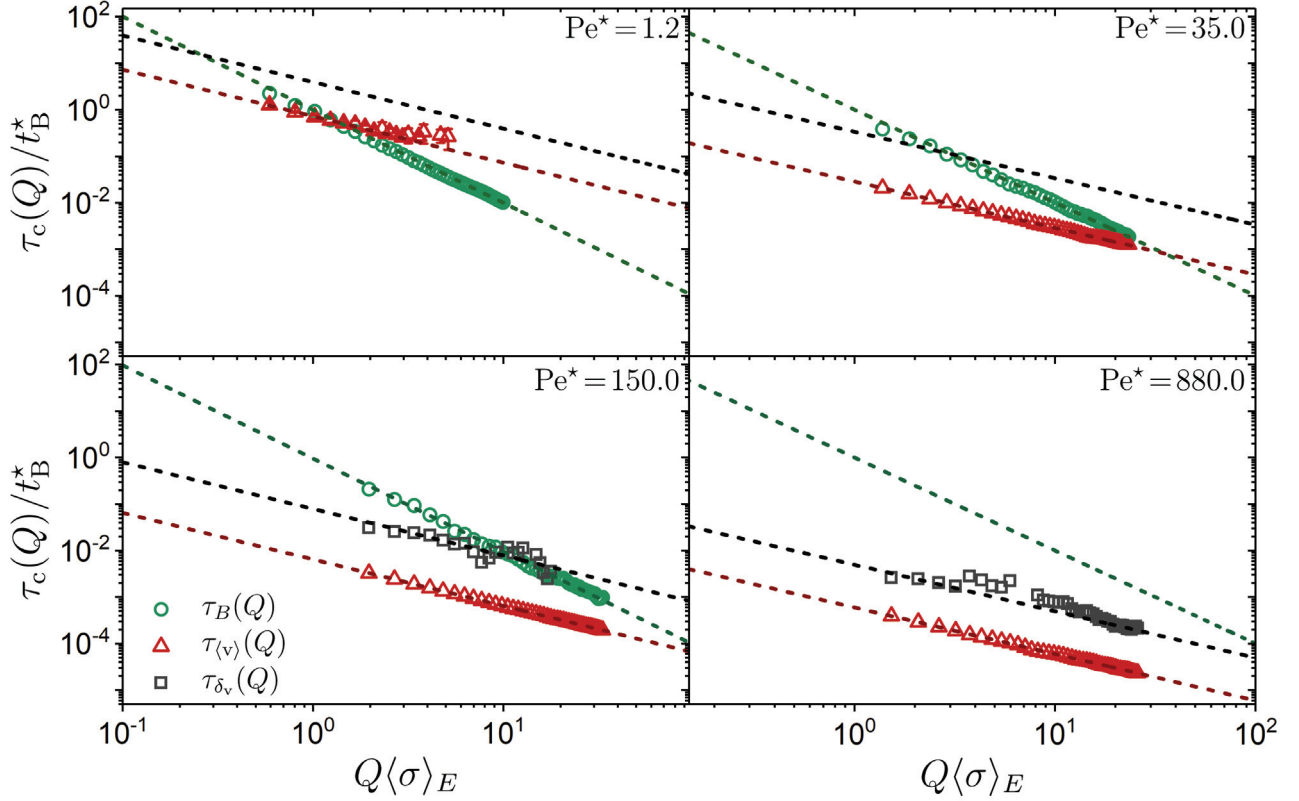


Fig. 34: Characteristic delay times obtained for each studied  $Pe^*$  (indicated as open symbols),  $\tau_B(Q) = 1/Q^2 \langle D \rangle_E$  corresponds to the characteristic time due to Brownian motion,  $\tau_{\langle v \rangle}(Q) = 1/Q \langle v \rangle_E$  and  $\tau_{\delta_v}(Q) = \sqrt{2}/Q \delta_v$  represents the mean and standard deviation from the imposed velocity distribution. The different  $Pe^*$  values were obtained by different particle sizes (a summary of these is indicated in Table 3). The dashed lines represent the average values of each characteristic time. In addition, both axes are shown normalized for comparing with dynamical phase diagram in Fig.32.

We continued by obtaining the relevant characteristic times from  $f(Q, \tau)$  using Eq.(160). This was performed by a custom written program of numerical non linear curve fitting using Matlab. Then, we proceeded to normalize the extracted data accordingly. Results obtained from the average of three independent measurements per  $Pe^*$  are shown as open symbols in Fig.34. Additionally, we have included the reference average values of each characteristic time (dashed lines).

For the case of  $Pe^* = 1.2$  (upper-left Fig.34), we could not extract  $\tau_{\delta_v}$ , as the main contribution for the decorrelation of  $f(Q, \tau)$  comes from  $\tau_B$ . The corresponding dashed line was computed by using the polydispersity value from the SLS measurement. Moreover, due to the small  $Pe^*$ , we were able to extract  $\tau_{\langle v \rangle}$  around the colloidal length scale  $Q_c^* = Pe^* = 1.2$ . Hence, for this  $Pe^*$ , a mixed dynamical behaviour was found, obtaining a mainly colloidal description for the dynamics of the system (as shown in Fig.32). Furthermore, the colloidal dynamical behaviour was found for length scales where the separation of  $\tau_{\langle v \rangle}$  and  $\tau_B$  become significant  $Q\langle\sigma\rangle_E > 5$ . The next dynamical behaviour was found for  $Pe^* = 35.0$  (upper-right). It corresponds to the colloid in the presence of an external force. As  $f(Q, \tau)$  is

mainly described by the corresponding terms of  $\tau_{\langle v \rangle}$  and  $\tau_B$ . Furthermore, the extracted characteristic times are found at  $Q^* < Q_c^* = \text{Pe}^* = 35.0$ . Similarly to  $\text{Pe}^* = 1.2$ , we were not able to extract  $\tau_{\delta_v}$  for this  $\text{Pe}^*$ . The reason of this is due to the level of similarities between the two characteristic times. This is in agreement with the previously shown from the numerical simulations, as for this  $\text{Pe}^*$  and polydispersity, the information regarding  $\text{CV}_v$  can not be retrieved (Fig.31). This limitation was not found at  $\text{Pe}^* = 150.0$ , where we were able to extract the information by the deconvolution of the cosine term of  $f(Q, \tau)$  and performing a short time analysis to  $\ln(f(Q, \tau))$ . At the measured length scales, the dynamical information is described by the colloidal-granulate mixed dynamical behaviour. This is seen as the captured length scales are around  $Q_{c-g}^* = \text{Pe}^* \text{CV}_v / \sqrt{2} \sim 16$ . It is worth mentioning that, similarly as  $\text{Pe}^* = 35.0$  for  $Q^* > Q_{c-g}^*$ , the information regarding  $\text{CV}_v$  becomes hardly accessible. Finally, we found the third dynamical behaviour at  $\text{Pe}^* = 880$ , where no  $\tau_B$  was found. Theoretically this characteristic time is found to be more than one order of magnitude above  $\tau_{\delta_v}$  and  $\tau_{\langle v \rangle}$ . Hence, the dynamics of this  $\text{Pe}^*$  are characterized by the granular description.

With the previous, we corroborate the dynamical phase diagram shown in Fig.32, as all of the extracted dynamical behaviour is properly described by the presented theoretical framework. Moreover, this framework provides a rich description depending on the probed length scale and the system conditions, such as mean particle size ( $\langle \sigma \rangle_E$ ), polydispersity ( $\text{CV}_\sigma$ ) and the strength of external force (quantified by  $\text{Pe}^*$ ). We found that the most dynamical content is found in the colloidal-granulate regime. In these regime, it is possible to fully characterize systems in the presence of external force, as all of the dynamical contributions, i.e.,  $\tau_B, \tau_{\langle v \rangle}, \tau_{\delta_v}$ , are obtained. We would like to stress out the simplicity of the theoretical framework, as all of the presented quantities are related to experimentally accessible average quantities.

## 4.6 Digital Fourier Analysis of X-Ray radiographs of granular suspensions

Granular suspensions are defined as suspensions where the particle dynamics are not governed by thermal agitation, thus these systems are also known as athermal [119, 120] or as noncolloidal suspensions [121]. In contrast to colloidal samples, granular suspensions exhibit dissipative dynamics, becoming very sensitive to friction due to particle-particle collisions. Many of these systems are found in nature as powders, sand, grains, among others.

Granular particles sediment due to their particle size, hence in order to overcome sedimentation, additional energy needs to be supplied to the system. This is experimentally achieved by vibration or by fluidization, either in liquid or air fluidized beds. Furthermore, due to the properties of granular materials, the particle dynamics have been mainly studied by Diffusing Wave Spectroscopy (DWS) [122–129], Dynamic Sound scattering (DSS) [130–135], X-Ray scattering [136], and through image analysis from light and X-Ray sources [118, 137–147].

X-Ray Radiography has been a key imaging technique for studying dynamics of systems that are opaque to visible light [139]. It allows the study of a variety of systems, ranging from microscopic biological samples like blood [139, 140], to macroscopic systems, such as glass beads, lentils or rice. The previous studies were achieved by performing Particle Image Velocimetry (PIV) on the acquired images [145].

PIV is employed for obtaining density displacements within consecutive images, thus it is possible to infer a velocity map that captures the motion of the imaged system. This type of motion can be random, such as Brownian motion, or ballistic directed motion like sedimentation [137, 138, 148]. In addition, for a system that presents a distribution of ballistic velocities, the motion can be decomposed into two types, the mean collective motion, and the individual motion relative to the mean directed motion. Density fluctuations can also be analyzed in the Fourier space, such analysis scheme is known as Digital Fourier Analysis (DFA). This leads to similar information as in static and dynamic light scattering experiments. It has been employed for studying motion from a variety of colloidal suspensions, where images from various visible light microscopy techniques were analyzed [7]. One of the advantages of a Fourier approach is the ability to differentiate the nature of the type of motion due to its wavelength dependence, i.e. having  $Q^2$  for random motion and  $Q$  for ballistic motion.

In the following, we show an extension of the use of the DFA image analysis to X-ray radiographs (X-DFA). This was achieved by firstly performing DFA in different series of synthetic radiographs and validated by comparison with the results

from PIV. In order to test the information content from the analysis scheme, we have simulated four different types of motion: directed, a normal distribution of directed motions, random motion, and a combination of all of the previous. The synthetic X-Ray radiographs were generated by using the Beer-Lambert law with extinction coefficients that take into account the X-ray beam hardening. In addition, the validated analysis scheme was employed to experimentally study the sedimentation of granular suspensions, and to characterize the motion of particles in a liquid fluidized bed. This work was done in collaboration with the Institute for Multiscale Simulation, Erlangen [149].

#### 4.6.1 Samples, X-ray Radiographs and Data Analysis

Experimentally, we used granular particles immersed in 50% v/v water-glycerol mixture (150-180 $\mu\text{m}$  soda-lime glass spheres (GL0191B5/150-180 MoSci) of mass density  $2.48 \pm 0.03 \text{ g/cm}^3$ ). The solvent mixture was chosen to have a viscosity of 7.1 mPa·s at 298K. The value of the viscosity slowed down the overall sedimentation kinetics, thus becoming detectable by our detection unit set at the maximum recording speed, without compromising spatial resolution by binning among pixels for increasing acquisition speed. The samples were inside of a polystyrene 10 mm rectangular cuvette, and were fluidized by an upwards homogeneous fluid flow. The flow was generated by a syringe pump (Harvard Apparatus PHD-ULTRA 4400 combined with a 100 ml Hamilton GasTight syringe) that pumped a fluid at a constant rate. In order to ensure a homogeneous fluid, the pumped fluid passed through a reservoir and a distributor before entering the sample [150]. Sedimentation was avoided by an increased and constant pump speed of 2000  $\mu\text{l}/\text{min}$  and 1500  $\mu\text{l}/\text{min}$ . These pump speeds were chosen as we found they produced a constant and steady fluidization that was successfully captured.

The sedimentation experiments consisted in studying the kinetics of sedimentation from a suspension of spherical glass granulates. This was realized after the cessation of the fluidization of the suspension. We controlled the different starting fluidization states by selecting different pump speeds from our fluidized bed setup, ranging from 300  $\mu\text{l}/\text{min}$  to 750  $\mu\text{l}/\text{min}$ . The fluidization led to an expanded initial state of the fluidized bed, where bigger pump rates translated in larger expansions, thus smaller particle volume fractions were achieved. This, allowed us to prepare different volume fractions ( $\phi$ ), estimated via Eq.(162) with the correspondent beam hardening effective attenuation coefficient [151]. Our estimation led to volume fractions in the range of (0.55–0.45). For more experimental details, please refer to [149].

X-ray radiographs consist of transmission images obtained from radiating a sample with X-rays produced from an X-Ray tube, then the transmitted X-rays are collected via a scintillator coupled to a CCD camera in order to digitalize the produced image. The images were obtained by radiating the granular samples using an XWT-160-TCHE Plus X-ray tube with a tungsten transmission target, it worked under an acceleration voltage of 80 kV and an anode current of  $550 \mu\text{A}$ . The transmitted X-rays were detected by a PerkinElmer DEXELA 1512 flat panel detector [152], which produced a 14 bit images consisting of  $1944 \times 1536$  pixels. The image acquisition setup was configured to capture consecutive frames at a rate of 26.31 FPS, each with an average pixel size of  $9.74 \mu\text{m}$ . In addition, due to the size of the detector, we have selected and analyzed regions of the image corresponding of signal coming within the sample cell. An example of the type of radiographs used in this work is shown in Fig.35. The left panel shows an experimentally acquired one, where the selected region of interest is enclosed within the white square, the middle panel corresponds to the close up from the analyzed region of interest and the right panel represents a generated synthetic radiograph produced from the following description.

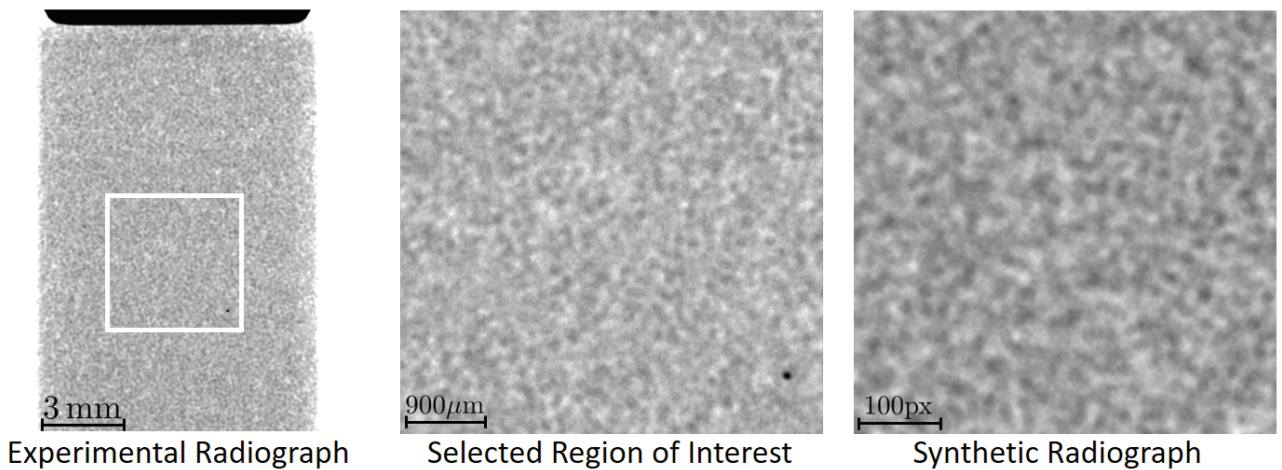


Fig. 35: Examples of the type of radiographs used in this work. The left panel depicts an experimentally obtained radiograph. Due to the sensor size, a small region of interest (ROI) was selected and analyzed (indicated by the white square). The middle panel shows the selected ROI. The right displays a synthetic radiograph generated by modeling the beam hardening of X-Rays passing through a granular sample using computer simulated particle positions.

The radiograph image content is obtained by taking into account the change of the X-ray spectrum due to beam hardening over the whole traveled path of the photons ( $z$ ). This is described by the effective Beer-Lambert law via an effective attenuation coefficient  $\mu_{\text{eff}}$  [151, 153], that depends on the energy spectrum of the radiation source, material composition, and on the sensitivity of the detector. Hence, the attenuated measured X-ray intensity  $I(z)$  for a given pixel is given by,

$$I(z) = I_0 \exp[-\mu_{\text{eff}}(z)z] \quad (162)$$

$I_0$  corresponds to the incoming X-Ray intensity. For a material with homogeneous

chemical composition, the radiographs provide a local measurement of the bulk density of the medium averaged over the path of the ray [145], i.e a projection. Our simplified synthetic X-ray radiographs were generated from a time series of particle positions from computer simulations, where parallel X-ray beams traveled in straight lines across the whole sample. The  $z$  coordinate was defined along the X-ray propagation path, additionally we have considered a constant value of  $\mu_{\text{eff}}$  and no detection smearing effects. Those rays are imagined to impinge on all of the particles in their propagation path, and only the transmitted ones are then projected onto a plane resulting in a landscape of penetration lengths for the whole particle system. The X-ray trajectory was added up linearly over the result of overlapping particles. Finally, the path length per particle was computed using a mask that accounted for the particles spherical shape. For more details please refer to [149].

### Digital Fourier Analysis

Digital Fourier Analysis (DFA) or Differential Dynamic Algorithm (DDA) [7, 72] is an analysis scheme applied to images that represent a density map of the studied sample. It provides information on the spatio-temporal density fluctuations in the spatial reciprocal space, obtaining information as in a static (SLS) and dynamic light scattering (DLS) experiments. DFA is performed as follows. First, record a series of  $N$  images denoted by  $i(\mathbf{x}, t_k)$ , where  $\mathbf{x}$  represents the position,  $t_k = k\Delta t$ ,  $\Delta t = 1/\text{FPS}$ , with FPS the sampling rate,  $k \in \mathbb{N}$ ,  $k \leq N$ . Resulting in the maximum acquired time  $t_N = N\Delta t$ . Then, calculate the fluctuating signal as,

$$\Delta i(\mathbf{x}, t, \tau) = i(\mathbf{x}, t + \tau) - i(\mathbf{x}, t) \quad (163)$$

which accounts for the difference between two images separated by a delay time  $\tau = p\Delta t$ ;  $p \in \mathbb{N}$ , and  $p \leq N - 1$ . This is followed by obtaining the power spectrum of the fluctuating signal, which is calculated by a discrete Fourier transform. The result is an image denoted by  $\mathcal{T}_{\text{rs}}(\mathbf{Q}, t, \tau)$ ,

$$\mathcal{T}_{\text{rs}}(\mathbf{Q}, t, \tau) = |\mathcal{F} [\Delta i(\mathbf{x}, t, \tau)]|^2. \quad (164)$$

where  $\mathbf{Q}$  is the image wave vector. Its magnitude is discretized by  $Q = n\Delta Q$ , with  $\Delta Q = 2\pi/L$ ,  $L$  is the image size and  $n$  the pixel number [7, 54, 75]. Special care has to be taken while performing the numerical Fourier transform in order to avoid spectral leakage, which occurs when image inhomogeneities are present in the borders of the image. To overcome this, a careful window scheme should be applied [74]. Finally, for signals that can be considered stationary, the signal statistics and hence the power spectrum do not depend on the start time  $t$ . An average over  $t$  is performed, obtaining the time averaged structure function  $D(\mathbf{Q}, \tau)$  [75],

$$D(\mathbf{Q}, \tau) = \langle \mathcal{T}_{\text{rs}}(\mathbf{Q}, t, \tau) \rangle_t. \quad (165)$$

This is related to the real part of the intermediate scattering function (ISF),  $f(\mathbf{Q}, \tau)$  via [7],

$$D(\mathbf{Q}, \tau) = A(\mathbf{Q}) [1 - f(\mathbf{Q}, \tau)] + B(\mathbf{Q}) \quad (166)$$

where the ISF captures the temporal density-density correlations in the spatial Fourier plane. The term  $A(\mathbf{Q})$  describes the static power spectrum of the signal, and it is mainly composed by three terms,

$$A(\mathbf{Q}) \sim T(\mathbf{Q})P(\mathbf{Q})S(\mathbf{Q}). \quad (167)$$

$T(\mathbf{Q})$  takes into account the modulated transfer function of the imaging system. The terms  $P(\mathbf{Q})$  and  $S(\mathbf{Q})$  are analogous to the form and structure factor obtained from static light scattering, as they are the power spectrum of the individual imaged object, and the Fourier transform of the spatial correlation among the imaged objects. Finally,  $B(\mathbf{Q})$  is the power spectrum of the detection noise.

Numerically,  $A(\mathbf{Q})$  and  $B(\mathbf{Q})$  were estimated according to the following procedure, the background term  $B(\mathbf{Q})$  was approximated from an average of all  $D(\mathbf{Q}, \tau)$  determined at short delay times and large enough  $\mathbf{Q}$  values that, due to the limited spatial resolution of the imaging set-up, they barely contain information of the system but rather of the background [36, 50]. Additionally, we have assumed  $B(\mathbf{Q})$  to be constant for all  $\mathbf{Q}$  values. Thus,

$$B(\mathbf{Q}) \simeq B'(\mathbf{Q}) = D(\mathbf{Q} \rightarrow \mathbf{Q}_{\max}, \tau \rightarrow 0). \quad (168)$$

Having estimated  $B(\mathbf{Q})$ ,  $A(\mathbf{Q})$  was determined from the long-time decorrelation plateau, as  $D(\mathbf{Q}, \tau \rightarrow \infty) = A(\mathbf{Q}) + B(\mathbf{Q})$ . Finally, the Intermediate scattering function can be obtained via the following equation,

$$\beta(\mathbf{Q})f(\mathbf{Q}, \tau) = \frac{D(\mathbf{Q}, \tau \rightarrow \infty) - D(\mathbf{Q}, \tau)}{D(\mathbf{Q}, \tau \rightarrow \infty) - B'(\mathbf{Q})}, \quad (169)$$

where  $\beta(\mathbf{Q}) \simeq 1 - [B(\mathbf{Q}) - B'(\mathbf{Q})] / A(\mathbf{Q})$ . The value of  $\beta(\mathbf{Q})$  reflects the signal to noise ratio, and the accuracy of the estimation of  $B(\mathbf{Q})$ . Hence, in order to achieve  $\beta(\mathbf{Q}) \simeq 1$ , a high signal to noise ratio has to be met i.e.  $A(\mathbf{Q}) \gg B(\mathbf{Q})$ , and  $B'(\mathbf{Q}) \simeq B(\mathbf{Q})$ .

The expression for  $f(\mathbf{Q}, \tau)$  depends on the type of motion projected in the direction of the scattering wave vector  $\mathbf{Q}$ . For a system that undergoes random motion and a distribution of collective motion,  $f(\mathbf{Q}, \tau)$  takes the following (Sec.2.7):

$$f(Q, \tau) = \exp \left[ -Q^2 D\tau - \frac{1}{2} Q^2 \delta_v^2 \tau^2 \right] \cos(Q \langle v \rangle \tau) \quad (170)$$

where  $D$  is the diffusion coefficient from the random motion,  $\langle v \rangle$  is the mean directed velocity, and  $\delta_v$  is the standard deviation of the velocity distribution

from the directed motion. The corresponding characteristic times are given by  $\tau_D(Q) = 1/DQ^2$  for the diffusive time scale,  $\tau_{\delta_v}(Q) = \sqrt{2}/Q\delta_v$ , and  $\tau_{\langle v \rangle}(Q) = 1/Q\langle v \rangle$  for the velocity deviations and mean velocity characteristic times respectively. Noting the  $Q$  scale dependence for the type of dynamics described, having  $Q^2$  dependence for random motion as  $1/Q^2 \sim L^2 \sim D\tau$ , and  $Q$  for directed motion, where  $1/Q \sim L \sim \langle v \rangle\tau$ . Hence, by using the  $Q$  dependence it is possible to determine the nature of the motion. Furthermore, the  $Q$  range "selects" which type of motion dominates or can be particularly determined.

In the following section, we tested X-DFA on synthetic radiographs from computer simulations, where each term of Eq.(170) was calibrated. This was achieved by changing the type of dynamics in each simulation series, having simulated mean directed motion, directed motion with a distribution of velocities, random motion, and a superposition of all of the above.

### 4.6.2 X-DFA on Synthetic Radiographs

In the following, we show the analysis of four series of 10,000 synthetic radiographs, each of size  $512 \times 512$  pixels. The synthetic radiographs were image plane projections from our idealized model of the beam hardening of X-rays. The hardening arises from the wavelength-dependent attenuation of passing X-rays through particle configurations. The particle configurations consisted of three-dimensional particle coordinates, each having a particle diameter of 19 pixels.

The four series of radiographs consisted of different types of particle dynamics, they were fixed through the equation of motion from each simulated particle. Our results are shown in Fig.36 and they are organized as follows, each row of the main figure summarizes the information per type of dynamics. We have simulated, mean directed motion (A), directed motion with a distribution of velocities (B), random motion (C), and a combination of all of the above (D). Furthermore, the first column contains the information regarding the simulation properties, and for corroboration purposes results from PIV. The second column contains the obtained  $f(Q, \tau)$  for different wave vectors  $Q$  from our X-DFA analysis. Finally, the extracted characteristic times from fitting  $f(Q, \tau)$  with the corresponding analytical model is shown in column three. The table of Fig.36 shows the analytical model of  $f(Q, \tau)$  and its characteristic times  $\tau_c(Q)$  describing each of the mentioned type of dynamics.

As first example, we show results of directed motion in Fig.36A. This type of motion is defined for systems in which all particles move with an identical constant velocity  $v$ . In the following, we fixed each particle velocity along the vertical axis of the image to be  $\langle v \rangle = 2.00$  px/frame. The imposed single velocity is modeled as a delta distribution, and it is shown as the red line in Fig.36A-1.

In order to verify the imposed velocity in the resulting radiographs, we performed PIV analysis. It was made using a software package known as PIVlab [154]. We selected an image separation of 5 frames, this translates into a 10 pixel displacement, ensuring enough particle displacement in order to be correctly detected [155,156]. The gray histogram in Fig.36A-1 corresponds to a frequency count from the results coming from all of the probed interrogation windows and images analyzed with PIV, it is hardly visible as it superimposes to the one from the simulation. In addition, a small region of interest from the original synthetic radiographs including the arrows from the PIV analysis is shown as an inset in Fig.36A-1. From the PIV analysis we obtained an average mean velocity of 1.99px/frame, matching perfectly with the one introduced in the computer simulation. Hence, the input information in the simulation is properly projected onto the synthetic radiographs and measured by PIV.

We proceeded to perform X-DFA and obtained the intermediate scattering functions  $f(Q, \tau)$  for different wave vectors  $Q$ . As we are interested in the directed motion dynamics, we selected and azimuthally averaged  $Q$  values parallel to  $\langle \mathbf{v} \rangle \pm 5^\circ$ , leading to a smearing of at most 2%. These results are presented in Fig.36A-2, where the  $f(Q, \tau)$  from all of the wave vectors show an oscillatory behaviour. The analytical expression of  $f(Q, \tau)$  is given by the cosine function written in the (A) entry of the table in Fig.36. Moreover, all  $f(Q, \tau)$  overlap onto a master curve in a  $\tau Q$  scale, this is expected for particles undergoing ballistic motion. Finally, we extracted the characteristic times  $\tau_{\langle \mathbf{v} \rangle}(Q)$  by performing a numerical fit of the analytical expression to each of the obtained data. Results are shown in log-log scale in Fig.36A-3, the value of  $-1$  from the slope corroborates the  $Q$  scaling, and from the intercept the value  $\langle \mathbf{v} \rangle = 1.99$  px/frame was obtained. The obtained value agrees with the PIV and the simulated values, thus validating the X-DFA analysis for extracting information from a mean directed motion.

We continue by showing our second example of dynamics, a directed motion with a distribution of velocities (Note that although we consider a distribution of velocities, the spheres are still assumed to all have the same size). The summary of these results are shown in row (B) of Fig.36. We chose a normal distribution of velocities and randomly assigned them to each particle in the simulation, having fixed the mean velocity  $\langle \mathbf{v} \rangle = 2.00$  px/frame, and the standard deviation of the distribution  $\delta_v = 0.4$  px/frame. This is represented as the red line in Fig.36B-1. As before, we proceeded to perform a PIV analysis of our synthetic radiographs. An illustration of the velocity map in a small ROI is shown as an inset in Fig.36B-1, along with the corresponding frequency count from all of the interrogation windows and images analyzed (shown in grey).

We have recovered the input value from the computer simulation, obtaining  $\langle \mathbf{v} \rangle = 1.98$  px/frame. However, the width of the velocity distribution was not correctly obtained. This can be explained by considering how the dynamical information in the image was constructed and determined. As we have randomly assigned to each individual particle a velocity, each region of interest represents a small sampling region from the overall distribution. The PIV analysis obtains the mean displacement per region. Hence, the frequency count from PIV only represents a spatially smoothed mean displacement, and does not contain the full range of relative motion [155].

It is worth mentioning that, in order to be able to obtain the full three dimensional velocity distributions using PIV, the images should be obtained using a different type of image configuration, such as the one from light sheet PIV or stereoscopic PIV [155]. Furthermore, ideally, the particle concentration and optical resolution should be such that each interrogation window of the PIV analysis contains single-particle information, as opposed to the 'extended' and projected 3D information

of the radiographs. Nevertheless, in real flow experiments or sedimentation experiments, the velocity distribution can be spatially heterogeneous [138, 145]. Thus, a PIV analysis can yield the fluctuations from a velocity distribution per analyzed interrogation window.

To continue the analysis, we performed X-DFA using the same criteria as before. The obtained  $f(Q, \tau)$  are shown in Fig.36B-2. Here, two features from the previous case are present: the first one, is the oscillatory behaviour of  $f(Q, \tau)$ . The second one, is the collapse to a master curve for all of the wave vectors in the ballistic  $\tau Q$  scale. In contrast, the amplitude of the oscillation is found to be damped. This is characterized by the exponential decay expressed in the (B) entry of the lower table of Fig.36, as it is the result from the relative to the mean motion from the particle velocity distribution 4.4. Moreover, we numerically fitted the analytical expression and obtained the two corresponding characteristic times (plotted in Fig.36B-3). These results confirm the ballistic  $Q$  scaling by having a  $-1$  slope for both characteristic times, and with the intercept value we estimated  $\langle v \rangle = 1.99 \text{ px/frame}$ ,  $\delta_v = 0.39 \text{ px/frame}$ . The obtained values are in perfect match with the input ones from the computer simulation, proving even further the validity of X-DFA to capture velocity deviations. In addition, it also illustrates the complementary information from a Fourier analysis to a real space correlation one like PIV. As it is able to easily describe not only the average mean motion, but also the relative motion to it.

Random motion is the third example of particle dynamics that we show. For our context we considered it exactly as colloidal Brownian motion or free diffusion. The summary of these results are shown in row (C) of Fig.36. In our case, the system is freely diffusive with a diffusion coefficient  $D = 0.781 \text{ px}^2/\text{frame}$  (red line Fig.36C-1). This type of particle dynamics is not usually quantified via PIV, as it rather tends to be included in the PIV description to estimate its contribution to the error of detecting directed motion [155]. For our purposes, we computed it only to illustrate the randomness of the motion within a small ROI from the synthetic radiographs (inset Fig.36C-1). Random motion is well known to be studied using DFA, as it was the first type of motion studied using Differential Dynamic Microscopy (DDM), and other type of techniques from Digital Fourier Microscopy (DFM) [7]. This type of particle dynamics has a  $\tau Q^2$  scaling as the main feature of  $f(Q, \tau)$ , leading to a collapse onto a master curve for all of the  $Q$  values. It can be seen in our results of X-DFA in Fig.36C-2. In addition, as the motion is homogeneous and isotropic, a full azimuthal averaging in the power spectra can be performed to improve statistics. The theoretical expression of  $f(Q, \tau)$  for random motion is an exponential decay, having a  $Q^2$  dependence on the characteristic decay time. The analytical expression, and the characteristic time is shown in the panel (C) of the lower table of Fig.36.

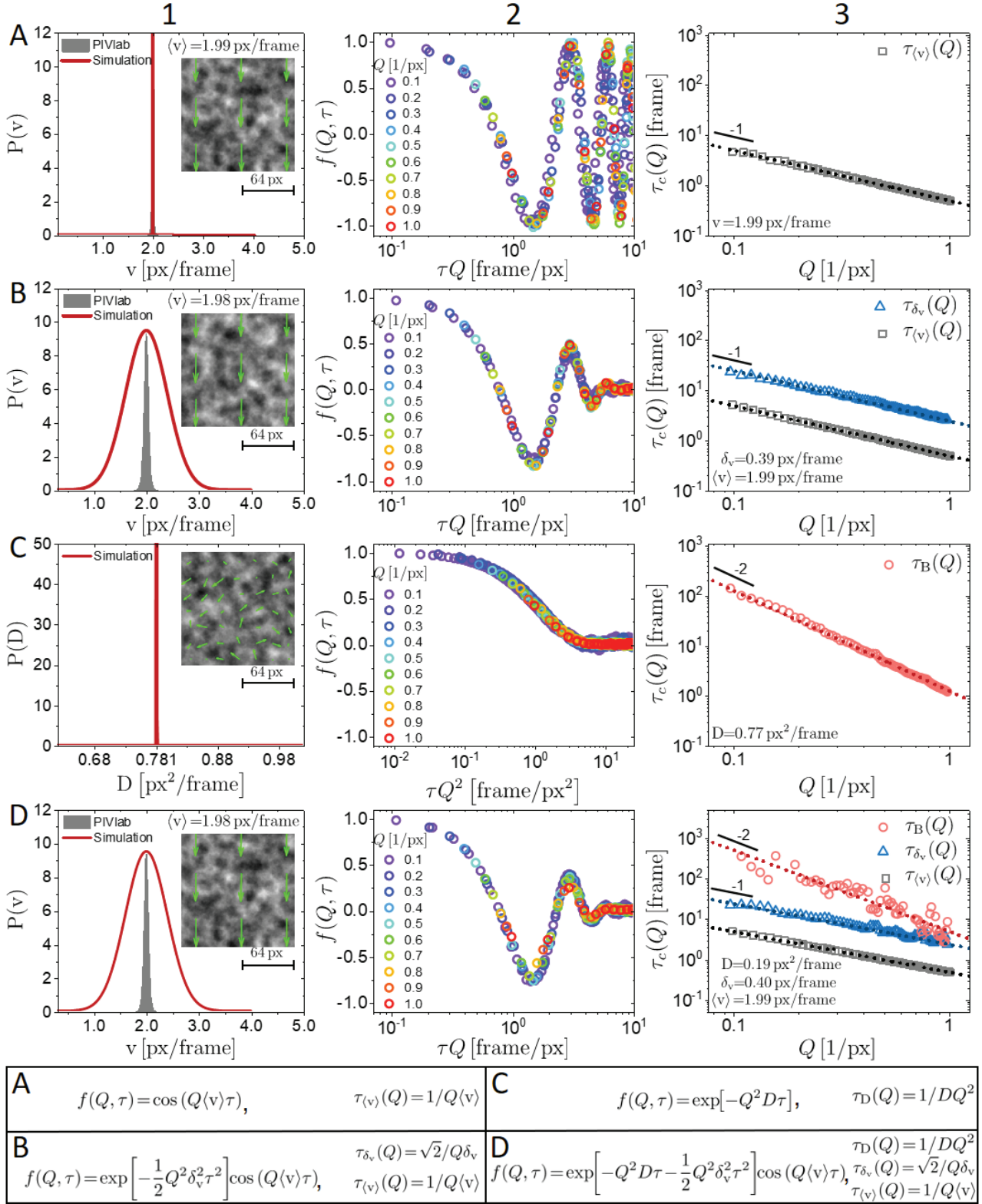


Fig. 36: Results obtained from the four series of synthetic radiographs, they consisted of different types of particle dynamics. The information per type of dynamics is summarized in each row of the main figure. Row (A) contains results from homogeneous directed motion, (B) from a directed motion with a distribution of velocities, (C) from random motion, and (D) from a combination of all of the above. Furthermore, column (1) contains the information regarding the simulation properties and a region of interest from our synthetic radiographs. For corroboration purposes, results from PIV are included. Column (2) shows the obtained  $f(Q, \tau)$  for different wave vectors  $Q$  from our X-DFA analysis. Finally, the extracted characteristic times from fitting  $f(Q, \tau)$  with the corresponding analytical model is shown in column (3). The lower table shows the analytical model of  $f(Q, \tau)$  that describes each of the mentioned types of dynamics, along with its corresponding characteristic times  $\tau_c(Q)$ .

We proceeded to fit all of the computed  $f(Q, \tau)$  with the analytical model, obtaining the characteristic Brownian times  $\tau_B(Q)$ . The results are shown in Fig.36C-3, and for this case, they show a slope of  $-2$ . The latter corroborates the diffusive scaling of the dynamics and from the intercept of Fig.36C-3 we obtained  $D = 0.77\text{px}^2/\text{frame}$ . The value is in very good agreement with the fixed value from the simulation, having a relative deviation of 1.5%. These results corroborate the validity of extracting random motion information via X-DFA, widening the applicability of the analysis to extract dynamical information of directed and random motion.

To conclude, we show the results from our fourth example. It is composed of a superposition of all of the above particle dynamics, i.e. a directed motion with a velocity distribution and a random motion. The random motion was described by a diffusion coefficient of  $D \simeq 0.19\text{px}^2/\text{frame}$ . This resulted in a Péclet number  $Pe = \langle v \rangle \sigma / D = 200$ . Systems with this Péclet number are mainly driven by the directed motion, while still having a very small contribution from the random motion [118], making this the perfect testing conditions to check the capabilities of extracting the dynamical information using X-DFA.

We proceeded the same way as before, thus the summary of the results are shown in row (D) of Fig.36. Here, the PIV analysis gives the same result as the distribution of directed motion from row (B) because the effect of the Brownian motion is small as quantified by  $Pe = 200$ . However, there are some differences for X-DFA (Fig.36D-2), a small shift can be appreciated in the first maximum of the oscillation at the overlapped  $f(Q, \tau)$  ( $\tau Q = 0.3$ ). This, is due to the additional damping term due to the random motion, where the complete theoretical description is composed of three terms: the first two are two damping terms, the random, and the relative to the mean motion from the velocity distribution. The third one is the oscillatory term from the mean directive motion. The full expression, and the corresponding characteristic times are written in panel (D) of the lower table from Fig.36. Following the same approach, we fitted the analytical expression to the extracted  $f(Q, \tau)$ , obtaining the three correspondent characteristic times (shown in Fig.36D-3). These have the corresponding slope according to the type of  $Q$  scaling from the nature of the dynamics, and from the intercept we estimated  $D = 0.19\text{px}^2/\text{frame}$ ,  $\langle v \rangle = 1.99\text{px}/\text{frame}$ , and  $\delta_v = 0.40\text{px}/\text{frame}$  respectively.

The very good agreement obtained by the X-DFA results and the simulated values confirms the conceptual framework of the analysis method, being able to extract complementary information to PIV, even when mixed dynamics are present, such as directed motion and random. Making X-DFA a powerful analysis scheme for obtaining information from X-ray radiographs.

Last but not least, we want to stress that the previous description was only about the dynamical information contained in the series of radiographs. In addition, static information can also be obtained as it is contained in the  $A(Q)$  term of Eq.(167) and in analogy to light scattering, observables like the particle size and particle size distribution can be extracted. This is valid if the expression of the power spectra is known. For radiographs, the analytical expression of the power spectrum of the absorbance image of a sphere leads to the same expression as the form factor of a sphere described by the Raleigh-Gans-Debye (RGD) description [37]. To illustrate it, we present in Fig.37 the comparison of a computed RGD form factor for monodisperse spheres of size  $\langle\sigma\rangle = 19\text{px}$ , with the  $A(Q)$  extracted from all our four different series of synthetic radiographs. The results show a perfect agreement, thus validating the use of the RGD description as an analogous for the power spectrum of the absorbance image of a sphere. This result wideness the output information from X-DFA, making it capable to characterize spherical granulates average size and estimate the sample polydispersity.

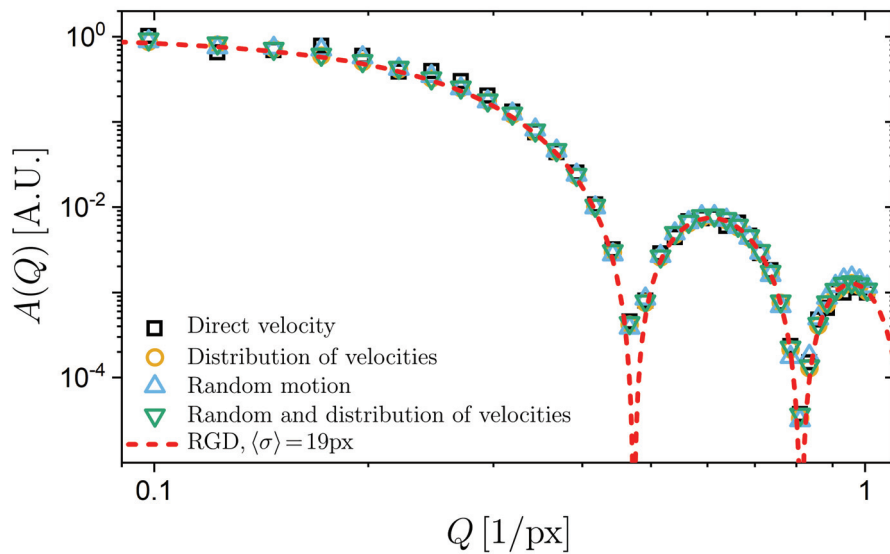


Fig. 37: Comparison of the RGD form factor of  $\langle\sigma\rangle = 19\text{px}$  spherical particle (red dashed line), with the extracted  $A(Q)$  from all of the different simulation examples (symbols).

In the following section we exploited the capabilities of X-DFA in two experimental conditions. We have used it to study sedimentation of granular suspensions and to characterize the fluidization of a liquid granular bed.

### X-DFA on Sedimentation Experiments

The experiments consisted in studying the sedimentation of a suspension of spherical glass granulates. The granulates start to sediment after the cessation of the fluidization. We controlled the starting fluidization state by selecting the pump speed in the fluidized bed. The fluidization led to an expanded initial state of the fluidized bed, where bigger pump rates translated into larger expansions, thus smaller particle volume fractions. The measurement protocol consisted in preparing a fluidized phase to homogenize the system, then stopping the fluidization and starting the image acquisition. An example of the acquired images can be seen in the middle panel of Fig.35. The field of view of the images was bigger than the cuvette containing the granular suspension, thus a small ROI of  $900 \times 300$  pixels of the acquired images was selected for analysis. The width was chosen to cover the majority of the cuvette width neglecting the borders to only observe bulk sedimentation. The height was chosen large enough to capture as large as possible a sedimentation column passing through the selected region, thus increasing the time of the experiment.

To illustrate our results, we show the obtained data from the cessation of fluidization of with a pump rate of  $750 \mu\text{l}$ . An example of the selected ROI is in the upper-left panel of Fig.38. The image analysis was performed as in the synthetic radiographs section. We analyzed the selected ROI using PIV and X-DFA. The PIV analysis was performed following the same protocol as before, selecting a temporal separation of the images of  $0.72 \text{ s}$ . Contrary to the simulation results, some velocity differences over the ROI can be observed in the velocity map, namely slight changes in the orientation of some of the arrows in the velocity map (green arrows Fig.38). Hence, we conclude that the velocity distribution is spatially heterogeneous as previously seen in experiments [148]. This can additionally be quantified.

To quantify the velocity distribution, we computed a frequency count over the projected vertical velocity for all interrogation windows and images, and obtained an estimate of the velocity distribution  $P(v)$  by normalizing the frequency count. The result is shown in grey in Fig.38. Furthermore, suggested by the shape of the distribution, we fitted a normal distribution and obtained an average velocity  $\langle v \rangle = 130.6 \mu\text{m/s}$  and velocity fluctuations captured by the standard deviation  $\delta_v = 12.5 \mu\text{m/s}$ .

For the X-DFA analysis, we divided the ROI into three subsections of  $300 \times 300$  pixels, as it is convenient to use square images for the numerical Fourier transform (FFT). We processed them individually and averaged the 2-D structure functions. The result is a spatially averaged  $D(\mathbf{Q}, \tau)$ . Then, we extracted

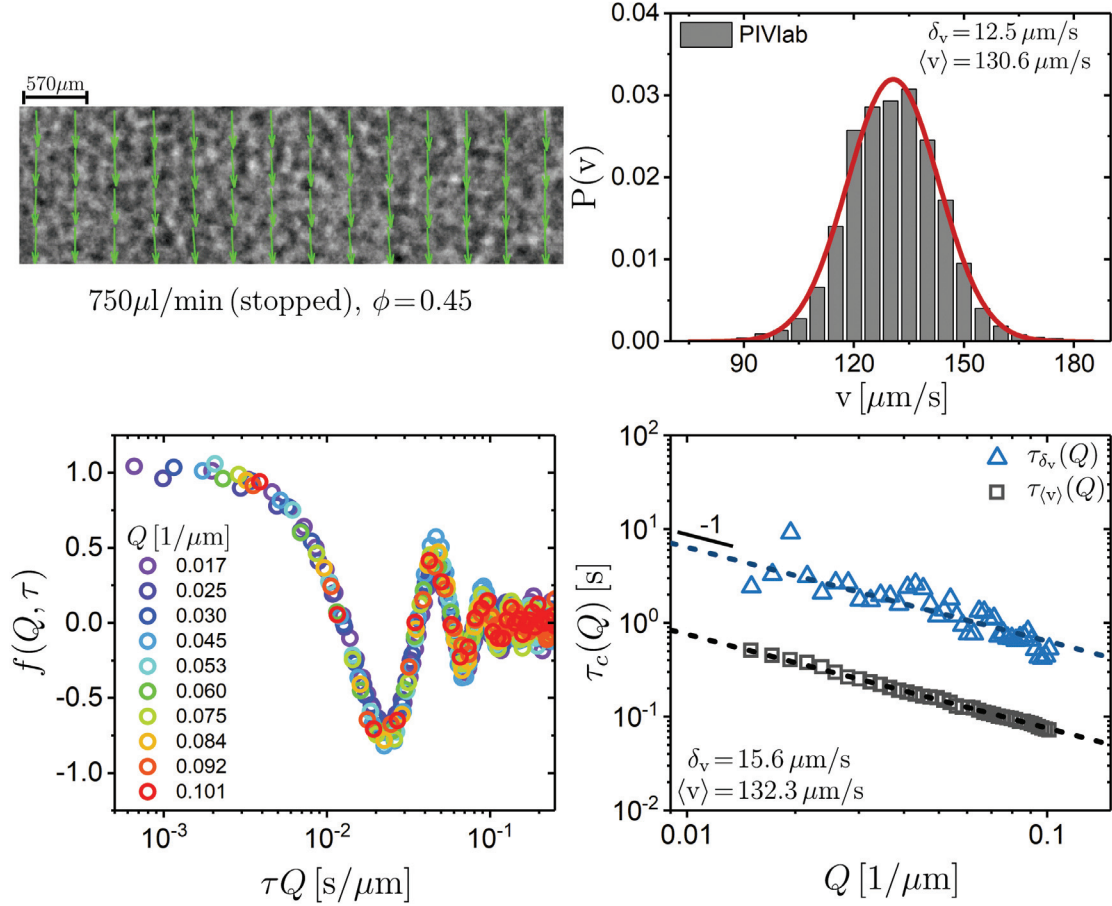


Fig. 38: Summary of the obtained results using PIV and X-DFA for the cessation of fluidization with a pump rate of  $750 \mu\text{l}$ . The upper-left panel shows an example of an analyzed ROI that covers the majority of the cuvette's width ( $900 \times 300$  pixels). The slightly different orientations of the arrows indicate a spatially heterogeneous velocity distribution captured by the PIV analysis. The upper right panel shows the quantification of the velocity distribution, obtained by the normalized frequency counts of the vertical components of all obtained velocities from interrogation windows and images. The lower-left panel shows the spatially averaged intermediate scattering functions obtained from X-DFA. The presented  $Q$  range covers the majority of the length scales contained in the image. The lower-right panel shows the extracted characteristic times from fitting the analytical model of  $f(Q, \tau)$  for directed motion with a distribution of velocities.

the corresponding azimuthally averaged  $f(Q, \tau)$ , for  $\mathbf{Q}$  oriented along the vertical axis  $\pm 5^\circ$ . The results are shown in  $\tau Q$  scale in the lower-left panel from Fig.38, showing a collapse of all the extracted  $f(Q, \tau)$  onto a master curve, as expected for directed motion dynamics.

Finally, we extracted the characteristic times  $\tau_{\langle v \rangle}(Q)$ ,  $\tau_{\delta_v}(Q)$  by fitting the corresponding analytical expression of  $f(Q, \tau)$  (panel B of the table in Fig.36). These are shown as open symbols in the lower-right panel of Fig.(38). The dashed lines indicate linear regressions to the characteristic times, both with a slope of -1, and from the intercept  $\langle v \rangle = 132.3 \mu\text{m/s}$  and  $\delta_v = 15.6 \mu\text{m/s}$  were obtained. The results led to a very good agreement between PIV and X-DFA, hence validating this analysis method and confirming the finding in the synthetic radiographs section.

We also performed experiments for other volume fractions prepared by applying

different pump speeds. Those experiments were subsequently analyzed by PIV and X-DFA as described above. The obtained  $\langle v \rangle$  and  $\delta_v$  for the different explored  $\phi$  are shown in Fig.39 as open symbols and error bars respectively.

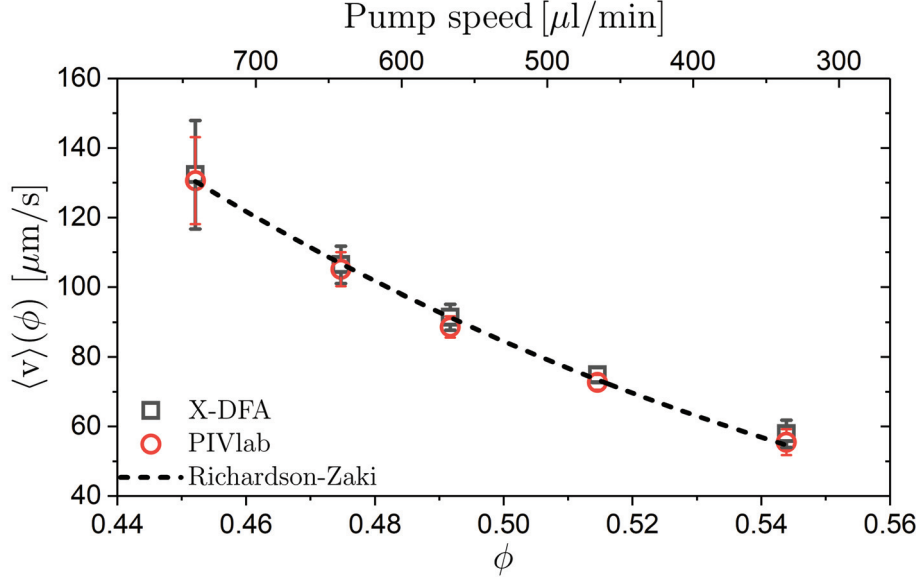


Fig. 39: Obtained mean sedimentation velocity  $\langle v \rangle$  (open symbols) and  $\delta_v$  represented as error bars for the different explored volume fractions  $\phi$  or pump speeds using X-DFA (squares) and PIV (circles) for the cessation of fluidization experiments. The dashed line represents the calculation of the Richardson-Zaki expression without any free parameters.

The mean settling velocity  $\langle v \rangle$  is seen to decrease as a function of  $\phi$ . This trend is in perfect agreement with the Richardson and Zaki expression [157, 158] without any free parameters (dashed line in Fig.39). The expression  $\langle v \rangle(\phi) = v_s(1 - \phi)^n$  was obtained by Richardson and Zaki to describe the settling velocity of granulate suspensions with different volume fractions. In this expression,  $v_s = \Delta\rho g \sigma^2 / 18\eta$  is the Stokes settling velocity,  $\Delta\rho = \rho_p - \rho_s$  the density difference between the particles and the solvent,  $\eta$  the kinematic viscosity of the solvent, and  $\sigma$  the particle diameter. The expression of the exponent  $n$  was found to be  $n = 4.35\text{Re}^{-0.03}$  with the Reynolds number  $\text{Re} = \rho_s v_s \sigma / \eta$ . The values of our experimental system result in  $n \sim 4.74$ ,  $\text{Re} \sim 0.0556$  and  $v_s \sim 2264 \mu\text{m/s}$ . We have used  $\rho_p = 2.40\text{g/ml}$ ,  $\rho_s = 1.14\text{g/ml}$  at 298K and from the analysis of  $A(Q)$ , the value  $\sigma = 153 \mu\text{m}$  was obtained (left panel Fig.40). The very good agreement between the Richardson-Zaki expression with the PIV and X-DFA proves the validity of our experimental procedure, thus enabling us to characterize the sedimentation of granulars by two different analysis methods applied to the X-Ray radiographs in the real and in the Fourier space. In addition,  $\delta_v$  has been determined. It is larger for the smallest volume fraction ( $\phi = 0.45$ ) and decreases as the volume fraction increases. This can be explained by the smaller particle density which provides more available space for fluctuations to occur.

Complementary to PIV, X-DFA allow us to extract static properties of the sam-

ple. These are form factor  $P(Q)$ , and structure factor  $S(Q)$ . We obtained them by the analysis of  $A(Q)$  using Eq.(167). We fitted the RGD polydisperse expression to match the large  $Q$  ( $Q > 0.45 \mu\text{m}^{-1}$ ) behaviour of  $A(Q)$ . This resulted in an estimate particle size  $\langle\sigma\rangle \approx 153 \mu\text{m}$  and coefficient of variation  $CV_\sigma = \delta_\sigma / \langle\sigma\rangle \sim 0.13$ . These results are in agreement with the manufacturers specification.

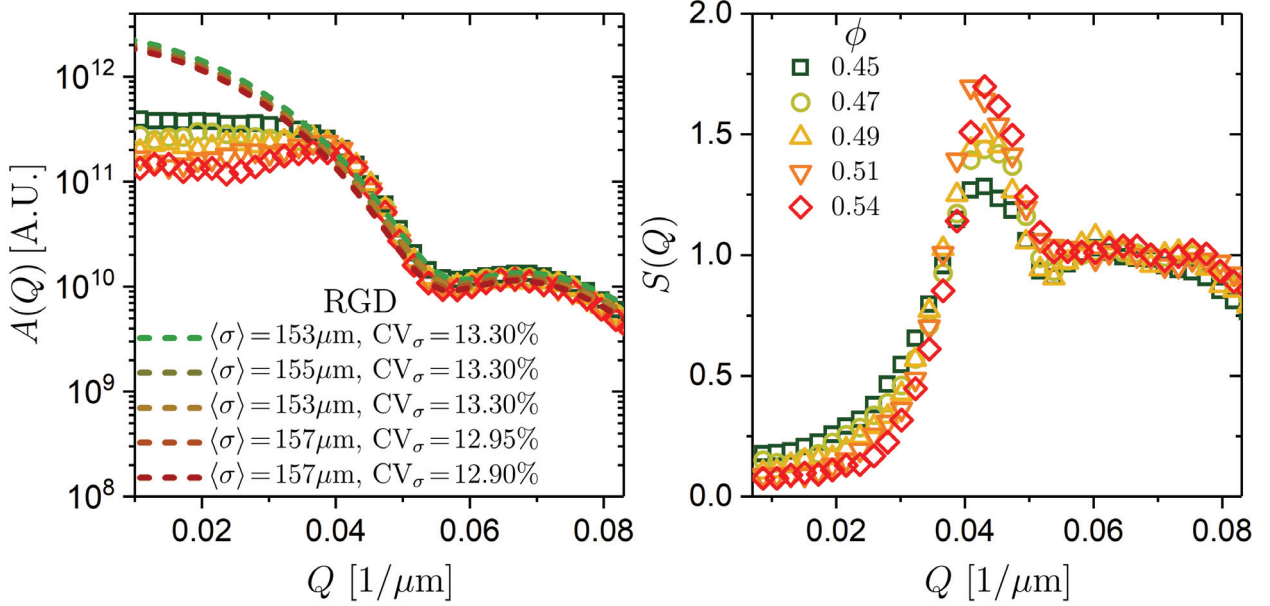


Fig. 40: X-DFA Analysis of the static properties. The left panel shows  $A(Q)$  as a function of the scattering wave vector  $Q$  for the different volume fractions ( $\phi$ ). The values of the mean particle size ( $\langle\sigma\rangle$ ) and the coefficient of variation ( $CV_\sigma = \delta_\sigma / \langle\sigma\rangle$ ) were obtained from fitting the polydisperse RGD to the large  $Q$  behaviour of  $A(Q)$  ( $Q > 0.45 \mu\text{m}^{-1}$ ). The right panel shows the extracted structure factor ( $S(Q)$ ) by the deconvolution of  $A(Q)$ . The different volume fractions are indicated.

We also obtained  $S(Q)$  by deconvolving  $P(Q)$  from  $A(Q)$  (shown in the right panel of Fig.40). The overall behaviour of  $S(Q)$  follows the same trend as expected for concentrated systems. It shows a peak at  $Q \sim 0.42 \mu\text{m}^{-1}$  for  $\phi = 0.45$ , which translates into a mean inter-particle distance  $\langle d \rangle = 2\pi/Q \sim 150 \mu\text{m}$ . That this value is slightly smaller than  $\langle\sigma\rangle$  and it is characteristic of polydisperse systems. Moreover, as the volume fraction increases, the position of the peak shifts to slightly large  $Q$  and the amplitude increases. Hence, the overall system becomes more tightly packed as the volume fraction increases, as expected.

### X-DFA on Fluidization Experiments

We furthermore exploited X-DFA to characterize the random dynamics of a fluidized state. For this set of experiments, we recorded two series of images that covered 5 minutes ( $1500 \mu\text{l}/\text{min}$ ) and 2.5 minutes ( $2000 \mu\text{l}/\text{min}$ ) of random fluidization correspondingly. We selected ROIs of  $512 \times 512$  pixels that were centered inside of the cuvette (as illustrated in Fig.35). To illustrate the dynamics, we performed PIV to obtain the velocity map. These are shown for reduced ROIs ( $256 \times 256$  pixels) in the left column of Fig.41, the arrow length represents the obtained velocity. Showing higher velocities for the  $2000 \mu\text{l}/\text{min}$  pump speed.

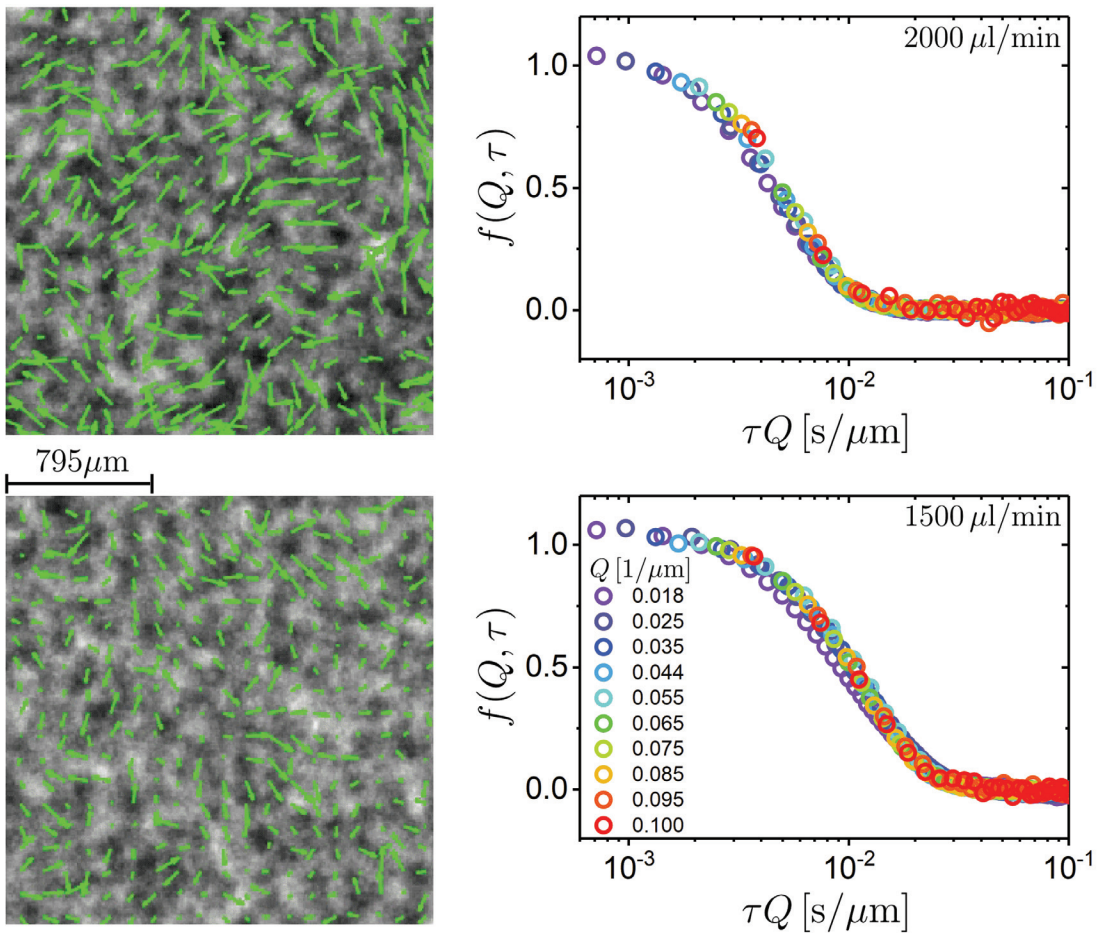


Fig. 41: Random motion during fluidization achieved by a pump speed of  $2000 \mu\text{l}/\text{min}$  (upper row) and  $1500 \mu\text{l}/\text{min}$  (lower row). The images in the left column represent a quarter of the original acquired images along with the velocity map that was computed using PIV. The right column shows the intermediate scattering function  $f(Q, \tau)$  obtained by means of X-DFA, showing a collapse onto a master curve for all of the extracted wave vectors  $Q$  in the  $\tau Q$  scale.

Supported by the randomness of the velocity map, the X-DFA analysis was performed as in the case of the random motion in the synthetic radiographs. We performed a full azimuthal average of  $D(\mathbf{Q}, \tau)$  and extracted the corresponding  $f(Q, \tau)$ . All of the extracted  $f(Q, \tau)$  scale with a  $\tau Q$  scale for both pump speeds. This scaling suggests that the dynamics are dominated by ballistic motion. The re-

sults are shown in the right column of Fig.41. Our results show similar behaviour as the ones obtained with sound scattering for systems running under similar conditions [135]. We characterized the sample dynamics by fitting to the data the intermediate scattering function given by Eq.(170) and setting the the average velocity to zero. This was used as it takes into account the ballistic term from the velocity fluctuations ( $\delta_v^2$ ) and a possible diffusion term (D). No significant contribution of the diffusion term was found, as the data was scattered without the characteristic  $Q^2$  scaling. Hence, we concluded that the only relevant term from Eq.(170) to describe the sample dynamics from our measurements is the exponential decay due to the velocity fluctuations.

The extracted characteristic times from the velocity fluctuations  $\tau_{\delta_v}(Q)$  are shown in Fig.42. For both experimental configurations a slope of -1 was found in log-log representation, thus validating the ballistic characteristics of the motion in the fluidized bed. We extracted the velocity fluctuation obtaining  $\delta_v = 108 \mu\text{m/s}$  for the  $1500 \mu\text{l/min}$  pump speed and  $\delta_v = 233 \mu\text{m/s}$  for the  $2000 \mu\text{l/min}$ . This is in agreement with the velocity map obtained with PIV, showing higher velocity fluctuations for the higher pump speed.

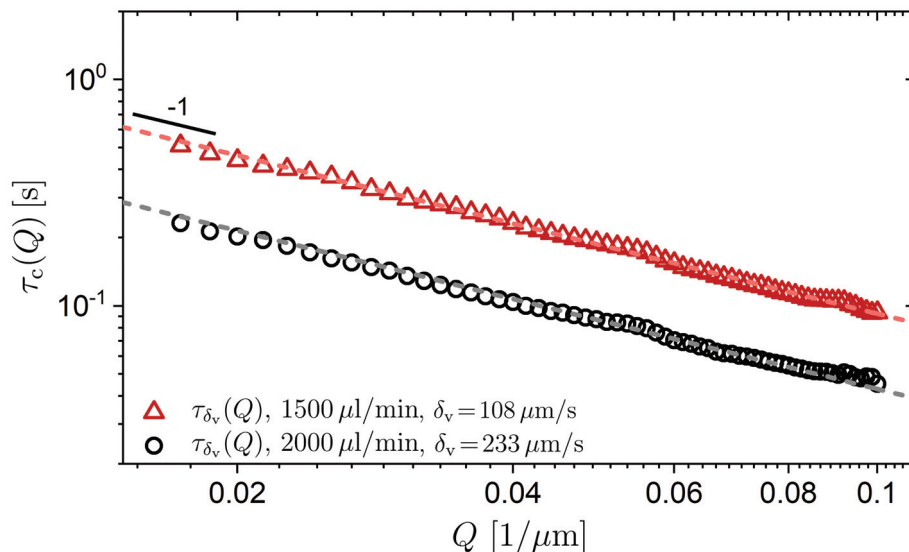


Fig. 42: Characteristic times  $\tau_{\delta_v}(Q)$  obtained by fitting the exponential decay term of the velocity fluctuations ( $\delta_v$ ) from Eq.(170) to the extracted intermediate scattering function  $f(Q, \tau)$ . The dash lines represent linear fits to  $\tau_{\delta_v}(Q)$ . The slope of -1 indicates ballistic dynamics, and from the intercept we estimated the velocity fluctuations (given in the legend).

Finally, we analyzed the statical properties contained in  $A(Q)$  for both pump speeds (Fig.43). We performed it in a similar manner as the sedimentation experiments, using the polydisperse RGD expression for the form factor to match the large  $Q$  behavior of  $A(Q)$ . We extracted very similar values as before,  $\langle \sigma \rangle = 153 \mu\text{m}$  and  $\text{CV}_\sigma = \delta_\sigma / \langle \sigma \rangle = 0.13$ . Furthermore, the deviations at smaller

$Q$  values are due to structure present in the sample, they are described by  $S(Q)$  and obtained by deconvolution of  $A(Q)$  (shown in the right panel of Fig.43). The results of  $S(Q)$  show a similar peak position as the sedimentation case. But in addition, they display a higher value for  $S(Q \rightarrow 0)$ . By recalling the relationship between the structure factor and the isothermal compressibility [15], we assume that this indicates the different compressibility state of the systems, showing a looser state for the fluidized experiments and a more compacted state for the sedimentation experiments (right panel Fig.41).

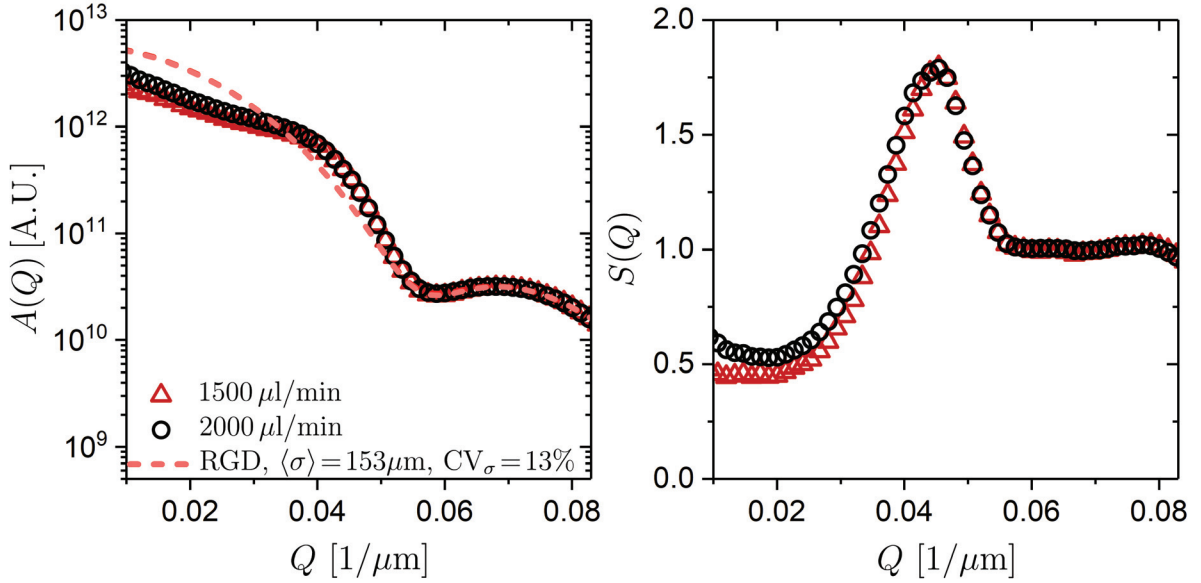


Fig. 43: X-DFA Analysis of the static properties. The left panel shows  $A(Q)$  as a function of the scattering wave vector and the mean particle size ( $\langle\sigma\rangle$ ) and coefficient of variation ( $CV_\sigma = \delta_\sigma / \langle\sigma\rangle$ ) obtained from fitting the polydisperse RGD to the large  $Q$  behaviour of  $A(Q)$  ( $Q > 0.45 \mu\text{m}^{-1}$ ) to the two different fluidization experiments. The deviations at smaller  $Q$  values are due to structure present in the sample, they are described by  $S(Q)$  and are obtained by deconvolution of  $A(Q)$ . The right panel shows the extracted structure factors ( $S(Q)$ ) for both fluidized experiments.

#### 4.7 Dynamics of sheared particles: Rheo-DFM

Rheology is the branch of physics that studies the flow of matter subjected to a macroscopic deformation [10]. Depending on its response, many mechanical properties such as viscosity, store ( $G'$ ) or loss ( $G''$ ) modulus, and other transient properties (relaxation, retardation) are defined [9]. In general, for soft systems, the dynamical viscoelastic response i.e. the system's ability to store or lose energy upon deformation, can be related to the system's micro-structure and the interaction among the constituents of the system [9, 159].

Macroscopic rheology of soft systems is mainly performed by rotational rheometers or shear cells [9]. These are instruments that enclose the system under a certain geometry to apply deformations using a controlled scheme. Some examples of geometries are parallel plates or cone-plate configurations, while for controlled schemes, the most common ones are constant and/or oscillatory deformation. Furthermore, microscopic information of soft systems is mainly studied via quantitative microscopy using particle tracking tools [11], or via scattering experiments [14]. Hence, the combination of macroscopic and microscopic experimental techniques becomes very useful for linking both properties of soft systems, enabling to study the internal microscopic structure while simultaneously undergoing through a macroscopic deformation.

Another experimental approach to study the dynamics of microscopic structures is Digital Fourier Microscopy (DFM) [7]. It is a framework based in combining optical microscopy images with a differential Fourier analysis. It allows to quantify density fluctuations in the spatial Fourier space, obtaining similar information as in Static Light Scattering (SLS) and Dynamic light scattering (DLS) experiments. The main advantage of DFM compared to particle tracking techniques is its computational simplicity for quantifying the dynamical information. And, in contrast to the relative dynamical information supplied by conventional far field light scattering, DFM provides information of the collective and relative motion. Hence, DFM is a suitable candidate for characterizing the imposed motion from a rheology experiment. In addition, when DFM is performed by means of confocal microscopy, the overall sample volume can be scanned. Thus, it is possible to quantify the imposed effect from a rheology experiment among different sections or layers of the system. The combination of both techniques, i.e. Rheology and Digital Fourier Microscopy, will be denoted as Rheo-DFM.

The purpose of this section is to illustrate the preliminary results of Rheo-DFM. It was employed to characterize the effect of a constant deformation made by a plate-plate shear cell to a colloidal suspension. It allowed us to quantifying the

imposed velocity profile across the sample gap, and from these results the shear rate ( $\dot{\gamma}$ ) was also obtained.

The shear cell consists of two parallel plates (top and bottom) separated by a gap size of about  $70\mu\text{m}$ . The plates have circular windows on each surface that are covered by glued coverslips. Thus, it is possible to image the sample contained between the plates. The motion of the plates is anti-parallel, this is achieved by precise displacements of the bottom plate by the push of a piezo actuator (PI Instruments, model P-841.6B). The motion is transferred to the upper plate by a lever with fixable height, its position allows to adjust the height of the zero velocity plane in the sample. In order to reverse the motion, two springs are attached at the opposite side of the upper plate. A further detailed description of the shear cell design and performance can be found in [106, 160–163].

The shear cell was coupled to a Nikon Ti-U inverted microscope, and the images were acquired using a Nikon A1R-MP confocal scanning unit. We have used a solid state laser ( $\lambda = 561\text{nm}$ ) as excitation source, and as collecting optics a 40X Nikon Plan Fluor microscope objective (NA=0.75). The confocal scanning unit was configured to record images at a rate of 60FPS. Each image had an optical depth of  $4\mu\text{m}$  and consisted of  $256 \times 256$  pixels, corresponding to a sample area of  $79.4 \times 79.4\mu\text{m}^2$ . With these scanning configurations, we acquired images for 10 sections separated by  $5\mu\text{m}$ , probing a total height of  $50\mu\text{m}$ . Finally, the constant deformation of the shear cell was controlled by supplying a 5V triangle signal to the piezo actuator controller. We set the frequency to be 0.05Hz, ensuring enough measuring time for forward and backward motion.

The studied sample consisted of a suspension of crossed-linked poly(methyl methacrylate) (PMMA) particles of diameter  $1.1\mu\text{m}$ . They were fluorescently labelled with monomerized methyl methacrylate rhodamine B, and were in-house synthesized based on previously established methods [107]. The particles were suspended in a (50:50)% V/V acrylic double matching liquid (Cargille Laboratories CAT: 19577) and Bromocycloheptane (97% Alfa Aesar CAT:B23110). We fixed the particle volume fraction to  $\phi = 0.2$ , this allowed us to have a enough signal in each of the acquired sections while avoiding any shear thickening effects due to concentration effects [9]. For the solvent mixture, we assumed a linear dependence of the refractive indexes and viscosities, leading us to estimate a theoretical refractive index of 1.499, matching the one of PMMA, and a theoretical viscosity value of  $150\text{mPa}\cdot\text{s}$ , this value allow us to safely neglect any contribution from Brownian motion. Hence, only shear-imposed dynamics were assumed to be sampled.

The experimental procedure was as follows, we loaded the particle suspension into the shear cell, making sure that no air bubbles were left inside. Then, the shear cell was turned on by using the same triangle shape signal, and it was left to run for the rest of the full experimental campaign. We waited for a period of 20 minutes in order to let the system stabilize, and by visual inspection with the confocal microscope, we located the stagnation point (zero velocity plane). This plane was labeled as zero height. We then focused the microscope at a distance of  $2\mu\text{m}$  above the bottom plate ( $-27\mu\text{m}$  from the stagnation point) and proceeded to record a series of 14,425 images. This number of images allowed us to record 13 full shear cycles. After completion, each of the next heights were focused and measured using the same number of images.

Prior to the DFM data analysis, we pre-processed each of the image series in order to obtain the starting and the ending of the effective image series that contained a constant displacement motion. This was achieved in a similar fashion as in Particle Image Velocimetry (PIV) [154–156], by tracking the displacement peak of the image correlation between frames separated 5 frames. A representation of the obtained displacement for different heights within the sample is shown in Fig. 44. It is shown for two shear cycles out of the 13 measured. The gray zone depicts the effective image series where only directional motion was found. Deviations of constant displacement are due to inertial effects coming from the flow reversibility imposed by the shear cell along the sample height.

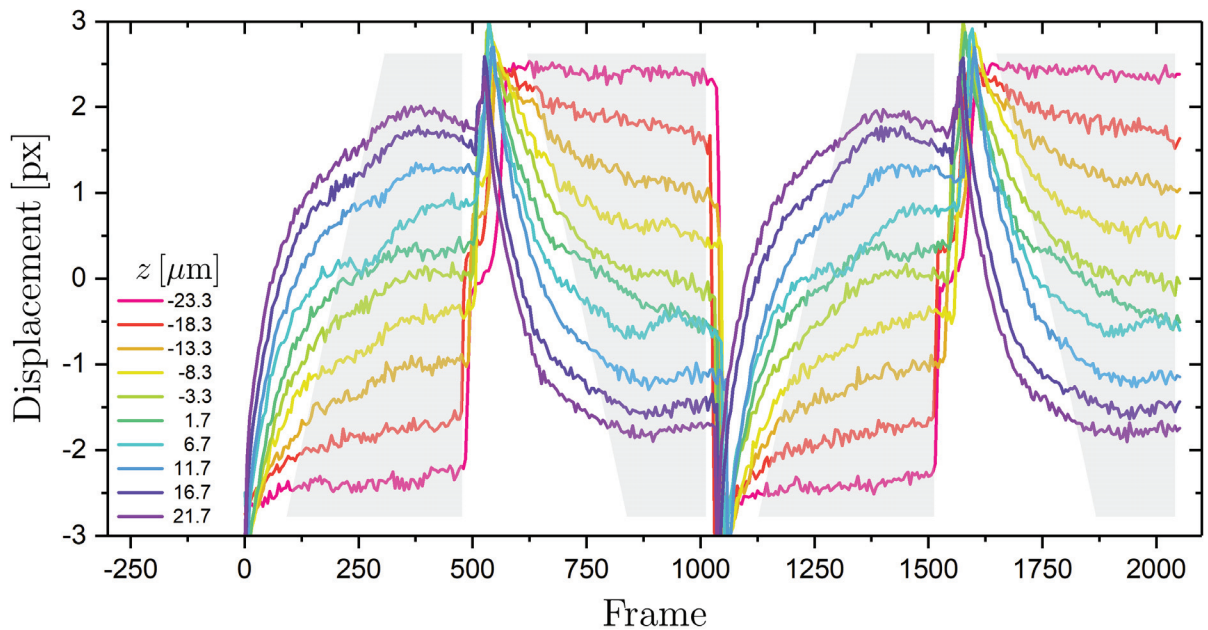


Fig. 44: Representation of the obtained displacements for different heights within the sample gap of the plate-plate shear cell geometry. Shown for two shear cycles out of the 13 measured. The gray zone depicts the effective image series where only directional motion was found.

Once the effective image series was found, we proceeded to analyze it using the DFM framework, starting by obtaining the fluctuating signal

$$\Delta i(\mathbf{x}, t, \tau) = i(\mathbf{x}, t + \tau) - i(\mathbf{x}, t) \quad (171)$$

which accounts for the difference between two images ( $i(\mathbf{x}, t)$ ) separated by a delay time  $\tau = m\Delta t$ , where  $m \in \mathbb{N}$ ,  $\Delta t = 1/\text{FPS}$ . Then, the power spectrum of the fluctuating signal is calculated and averaged over different starting times ( $t$ ), leading to the time averaged structure function

$$D(\mathbf{Q}, \tau) = \langle |\mathcal{F} [\Delta i(\mathbf{x}, t, \tau)]|^2 \rangle_t. \quad (172)$$

Where  $\mathbf{Q}$  is the scattering vector, and it is discretized as  $Q = n\Delta Q$ , having  $\Delta Q = 2\pi/L$ , where  $L$  is the image size and  $n$  the pixel number [7, 54]. Special care has to be taken while performing the numerical Fourier transform in order to avoid spectral leakage, it occurs when image inhomogeneities are present in the borders of the image. This can be overcome by applying a window scheme [74]. The structure function  $D(\mathbf{Q}, \tau)$  is related to the intermediate scattering function  $f(\mathbf{Q}, \tau)$  via,

$$D(\mathbf{Q}, \tau) = A(\mathbf{Q}) [1 - f(\mathbf{Q}, \tau)] + B(\mathbf{Q}). \quad (173)$$

The term  $A(\mathbf{Q})$  describes the static power spectrum of the signal, it is mainly composed by three terms, as

$$A(\mathbf{Q}) \sim T(\mathbf{Q})P(\mathbf{Q})S(\mathbf{Q}). \quad (174)$$

$T(\mathbf{Q})$  takes into account the modulated transfer function of the imaging system,  $P(\mathbf{Q})$  and  $S(\mathbf{Q})$  are analogous to the Form and Structure factor obtained from Static light scattering, as they are the power spectrum of the individual imaged object, and the Fourier transform of the spatial correlation among the imaged objects. Finally,  $B(\mathbf{Q})$  is the power spectrum of the detection noise.

Numerically,  $A(\mathbf{Q})$  and  $B(\mathbf{Q})$  were estimated according to the following procedure, the background term  $B(\mathbf{Q})$  was approximated from an average of all  $D(\mathbf{Q}, \tau)$  determined at short delay times and large enough  $\mathbf{Q}$  values that, due to the limited spatial resolution of the imaging set-up, they barely contain information of the system but rather of the background [36, 50]. Additionally, we have assumed  $B(\mathbf{Q})$  to be constant for all  $\mathbf{Q}$  values. Thus,

$$B(\mathbf{Q}) \simeq B'(\mathbf{Q}) = D(\mathbf{Q} \rightarrow \mathbf{Q}_{\max}, \tau \rightarrow 0). \quad (175)$$

Having estimated  $B(\mathbf{Q})$ ,  $A(\mathbf{Q})$  was determined from the long-time decorrelation plateau, as  $D(\mathbf{Q}, \tau \rightarrow \infty) = A(\mathbf{Q}) + B(\mathbf{Q})$ . Finally, the Intermediate scattering function can be obtained via the following equation,

$$\beta(\mathbf{Q})f(\mathbf{Q}, \tau) = \frac{D(\mathbf{Q}, \tau \rightarrow \infty) - D(\mathbf{Q}, \tau)}{D(\mathbf{Q}, \tau \rightarrow \infty) - B'(\mathbf{Q})}, \quad (176)$$

where  $\beta(\mathbf{Q}) \simeq 1 - [B(\mathbf{Q}) - B'(\mathbf{Q})] / A(\mathbf{Q})$ . The value of  $\beta(\mathbf{Q})$  reflects the signal to noise ratio, and the accuracy of the estimation of  $B(\mathbf{Q})$ . Hence, in order to achieve  $\beta(\mathbf{Q}) \simeq 1$ , a high signal to noise ratio has to be met i.e.  $A(Q) \gg B(Q)$ , and  $B'(Q) \simeq B(Q)$ .

The expression for  $f(\mathbf{Q}, \tau)$  depends on the type of the motion projected in the direction of the scattering wave vector  $\mathbf{Q}$ . For our case, we assume Brownian motion to be neglected, and a narrow distribution of directed motion in the observed region is an effect of the imposed shear. Thus,  $f(\mathbf{Q}, \tau)$  takes the following form:

$$f(Q, \tau) = \exp \left[ -\frac{1}{2} Q^2 \delta_v^2 \tau^2 \right] \cos(Q \langle v \rangle \tau) \quad (177)$$

where  $\langle v \rangle$  is the mean directed velocity, and  $\delta_v$  is the standard deviation of the velocity distribution of the directed motion. The corresponding characteristic times are given by  $\tau_{\delta_v}(Q) = \sqrt{2}/Q\delta_v$ , and  $\tau_v(Q) = 1/Q\langle v \rangle$ . Noting the  $Q$  scale dependence for the type of dynamics described, having  $Q$  for directed motion, as the displacement is proportional to time i.e.  $1/Q \sim L \sim v\tau$ .

We tested the validity of our assumption over the imposed velocity distribution in the imaged region and the analytical expression of  $f(Q, \tau)$  by computing Particle Image Velocimetry (PIV) over the effective image series [154]. An illustration of the obtained data can be seen in Fig.(45), the data corresponds to the acquired images for height  $7\mu\text{m}$  above the bottom plate ( $-18\mu\text{m}$  from the stagnation point). The inset of the left panel of Fig.(45) shows a region of interest of one of the acquired images, along with the obtained velocity map from PIV (arrows). The slight different orientations of the arrows indicates the existence of a velocity distribution over the sampled image, this arises from the spatially heterogeneous velocity map imposed by the flow from the sheared deformation.

The velocity distribution  $P(v)$  was estimated in the flow direction (horizontal axis) by normalizing a frequency count. It was made over the different velocity maps, taking into account all of the different starting times with the same temporal spacing between frames ( $\sim 0.08\text{s}$ ) including the total 13 sheared cycles. Moreover, a careful selection of the PIV parameters was done in order to reduce typical PIV artifacts [155, 156].

Our results are presented in the left panel of Fig.(45). The shape of  $P(v)$  suggests that can be analytically described by a Gaussian distribution, being corroborated by a Gaussian fit (red line). The fit led to an estimation of the mean velocity of  $\langle v \rangle = 6.74\mu\text{m/s}$  and standard deviation of the distribution of  $\delta_v = 0.65\mu\text{m/s}$ . These results prove our original assumption of the shape of the velocity distribu-

tion, thus validating Eq.(177) as the analytical expression of  $f(Q, \tau)$  for describing these type of particle dynamics.

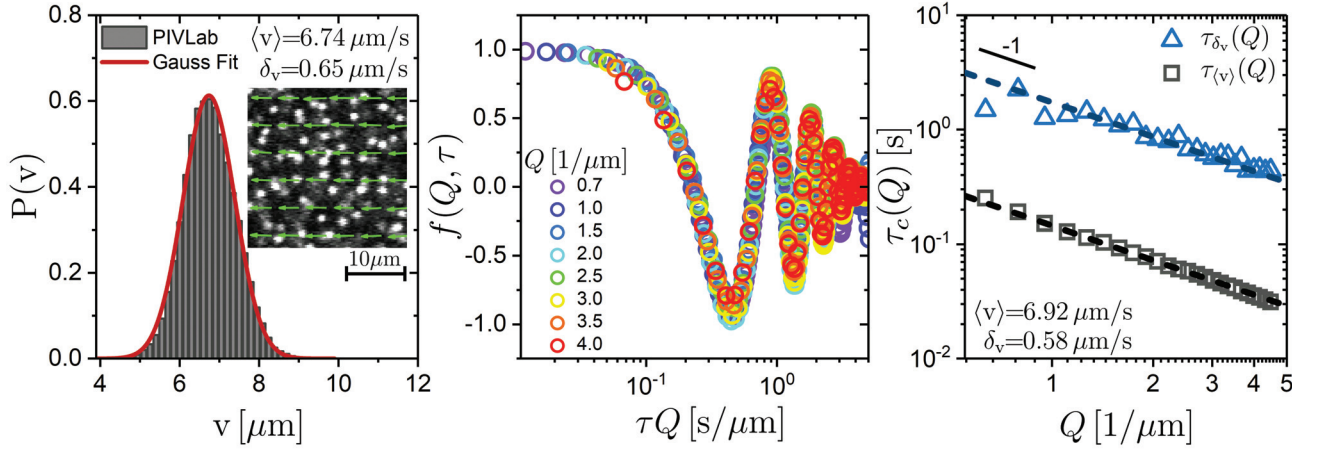


Fig. 45: Illustration of the obtained information from the acquired images at height  $7\mu\text{m}$  above the bottom plate ( $-18\mu\text{m}$  from the stagnation point). The main figure from the left panel illustrates the velocity distribution  $P(v)$  obtained from a PIV analysis, the inset shows an example of the obtained velocity map over a small region of interest. The middle panel shows our estimation of  $f(Q, \tau)$  by the application of the DFM framework. All of the obtained  $f(Q, \tau)$  shows an oscillatory plus a damping term, suggested by Eq.(177). Furthermore, all of them collapse onto a master curve when plotted in  $\tau Q$  scale, as expected for particles undergoing ballistic motion. The right panel shows a log-log representation of the extracted  $\tau_v(Q)$ , and  $\tau_{\delta_v}(Q)$  by fitting the corresponding analytical expression. In this representation we obtained the slope of -1. It represents the ballistic  $Q$  scale, and from the intercept,  $v$  and  $\delta_v$  were obtained.

We proceeded to apply the DFM framework to estimate  $f(Q, \tau)$ . It was computed from the azimuthal average of  $D(\mathbf{Q}, \tau)$  for  $\mathbf{Q}$  oriented parallel in the direction of the flow  $\pm 5^\circ$ . In addition,  $D(\mathbf{Q}, \tau)$  was the result of all of the 13 sheared cycles. Our results are illustrated in the middle panel of Fig.(45), and are shown for a  $Q$  range that covers the majority of the sampled wavelengths within an image (as indicated). All of the obtained  $f(Q, \tau)$  collapse onto a master curve when plotted in  $\tau Q$  scale, as expected for particles undergoing ballistic motion. Moreover, an oscillatory with a damping behaviour can be seen from all of the obtained functions, suggesting that Eq.(177) can be used to extract the velocity distribution properties.

We continued our analysis by obtaining the characteristic times  $\tau_v(Q)$ , and  $\tau_{\delta_v}(Q)$ . This was achieved by fitting  $f(Q, \tau)$  with the expression given by Eq.(177). Our results are shown in a log-log scale in the right panel of Fig.(45). In this representation, both characteristic times have a slope of -1, indicating the ballistic  $Q$  scaling. Furthermore, by the intercept value obtained from a linear regression (dashed lines), the values of  $\langle v \rangle = 6.92\mu\text{m/s}$  and  $\delta_v = 0.58\mu\text{m/s}$  were estimated. These results are in very good agreement with the previously shown PIV results, thus proving the validity of the usage of Rheo-DFM by means of the analytical expression of  $f(Q, \tau)$ .

Finally, we applied the DFM framework to obtain  $\langle v \rangle$  and  $\delta_v$  for all of the mea-

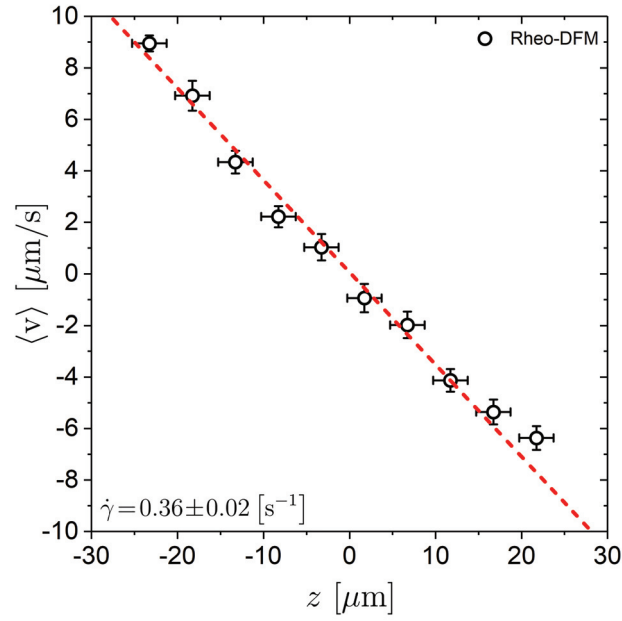


Fig. 46: Velocity profile characterized by means of Rheo-DFM. The dashed line represents a linear

sured heights ( $z$ ). Our results are shown in Fig.(46), where the error bar of the velocity represents  $\delta_v$  and the error bar of  $z$  corresponds to plus minus half of the optical thickness. As expected from a plate-plate geometry, the velocity profile along the plates is linear. Moreover, by applying a linear regression taking into account the deviations from both axes [164], we obtained the value of the shear rate  $\dot{\gamma} = 0.36 \text{ s}^{-1}$ .

## 5 Conclusions

The following section summarizes the main results of the research presented in this thesis: Optimized algorithms for DFM (Sec.4.1), Effect of moderate multiple scattering in heterodyne near field scattering (Sec.4.2), Microliter viscometry (Sec.4.3), Velocity deviations from sedimentation of dilute systems (Sec.4.4), From colloid to grain, a dynamic description of sedimentation in dilute systems (Sec.4.5), Digital Fourier Analysis of X-Ray radiographs from granular suspensions (Sec.4.6), and Dynamics of sheared particles: Rheo-DFM (Sec.4.7).

In this thesis, we optimized the DFM analysis scheme and showed a variety of applications of DFM to study the static and dynamical properties of colloidal and granular suspensions. Moreover, we presented different optimized algorithms that decreased the computational time to extract reliable information. Furthermore, we extended the theoretical framework of heterodyne near field scattering (HNFS) by including the effects of moderate multiple scattering, allowing us to define a limit of applicability of the techniques for moderately turbid suspensions. Additionally, we have used DFM to extract microrheological properties such as the complex viscosity for various systems, including viscous, visco-elastic, biological, and other complex fluids. In addition, we used heterodyne near field scattering to study the contribution of polydispersity to the velocity deviations of sedimenting colloidal systems. Moreover, we extended the physical understanding of the transition between colloidal and granular dynamics by using observables in the real and reciprocal space. We achieved the previous by employing the polydisperse Langevin model, computer simulations, and experimental results. Furthermore, we studied the extension of the DFM framework to X-Ray radiograms, where we extracted the dynamics of sedimenting and fluidized granular suspensions. Finally, we introduced the Rheo-DFM framework and used it to characterize the shear profile imposed by a plate-plate shear cell to a colloidal system.

### Optimized algorithms for DFM

In this work we have introduced the concept of temporal and space redundancy for the DFM framework. We presented three different algorithms for the temporal computation part: the standard redundant algorithm (R), which computes the time average by accounting for all available elements, and two more efficient algorithms, the Reduced Redundant (RR) and the Sampling Uniformly at Random (SUR), where each algorithm introduces a sampling rule to remove redundancy. The previous reduces significantly the amount of information taken for computing the time averages. Thus, a significant reduction in computational time is obtained

without altering the overall result. Moreover, we have analyzed the convergence of our proposed algorithms, having SUR the highest optimization for performing time averages as it is the one that converges with the smallest number of elements.

We have shown that, by using Digital Data Reduction (DDR), it is possible to reduce the computational memory consumption up to 16 times without losing dynamical physical information, leading to lower computational times, obtaining a speed up of a factor of 5 without GPU acceleration. The previous was achieved by digitally matching (binning) the imaging system's resolution frequency ( $K_R$ ) to the Nyquist frequency of the detector ( $K_{Ny}$ ). Then, by knowing the optical features of an imaging set-up, and using the definition of  $\delta = K_R/K_{Ny}$ , it is possible to optimize image treatment. This, by selecting the appropriate digital binning or, by the knowledge of  $\delta$ , an optimum data acquisition can be designed, while keeping in mind that an effective optical transfer function is introduced as an artefact at higher  $Q$  values without compromising the dynamics.

### Effect of moderate multiple scattering in heterodyne near field scattering

In this work, we systematically investigated the effects of multiple scattering in heterodyne near field scattering (HNFS) experiments. We controlled the degree of multiple scattering by tuning the concentration of aqueous suspensions of colloidal particles, as, by increasing concentration, a reduction of transmitted light is seen. This phenomenon was quantified by the reflectance defined as  $\mathcal{R} = 1 - \mathcal{T}$  with  $\mathcal{T} = I_T/I_0$  the transmittance, i.e., the ratio of the transmitted light through a sample ( $I_T$ ) by the transmitted light through a sample made of pure solvent under the same optical configuration. We also analyzed the statistical properties of the heterodyne signal in real space for different  $\mathcal{R}$  values, changing from a Gaussian to a Laplace probability distribution of the intensity differences. Where the change of the probability distribution allowed us to define four regions: single scattering ( $0 < \mathcal{R} < 0.15$ ), moderate multiple scattering ( $0.15 < \mathcal{R} < 0.30$ ), a cross over region ( $0.30 < \mathcal{R} < 0.45$ ) and the multiple scattering ( $\mathcal{R} > 0.45$ ). Furthermore, we studied the effects of increasing  $\mathcal{R}$  in the image structure function  $D(Q, \tau)$ . Where we found that given the low  $Q$  wave vectors and the slow acquisition time, the effect of moderate multiple scattering leads to an effective background contribution  $B_{\text{eff}}(Q)$ . We used this result in the data analysis to extract the single scattering intermediate scattering function  $f(Q, \tau)$  and hydrodynamic radius  $R_h$ . Finally, we obtained the limit of applicability of the technique for  $\mathcal{R} < 0.30$ .

### Microliter viscometry

In this work we have presented  $\eta$ -DFM, an extension of the applicability of the DFM framework in order to extract micro-viscometry information from a vari-

ety of colloidal systems, i.e., an ideal viscous fluid (glycerol-water mixtures), a biological colloidal system (lysozyme proteins), a visco-elastic polymer suspension (aqueous-based poly(ethylene oxide)) and a hard sphere fluid (Poly(methyl methacrylate) particles in organic solvents). The  $\eta$ -DFM framework was tested for all systems and compared to macroscopic Small Amplitude Oscillatory Shear (SAOS) rheology experiments and macroscopic steady shear viscosity measurements. As a result, we obtained perfect matching between them, validating the  $\eta$ -DFM framework. Moreover,  $\eta$ -DFM could access lower frequencies than that obtained in conventional rheometry. Furthermore, we exploited the versatility of the DFM framework by using confocal fluorescence microscopy as an imaging technique. We tested the possibility of having a colloidal system with a small portion acting as tracers, stressing the tracer/system size condition. Again, our results showed an excellent agreement between  $\eta$ -DFM and SAOS, corroborating the validity of the Generalized-Stokes Einstein relations for hard sphere liquids. It is essential to mention that further testing needs to be performed, specifically towards the different phase transitions of the hard sphere fluid at higher volume fractions than the ones tested here and, additionally, other types of fluids with different particle interactions.

### Velocity deviations from the sedimentation of dilute systems

In this work, we described the dynamics of sedimentation using the polydisperse Langevin model, studied the analytical expression of the real part of the intermediate scattering function  $f(Q, \tau)$ , and used the model to study the effect of polydispersity in sedimentation using computer simulations. We performed dynamic light scattering experiments for three systems with different particle sizes, polydispersity indexes and two different optical properties. However, all systems fall within the same ensemble Péclet range ( $Pe^*$ ), thus having similar dynamical behavior. With the previous, we proved the theoretical model's validity for the description and the validity of our computer simulations. Moreover, the extracted dynamical polydispersity was corroborated by the Mie theory analysis of the static light scattering information of the experiments. Furthermore, we have shown the versatility of using HNFS for these experiments, as it simultaneously provides both static and dynamic information.

### From colloid to grain. A dynamic description of sedimentation in dilute systems

In this work, we showed the different dynamical regimes that arise from introducing an external force to the description of the dynamics of colloidal particle systems, where we found that the ensemble Péclet number ( $Pe^*$ ) helps quantify the contribution of the external force vs. thermal agitation. Moreover, we extended the physical description of the system's dynamics by including size polydisper-

sity in the theoretical framework and applied it to Brownian dynamics computer simulations. We performed a systematic study on different polydispersity values, characterizing in a quantitative manner, the impact on the mean squared displacement and the intermediate scattering function by the overall description. Based on the behavior of the MSD and the characteristic decorrelation of the ISF, we found a very rich dynamical phase diagram that is summarized in the following way: for ( $Pe^* < 1$ ), the majorly dynamical behavior of the system is only driven by thermal agitation and can be considered to be Brownian, then for ( $1 < Pe^* < 33$ ) the colloid in the presence of an external force region appears, as the contribution of the external force starts to become significant. Then, for ( $33 < Pe^* < 800$ ), the effect of the external force is stronger, and the external force mainly describes the overall particle dynamics. However, a trace of thermal agitation is still detectable. Finally, for ( $Pe^* > 800$ ) the granular regime is defined. Here, no thermal agitation is detected, and only the external force is responsible for the system dynamics. Furthermore, we corroborate our theoretical results with Heterodyne Near Field scattering sedimentation experiments of different particle sizes that allowed us to control the  $Pe^*$  of the system.

### **Digital Fourier Analysis of X-Ray radiographs of granular suspensions**

In this work, we extended the capability of the Digital Fourier Analysis framework to X-Ray radiographs, widening its range of applicability. We used computer simulations to produce synthetic radiographs that encompassed different dynamical information. We modeled the image content by taking into account the change of the X-ray spectrum due to beam hardening over the whole traveled path of the photons via an effective attenuation coefficient. We tested four different types of dynamics: homogenous directed, directed with a distribution of velocities, random motion, and a combination of the above. The excellent agreement between the fixed computer simulation values and the ones obtained from the X-DFA validated the conceptual framework of the analysis method. Moreover, we extracted equivalent information as in static light scattering experiments, such as the form and structure factor out of the static quantities in the DFA ( $A(Q)$ ). Furthermore, we showed its applicability to sedimentation and fluidization experiments.

### **Dynamics of sheared particles: Rheo-DFM**

In this work, we presented preliminary results of Rheo-DFM. We performed DFM employing confocal microscopy, exploiting its optical capabilities to scan different sections or layers of the sheared system. We employed it to characterize the effect of a constant deformation made by a plate-plate shear cell to a colloidal suspension consisting of PMMA particles in a highly viscous double matching solvent dispersed at a volume fraction of ( $\phi = 0.2$ ). This system allowed us to safely

discard any contribution from diffusion to the intermediate scattering function to extract the imposed velocity distribution of the particles due to shear. Moreover, we quantified the imposed velocity profile across the sample gap and, from these results, the shear rate ( $\dot{\gamma}$ ) was also obtained. Our findings were corroborated by Particle Image Velocimetry, another image analysis scheme based on real space. Hence, Rheo-DFM could be used as a complementary tool to access dynamical information of sheared systems.

## Acknowledgements

First and foremost, I would like to thank my *Doktorvater* Prof. Dr. Stefan U. Egelhaaf for providing me with the opportunity to perform this work. Moreover, for always making time to discuss and share his point of view on every subject with a welcoming smile and interest in my learning experience and personal growth.

To my daughter Valentina and my wife Maria for being my strongest teachers, driving force, and a constant inspiration.

To the strong support of my parents, brothers, and family in-law. Thank you for your loving care, always being there, and for providing a safety net.

To all of my dearest people whose time came during the process of this thesis.

To Angel, for your friendship, excellent discussions, and teaching me how to be pragmatic, patient, and express myself.

To JP, for your support, friendship, and being part of this experience.

To Roberto, for your friendship, advice, and having time to share and discuss new and old ideas.

Thank you, Jörg, Christoph, Dana, Patrick, Jan, and Philipp, for giving me a warm welcome to the group and helping me in the transition to the German culture.

Thank you to all my friends in armor, Andreas and Debasish, for providing me backup whenever it was needed.

Thank you, Alejandro, Ramón, Erick, Luis, for your friendship and for being part of this experience.

Last but not least, I would like to thank to all of the students that accepted my supervision, your positive energy towards the work was like fuel to me.

## References

- [1] J. Dhont, *An Introduction to Dynamics of Colloids*. Elsevier, 2003.
- [2] M. Doi, *Soft Matter Physics*. Oxford University Press, 2013.
- [3] T. Vilgis *Reports on Progress in Physics*, vol. 78, no. 12, p. 124602, 2015.
- [4] R. Jones, *Soft Condensed Matter*. Oxford University Press, 2002.
- [5] W. C. K. Poon and D. Andelman, *Soft Condensed Matter Physics in Molecular and Cell Biology*. Taylor and Francis.
- [6] T. Lee, B. Senyuk, R. P. Trivedi, and I. I. Smalyukh, *Optical Microscopy of Soft Matter Systems*. John Wiley and Sons, Ltd, 2016.
- [7] F. Giavazzi and R. Cerbino, “Digital fourier microscopy for soft matter dynamics,” *Journal of Optics*, vol. 16, p. 083001, 2014.
- [8] B. Berne and R. Pecora, *Dynamic Light Scattering: With Applications to Chemistry, Biology, and Physics*. Courier Corporation.
- [9] J. Mewis and N. Wagner, *Colloidal Suspensions Rheology*. Cambridge University Press, 2012.
- [10] C. W. Macosko, *Rheology: Principles, Measurements, and Applications*. Wiley-VCH, 1994.
- [11] T. Sentjabrskaja, P. Chaudhuri, M. Hermes, W. C. K. Poon, J. Horbach, S. U. Egelhaaf, and M. Laurati, “Creep and flow of glasses: strain response linked to the spatial distribution of dynamical heterogeneities,” *Scientific Reports*, vol. 5, no. 11884, pp. 2045–2322, 2015.
- [12] S. Aime and L. Cipelletti, “Probing shear-induced rearrangements in fourier space. i. dynamic light scattering,” *Soft Matter*, vol. 15, pp. 200–212, 2019.
- [13] S. Aime and L. Cipelletti, “Probing shear-induced rearrangements in fourier space. ii. differential dynamic microscopy,” *Soft Matter*, vol. 15, pp. 213–226, 2019.
- [14] D. Kushnir, N. Beyer, E. Bartsch, and P. Hébraud, “Wide-angle static and dynamic light scattering under shear,” *Review of Scientific Instruments*, vol. 92, no. 2, p. 025113, 2021.
- [15] D. McQuarrie, *Statistical Mechanics*. Harper Collins Publishers, 1973.
- [16] J. Hansen and I. McDonald, *Theory of simple liquids 2nd ed.* AP Academic Press, 1990.

- 
- [17] G. D. J. Phillies, *Elementary Lectures in Statistical Mechanics*. Springer-Verlag, 2000.
- [18] M. Allen and D. Tildesley, *Computer Simulation of Liquids*. Oxford University Press.
- [19] N. van Kampen, *Stochastic Processes in Physics and Chemistry*. Elsevier, 2007.
- [20] I. Florescu, *Probability and Stochastic Processes*. Wiley, 2015.
- [21] W. Brown, *Dynamic Light Scattering, The Method and Some Applications*. Oxford University Press.
- [22] L. Van Hove, “Correlations in space and time and born approximation scattering in systems of interacting particles,” *Phys. Rev.*, vol. 95, pp. 249–262, 1954.
- [23] W. van Meegen, S. M. Underwood, and I. Snook, “Tracer diffusion in concentrated colloidal dispersions,” *The Journal of Chemical Physics*, vol. 85, no. 7, pp. 4065–4072, 1986.
- [24] F. Ferri, D. Magatti, D. Pescini, M. A. C. Potenza, and M. Giglio, “Heterodyne near-field scattering: A technique for complex fluids,” *Phys. Rev. E*, vol. 70, p. 041405, 2004.
- [25] J. C. Crocker and D. G. Grier, “Methods of digital video microscopy for colloidal studies,” vol. 179, pp. 298–310.
- [26] A. Einstein, “Über die von der -molekularkinetischen Theorie der Wärme geforderte Bewegung von in ruhenden Flüssigkeiten suspendierten Teilchen,” *Annalen der Physik*, vol. 322, pp. 549–560, 1905.
- [27] A. Fick, “Über Diffusion,” *Annalen der Physik*, vol. 170, pp. 59–86, 1855.
- [28] M. von Smoluchowski, “Zur kinetischen Theorie der Brownschen Molekularbewegung und der Suspensionen,” *Annalen der Physik*, vol. 326, pp. 756–780, 1906.
- [29] R. Huilgol and N. Phan-Thien, *Fluid Mechanics of Viscoelasticity*. Elsevier, 1997.
- [30] H. Risken, *The Fokker-Planck Equation Methods of Solution and Applications*. Springer-Verlag.
- [31] D. Lemons and A. Gythiel, “Paul langevin’s 1908 paper “on the theory of brownian motion” [“sur la théorie du mouvement brownien,” c. r. acad. sci. (paris) 146, 530–533 (1908)],” *American Journal of Physics*, vol. 65, pp. 1079–1081, 1997.

- [32] D. Ermak and J. A. McCammon, “Brownian dynamics with hydrodynamic interactions,” *The Journal of Chemical Physics*, vol. 69, pp. 1352–1360, 1978.
- [33] R. Kubo, “The fluctuation-dissipation theorem,” *Reports on Progress in Physics*, vol. 29, pp. 255–284, 1966.
- [34] D. J. Evans and F. P. Morriss, “The green–kubo relations,” in *Statistical Mechanics of Nonequilibrium Liquids*, pp. 77–93, Academic Press, 1990.
- [35] B. R. Dasgupta, S. Tee, J. C. Crocker, B. J. Frisken, and D. A. Weitz, “Microrheology of polyethylene oxide using diffusing wave spectroscopy and single scattering,” *Phys. Rev. E*, vol. 65, p. 051505, 2002.
- [36] M. A. Escobedo-Sánchez, J. P. Segovia-Gutiérrez, A. B. Zuccolotto-Bernez, J. Hansen, C. C. Marciniak, K. Sachowsky, F. Platten, and S. U. Egelhaaf, “Microliter viscometry using a bright-field microscope:  $\eta$ –DDM,” *Soft Matter*, vol. 14, pp. 7016–7025, 2018.
- [37] P. Lindner and T. Zemb, *Neutrons, X-Rays and Light Scattering Methods Applied to Soft Condensed Matter*. Elsevier, 2002.
- [38] B. Frisken, “Revisiting the method of cumulants for the analysis of dynamic light-scattering data,” *Appl. Opt.*, vol. 40, pp. 4087–4091, 2001.
- [39] T. Mason, “Estimating the viscoelastic moduli of complex fluids using the generalized stokes-einstein equation,” *Rheologica Acta*, vol. 39, pp. 371–378, 2000.
- [40] T. Mason and D. Weitz, “Optical measurements of frequency-dependent linear viscoelastic moduli of complex fluids,” *Phys. Rev. Lett.*, vol. 74, pp. 1250–1253, 1995.
- [41] T. Mason, H. Gang, and D. Weitz, “Diffusing-wave-spectroscopy measurements of viscoelasticity of complex fluids,” *J. Opt. Soc. Am. A*, vol. 14, pp. 139–149, 1997.
- [42] T. A. Waigh, “Microrheology of complex fluids,” *Reports on Progress in Physics*, vol. 68, pp. 685–742, 2005.
- [43] M. Gardel, M. Valentine, and D. Weitz, *Microrheology*, pp. 1–49. Springer Berlin Heidelberg, 2005.
- [44] P. Cicuta and A. M. Donald, “Microrheology: a review of the method and applications,” *Soft Matter*, vol. 3, pp. 1449–1455, 2007.
- [45] D. Wirtz, “Particle-tracking microrheology of living cells: Principles and applications,” *Annual Review of Biophysics*, vol. 38, pp. 301–326, 2009.

- 
- [46] Q. Li, X. Peng, and G. Chen, D. and McKenna, “The laplace approach in microrheology,” *Soft Matter*, vol. 16, pp. 3378–3383, 2020.
- [47] P. Chaikin and T. Lubesky, *Principles of Condensed Matter Physics*. Cambridge University Press, 1995.
- [48] A. Levine and T. Lubensky, “One- and two-particle microrheology,” *Phys. Rev. Lett.*, vol. 85, pp. 1774–1777, 2000.
- [49] S. Li, G. Zhao, and H. Chen, “The relationship between steady shear viscosity and complex viscosity,” *Journal of Dispersion Science and Technology*, vol. 26, pp. 415–419, 2005.
- [50] F. Giavazzi, C. Malinverno, G. Scita, and R. Cerbino, “Tracking-free determination of single-cell displacements and division rates in confluent monolayers,” *Frontiers in Physics*, vol. 6, p. 120, 2018.
- [51] S. Kim and S. Karrila, *Microhydrodynamics: Principles and Selected Applications*. Butterworth Heinemann, 1991.
- [52] D. Pimponi, M. Chinappi, P. Gualtieri, and C. Casciola, “Mobility tensor of a sphere moving on a superhydrophobic wall: application to particle separation,” *Microfluidics and Nanofluidics*, vol. 16, pp. 571–585, 2014.
- [53] P. Lu, F. Giavazzi, T. Angelini, E. Zaccarelli, F. Jargstorff, A. Schofield, J. Wilking, M. Romanowsky, D. Weitz, and R. Cerbino, “Characterizing concentrated, multiply scattering, and actively driven fluorescent systems with confocal differential dynamic microscopy,” *Phys. Rev. Lett.*, vol. 108, p. 218103, 2012.
- [54] D. Germain, M. Leocmach, and T. Gibaud, “Differential dynamic microscopy to characterize brownian motion and bacteria motility,” *Am. J. Phys.*, vol. 84, pp. 202–210, 2016.
- [55] L. G. Wilson, V. Martinez, J. Schwarz-Linek, J. Tailleur, G. Bryant, P. Pusey, and W. Poon, “Differential dynamic microscopy of bacterial motility,” *Phys. Rev. Lett.*, vol. 106, p. 018101, 2011.
- [56] V. A. Martinez, R. Besseling, O. A. Croze, J. Tailleur, M. Reufer, J. Schwarz-Linek, L. G. Wilson, M. A. Bees, and W. C. K. Poon, “Differential dynamic microscopy: A high-throughput method for characterizing the motility of microorganisms,” *Biophys. J.*, vol. 103, no. 8, pp. 1637–1647, 2012.
- [57] C. Kurzthaler, C. Devailly, J. Arlt, T. Franosch, W. C. K. Poon, V. A. Martinez, and A. T. Brown, “Probing the spatiotemporal dynamics of catalytic janus particles with single-particle tracking and differential dynamic microscopy,” *Phys. Rev. Lett.*, vol. 121, p. 078001, 2018.

- [58] K. Eitel, G. Bryant, and H. J. Schöpe, “A hitchhiker’s guide to particle sizing techniques,” vol. 36, pp. 10307–10320.
- [59] I. M. Krieger, “Statistics of narrow distributions,” *Journal of Macromolecular Science, Part B*, vol. 4, pp. 437–440, 1970.
- [60] J. Jover, A. J. Haslam, A. Galindo, G. Jackson, and E. A. Müller, “Pseudo hard-sphere potential for use in continuous molecular-dynamics simulation of spherical and chain molecules,” *The Journal of Chemical Physics*, vol. 137, no. 14, p. 144505, 2012.
- [61] C. A. Báez, A. Torres-Carbajal, R. Castañeda Priego, A. Villada-Balbuena, J. M. Méndez-Alcaraz, and S. Herrera-Velarde, “Using the second virial coefficient as physical criterion to map the hard-sphere potential onto a continuous potential,” *J. Chem. Phys.*, vol. 149, p. 164907, 2018.
- [62] H. A. Lorentz, “Ueber die anwendung des satzes vom virial in der kinetischen theorie der gase,” *Annalen der Physik*, vol. 248, no. 1, p. 127–136, 1881.
- [63] D. Berthelot, “Sur le mélange des gaz,” *Comptes rendus hebdomadaires des séances de l’Académie des Sciences*, vol. 126, pp. 1703–1855, 1898.
- [64] J. Rowlinson and F. Swinton, *Liquids and Liquid Mixtures*. Butterworth Scientific, 1982.
- [65] R. Cerbino and A. Vailati, “Near-field scattering techniques: Novel instrumentation and results from time and spatially resolved investigations of soft matter systems,” *Current Opinion in Colloid and Interface Science*, vol. 14, pp. 416–425, 2009.
- [66] R. Piazza, “Optical correlation techniques for the investigation of colloidal systems,” in *Colloidal Foundations of Nanoscience* (D. Berti and G. Palazzo, eds.), pp. 233–266, Elsevier, 2014.
- [67] A. Gatti, D. Magatti, and F. Ferri, “Three-dimensional coherence of light speckles: theory,” *Phys Rev, A*, vol. 78, p. 063806, 2008.
- [68] F. Croccolo and D. Brogioli, “Quantitative fourier analysis of schlieren masks: the transition from shadowgraph to schlieren,” *Appl. Opt.*, vol. 50, pp. 3419–3427, Jul 2011.
- [69] J. Rička, “Dynamic light scattering with single-mode and multimode receivers,” *Appl. Opt.*, vol. 32, no. 15, pp. 2860–2875, 1993.
- [70] D. Magatti, M. D. Alaimo, M. A. C. Potenza, and F. Ferri, “Dynamic heterodyne near field scattering,” *Applied Physics Letters*, vol. 92, p. 241101, 2008.

- 
- [71] B. Chu, *Laser Light Scattering: Basic Principles and Practice*. Dover Publications, Incorporated, 2007.
- [72] F. Croccolo, C. Giraudet, H. Bataller, R. Cerbino, and A. Vailati, “Shadowgraph analysis of non-equilibrium fluctuations for measuring transport properties in microgravity in the gradflex experiment,” *Microgravity Science and Technology*, vol. 28, pp. 467–475, 2016.
- [73] F. Giavazzi, D. Brogioli, V. Trappe, T. Bellini, and R. Cerbino, “Scattering information obtained by optical microscopy: Differential dynamic microscopy and beyond,” *Phys. Rev. E*, vol. 80, p. 031403, 2009.
- [74] F. Giavazzi, P. Edera, P. Lu, and R. Cerbino, “Image windowing mitigates edge effects in differential dynamic microscopy,” *The European Physical Journal E*, vol. 40, p. 97, 2017.
- [75] R. Cerbino and V. Trappe, “Differential dynamic microscopy: Probing wave vector dependent dynamics with a microscope,” *Phys. Rev. Lett.*, vol. 100, p. 188102, 2008.
- [76] G. Cerchiari, F. Croccolo, F. Cardinaux, and F. Scheffold, “Quasi-real-time analysis of dynamic near field scattering data using a graphics processing unit,” *Review of Scientific Instruments*, vol. 83, p. 106101, 2012.
- [77] M. A. Escobedo-Sánchez, L. F. Rojas-Ochoa, M. Laurati, and S. U. Egelhaaf, “Investigation of moderately turbid suspensions by heterodyne near field scattering,” *Soft Matter*, vol. 13, pp. 5961–5969, 2017.
- [78] M. A. Escobedo-Sánchez, H. A. De la Cruz-Burelo, J. L. Arauz-Lara, C. Haro-Pérez, and L. F. Rojas-Ochoa, “Study of translational and rotational dynamics of birefringent colloidal particles by depolarized light scattering in the far- and near-field regimes,” *J. Chem. Phys.*, vol. 143, p. 044902, 2015.
- [79] K. Schätzel, “Signal preprocessing for digital correlators,” *Applied physics*, vol. 22, pp. 251–256, 1980.
- [80] K. Schätzel, “Rate correlation and data preprocessing with digital correlators and structurators,” in *Photon Correlation Techniques in Fluid Mechanics* (E. O. Schulz-DuBois, ed.), (Berlin, Heidelberg), pp. 226–241, Springer Berlin Heidelberg, 1983.
- [81] K. Rao, D. Kim, and J. Hwang, *Fast Fourier Transform: Algorithms and Applications*. Springer.
- [82] R. Gonzalez and R. Woods, *Digital Image Processing*. Pearson, 2008.
- [83] S. U. Egelhaaf, *Optical microscopy in Soft Matter From Synthetic to Biological Materials*. Forschungszentrum Jülich GmbH, 2008.

- [84] E. Sevenard and W. Schröer, “Correlation functions of singly and multiply scattered light analysed by the 3-d cross-correlation technique,” *Phys. Chem. Chem. Phys.*, vol. 4, pp. 1900–1906, 2002.
- [85] C. M. Sorensen, R. C. Mockler, and W. J. O’Sullivan, “Multiple scattering from a system of brownian particles,” *Phys. Rev. A*, vol. 17, pp. 2030–2035, 1978.
- [86] G. Koopmans, P. C. Hopman, and J. Greve, “Double-scattering effects in depolarised light scattering spectrometry,” *J. Phys. A: Math. Gen.*, vol. 12, pp. 581–590, 1979.
- [87] J. Goodman, *Speckle Phenomena in Optics*. Englewood: Roberts and Company, 2007.
- [88] S. E. Skipetrov, J. Peuser, R. Cerbino, P. Zakharov, B. Weber, and F. Schefold, “Noise in laser speckle correlation and imaging techniques,” *Opt. Expr.*, vol. 18, pp. 14519–14534, 2010.
- [89] S. Kotz, T. J. Kozubowski, and K. Podgórski, *The Laplace Distribution and Generalizations: A Revisit with Applications to Communications, Economics, Engineering, and Finance*. Springer Science+Business Media, LLC, 2001.
- [90] W. P. Cox and E. H. Merz, “Correlation of dynamic and steady flow viscosities,” *Journal of Polymer Science*, vol. 28, pp. 619–622, 1958.
- [91] P. Edera, D. Bergamini, V. Trappe, F. Giavazzi, and R. Cerbino, “Differential dynamic microscopy microrheology of soft materials: A tracking-free determination of the frequency-dependent loss and storage moduli,” *Phys. Rev. Materials*, vol. 1, p. 073804, 2017.
- [92] A. Bayles, T. Squires, and M. Helgeson, “Probe microrheology without particle tracking by differential dynamic microscopy,” *Rheologica Acta*, vol. 56, pp. 2440–2452, 2017.
- [93] F. Del Giudice, M. Tassieri, C. Oelschlaeger, and A. Q. Shen, “When microrheology, bulk rheology, and microfluidics meet: Broadband rheology of hydroxyethyl cellulose water solutions,” *Macromolecules*, vol. 50, pp. 2951–2963, 2017.
- [94] W. van Megen and S. M. Underwood, “Tracer diffusion in concentrated colloidal dispersions. iii. mean squared displacements and self-diffusion coefficients,” *The Journal of Chemical Physics*, vol. 91, pp. 552–559, 1989.
- [95] W. van Megen and S. M. Underwood, “Tracer diffusion in concentrated colloidal dispersions. ii. non-gaussian effects,” *The Journal of Chemical Physics*, vol. 88, no. 12, pp. 7841–7846, 1988.

- [96] N.-S. Cheng, “Formula for the viscosity of a glycerol water mixture,” *Industrial and Engineering Chemistry Research*, vol. 47, pp. 3285–3288, 2008.
- [97] P. D. Godfrin, S. D. Hudson, K. Hong, L. Porcar, P. Falus, N. J. Wagner, and Y. Liu, “Short-time glassy dynamics in viscous protein solutions with competing interactions,” *Phys. Rev. Lett.*, vol. 115, p. 228302, 2015.
- [98] V. Sharma, A. Jaishankar, Y. Wang, and G. H. McKinley, “Rheology of globular proteins: apparent yield stress, high shear rate viscosity and interfacial viscoelasticity of bovine serum albumin solutions,” *Soft Matter*, vol. 7, pp. 5150–5160, 2011.
- [99] A. M. Puertas and T. Voigtmann, “Microrheology of colloidal systems,” *Journal of Physics: Condensed Matter*, vol. 26, p. 243101, 2014.
- [100] A. S. Parmar and M. Muschol, “Hydration and hydrodynamic interactions of lysozyme: Effects of chaotropic versus kosmotropic ions,” *Biophysical Journal*, vol. 97, pp. 590–598, 2009.
- [101] P. N. Pusey and W. van Megen, “Phase behaviour of concentrated suspensions of nearly hard colloidal spheres,” *Nature*, vol. 320, pp. 340–342, 1986.
- [102] P. N. Pusey, *Colloidal Suspensions*, In: *Liquids, Freezing and Glass Transition* (J. P. Hansen and D. Levesque and J. Zinn-Justin, eds.). North-Holland, Amsterdam, 1991.
- [103] G. Bryant, S. R. Williams, L. Qian, I. K. Snook, E. Perez, and F. Pincet, “How hard is a colloidal “hard-sphere” interaction?,” *Phys. Rev. E*, vol. 66, p. 060501, 2002.
- [104] C. P. Royall, W. C. K. Poon, and E. R. Weeks, “In search of colloidal hard spheres,” *Soft Matter*, vol. 9, pp. 17–27, 2013.
- [105] L. Antl, J. Goodwin, R. Hill, R. Ottewill, S. Owens, S. Papworth, and J. Waters, “The preparation of poly(methyl methacrylate) latices in non-aqueous media,” *Colloids and Surfaces*, vol. 17, pp. 67 – 78, 1986.
- [106] P. Maßhoff, I. Elsner, M. A. Escobedo-Sánchez, J. P. Segovia-Gutiérrez, A. Pamvouxoglou, and S. U. Egelhaaf, “Shear-induced crystallisation in binary colloidal suspensions investigated using confocal microscopy,” *Journal of Physics: Materials*, vol. 3, p. 035004, 2020.
- [107] J. P. Segovia-Gutiérrez, M. A. Escobedo-Sánchez, E. Sarmiento-Gómez, and S. U. Egelhaaf, “Diffusion of anisotropic particles in random energy landscapes—an experimental study,” *Frontiers in Physics*, vol. 7, p. 224, 2020.
- [108] D. Quemada, “Rheology of concentrated disperse systems and minimum energy dissipation principle,” *Rheologica Acta*, vol. 16, pp. 82–94, 1977.

- 
- [109] A. J. Banchio, J. Bergenholtz, and G. Nägele, “Rheology and dynamics of colloidal suspensions,” *Phys. Rev. Lett.*, vol. 82, pp. 1792–1795, 1999.
- [110] T. Zemb and P. Lindner, *Neutron, X-rays and Light. Scattering Methods Applied to Soft Condensed Matter*. Elsevier.
- [111] P. N. Pusey and W. van Meegen, “Detection of small polydispersities by photon correlation spectroscopy,” *The Journal of Chemical Physics*, vol. 80, pp. 3513–3520, 1984.
- [112] H. C. van de Hulst, *Light Scattering from Small Particles*. Dover, 1981.
- [113] C. Bohren and D. R. Huffman, *Absorption and Scattering of Light by Small Particles*. John Wiley and Sons, Ltd., 2007.
- [114] C. Mätzler, “Matlab functions for mie scattering and absorption: Research report no. 2002-08,”
- [115] <http://www.philiplaven.com/mieplot.htm>.
- [116] B. L. Inc., “Tech support doc 0021: Material properties of polystyrene and poly(methyl methacrylate)(pmma) microspheres.” <https://www.bangslabs.com/sites/default/files/imce/docs/TSD0021MaterialPropertiesWeb.pdf>.
- [117] G. J. Ojeda-Mendoza, H. Contreras-Tello, and L. F. Rojas-Ochoa, “Refractive index matching of large polydisperse silica spheres in aqueous suspensions,” *Colloids and Surfaces A: Physicochemical and Engineering Aspects*, vol. 538, pp. 320–326, 2018.
- [118] A. Bérut, O. Pouliquen, and Y. Forterre, “Brownian granular flows down heaps,” *Phys. Rev. Lett.*, vol. 123, p. 248005, 2019.
- [119] D. Bi, S. Henkes, K. E. Daniels, and B. Chakraborty, “The statistical physics of athermal materials,” *Annual Review of Condensed Matter Physics*, vol. 6, pp. 63–83, 2015.
- [120] K. Kanazawa, T. G. Sano, T. Sagawa, and H. Hayakawa, “Minimal model of stochastic athermal systems: Origin of non-gaussian noise,” *Phys. Rev. Lett.*, vol. 114, p. 090601, 2015.
- [121] C. Ancey, N. Andreini, and G. Epely-Chauvin, “Granular suspension avalanches. i. macro-viscous behavior,” *Physics of Fluids*, vol. 25, p. 033301, 2013.
- [122] N. Menon and D. J. Durian, “Particle motions in a gas-fluidized bed of sand,” *Phys. Rev. Lett.*, vol. 79, pp. 3407–3410, 1997.

- 
- [123] N. Menon and D. J. Durian, “Diffusing-wave spectroscopy of dynamics in a three-dimensional granular flow,” *Science*, vol. 275, pp. 1920–1922, 1997.
- [124] L. L. Xie, M. J. Biggs, D. . Glass, A. S. McLeod, S. U. Egelhaaf, and G. Petekidis, “Granular temperature distribution in a gas fluidized bed of hollow microparticles prior to onset of bubbling,” *Europhysics Letters (EPL)*, vol. 74, pp. 268–274, 2006.
- [125] M. Biggs, D. Glass, L. Xie, V. Zivkovic, A. Buts, and M. A. Curt Kounders, “Granular temperature in a gas fluidized bed,” *Granular Matter*, vol. 10, pp. 63–73, 2008.
- [126] V. Zivkovic, M. Biggs, D. Glass, P. Pagliai, and A. Buts, “Granular temperature in a liquid fluidized bed as revealed by diffusing wave spectroscopy,” *Chemical Engineering Science*, vol. 64, pp. 1102–1110, 2009.
- [127] K. Kim and H. K. Pak, “Diffusing-wave spectroscopy study of microscopic dynamics of three-dimensional granular systems,” *Soft Matter*, vol. 6, pp. 2894–2900, 2010.
- [128] P. Born, S. Reinhold, and M. Sperl, “Probing density waves in fluidized granular media with diffusing-wave spectroscopy,” *Phys. Rev. E*, vol. 94, p. 032901, 2016.
- [129] A. Amon, A. Mikhailovskaya, and J. Crassous, “Spatially resolved measurements of micro-deformations in granular materials using diffusing wave spectroscopy,” *Review of Scientific Instruments*, vol. 88, p. 051804, 2017.
- [130] M. L. Cowan, J. H. Page, and D. A. Weitz, “Velocity fluctuations in fluidized suspensions probed by ultrasonic correlation spectroscopy,” *Phys. Rev. Lett.*, vol. 85, pp. 453–456, 2000.
- [131] M. Kohyama, T. Norisuye, and Q. Tran-Cong-Miyata, “High frequency dynamic ultrasound scattering from microsphere suspensions,” *Polymer Journal*, vol. 40, pp. 398–399, 2008.
- [132] M. Kohyama, T. Norisuye, and Q. Tran-Cong-Miyata, “Dynamics of microsphere suspensions probed by high-frequency dynamic ultrasound scattering,” *Macromolecules*, vol. 42, pp. 752–759, 2009.
- [133] A. Nagao, M. Kohyama, T. Norisuye, and Q. Tran-Cong-Miyata, “Simultaneous observation and analysis of sedimentation and floating motions of microspheres investigated by phase mode-dynamic ultrasound scattering,” *Journal of Applied Physics*, vol. 105, p. 023526, 2009.
- [134] A. Nagao, T. Norisuye, T. Yawada, M. Kohyama, and Q. Tran-Cong-Miyata, “Collective motion of microspheres in suspensions observed by phase-mode

- dynamic ultrasound scattering technique,” *Ultrasonics*, vol. 52, pp. 628–635, 2012.
- [135] M. L. Cowan, J. H. Page, T. Norisuye, and D. A. Weitz, “Dynamic sound scattering: Field fluctuation spectroscopy with singly scattered ultrasound in the near and far fields,” *The Journal of the Acoustical Society of America*, vol. 140, pp. 1992–2001, 2016.
- [136] R. Cerbino, L. Peverini, M. A. C. Potenza, A. Robert, P. Bösecke, and M. Giglio, “X-ray-scattering information obtained from near-field speckle,” *Nat. Phys.*, vol. 4, pp. 238–243, 2008.
- [137] R. J. Adrian, “Particle-imaging techniques for experimental fluid mechanics,” *Annu. Rev. Fluid Mech.*, vol. 23, pp. 261–304, 1991.
- [138] P. N. Segrè, E. Herbolzheimer, and P. M. Chaikin, “Long-range correlations in sedimentation,” *PRL*, vol. 79, pp. 2574–2577, 1997.
- [139] S.-J. Lee and G.-B. Kim, “X-ray particle image velocimetry for measuring quantitative flow information inside opaque objects,” *Journal of Applied Physics*, vol. 94, pp. 3620–3623, 2003.
- [140] G. B. Kim and S. J. Lee, “X-ray piv measurements of blood flows without tracer particles,” *Experiments in Fluids*, vol. 41, pp. 195–200, 2006.
- [141] Y. Wang, X. Liu, K.-S. Im, W.-K. Lee, J. Wang, K. Fezzaa, D. L. S. Hung, and J. R. Winkelman, “Ultrafast x-ray study of dense-liquid-jet flow dynamics using structure-tracking velocimetry,” *Nature Physics*, vol. 4, pp. 305–309, 2008.
- [142] A. Fouras, M. J. Kitchen, S. Dubsy, R. A. Lewis, S. B. Hooper, and K. Hourigan, “The past, present, and future of x-ray technology for in vivo imaging of function and form,” *Journal of Applied Physics*, vol. 105, p. 102009, 2009.
- [143] S. J. Lee, G. B. Kim, D. H. Yim, and S. Y. Jung, “Development of a compact x-ray particle image velocimetry for measuring opaque flows,” *Review of Scientific Instruments*, vol. 80, no. 3, p. 033706, 2009.
- [144] S. Dubsy, R. A. Jamison, S. C. Irvine, K. K. W. Siu, K. Hourigan, and A. Fouras, “Computed tomographic x-ray velocimetry,” *Appl. Phys. Lett.*, vol. 96, p. 023702, 2010.
- [145] F. Guillard, B. Marks, and I. Einav, “Dynamic x-ray radiography reveals particle size and shape orientation fields during granular flow,” *Scientific Reports*, vol. 7, p. 8155, 2017.

- [146] M. Y. Naz, S. A. Sulaiman, S. Shukrullah, A. Ghaffar, Y. Khan, and I. Ahmad, “Piv investigations on particle velocity distribution in uniform swirling regime of fluidization,” *Granular Matter*, vol. 19, p. 40, 2017.
- [147] A. Ruhlandt and T. Salditt, “Time-resolved x-ray phase-contrast tomography of sedimenting micro-spheres,” *New Journal of Physics*, vol. 21, p. 043017, 2019.
- [148] P. N. Segrè, W. van Meegen, P. N. Pusey, K. Schätzel, and W. Peters, “Two-colour dynamic light scattering,” *J. Mod. Opt.*, vol. 42, pp. 1929–1952, 1995.
- [149] M. Baur, *X-ray radiography of granular systems - particle densities and dynamics: Röntgen Radiographie granularer Systeme - Dichte und Dynamik der Teilchen*. PhD thesis, 2020.
- [150] M. Schröter, D. I. Goldman, and H. L. Swinney, “Stationary state volume fluctuations in a granular medium.,” *Physical review. E, Statistical, nonlinear, and soft matter physics*, vol. 71, p. 030301, 2005.
- [151] M. Baur, J. Claussen, S. Gerth, J. Kollmer, T. Shreve, N. Uhlmann, and T. Pöschel, “How to measure the volume fraction of granular assemblies using x-ray radiography,” *Powder Technology*, vol. 356, pp. 439–442, 2019.
- [152] A. C. Konstantinidis, M. B. Szafraniec, R. D. Speller, and A. Olivo, “The dexela 2923 cmos x-ray detector: A flat panel detector based on cmos active pixel sensors for medical imaging applications,” *Nuclear Instruments and Methods in Physics Research Section A: Accelerators, Spectrometers, Detectors and Associated Equipment*, vol. 689, pp. 12–21, 2012.
- [153] M. Baur, N. Uhlmann, T. Pöschel, and M. Schröter, “Correction of beam hardening in x-ray radiograms,” *Review of Scientific Instruments*, vol. 90, p. 025108, 2019.
- [154] W. Thielicke and E. Stamhuis, “Towards user-friendly, affordable and accurate digital particle image velocimetry in matlab,” *Journal of Open Research Software*, vol. 2(1), p. 30.
- [155] M. Raffel, C. Willert, F. Scarano, C. J. Kähler, S. T. Wereley, and J. Kompenhans, *Particle Image Velocimetry A Practical Guide*. Springer-Verlag, 2018.
- [156] W. Thielicke, *The flapping flight of birds: Analysis and application*. PhD thesis, 2014.
- [157] J. F. Richardson and W. N. Zaki, “Sedimentation and fluidisation: Part i,” *Chemical Engineering Research and Design*, vol. 75, pp. S82–S100, 1997.

- [158] A. S. Michaels and J. C. Bolger, “Settling rates and sediment volumes of flocculated kaolin suspensions,” *Ind. Eng. Chem. Fund.*, vol. 1, pp. 24–33, 1962.
- [159] D. T. N. Chen, Q. Wen, P. A. Janmey, J. C. Crocker, and A. G. Yodh, “Rheology of soft materials,” *Annu. Rev. Condens. Matter Phys.*, vol. 1, pp. 301–322, 2010.
- [160] G. Petekidis, P. N. Pusey, A. Moussaïd, S. Egelhaaf, and W. C. K. Poon, “Shear-induced yielding and ordering in concentrated particle suspensions,” *Physica A: Statistical Mechanics and its Applications*, vol. 306, pp. 334–342, 2002.
- [161] P. A. Smith, *Colloidal gels under oscillatory shear*. PhD thesis, School of Physics, University of Edinburgh, 2004.
- [162] M. Laurati, K. J. Mutch, N. Koumakis, J. Zausch, C. P. Amann, A. B. Schofield, G. Petekidis, J. F. Brady, J. Horbach, M. Fuchs, and S. U. Egelhaaf, “Transient dynamics in dense colloidal suspensions under shear: shear rate dependence,” *Journal of Physics: Condensed Matter*, vol. 24, p. 464104, 2012.
- [163] P. Maßhoff, *Colloidal Spheres under Shear: The Interplay between Macroscopic Deformation and Microscopic Properties*. PhD thesis, Heinrich Heine Universität Düsseldorf, 2019.
- [164] D. York, “Least-squares fitting of a straight line,” *Can. J. Phys.*, vol. 44, pp. 1079–1086, 1966.